Studies of Beam Instabilities and Associated Beam-Loss on a High-Intensity Proton Synchrotron



Robert Williamson

Trinity College

University of Oxford

A thesis submitted for the degree of

Doctor of Philosophy

Hilary Term, 2023

Dedication

This thesis has been 8 years in the making and a lot has happened in that time. I have gone through seasons of joyful elation such as the birth of my two sons: George (2015) and Samuel (2018), moving house and successful promotion (2020). Unfortunately, there have also been periods of great sadness, such as my father's deteriorating health and the global coronavirus pandemic, both of which have had far reaching consequences for my family and me.

I dedicate this thesis firstly to God who has blessed me with a curiosity regarding how things work together with the necessary skills to delve into the mechanics. Secondly, this is dedicated to my wife, Michelle, without whose consistent love and support I would not even have dreamt of starting on this journey, let alone completing it. Together, we've shared the highs and the lows of life where Michelle's hopeful and empassioned outlook on life has been a constant source of strength. Although raising two children during the course of these studies has been challenging at times, they have also provided a welcome grounding in what really matters in life and an unending source of delight and wonder.

I also dedicate this work to my wider family who have, in a myriad of different ways, supported and encouraged me. My mother, Diane, has always believed in my abilities even when I have had my doubts. Her wise words through this study, as always, have been more than welcome. My father, Malcolm, has instilled in me a love of science and physics in particular. My brothers: James, Christopher and Simon, have pushed me to do my best as well as being a ready (and welcome) source of humour. My mother and father-in-law, Celia and Trevor, have provided steady support throughout, with a curiosity in my research and a focus on its relevance to society.

Acknowledgements

There are many people who have helped me get to this point:

- My supervisors: Prof. Brian Foster and Dr. Chris Warsop (although I would also like to acknowledge the support of my two previous supervisors Dr. Andrei Seryi and Dr. Ivan Konoplev).

  - I thank Brian for his insight into the Oxford DPhil process and huge experience with accelerators and the mechanics of PhDs.

  - I thank Chris for his consistant patience, tenacity, passion for the subject and belief in my abilities over many years (not just the last 8). Also, a special thanks for sharing in my stresses, fears and worries whilst pushing me forwards with a healthy mix of beer, politics, humour and a good dose of friendship.

- Dr. Ben Pine, Bryan Jones and Rob Mathieson for experimental, technical and many other kinds of support.

- Dr. John Thomason, Dean Adams and Hayley Cavanagh for directly (and indirectly) supporting me in the work of this thesis and shouldering various commitments so I could retain my focus.

- The Diagnostics Section, Ring Accelerator Physics Section and ISIS Crew.

- The ISIS Facility, Accelerator Division and Synchrotron Group.

- The John Adams Institute and the Science and Technology Facilities Council.

Abstract

High-intensity hadron accelerators provide beams for many different applications around the world: from high energy particle physics to drivers of spallation neutron sources such as ISIS. These facilities face a common, significant challenge: the control and mitigation of beam-loss, often defining the limit to the beam intensity achievable.

Beam-loss may be driven by many different processes including transitions between accelerators, RF capture and non-linearities in the accelerator's magnetic lattice. Collective effects, such as space charge and beam instabilities, may also be a major source of beam-loss, particularly in accelerators pushing for higher intensities. The interaction of space charge with beam instabilities is a key topic of current research and development.

The head-tail instability drives beam-loss on a number of high intensity hadron accelerators around the world. Measurements of the instability are shown from the ISIS Neutron and Muon Source at the Rutherford Appleton Laboratory in the UK. These are shown in normal, Rapid Cycling Synchrotron, operation as well as in a new operating mode: bunched beams stored at injection energy. The new mode is utilised to explore the instability on ISIS systematically, with a simplified experimental setup for comparison with established theory, as a function of the vertical betatron tune and the vertical beam size.

Particle-in-cell tracking simulations of ISIS in the new operating mode are performed, varying the associated beam and accelerator parameters, and the results compared to observed instability characteristics. Further simulations include a self-consistent model of the beam's transverse space charge field, allowing analyses of its effect on the instability characteristics.

Experimental and simulation results are compared with predictions derived from a well established theory of head-tail dynamics which does not include the effects of space charge. Recent theories including these effects are summarised and the results discussed in the light of those theories.

Key agreements and discrepancies between experiment, simulation and theory are presented together with directions for future research. Finally, the impact of this research on the operation of current and future high intensity hadron accelerators is discussed with particular focus on current ISIS operations.

Contents

List of Figures **x**

List of Tables **xxi**

List of Abbreviations **xxiv**

1 Introduction **1**

1.1 Motivation for High-Intensity Hadron Machines 3

1.1.1 Examples of Existing High-Intensity Hadron Machines . . . 4

1.1.1.1 Paul Scherrer Institute, PSI 4

1.1.1.2 Spallation Neutron Source, SNS 4

1.1.1.3 European Spallation Source, ESS 5

1.1.1.4 China Spallation Neutron Source, CSNS 6

1.1.1.5 Japan Proton Accelerator Research Complex, J-PARC 6

1.1.1.6 European Organization for Nuclear Research, CERN 7

1.1.1.7 Fixed Field Accelerators, FFAs 8

1.2 Challenges for High-Intensity Accelerators 9

1.3 Beam Instabilities 10

1.3.1 Head-Tail Instability 11

1.4 Wakes and Impedances 11

1.5 Motivation for this Study 13

1.6 Importance for Current and Future Accelerators 14

1.7 Thesis Outline 14

2 ISIS and ISIS-II **16**

2.1 ISIS Neutron and Muon Source 16

2.1.1 ISIS Injector 17

2.1.1.1 Ion Source 17

2.1.1.2 Low-Energy Beam Transport and Radio-Frequency Quadrupole 19

2.1.1.3 Drift-Tube Linac 19

2.1.1.4 High-Energy Drift Space 20

2.1.2 ISIS Synchrotron 20

2.1.2.1 Injection . . . 21
2.1.2.2 Acceleration and Trapping . . . 23
2.1.2.3 Transverse Dynamics . . . 25
2.1.2.4 Collimation and Loss Control . . . 25
2.1.2.5 Extraction . . . 26
2.1.2.6 High-Intensity Operation . . . 27
2.1.2.7 Machine Physics Operation . . . 27
2.1.2.8 Storage Ring Mode . . . 28
2.1.3 Diagnostics on the ISIS Synchrotron . . . 28
2.1.3.1 Beam Intensity Monitor . . . 29
2.1.3.2 Beam-Loss Monitor . . . 29
2.1.3.3 Beam Position Monitor . . . 31
2.1.3.4 Beam Profile Monitor . . . 32
2.1.3.5 Other Diagnostics . . . 33
2.2 ISIS-II Concept . . . 34
2.2.1 ISIS-II Beam Specification . . . 35

3 Head-Tail Instability Theory 37
3.1 Introduction . . . 37
3.2 Wakes and Impedances . . . 37
3.2.1 Wake Fields and Wake Functions . . . 38
3.2.2 Impedances . . . 39
3.2.3 Common Examples of Wake Functions and Impedances . . . 40
3.2.3.1 Resistive Wall . . . 41
3.2.3.2 Resonator . . . 42
3.2.3.3 Broadband impedances . . . 42
3.3 Head-Tail Instability Theory . . . 43
3.3.1 Sacherer's Theory . . . 43
3.3.1.1 Linearised Vlasov Equation . . . 43
3.3.1.2 The Wake Force . . . 45
3.3.1.3 Sacherer's Integral Equation . . . 46
3.3.1.4 Solutions of Sacherer's Integral Equation . . . 47
3.3.1.5 Sacherer's Radial Modes . . . 49
3.3.1.6 Growth Rate . . . 52
3.3.2 Rees' Theory . . . 53
3.3.3 Transverse Mode Coupling Instability, TMCI . . . 54
3.4 Influence of Space Charge . . . 54
3.4.1 What is Space Charge? . . . 54
3.4.1.1 Space Charge Tune Shift . . . 56
3.4.2 Role of Space Charge in Instabilities . . . 57

3.4.2.1 Theoretical Treatments . . . 58
3.4.2.2 Simulations . . . 59
3.4.2.3 Experiments . . . 61
3.5 Instability Simulation . . . 61
3.5.1 PyHEADTAIL . . . 63
3.5.1.1 Collective Effects . . . 63
3.5.1.2 High Performance Computing . . . 65

4 Head-Tail in ISIS Operations 66
4.1 Introduction . . . 66
4.2 Categorisation of Instability . . . 66
4.2.1 Mode Structure . . . 67
4.2.2 Instability Growth Rate . . . 70
4.2.3 Theoretical Interpretation . . . 73
4.3 Head-Tail Mitigation . . . 74
4.3.1 Vertical Tune . . . 74
4.3.2 Longitudinal Bunch Shape . . . 75
4.3.3 Injection Painting . . . 75
4.4 Current and Future Operations . . . 76

5 SRM: Head-Tail Instability as a Function of Vertical Tune 78
5.1 Introduction . . . 78
5.2 Measurement of Effective Impedance Using Coasting Beams . . . 79
5.3 Overview of Measurements in BSRM . . . 82
5.4 Head-Tail Instability as a Function of Vertical Tune . . . 86
5.4.1 Introduction . . . 86
5.4.2 Head-Tail Instability Mode Structure . . . 93
5.4.3 Head-Tail Instability in Frequency Domain . . . 94
5.4.4 Head-Tail Instability Growth Rate Versus Frequency . . . 96
5.5 Simulations of Head-Tail Instability as a Function of Vertical Tune . 97
5.5.1 Setup and Introduction . . . 97
5.5.1.1 Beam and Lattice Parameters . . . 98
5.5.1.2 PyHEADTAIL Simulation Setup . . . 100
5.5.2 Without Transverse Space Charge . . . 101
5.5.2.1 Head-Tail Instability Mode Structure . . . 103
5.5.2.2 Head-Tail Instability in Frequency Domain . . . 107
5.5.2.3 Head-Tail Instability Growth Rate Versus Frequency 108
5.5.3 With Transverse Space Charge . . . 109
5.5.3.1 Head-Tail Instability Mode Structure . . . 111
5.5.3.2 Head-Tail Instability in Frequency Domain . . . 115
5.5.3.3 Head-Tail Instability Growth Rate Versus Frequency 116
5.6 Summary . . . 117

6 SRM: Head-Tail Instability as a Function of Vertical Beam Size 119
6.1 Introduction . . . 119
6.1.1 Experimental Setup . . . 120
6.1.1.1 Vertical Beam Profile Measurement . . . 122
6.2 Head-Tail Instability as a Function of Vertical Beam Size . . . 124
6.2.1 Head-Tail Instability Mode Structure . . . 132
6.2.2 Head-Tail Instability in Frequency Domain . . . 134
6.2.3 Head-Tail Instability Growth Rate Versus Frequency and Beam Size . . . 135
6.3 Simulations of Head-Tail as a Function of Vertical Beam Size . . . 138
6.3.1 Setup and Introduction . . . 138
6.3.1.1 Beam and Lattice Parameters . . . 138
6.3.2 Simulations Without Transverse Space Charge . . . 140
6.3.2.1 Head-Tail Instability Mode Structure . . . 142
6.3.2.2 Head-Tail Instability in Frequency Domain . . . 151
6.3.2.3 Head-Tail Instability Growth Rate Versus Frequency and Beam Size . . . 152
6.3.3 With Transverse Space Charge . . . 153
6.3.3.1 Head-Tail Instability Mode Structure . . . 156
6.3.3.2 Head-Tail Instability in Frequency Domain . . . 163
6.3.3.3 Head-Tail Instability Growth Rate Versus Frequency and Beam Size . . . 164
6.4 Summary . . . 167

7 Comparison with Theory 170
7.1 Introduction . . . 170
7.1.1 Head-Tail in ISIS RCS Operations . . . 170
7.1.1.1 Role of Space Charge . . . 172
7.2 Head-Tail Instability as a Function of Vertical Tune . . . 173
7.2.1 Introduction . . . 173
7.2.2 Predictions from Sacherer's theory . . . 173
7.2.2.1 Head-Tail Instability Mode Structure . . . 174
7.2.2.2 Head-Tail Instability in Frequency Domain . . . 176
7.2.2.3 Head-Tail Instability Growth Rate Versus Baseband Frequency . . . 177
7.2.3 Comparison Between Theory and Experiment . . . 178
7.2.3.1 Head-Tail Instability Mode Structure . . . 178
7.2.3.2 Head-Tail Instability in Frequency Domain . . . 179
7.2.3.3 Head-Tail Instability Growth Rate Versus Baseband Frequency . . . 182

7.2.3.4 Summary and Effect of Transverse Space Charge . 183
7.2.4 Comparison Between Theory and Simulations 186
7.2.4.1 Head-Tail Instability Mode Structure 186
7.2.4.2 Head-Tail Instability in Frequency Domain 188
7.2.4.3 Head-Tail Instability Growth Rate Versus Baseband Frequency 190
7.2.4.4 Summary and Effect of Transverse Space Charge . 192
7.3 Head-Tail Instability as a Function of Vertical Beam Size 193
7.3.1 Introduction 193
7.3.2 Predictions from Sacherer's Theory 193
7.3.3 Comparison Between Theory and Experiment 195
7.3.3.1 Head-Tail Instability Mode Structure 195
7.3.3.2 Head-Tail Instability in Frequency Domain 196
7.3.3.3 Head-Tail Instability Growth Rate Versus Baseband Frequency and Beam Size 197
7.3.3.4 Summary and Effect of Transverse Space Charge . 198
7.3.4 Comparison Between Theory and Simulations 200
7.3.4.1 Head-Tail Instability Mode Structure 200
7.3.4.2 Head-Tail Instability in Frequency Domain 201
7.3.4.3 Head-Tail Instability Growth Rate Versus Baseband Frequency and Beam Size 203
7.3.4.4 Summary and Effect of Transverse Space Charge . 206
7.4 Summary 208

8 Conclusion **210**
8.1 Introduction 210
8.2 Head-Tail Instability Experiments on ISIS 210
8.2.1 Thesis Achievements 210
8.2.2 Plans for Future Research 212
8.3 Simulations of the Head-Tail Instability 213
8.3.1 Thesis Achievements 213
8.3.2 Plans for Future Research 214
8.4 Comparison with Head-Tail Instability Theory 215
8.4.1 Thesis Achievements 215
8.4.2 Plans for Future Research 217
8.5 Application and Impact on ISIS Operations 217
8.5.1 Thesis Achievements 217
8.5.2 Plans for Future Research 219

References **220**

List of Figures

1.1 Beam current versus beam energy showing the beam power of some of the world's high-intensity proton accelerators. 3
1.2 The 590 MeV proton cyclotron at PSI. Source: PSI website [3]. . . . 5
1.3 Layout of the SNS at ORNL [8]. 5
1.4 Schematic of the ESS. Source: ESS website [4]. 6
1.5 Layout of the CSNS. Source: CSNS website [10]. 6
1.6 Layout of J-PARC. Source: J-PARC website [6]. 7
1.7 Schematic of the CERN accelerator complex. Source: CERN website [13]. 8
1.8 Schematic of a source particle a distance z in front of a witness particle within a bunch, both travelling at velocity $\vec{v}$ through a discontinuity. 12

2.1 Aerial view of the Rutherford Appleton Laboratory on the Harwell Campus including the ISIS Facility (highlighted in red). Taken October 2021 [30]. 16
2.2 The ISIS Neutron and Muon Source from the air. Taken October 2021 [30]. 17
2.3 Schematic of the ISIS Neutron and Muon Facility [30]. 18
2.4 ISIS Penning type H^- ion source [30]. 19
2.5 ISIS 4-vane, 665 keV RFQ prior to installation [30]. 19
2.6 Tank 3 of the ISIS drift-tube linac during cleaning and maintenance [30]. 19
2.7 The ISIS HEDS as it crosses over the synchrotron for injection from the inside radius [30]. 20
2.8 Schematic of the ISIS synchrotron [30]. 22
2.9 Oscilloscope traces of vertical sweeper current (yellow), injection dipole current (blue) and a ring IM (pink) over the injection period. The trigger point is at -0.2 ms and there are 100 µs per division. . . 22
2.10 The ISIS cycle with reference to the main dipole field. 23
2.11 An ISIS 1RF ($h = 2$) cavity prior to installation [30]. 24
2.12 Extraction straight in the ISIS synchrotron (kickers highlighted in yellow and septum in red) [30]. 26

2.13 One of two beam intensity monitors in the ISIS synchrotron [30]. . . 29
2.14 One of the synchrotron BLMs, highlighted in red [30]. 30
2.15 Beam intensity and sum beam-loss traces as a function of time through the injection and acceleration cycle. 31
2.16 Beam-loss monitoring scintillators within one of the ISIS main dipoles [30]. 31
2.17 A synchrotron BPM being calibrated in the laboratory [30]. 32
2.18 A horizontal multi-channel ionisation profile monitor [30]. 33
2.19 A schematic showing the inside of the ionisation profile monitor pictured in figure 2.18. 33
2.20 Example ISIS-II lattice design: dipoles in red, quadrupoles in green and sextupoles in orange [39]. 36

3.1 Schematic showing the "pancake" like electromagnetic fields emitted by a relativistic charged particle. 38
3.2 Frequency spectrum $h_m(\omega)$ for modes 0 to 4 with zero chromaticity. 50
3.3 Longitudinal phase space showing the accumulated chromatic phase slip between the head and the tail of the bunch (assuming negative chromaticity). 50
3.4 BPM difference signal of a single bunch on the k^{th} turn and six turns overlaid for $Q = 4.833$ and: $\chi = 0\,\text{rad}$ (left); $\chi = 5\,\text{rad}$ (middle) and $\chi = 9\,\text{rad}$ (right). Taken from figure 13 in [22]. 51
3.5 Fourier spectrum for four bunches and $Q = 3.75$ for different coupled-bunch modes $n = 0, 1, 2, 3$. The envelope is drawn for $m = 0$ head-tail mode and shifted by the chromatic frequency $\omega_\xi = 1.22\omega_0$. Green lines show the positive and negative frequencies, whereas a network analyzer "sees" the blue lines as reflected in the zero frequency line. 51
3.6 A resistive wall impedance (red) and azimuthal modes $m = 0$ (purple) and $m = 1$ (blue) in the case of a positive chromatic frequency ω_ξ. . 52
3.7 Longitudinal phase space indicating Rees' theory with cancellation between betatron motions of large and small synchrotron amplitude particles. In this $m = 1$ case, there is a single node in the bunch's differential signal. 53

4.1 Beam intensity and sum beam-loss traces as a function of time through the cycle. Loss in the timeframe highlighted is associated with the beam instability. 67
4.2 Turn-by-turn vertical BPM sum (left) and difference (right) signals from the end of injection (0 ms) to half-way through acceleration (5 ms). 68

4.3 Zoomed-in version of figure 4.2. Turn-by-turn vertical BPM sum (left) and difference (right) signal, 2 – 3 ms through acceleration. . . 68
4.4 a) BPM sum (red) and difference (blue) signals showing head-tail behaviour at 2 ms through acceleration. b) FFT of BPM sum and difference signals (red and blue respectively) at 2 ms. Dashed purple lines indicate the position of betatron sidebands. 69
4.5 BPM sum (red) and difference (blue) signal showing head-tail behaviour at 2.6 ms through acceleration. b) FFT of BPM sum and difference signals (red and blue respectively) at 2.6 ms. Dashed purple lines indicate the position of betatron sidebands. 69
4.6 BPM sum (red) and difference (blue) signal showing head-tail behaviour at 1.2 ms through acceleration with 1RF only and low intensity (2.5×10^{12} ppb). b) FFT of BPM sum and difference signals (red and blue respectively) at 1.2 ms. Dashed purple lines indicate the position of betatron sidebands. 70
4.7 FFT of a typical vertical BPM difference signal from 0 – 5 ms. Vertical betatron baseband (BB), first RF harmonic (RF1) and upper and lower betatron sidebands about the first RF harmonic (USB1 and LSB1 respectively) are labelled. 71
4.8 The same vertical BPM difference spectra as figure 4.7 but over a wider frequency range and with the RF harmonics removed for clarity. 71
4.9 Absolute magnitude of the vertical BPM difference signal from 1.5 – 3.0 ms in blue with peaks picked out in red (top: linear vertical scale, bottom: logarithmic vertical scale). Two exponentials are fitted: red dashed from 2.05 – 2.25 ms and black dashed from 2.6 – 2.7 ms with the corresponding fitting equations shown. 72
4.10 Vertical betatron baseband amplitude as a function of time in blue (top: linear vertical scale, bottom: logarithmic vertical scale). Exponential fit from 1 – 2.6 ms in red with fitted equation shown. . 73
4.11 Typical vertical and horizontal tune settings as a function of time through the acceleration cycle. 75
4.12 BPM sum signal at 1.4 ms (red) and 2 ms (blue) showing the deliberate longitudinal profile asymmetry. 76

5.1 Vertical BPM difference signal, top; its Fourier transform as a function of time, middle; dominant betatron sideband (red), exponential fit (dashed black) and normalised beam intensity (dotted blue) as a function of time, bottom. 80
5.2 Measured transverse effective impedance as a function of baseband frequency, measured at a beam intensity of 9.8×10^{12} ppp [91]. . . . 81

5.3 Total RF voltage per revolution as a function of time. 83
5.4 Vertical BPM sum signal (a) and difference signal (b) sliced to show each turn against time (measured $Q_y = 3.882$). 85
5.5 a) FFT of the difference signal from figure 5.4 over the first 2 ms illustrating sideband growth. b) Selected BPM sum and difference spectra with the first few betatron sidebands labelled. 85
5.6 a) A 20-turn extract of the vertical BPM sum signal (blue) and difference signal (red) in figure 5.4, 1.2 ms after injection showing both bunches (head on the left, tail on the right). b) IM (red) and sum of all 39 ring BLMs (blue) versus time. 86
5.7 Vertical betatron sidebands from figure 5.5 (baseband in red and lower and upper sidebands around the first RF harmonic in blue and purple; top: linear vertical axis, bottom: logarithmic vertical axis). Exponential functions are shown in dashed lines with colour matching the sideband fitted and its equation also shown. 87
5.8 Experimental data from head-tail measurements at different vertical tunes (3.690 – 3.800, measured Q_y in brackets): intensity and beam-loss (a – d), vertical BPM sum signal over time (e – h), vertical BPM difference signal over time (i – l), BPM traces over 20 turns (m – p), FFT of BPM data around time of interest (q – t), growth rate fits to betatron sidebands (u – x). 88
5.9 Experimental data from head-tail measurements at different vertical tunes (3.810 – 3.825, measured Q_y in brackets): intensity and beam-loss (a – d), vertical BPM sum signal over time (e – h), vertical BPM difference signal over time (i – l), BPM traces over 20 turns (m – p), FFT of BPM data around time of interest (q – t), growth rate fits to betatron sidebands (u – x). 89
5.10 95 % bunch length (blue), effective bunch length (orange) and oscillating fraction of the bunch (grey) versus tune. Head-tail mode number also indicated. 94
5.11 Growth rate versus betatron BB frequency for "Set 1" in blue and "Set 2" in orange. The effective impedance, as determined from beam-based measurements of coasting beams (figure 5.2), is also shown. 96
5.12 a) Simulated longitudinal parabolic distribution (blue) and a vertical BPM sum signal (red, $Q_{y,\mathrm{set}} = 3.820$, 2.3 ms). b) Simulated transverse waterbag distribution (blue) and a vertical IPM measurement ($I_{\mathrm{VS}} = 35\,\mathrm{A}$), corrected for drift field and space charge distortions (red). . . 100
5.13 Narrowband resonator impedance (orange) as a function of frequency ($f_{\mathrm{res}} = 82\,\mathrm{kHz}$, $Q_{\mathrm{res}} = 10$ and $R_s = 17.2\,\mathrm{k\Omega\,m^{-2}}$). Growth rate as a function of frequency from instability measurements (grey) as a function of vertical tune (figure 5.11). 100

5.14 Simulated vertical BPM sum signal (a) and difference signal (b) sliced to show each turn against time for $Q_y = 3.880$. 102
5.15 a) FFT of the difference signal from figure 5.14 versus time and b) intensity monitor and BLM sum signal versus time. 102
5.16 Simulated vertical BPM sum signal (blue) and difference signal (red) over 20 turns, after 1.4 ms of wakes. 103
5.17 PyHEADTAIL output without transverse space charge for different vertical tunes (3.860 – 3.875): intensity and beam-loss (a – d), longitudinal bunch population over time (e – h), simulated vertical BPM difference over time (i – l), simulated vertical BPM traces over 20 turns (m – p), FFT of simulated BPM data around the time of interest (q – t), growth rate fits to betatron sidebands (u – x). . . . 104
5.18 PyHEADTAIL output without transverse space charge for different vertical tunes (3.880 – 3.895): intensity and beam-loss (a – d), longitudinal bunch population over time (e – h), simulated vertical BPM difference over time (i – l), simulated vertical BPM traces over 20 turns (m – p), FFT of simulated BPM data around the time of interest (q – t), growth rate fits to betatron sidebands (u – x). . . . 105
5.19 Growth rate versus betatron BB frequency for PyHEADTAIL simulations without transverse space charge. 108
5.20 Simulated vertical BPM sum signal (a) and difference signal (b) sliced to show each turn against time for $Q_y = 3.880$. 110
5.21 a) FFT of the difference signal from figure 5.20 versus time and b) intensity monitor and BLM sum signal versus time. 111
5.22 Simulated vertical BPM sum signal (blue) and difference signal (red) over 20 turns, after 1.4 ms of wakes. 111
5.23 PyHEADTAIL output with transverse space charge for different vertical tunes (3.860 – 3.875): intensity and beam-loss (a – d), longitudinal bunch population over time (e – h), simulated vertical BPM difference over time (i – l), simulated vertical BPM traces over 20 turns (m – p), FFT of simulated BPM data around the time of interest (q – t), growth rate fits to betatron sidebands (u – x). . . . 112
5.24 PyHEADTAIL output with transverse space charge for different vertical tunes (3.880 – 3.895): intensity and beam-loss (a – d), longitudinal bunch population over time (e – h), simulated vertical BPM difference over time (i – l), simulated vertical BPM traces over 20 turns (m – p), FFT of simulated BPM data around the time of interest (q – t), growth rate fits to betatron sidebands (u – x). . . . 113
5.25 Growth rate versus betatron BB frequency for PyHEADTAIL simulations with transverse space charge. 116

6.1 Total RF voltage per revolution as a function of time. 121
6.2 Example vertical IPM measurement as a function of time ($I_{\mathrm{VS}} = 35\,\mathrm{A}$, $Q_{y,\mathrm{set}} = 3.810$, uncorrected). 122
6.3 Corrected vertical IPM measurements at 0.6 ms, normalised by profile area, as a function of vertical sweeper current ($Q_{y,\mathrm{set}} = 3.810$). . . . 123
6.4 RMS vertical emittance of the painted beam as a function of the peak "vertical sweeper" current. 124
6.5 Experimental data from head-tail measurements with $Q_{y,\mathrm{set}} = 3.800$ ($Q_{y,\mathrm{meas}} = 3.867$) for different RMS vertical emittances (ϵ_y): intensity and beam-loss (a – d), vertical BPM sum signal over time (e – h), vertical BPM difference signal over time (i – l), BPM traces over 20 turns (m – p), FFT of BPM data around time of interest (q – t), growth rate fits to betatron sidebands (u – x). 125
6.6 Experimental data from head-tail measurements with $Q_{y,\mathrm{set}} = 3.810$ ($Q_{y,\mathrm{meas}} = 3.876$) for different RMS vertical emittances (ϵ_y): intensity and beam-loss (a – d), vertical BPM sum signal over time (e – h), vertical BPM difference signal over time (i – l), BPM traces over 20 turns (m – p), FFT of BPM data around time of interest (q – t), growth rate fits to betatron sidebands (u – x). 126
6.7 Experimental data from head-tail measurements with $Q_{y,\mathrm{set}} = 3.820$ ($Q_{y,\mathrm{meas}} = 3.885$) for different RMS vertical emittances (ϵ_y): intensity and beam-loss (a – d), vertical BPM sum signal over time (e – h), vertical BPM difference signal over time (i – l), BPM traces over 20 turns (m – p), FFT of BPM data around time of interest (q – t), growth rate fits to betatron sidebands (u – x). 127
6.8 Ratio of the effective bunch length to the 95 % bunch length for $Q_{y,\mathrm{set}} = 3.800$ (blue), 3.810 (orange) and 3.820 (grey) versus RMS vertical emittance. 133
6.9 Instability growth rate versus betatron BB frequency for only those beam sizes shown in the previous figures ($\epsilon_{y,\,\mathrm{RMS}} = 10$, 13, 33 and $50\,\pi$ mm mrad). Previous vertical tune scan measurements (figure 5.11) are also shown in light brown. 136
6.10 Instability growth rate versus RMS vertical emittance and vertical tune shown as (a) a 3D surface graph and (b) a contour graph. . . . 137
6.11 Instability growth rate as a function of RMS vertical emittance. . . 137
6.12 Simulated transverse waterbag distributions (blue, yellow for $50\,\pi$ and $10\,\pi$ mm mrad respectively) compared to vertical IPM measurements, corrected for drift field and space charge distortions (red, green at $I_{\mathrm{VS}} = 35$ and 14 A respectively). 140

6.13 Simulated vertical BPM sum signal (a) and difference signal (b) sliced to show each turn against time ($Q_y = 3.880$, $\epsilon_{y,\mathrm{RMS}} = 10\,\pi$ mm mrad, without transverse space charge). 141
6.14 a) FFT of the simulated BPM difference signal from figure 6.13 versus time and b) simulated IM and BLM sum signals versus time ($Q_y = 3.880$, $\epsilon_{y,\mathrm{RMS}} = 10\,\pi$ mm mrad, without transverse space charge). 141
6.15 Simulated vertical BPM sum signal (blue) and difference signal (red) over 20 turns, after 1.64 ms of wakes showing both bunches (head on the left, tail on the right, $Q_y = 3.880$, $\epsilon_{y,\mathrm{RMS}} = 10\,\pi$ mm mrad, without transverse space charge). 142
6.16 PyHEADTAIL simulation output without transverse space charge for different vertical beam emittances at $Q_y = 3.860$: intensity and beam-loss (a – d), longitudinal bunch population over time (e – h), simulated vertical BPM difference over time (i – l), simulated vertical BPM traces over 20 turns (m – p), FFT of simulated BPM data around time point of interest (q – t), growth rate fits to betatron sidebands (u – x). 143
6.17 PyHEADTAIL simulation output without transverse space charge for different vertical beam emittances at $Q_y = 3.870$: intensity and beam-loss (a – d), longitudinal bunch population over time (e – h), simulated vertical BPM difference over time (i – l), simulated vertical BPM traces over 20 turns (m – p), FFT of simulated BPM data around time point of interest (q – t), growth rate fits to betatron sidebands (u – x). 144
6.18 PyHEADTAIL simulation output without transverse space charge for different vertical beam emittances at $Q_y = 3.880$: intensity and beam-loss (a – d), longitudinal bunch population over time (e – h), simulated vertical BPM difference over time (i – l), simulated vertical BPM traces over 20 turns (m – p), FFT of simulated BPM data around time point of interest (q – t), growth rate fits to betatron sidebands (u – x). 145
6.19 PyHEADTAIL simulation output without transverse space charge for different vertical beam emittances at $Q_y = 3.890$: intensity and beam-loss (a – d), longitudinal bunch population over time (e – h), simulated vertical BPM difference over time (i – l), simulated vertical BPM traces over 20 turns (m – p), FFT of simulated BPM data around time point of interest (q – t), growth rate fits to betatron sidebands (u – x). 146

6.20 PyHEADTAIL simulation output without transverse space charge for different vertical beam emittances at $Q_y = 3.900$: intensity and beam-loss (a – d), longitudinal bunch population over time (e – h), simulated vertical BPM difference over time (i – l), simulated vertical BPM traces over 20 turns (m – p), FFT of simulated BPM data around time point of interest (q – t), growth rate fits to betatron sidebands (u – x). 147
6.21 Growth rate versus betatron BB frequency for PyHEADTAIL simulations without transverse space charge as a function of vertical emittance: a) all emittances simulated, b) only those emittances shown in previous figures. 153
6.22 Simulated BPM sum signal (a) and difference signal (b) sliced to show each turn against time ($Q_y = 3.880$, $\epsilon_{y,\mathrm{RMS}} = 10\,\pi$ mm mrad, with transverse space charge). 155
6.23 a) FFT of the simulated BPM difference signal from figure 6.22 versus time and b) simulated intensity monitor and beam-loss monitor sum signals versus time ($Q_y = 3.880$, $\epsilon_{y,\mathrm{RMS}} = 10\,\pi$ mm mrad, with transverse space charge). 155
6.24 Simulated vertical BPM sum signal (blue) and difference signal (red) over 20 turns, after 1.74 ms of wakes ($Q_y = 3.880$, $\epsilon_{y,\mathrm{RMS}} = 10\,\pi$ mm mrad, with transverse space charge). 155
6.25 PyHEADTAIL simulation output with transverse space charge for different vertical beam emittances at $Q_y = 3.860$: intensity and beam-loss (a – d), longitudinal bunch population over time (e – h), simulated vertical BPM difference over time (i – l), simulated vertical BPM traces over 20 turns (m – p), FFT of simulated BPM data around time point of interest (q – t), growth rate fits to betatron sidebands (u – x). 157
6.26 PyHEADTAIL simulation output with transverse space charge for different vertical beam emittances at $Q_y = 3.870$: intensity and beam-loss (a – d), longitudinal bunch population over time (e – h), simulated vertical BPM difference over time (i – l), simulated vertical BPM traces over 20 turns (m – p), FFT of simulated BPM data around time point of interest (q – t), growth rate fits to betatron sidebands (u – x). 158
6.27 PyHEADTAIL simulation output with transverse space charge for different vertical beam emittances at $Q_y = 3.880$: intensity and beam-loss (a – d), longitudinal bunch population over time (e – h), simulated vertical BPM difference over time (i – l), simulated vertical BPM traces over 20 turns (m – p), FFT of simulated BPM data around time point of interest (q – t), growth rate fits to betatron sidebands (u – x). 159

6.28 PyHEADTAIL simulation output with transverse space charge for different vertical beam emittances at $Q_y = 3.890$: intensity and beam-loss (a – d), longitudinal bunch population over time (e – h), simulated vertical BPM difference over time (i – l), simulated vertical BPM traces over 20 turns (m – p), FFT of simulated BPM data around time point of interest (q – t), growth rate fits to betatron sidebands (u – x). 160
6.29 Growth rate versus betatron BB frequency for PyHEADTAIL simulations with transverse space charge as a function of vertical emittance: a) all emittances simulated, b) only those emittances shown in previous figures. 165
6.30 Instability growth rate versus initial RMS vertical emittance and vertical tune for PyHEADTAIL simulations with transverse space charge: (a) a 3D surface graph and (b) a contour graph. 166
6.31 Instability growth rate as a function of RMS vertical emittance for a) PyHEADTAIL simulations including transverse space charge and b) comparison between simulations at $Q_y = 3.870$ and 3.880 with experiment at $Q_{y,\mathrm{set}} = 3.810$ and 3.820. 166

7.1 Sacherer's $h_m(f - f_\xi)$ function for the parameters listed in table 5.3, a vertical tune of $Q_y = 3.880$ and a full bunch length of 450 ns. . . . 175
7.2 a) Zoomed-in bunch power spectrum at $Q_y = 3.880$ with narrowband resonator impedance and betatron sideband overlaid. b) Predicted BPM difference signal (red) and envelope (dashed green) for one bunch over 40 turns for a head-tail mode $m = 3$ at $Q_y = 3.880$ with bunch and lattice parameters used in section 5.4. 175
7.3 Sacherer's h_m function for a vertical tune of $Q_y = 3.880$ and a bunch length of 450 ns, indicating the betatron sideband envelope for a dominant $m = 3$ mode instability: a) with negative frequencies, b) expected observation on a network analyser. 176
7.4 Sacherer's h_m function for a vertical tune of $Q_y = 3.880$ and a bunch length of a) 380 ns and b) 500 ns indicating the betatron sideband envelope for a dominant $m = 2$ and $m = 4$ mode instability respectively. 177
7.5 Narrowband impedance, Sacherer's h_m function for $m = 2 - 4$ and range of vertical BB frequencies in the measurements as a function of vertical tune. 178
7.6 Predicted growth rate of the $m = 3$ head-tail mode as a function of vertical BB frequency. 178
7.7 BPM sum and difference signals over 20 turns, before beam was lost, for three selected vertical tunes ($Q_{y,\mathrm{meas}}$ in brackets). 179

7.8 FFT of BPM difference signals at time point of interest and a calculated h_m overlaid (dotted lines) for three selected vertical tunes ($Q_{y,\mathrm{meas}}$ in brackets). Measured full bunch lengths are a) $\tau_b = 450\,\mathrm{ns}$, b) $\tau_b = 480\,\mathrm{ns}$ and c) $\tau_b = 550\,\mathrm{ns}$. 180
7.9 FFT of BPM difference signals at time point of interest and a calculated h_m overlaid (dotted lines) for three selected vertical tunes ($Q_{y,\mathrm{meas}}$ in brackets). Effective bunch lengths are a) $\tau_\mathrm{e} = 280\,\mathrm{ns}$, b) $\tau_\mathrm{e} = 280\,\mathrm{ns}$ and c) $\tau_\mathrm{e} = 220\,\mathrm{ns}$. 181
7.10 Growth rate versus vertical betatron BB frequency for experimental results in grey ("Set 1" in figure 5.11) and that predicted from Sacherer's theory for a head-tail mode $m = 3$ in blue. 183
7.11 Simulated BPM sum and difference signals (without transverse space charge) over 20 turns, before beam was lost, for three selected vertical tunes. 186
7.12 Simulated BPM sum and difference signals (with transverse space charge) over 20 turns, before beam was lost, for three selected vertical tunes. 187
7.13 FFT of simulated BPM data without transverse space charge, prior to beam-loss, for three selected vertical tunes with h_m overlaid ($m = 0$ – 5, dotted lines). 188
7.14 FFT of simulated BPM data with transverse space charge, prior to beam-loss, for three selected vertical tunes with h_m overlaid ($m = 0$ – 5, dotted lines). 190
7.15 Growth rate versus vertical betatron BB frequency for simulated data with and without transverse space charge (red and purple respectively) and that predicted from Sacherer's theory for a head-tail mode $m = 3$ (blue). 191
7.16 BPM sum and difference signals over 20 turns, before beam was lost, for three selected initial vertical beam RMS emittances with $Q_{y,\mathrm{set}} = 3.800$. 195
7.17 FFT of BPM difference signal around time point of interest for $Q_{y,\mathrm{set}} = 3.800$ ($Q_{y,\mathrm{meas}} = 3.867$) and initial $\epsilon_{y,\mathrm{RMS}} = 10\,\pi\,\mathrm{mm\,mrad}$. Calculated h_m overlaid for a) full bunch length $\tau_b = 520\,\mathrm{ns}$ and b) effective bunch length $\tau_\mathrm{e} = 280\,\mathrm{ns}$. 196
7.18 Growth rate versus vertical betatron BB frequency for selected vertical beam sizes (dictated by the peak "vertical sweeper" current) and that predicted from Sacherer's theory for a head-tail mode $m = 3$ in blue. 198

7.19 Simulated BPM sum and difference signals (without transverse space charge) over 20 turns, before beam was lost, for three selected vertical RMS emittances at $Q_y = 3.890$. 200
7.20 Simulated BPM sum and difference signals (with transverse space charge) over 20 turns, before beam was lost, for three selected vertical RMS emittances at $Q_y = 3.880$. 201
7.21 FFT of simulated BPM data without transverse space charge, prior to beam-loss, for three selected vertical RMS emittances at $Q_y = 3.880$, with h_m overlaid ($m = 0$ – 5, dotted lines). 202
7.22 FFT of simulated BPM data with transverse space charge, prior to beam-loss, for three selected vertical RMS emittances at $Q_y = 3.880$, with h_m overlaid ($m = 0$ – 5, dotted lines). 202
7.23 Growth rate versus betatron BB frequency for PyHEADTAIL simulations without transverse space charge for selected initial RMS vertical emittances and that predicted from Sacherer's theory for a head-tail mode $m = 3$ in blue. 204
7.24 Growth rate versus betatron BB frequency for PyHEADTAIL simulations including transverse space charge for selected initial RMS vertical emittances and that predicted from Sacherer's theory for a head-tail mode $m = 3$ in blue. 205
7.25 Reproduction of figure 4 of [54]: 2D contours of the head-tail growth factor as a function of wake strength, Υ, and space charge parameter, $q = \Delta Q_{\mathrm{SC}}/Q_s$. 206

List of Tables

2.1 Important ISIS synchrotron parameters. 21
2.2 Comparison of main ISIS and ISIS-II synchrotron parameters. . . . 35

5.1 ISIS synchrotron parameters for RCS, SRM and BSRM operations. 79
5.2 Key experimental parameters for measurements of effective impedance in coasting beams as a function of vertical tune, Q_y. 81
5.3 Key experimental parameters for measurements of the head-tail instability in BSRM, as a function of vertical tune, Q_y. 84
5.4 Summary of head-tail instability characteristics in BSRM on ISIS as a function of vertical tune for experiment "Set 1". $Q_{y,\mathrm{set}}$, $Q_{y,\mathrm{meas}}$ = set and measured vertical tunes, m = head-tail mode number, sideband = largest amplitude betatron sideband, f_{BB} = BB frequency, the growth rate is that of the BB, $\tau_{\mathrm{b,\,95\,\%}}$ = 95 % bunch length, τ_{e} = effective bunch length, a figure reference is given, if present. 90
5.5 Summary of head-tail instability characteristics in BSRM on ISIS as a function of vertical tune for experiment "Set 2". $Q_{y,\mathrm{set}}$, $Q_{y,\mathrm{meas}}$ = set and measured vertical tunes, m = head-tail mode number, sideband = largest amplitude betatron sideband, f_{BB} = BB frequency, the growth rate is that of the BB, $\tau_{\mathrm{b,\,95\,\%}}$ = 95 % bunch length, τ_{e} = effective bunch length. 91
5.6 Key simulation parameters for comparison with measurements of the head-tail instability on ISIS in BSRM as a function of Q_y. 98
5.7 Summary of head-tail instability characteristics in simulations of BSRM on ISIS as a function of vertical tune without transverse space charge. Q_y and $Q_{y,\mathrm{meas}}$ = set and measured vertical tunes respectively, m = head-tail mode number, sideband = largest amplitude betatron sideband, f_{BB} = BB frequency, the growth rate is that of the BB, τ_{b} = 95 % bunch length, a figure reference is given, if present. . . . 106
5.8 Summary of head-tail instability characteristics in simulations of BSRM on ISIS as a function of vertical tune with transverse space charge. Q_y and $Q_{y,\mathrm{meas}}$ = set and measured vertical tunes respectively, m = head-tail mode number, sideband = largest amplitude betatron sideband, f_{BB} = BB frequency, the growth rate is that of the BB, τ_{b} = 95 % bunch length, a figure reference is given, if present. . . . 114

6.1 Key experimental parameters for measurements of the head-tail instability in BSRM as a function of vertical beam size. 120
6.2 Summary of head-tail instability characteristics in BSRM on ISIS as a function of vertical beam size for $Q_{y,\mathrm{set}} = 3.790$ and 3.800. $Q_{y,\mathrm{set}}$ and $Q_{y,\mathrm{meas}}$ = set and measured vertical tunes respectively, I_{VS} = peak "vertical sweeper" current, $\epsilon_{y,\ \mathrm{RMS}}$ = initial RMS vertical emittance, m = head-tail mode number, SB = largest amplitude betatron sideband, f_{BB} = baseband frequency, GR = growth rate of the baseband, $\tau_{\mathrm{b}} = 95\,\%$ bunch length, τ_{e} = effective bunch length and a figure reference for the data is given, if present. 128
6.3 Summary of head-tail instability characteristics in BSRM on ISIS as a function of vertical beam size for $Q_{y,\mathrm{set}} = 3.810$ and 3.820. $Q_{y,\mathrm{set}}$ and $Q_{y,\mathrm{meas}}$ = set and measured vertical tunes respectively, I_{VS} = peak "vertical sweeper" current, $\epsilon_{y,\ \mathrm{RMS}}$ = initial RMS vertical emittance, m = head-tail mode number, SB = largest amplitude betatron sideband, f_{BB} = baseband frequency, GR = growth rate of the baseband, $\tau_{\mathrm{b}} = 95\,\%$ bunch length, τ_{e} = effective bunch length and a figure reference for the data is given, if present. 129
6.4 Summary of head-tail instability characteristics in BSRM on ISIS as a function of vertical beam size for $Q_{y,\mathrm{set}} = 3.830$. $Q_{y,\mathrm{set}}$ and $Q_{y,\mathrm{meas}}$ = set and measured vertical tunes respectively, I_{VS} = peak "vertical sweeper" current, $\epsilon_{y,\ \mathrm{RMS}}$ = initial RMS vertical emittance, m = head-tail mode number, SB = largest amplitude betatron sideband, f_{BB} = baseband frequency, GR = growth rate of the baseband, $\tau_{\mathrm{b}} = 95\,\%$ bunch length, τ_{e} = effective bunch length and a figure reference for the data is given, if present. 130
6.5 Key simulation parameters for comparison with BSRM measurements of the head-tail instability as a function of vertical beam size. . . . 139
6.6 Summary of head-tail instability characteristics in PyHEADTAIL simulation results as a function of vertical beam size for $Q_y = 3.860$ and 3.870, without transverse space charge. Q_y and $Q_{y,\mathrm{meas}}$ = set and measured vertical tunes respectively, $\epsilon_{y,\mathrm{RMS}}$ = RMS vertical emittance, m = head-tail mode number, SB = largest amplitude betatron sideband, f_{BB} = BB frequency, GR = BB growth rate, $\tau_{\mathrm{b}} = 95\,\%$ bunch length, a figure reference is given, if present. 148
6.7 Summary of head-tail instability characteristics in PyHEADTAIL simulation results as a function of vertical beam size for $Q_y = 3.880$ and 3.890, without transverse space charge. Q_y and $Q_{y,\mathrm{meas}}$ = set and measured vertical tunes respectively, $\epsilon_{y,\mathrm{RMS}}$ = RMS vertical emittance, m = head-tail mode number, SB = largest amplitude betatron sideband, f_{BB} = BB frequency, GR = BB growth rate, $\tau_{\mathrm{b}} = 95\,\%$ bunch length, a figure reference is given, if present. 149

6.8 Summary of head-tail instability characteristics in PyHEADTAIL simulation results as a function of vertical beam size for $Q_y = 3.900$, without transverse space charge. Q_y and $Q_{y,\mathrm{meas}}$ = set and measured vertical tunes respectively, $\epsilon_{y,\mathrm{RMS}}$ = RMS vertical emittance, m = head-tail mode number, SB = largest amplitude betatron sideband, f_{BB} = BB frequency, GR = BB growth rate, $\tau_{\mathrm{b}} = 95\,\%$ bunch length, a figure reference is given, if present. 150

6.9 Summary of head-tail instability characteristics in PyHEADTAIL simulation results as a function of vertical beam size for $Q_y = 3.860$ and 3.870, with transverse space charge. Q_y and $Q_{y,\mathrm{meas}}$ = set and measured vertical tunes respectively, $\epsilon_{y,\mathrm{RMS}}$ = RMS vertical emittance, m = head-tail mode number, SB = largest amplitude betatron sideband, f_{BB} = BB frequency, GR = BB growth rate, $\tau_{\mathrm{b}} = 95\,\%$ bunch length, a figure reference is given, if present. 161

6.10 Summary of head-tail instability characteristics in PyHEADTAIL simulation results as a function of vertical beam size for $Q_y = 3.880$ and 3.890, with transverse space charge. Q_y and $Q_{y,\mathrm{meas}}$ = set and measured vertical tunes respectively, $\epsilon_{y,\mathrm{RMS}}$ = RMS vertical emittance, m = head-tail mode number, SB = largest amplitude betatron sideband, f_{BB} = BB frequency, GR = BB growth rate, $\tau_{\mathrm{b}} = 95\,\%$ bunch length, a figure reference is given, if present. 162

List of Abbreviations

1RF . . . . . 1st harmonic (fundamental) RF system.

2RF . . . . . 2nd harmonic RF system.

AR . . . . . Accumulator Ring.

BB . . . . . BaseBand betatron sideband.

BLM . . . . . Beam-Loss Monitor.

BPM . . . . . Beam Position Monitor.

BSRM . . . . . Bunched Storage Ring Mode.

CERN . . . . . European Organisation for Nuclear Research.

CSNS . . . . . Chinese Spallation Neutron Source.

DHRF . . . . . Dual Harmonic RF system.

EPB . . . . . Extracted Proton Beamline.

ESS . . . . . European Spallation Source.

FAIR . . . . . Facility for Antiproton and Ion Research in Europe.

FFA . . . . . Fixed Field Accelerator.

FFT . . . . . Fast Fourier Transform.

HEDS . . . . . High-Energy Drift Space.

IM . . . . . Intensity Monitor.

IPM . . . . . Ionisation Profile Monitor.

J-PARC . . . . Japan Proton Accelerator Research Complex.

LEBT . . . . . Low-Energy Beam Transport.

LHC . . . . . Large Hadron Collider.

LSB . . . . . Lower SideBand around an RF harmonic.

MCP . . . . . Micro-Channel Plate.

MEBT . . . . . Medium-Energy Beam Transport.

PIC . . . . . Particle-In-Cell.

ppb . . . . . Protons per bunch.

ppp . . . . . Protons per pulse.

pps . . . . . Pulses per second.

PSB . . . . . CERN's Proton Synchrotron Booster.

RAL . . . . . Rutherford Appleton Laboratory.

RCS . . . . . Rapid Cycling Synchrotron.

RF . . . . . Radio-Frequency.

RFQ . . . . . Radio-Frequency Quadrupole.

RMS . . . . . Root-Mean-Square.

SNS . . . . . Spallation Neutron Source.

SRM . . . . . Storage Ring Mode.

TMCI . . . . . Transverse Mode Coupling Instability.

TS1 . . . . . Target Station 1.

TS2 . . . . . Target Station 2.

USB . . . . . Upper SideBand around an RF harmonic.

And whatever you do, whether in word or deed, do it all in the name of the Lord Jesus, giving thanks to God the Father through him.

— Colossians 3:17 (NIV)

1 Introduction

Since the beginning of the 20$^{\text{th}}$ century, particle accelerators have become one of the primary workhorses of scientific discovery and have revolutionised commercial enterprises. They have been utilised for subjects as diverse as nuclear physics and food sterilisation, inertial fusion and radiotherapy, particle physics and molecular biology, security and information technology. Accelerators have allowed for great advances in science together with practical applications that support and enable our modern lives.

Although it is clear that the development of particle accelerators has increased our understanding of a wide variety of principles of physics, it may not be obvious that the physics of the accelerators themselves is of interest. However, the physics of particle accelerators is itself a very interesting and complex subject mixing together plasma physics, electromagnetism, relativity and many other topics.

The dynamics of single particles and low-intensity beams in complex, self-induced and external, electromagnetic fields already cannot be solved analytically; the situation for high-intensity beams is generally even more challenging. When large numbers of particles are considered, a Vlasov-Maxwell approach can be used. However, fully self-consistent analytical solutions of the Vlasov-Maxwell equations only exist in a small number of cases for the particles' collective motion [1]. As such, numerical methods must then be employed to compute and understand the dynamics.

The subject of beam instabilities is important in the field of accelerator physics, particularly in machines designed to push the boundaries of our current understanding of accelerators (high repetition rate, small beam size, high beam current, *etc.*). The growth rates and thresholds of instabilities, which perturb the beam or cause beam-loss, very often dictate the limits of beam intensity, energy or quality and, when considering new machines, can have a strong influence on the design of the accelerator and its constituent components. The appreciation of how beam instabilities occur, grow and how they may be mitigated or avoided has become a key part of designing and operating accelerators.

The aim of this thesis is to make an in-depth study of the instabilities currently experienced on the ISIS synchrotron with an extensive series of experiments and comparisons to simulations and established theoretical models. These comparisons will allow the creation of a realistic representation of the instabilities observed as a function of key parameters such as the betatron tune, beam size and space charge and will inform how they may be controlled or mitigated. As such, this thesis will include models of both impedances (resistive wall, resonators, *etc.*) and beam dynamics (longitudinal RF, transverse magnetic focusing and space charge). The results and conclusions of this study will be applicable not only to ISIS, but to other high-intensity machines and future accelerators such as ISIS-II.

This opening chapter introduces several concepts that are expounded in the following chapters. In section 1.1, the need for high-intensity hadron machines is outlined with examples of existing accelerators and their uses. Section 1.2 summarises the main challenges faced in operating high-intensity accelerators, including the predominant sources of beam-loss. Beam instabilities, and in particular the head-tail instability, are introduced in section 1.3, in its historical context. The theoretical description of instabilities through beam coupling impedances and their effect as a function of key parameters such as beam intensity, particle distribution and beam energy is established in section 1.4. Section 1.5 establishes the aim and motivation behind the work of this thesis, including how instabilities, their driving sources and effects, can limit machine performance. The importance of this study

for current and future high-intensity machines is summarised in section 1.6. Finally, the outline of this thesis is described in section 1.7.

1.1 Motivation for High-Intensity Hadron Machines

Intense hadron beams are useful in a wide variety of applications. They have been used to create and investigate radioactive nuclei, to serve as the facilities for high-energy particle physics and as drivers for spallation neutron sources such as ISIS [2]. Various proposed facilities also require intense hadron beams in order to achieve their final aim, including drivers for nuclear transmutation, muon accelerators and new designs of fission and fusion reactors. Examples of current and proposed facilities with their associated beam current, energy and power are shown in figure 1.1.

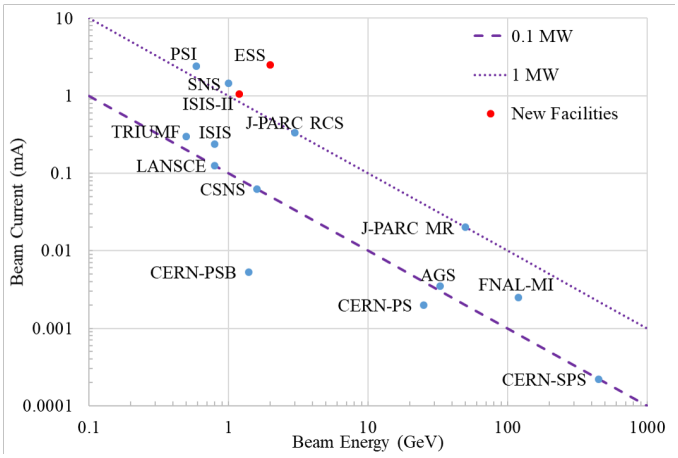


Figure 1.1: Beam current versus beam energy showing the beam power of some of the world's high-intensity proton accelerators.

Different technologies may be employed to create high-intensity particle beams, each with their own advantages and disadvantages. Linacs and cyclotrons are used to provide continuous or high repetition rate intense beams that are ideal for long-pulse neutron sources such as SINQ at the Paul Scherrer Institute [3] or ESS in Lund [4]. Accumulator rings take a continuous beam from a linac at the design energy and form it into bunches before extracting to a target, as at the Spallation Neutron Source (SNS) [5] at Oak Ridge National Laboratory.

Rapid-cycling synchrotrons (RCS), fed from linac front-ends, provide both short pulses as well as acceleration. These are utilised as the injectors for facilities such as the Nuclear and Particle Physics Facility at J-PARC [6] and for short-pulse neutron sources including ISIS (section 2.1) and the Materials and Life Science Experimental Facility at J-PARC. The prospect of using a Fixed Field Accelerator (FFA) to provide intense hadron beams is an active area of research and is a possible alternative design for an ISIS-II upgrade (see section 2.2).

Many existing research facilities employ accumulator rings or RCS accelerators as they are relatively flexible and have demonstrated the capability to provide a wide range of beams with different ions, charge states, emittances (the area occupied by the beam in position and momentum phase space, relating to the physical beam size) and intensities. The limits of these types of circular accelerators are of interest, particularly in reference to beam quality and intensity, with a view to higher performance facilities in the future, and is the subject of ongoing research.

1.1.1 Examples of Existing High-Intensity Hadron Machines

1.1.1.1 Paul Scherrer Institute, PSI

Based in Villigen, Switzerland, PSI performs research in natural and engineering sciences (figure 1.2). It operates a number of facilities including a high-intensity cyclotron operating at 590 MeV, regularly producing a continuous 2.4 mA beam of protons equating to a beam power of 1.4 MW. Operating since 1974, it delivers beam to several user facilities including the spallation neutron source SINQ [3] which uses a target composed of an array of lead rods enclosed in Zircaloy tubes.

1.1.1.2 Spallation Neutron Source, SNS

Operating since 2007, SNS [5] is a short-pulse neutron source driven by a 1 GeV beam of 1.5×10^{14} protons at 60 Hz based at the Oak Ridge National Laboratory in Tennessee, USA (figure 1.3). The design is based on a superconducting linac accelerating H^- ions to the design energy for charge-exchange injection into an accumulator ring. The resultant protons are focused using RF cavities to produce a short bunch (<1 µs long) which is then delivered to a liquid mercury target for

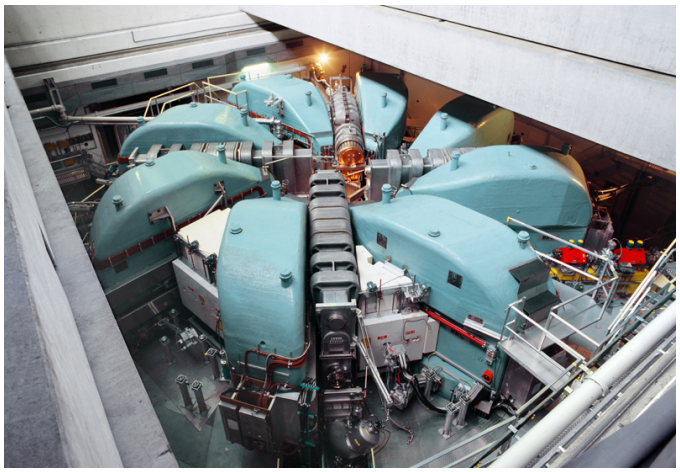


Figure 1.2: The 590 MeV proton cyclotron at PSI. Source: PSI website [3].

neutron production. Baseline operation provides 1.44 MW of beam power on a single target with plans to increase this to 2.8 MW, split between two targets [7].

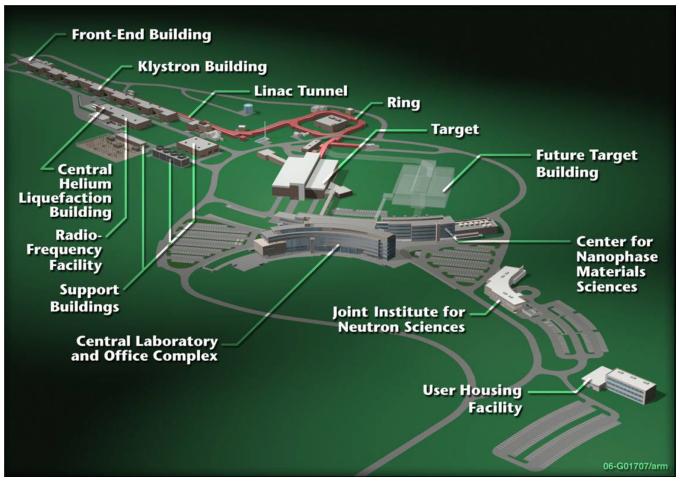


Figure 1.3: Layout of the SNS at ORNL [8].

1.1.1.3 European Spallation Source, ESS

Currently under construction in Lund, Sweden, the European Spallation Source, ESS [4] is a long-pulse neutron source (figure 1.4). A 2 GeV superconducting linac is designed to deliver a 2.86 ms long proton pulse at a repetition rate of 14 Hz, providing 5 MW of beam power on target. The protons will be transported to a target wheel consisting of hundreds of tungsten bricks encased in stainless steel, rotating at 23 1/3 revolutions per minute. First neutrons are expected at a lower beam power of 2 MW in 2025, with the start of a user program the following year [9].

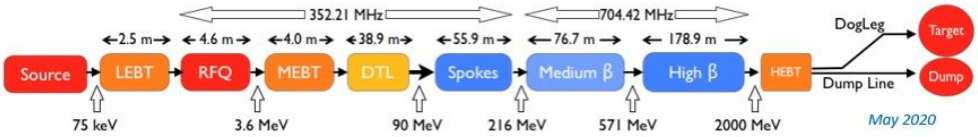


Figure 1.4: Schematic of the ESS. Source: ESS website [4].

1.1.1.4 China Spallation Neutron Source, CSNS

The China Spallation Neutron Source (CSNS) [10] in Dongguan, Guangdong province, China is driven by a 80 MeV H^- linac followed by a 1.6 GeV proton RCS operating at 25 Hz delivering 1.6×10^{13} protons (100 kW) on target for user operations (figure 1.5). The facility has been producing neutrons since August 2017 and reached its design beam power in February 2020. Plans are proposed to increase the linac energy to 300 MeV with superconducting technology and install second harmonic RF cavities in order to increase beam intensity and achieve 500 kW delivered to two targets [11].

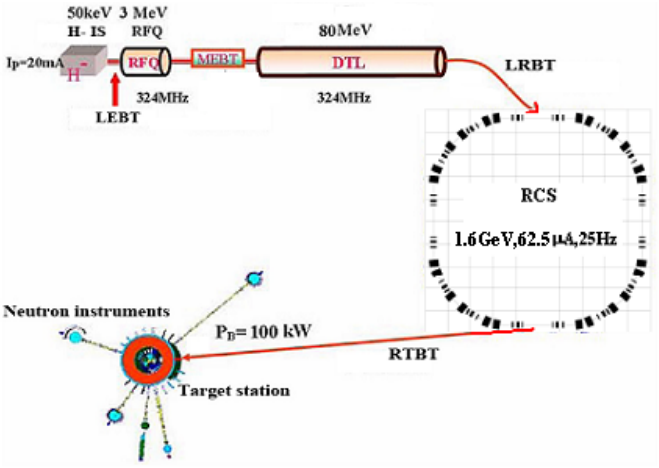


Figure 1.5: Layout of the CSNS. Source: CSNS website [10].

1.1.1.5 Japan Proton Accelerator Research Complex, J-PARC

A multi-disciplinary research complex based at the Tokai site in Ibaraki Prefecture, Japan, J-PARC [6] has been in operation since 2008 and is made up of a suite of accelerators serving three research facilities: the Nuclear and Particle Physics Facility, Nuclear Transmutation Research and the Materials and Life Science Experimental

Facility (figure 1.6). A 400 MeV H^- linac injects into a 25 Hz, 3 GeV proton RCS where most beam is then delivered to the muon and neutron production targets within the Materials and Life Science Experimental Hall. Beam power for user operation is 800 kW, equating to a beam intensity of 6.6×10^{13} protons per pulse, although 1 MW capability has been demonstrated [12]. The RCS also sends protons to a 0.3 Hz, 50 GeV proton synchrotron for hadron physics and neutrino studies.

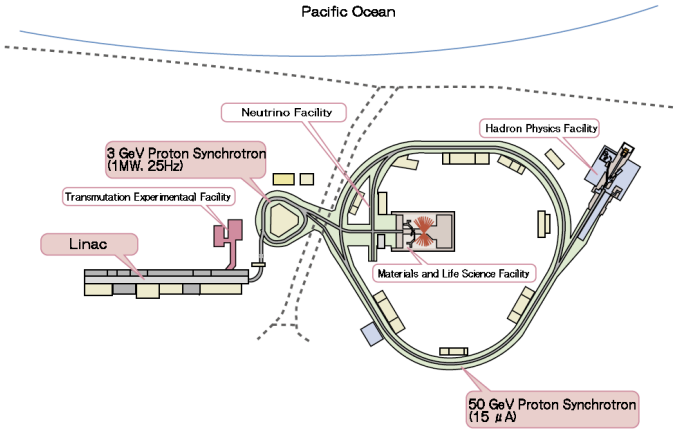


Figure 1.6: Layout of J-PARC. Source: J-PARC website [6].

1.1.1.6 European Organization for Nuclear Research, CERN

CERN [13] is the world's largest particle-physics laboratory and plays host to a large number of accelerators and experiments (figure 1.7). Ratified into existence in 1954 and with its first accelerator (the Synchrocyclotron) built in 1957, at present it operates a complex of nine accelerators and two decelerators, and includes the world's highest energy collider, the Large Hadron Collider (LHC). CERN also hosts a neutron production facility, n-TOF [14], which takes protons from the Proton Synchrotron (PS) and directs them onto a lead target. High-intensity operation and beam instabilities are challenges for many of their machines. It also forms a key part of their research and development in the High Luminosity LHC Project, which includes upgrading the LHC injector chain for, amongst other parameters, increased beam intensities [15].

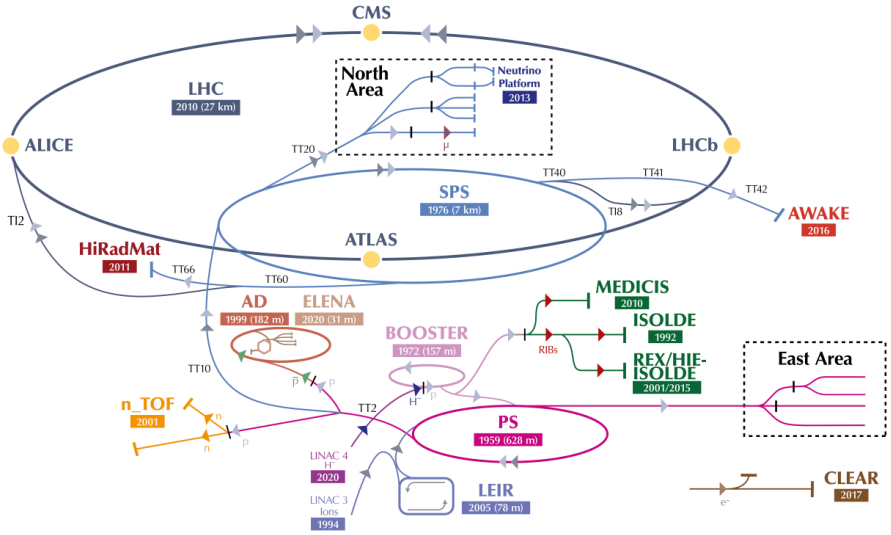


Figure 1.7: Schematic of the CERN accelerator complex. Source: CERN website [13].

Of the synchrotrons operating at CERN, the Proton Synchrotron Booster (PSB) is the most similar to ISIS with a similar energy range (50 MeV – 1.4 GeV) and circumference (157 m); however, it notably differs in that it consists of four stacked rings and currently achieves 1×10^{13} protons per pulse per ring. As part of the LHC Injectors Upgrade [16] just completed, space charge levels are reduced at injection and the PSB brightness doubled by moving to H^- charge-exchange injection from the new Linac 4 and increasing the injection energy to 160 MeV. Furthermore, the extraction energy of the PSB has been increased to 2 GeV to alleviate space charge issues in the next accelerator in the chain, the PS.

1.1.1.7 Fixed Field Accelerators, FFAs

Fixed Field Accelerators, or FFAs, are a very active area of research for intense beams [17]. This type of accelerator design enables high repetition rates to alleviate space charge issues as well as simpler power supplies with lower power consumption for operational cost savings. A test 3 – 12 MeV ring has been proposed at RAL to investigate the feasibility of a full-scale 0.4 – 1.2 GeV FFA to drive the ISIS-II spallation neutron source [18].

1.2 Challenges for High-Intensity Accelerators

The production of high-intensity hadron beams introduces some significant challenges, in particular the need to control and minimise accelerator activation or damage due to beam-loss. Even at relatively low hadron energies of 10s of MeV, beam-loss can result in the radioactivation of machine components, limiting hands-on maintenance and possibly causing physical damage. To allow for regular maintenance of accelerator components, radiation dose levels should be kept below $\sim$1 mSv/h, which have been found to correspond to beam-loss levels of around 1 W/m for beam energies between 0.1 and 10 GeV [19]. Loss at lower energies causes much less activation. Typical uncontrolled beam-loss specifications for high-intensity operation above 100 MeV are less than 0.01 % [20]. Beam-loss may also result in physical damage to accelerator components causing an interruption to user operations for investigation, repairs and an associated radiation dose to personnel involved.

The need to limit and control beam-loss imposes strict demands on the operation of intense hadron accelerators and may be achieved in a number of ways. Uncontrolled loss provides a limit to the achievable beam intensity; machines operating in such a regime may be referred to as "loss-limited". Diagnostic devices such as beam-loss and intensity monitors can be used to monitor actively the levels of beam-loss along an accelerator, allowing interlocks to automatically switch the accelerator off if excessive loss occurs. Collimators are used to restrict the machine aperture in order to localise and control beam-loss and activation to a well-shielded area, protecting other areas of the accelerator facility. Beam-loss may also be controlled such that particles are lost at lower energy, inducing less activation. This often involves a mix of theoretical and empirical optimisations to programmable accelerator systems including steering magnets, RF cavities, trim quadrupoles and higher-order magnets.

There are many different processes that can cause beam-loss in an accelerator. In rings, beam-loss can occur in a wide variety of ways from injection through to extraction. Unavoidable losses may arise due to the intrinsic physics of a process such as charge-exchange injection. Facilities will also encounter accidental beam-loss due to component or power supply failure. Beam-loss may also occur, even at

low intensities, due to mismatched parameters or misalignments which can easily become exacerbated when operating at high intensities. High-intensity effects result in additional mechanisms for loss, causing major concern for current and future facilities, and are the subject of this thesis.

Within synchrotrons the particle beam must be focused longitudinally with RF and transversely with the magnetic lattice structure. Precisely matching the focusing parameters can be a challenge and loss of particles on the edges of the distribution is likely. The magnetic lattice structure is designed to be linear for the most part, allowing for separation of horizontal and vertical dynamics. However, the addition of higher multipoles such as sextupoles for chromaticity correction and octupoles for Landau damping necessarily mixes the dynamics. (Chromaticity is the variation of focusing strength with particle energy and Landau damping is the suppression of unstable particle dynamics by the spread of oscillation frequencies within the particle beam [21].) Even without these higher-order magnets, misalignments and field errors in the linear dipole and quadrupole magnets lead to non-linear field components. This non-linearity leads to the need to avoid betatron resonances which may lead to emittance growth and beam-loss.

1.3 Beam Instabilities

Beam instabilities can be a major source of beam-loss and as such are an active topic of research. Where possible, they are separated into transverse and longitudinal effects (with respect to the beam's direction of travel) and are often dealt with using the concepts of wakes and impedances. Beam interactions with impedances result in an electromagnetic force that can act back on the beam in such a way as to excite resonant behaviour leading to changes in beam behaviour and/or instability (see section 3.3.1).

A key feature of beam instabilities is that their strength increases with beam intensity. Therefore, in order to study these effects, the beam intensity must be varied to explore how the instability changes: is there a threshold for instability? At what intensities can the effect be considered a perturbation on the single-particle

motion? Research and development into the mechanism and driving force behind instabilities is important to allow for appropriate mitigation or corrective measures to minimise degradation in beam quality or beam-loss, or remove the effect altogether.

1.3.1 Head-Tail Instability

Single bunch instabilities of the head-tail type have been observed and studied since the late 1960s. The instability occurs due to the coupling of the betatron oscillations of different particles within the bunch via the transverse electromagnetic wake, combined with the dynamics of synchrotron motion. Dipole oscillations at the head of the bunch drive an electromagnetic wake which interacts with the particles in the tail. After half a synchrotron period, particles at the head and the tail of the bunch switch positions and the process repeats. Depending on the particular beam parameters this may lead to instability, with transverse motion growing exponentially with time.

The standard, established theory to model and predict head-tail dynamics was put forward by Sacherer in the early 1970s [22] but the model makes a number of assumptions in order to simplify the problem and obtain analytical solutions. It assumes the beam is ultrarelativistic, low intensity (space charge is neglected) and makes assumptions about the longitudinal and transverse distributions. Recent work has put forward theoretical models to treat head-tail dynamics with space charge [23–25] (see section 3.4), however there is not yet an established, comprehensive treatment that agrees with all observations.

1.4 Wakes and Impedances

As charged particles move within an accelerator they not only experience forces from the magnets and RF systems, but also from electric and magnetic fields excited by the particles themselves which interact with the surroundings and may act back on the bunch. These self fields (termed wake fields) can deflect particles in longitudinal or transverse planes and generally depend on time and distance

in complicated ways. Longitudinal wakes change the energy of the particles and transverse wakes affect the particles' transverse momenta.

In order to calculate analytically the effects of wake fields on particles, two assumptions are traditionally made: the rigid-beam approximation and the impulse approximation. The former states that the beam passes a discontinuity in a vacuum pipe without being moved, just experiencing a change in momentum. This is valid for high, ultra-relativistic beam energies and implies that the distance z in figure 1.8 between source and witness particles does not change. The second assumption states that, despite carrying a charge and feeling a force due to the wake, the important factor for the witness particle is the change in momentum ($\Delta\vec{p}$), or impulse (equation 1.1, where $\vec{F}$ is the Lorentz force due to the electric and magnetic fields, $\vec{E}$ and $\vec{B}$, on a particle of charge q and velocity $\vec{v}$), as it passes through the discontinuity at fixed velocity.

$$\Delta\vec{p} = \int_{-\infty}^{\infty} \vec{F}\,dt = \int_{-\infty}^{\infty} q\left(\vec{E} + \vec{v} \times \vec{B}\right) dt \tag{1.1}$$

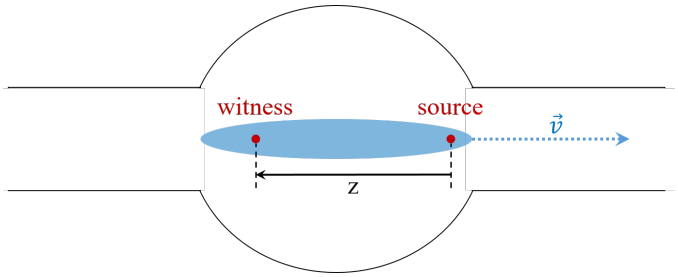


Figure 1.8: Schematic of a source particle a distance z in front of a witness particle within a bunch, both travelling at velocity $\vec{v}$ through a discontinuity.

These assumptions lead to the concept of wake functions, $W_m(z)$ (m is the azimuthal mode number), which can be used to describe the force on a witness particle from the wake induced by a source particle. Transverse effects are often dominated by the $m = 1$ mode and longitudinal effects by the $m = 0$ mode. As such, the wakes are often simply referred to as the transverse wake function ($W^{\perp}(z) = W_1(z)$), with units of V/(C m), and the longitudinal wake function ($W^{\parallel}(z) = W_0'(z)$),

with units of V/C, (equations 1.2 and 1.3 respectively where c is the speed of light).

$$W^{\perp}(z) = \frac{1}{q_{\text{source}}} \int_{-\infty}^{\infty} \left[\vec{E}_{\perp}(z) + c(\hat{z} \times \vec{B}) \right] \, dz \tag{1.2}$$

$$W^{\parallel}(z) = -\frac{1}{q_{\text{source}}} \int_{-\infty}^{\infty} \vec{E}_{\parallel}(z) \, dz \quad \equiv -\frac{d}{dz} W^{\perp}(z) \tag{1.3}$$

Wake fields can also be expressed in the frequency domain via a Fourier transform (equations 1.4 and 1.5 with i the imaginary unit, βc the speed and ω the angular frequency). Considering the circulating beam as an electric current, this function is called the impedance, $Z(\omega)$, which describes the strength of the wake field due to a given current modulation. Common wake functions and impedances are listed in section 3.2.1.

$$Z^{\perp}(\omega) = \frac{i}{\beta c} \int_{-\infty}^{\infty} W^{\perp}(z) e^{i\omega z/\beta c} dz \tag{1.4}$$

$$Z^{\parallel}(\omega) = \frac{1}{\beta c} \int_{-\infty}^{\infty} W^{\parallel}(z) e^{i\omega z/\beta c} dz \tag{1.5}$$

In general, the impedance is a complex function referring to fields that are in-phase or in quadrature ($\pi/2$ out of phase) to the dominant beam frequency (RF or revolution frequency in the longitudinal plane and the betatron frequency in the transverse plane). The real, or resistive, part describes the energy loss or gain due to the impedance and the imaginary, or reactive, part shifts the frequency of the collective oscillation. The impedance arises from accelerator components such as the resistive wall of the beam pipe, broadband impedances from vacuum ports or Beam Position Monitors (BPMs) for example and narrowband impedances from high-Q resonant structures such as RF cavities and extraction kickers.

1.5 Motivation for this Study

The main goal of this thesis is to study the head-tail instability as observed on the ISIS synchrotron and analyse its characteristics in comparison to the theoretical models available. Key features of the instability differ from those predicted from Sacherer's theory, the reasons for which are studied in detail in both experiment and simulation. Measurements in normal, RCS mode are difficult to interpret so a new

operating mode, Bunched beams in Storage Ring Mode (BSRM), has been developed. Measurements and simulations in this mode are organised in order of increasing complexity such that the importance of different processes may be discerned.

ISIS is a high-intensity proton accelerator with strong space charge and complex profiled beam pipes, operating with low levels of beam-loss making it a unique facility to make the observations presented in this thesis. Also, the injection and capture processes produce very long bunches (see section 2.1.2) which, together with the relatively low relativistic β, stretches the assumptions of wake field theory. A detailed, systematic study of head-tail in this context helps to produce a better understanding of the instability mechanism, enabling further work into mitigating the instability on ISIS as well as other existing and proposed high-intensity hadron accelerators.

1.6 Importance for Current and Future Accelerators

The head-tail instability has been observed at many operating accelerators including the CERN PSB [26] and Fermilab Main Ring [27] and has been cited as one of the main limitations expected for high-intensity operation at the future SIS100 synchrotron of the FAIR facility [28]. Most operating, high-intensity, machines routinely run with an instability damping system that actively combats the beam's transverse growth. As such, understanding and efficiently mitigating the instability, particularly in the presence of strong space charge, is an active subject of research.

1.7 Thesis Outline

Including this introductory chapter, the thesis is structured with eight chapters as outlined here.

Chapter 2 is an overview of the ISIS Facility, focusing on the accelerators and especially the synchrotron where the experimental results included in this thesis were made. An introduction is also given to the megawatt upgrade project, ISIS-II.

The theory of wake fields and impedances is presented in chapter 3. The established theory to model and predict head-tail dynamics is outlined here. A brief look at an alternative model of head-tail is also put forward. An overview of theoretical and experimental studies on the influence of space charge on head-tail is presented, together with a list of associated assumptions and approximations used. This chapter also summarises the existing computer codes available for tracking particles including the effects of wake fields. The simulation tools used throughout the thesis are explained with special attention given to wake field models and space charge solvers.

Experimental results illustrating the head-tail instability in normal, rapid cycling operations on the ISIS synchrotron are reported in chapter 4. These include measurements of beam intensity, loss and BPM measurements illustrating the characteristic intrabunch motion.

Results from RCS operation are followed by a comprehensive experimental campaign measuring the head-tail instability as a function of betatron tune (chapter 5) and vertical beam size (chapter 6) for single harmonic bunched beams stored at injection energy (BSRM). Performing measurements in this way removes a number of complicating beam dynamics processes and enables more precise measurements, albeit restricted to injection energy.

Dedicated particle tracking simulations are performed to compare with these experimental results (included at the end of chapters 5 and 6). These are performed with and without transverse space charge in order to ascertain its effect on the instability characteristics.

A discussion of the key similarities and differences between simulation, experiment and Sacherer's theory is presented in chapter 7. Qualitative comparisons are also made to proposed head-tail theories including the effects of transverse space charge.

Chapter 8 summarises the main achievements of the thesis together with plans for further research. The impact of the research on ISIS, ISIS-II and high-intensity hadron machines in general is discussed.

Equipped with his five senses, man explores the universe around him and calls the adventure Science.

— Edwin P. Hubble, "The Exploration of Space", Harper's Magazine 158:732, May 1929.

2 ISIS and ISIS-II

2.1 ISIS Neutron and Muon Source

ISIS is a neutron and muon source based at the Rutherford Appleton Laboratory (RAL), 16 miles south of Oxford in the UK [2, 29] (figures 2.1 and 2.2). Operating since 1984 and officially opened in 1985, it is a world-leading centre for research into the physical and life sciences. The facility supports a national and international community of more than 2000 scientists who utilise the facility's beams of neutrons and muons to probe materials and their properties at an atomic level. Around 600 publications are produced each year from work at ISIS, with well over 10,000 published overall to date.



Figure 2.1: Aerial view of the Rutherford Appleton Laboratory on the Harwell Campus including the ISIS Facility (highlighted in red). Taken October 2021 [30].



Figure 2.2: The ISIS Neutron and Muon Source from the air. Taken October 2021 [30].

Neutrons and muons are used by academic and commercial researchers in a wide array of disciplines from fundamental physics, chemistry and biology through to engineering and archaeology. By neutron scattering, reflectometry, diffraction and spectroscopy, as well as muon spectroscopy, ISIS provides insight into broad-ranging areas such as green technology, superconductors, energy, pharmaceuticals, nanotechnology and catalysis.

Beams of neutrons are typically produced for scattering and spectroscopy by two processes: nuclear fission reactions and accelerator-driven spallation. ISIS uses the latter and delivers high-energy protons to a heavy-metal target to produce neutrons. Muons are produced when a small portion of the beam interacts with a carbon target upstream of the neutron target to produce pions which then decay into muons. In order to produce a high-intensity pulse of energetic protons a chain of accelerators (figure 2.3) is used to accelerate 3×10^{13} protons per pulse (ppp) to 800 MeV at 50 Hz, resulting in an average beam power on target of 192 kW.

2.1.1 ISIS Injector

2.1.1.1 Ion Source

The ISIS facility begins with a negative hydrogen (H^-), Penning type, ion source [31], see figure 2.4. It produces a hydrogen plasma in the presence of hot caesium vapour which enhances the production of H^- ions. These are then extracted in a 200 – 240 µs long pulse and passed through a 90° sector magnet to remove any other

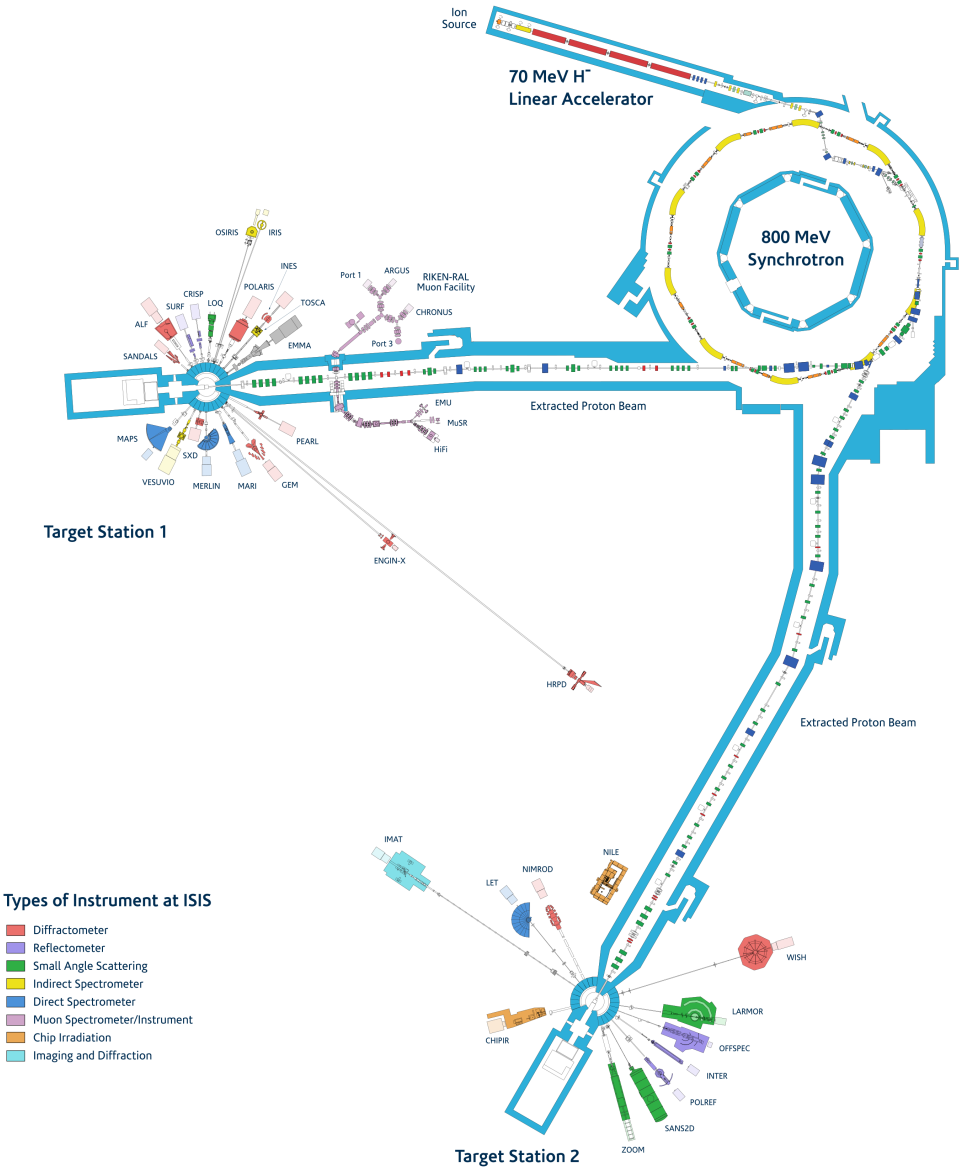


Figure 2.3: Schematic of the ISIS Neutron and Muon Facility [30].

negative ions or electrons. The resultant, typically 50 mA, beam passes across a DC acceleration gap, accelerating the ions to 35 keV.

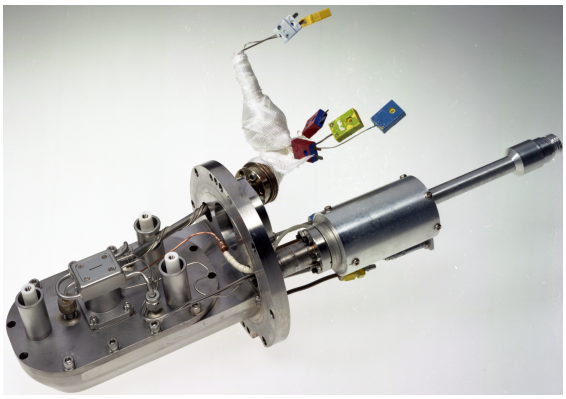


Figure 2.4: ISIS Penning type H^- ion source [30].

2.1.1.2 Low-Energy Beam Transport and Radio-Frequency Quadrupole

From the ion source the H^- beam passes through a three solenoid magnet Low-Energy Beam Transport (LEBT) and enters a 665 keV, 202.5 MHz, 4-vane Radio-Frequency Quadrupole (RFQ) [32], see figure 2.5. This provides acceleration, bunching and focusing for the H^- beam in preparation for entry into the linac.

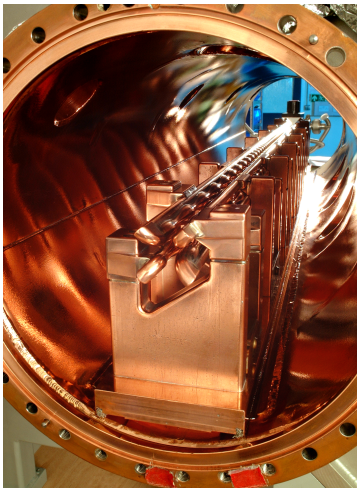


Figure 2.5: ISIS 4-vane, 665 keV RFQ prior to installation [30].



Figure 2.6: Tank 3 of the ISIS drift-tube linac during cleaning and maintenance [30].

2.1.1.3 Drift-Tube Linac

The beam is delivered straight from the RFQ into the first of four Alvarez type drift-tube linac tanks [33], see figure 2.6. All four operate at the same frequency as the RFQ (202.5 MHz) and accelerate to 10, 30, 50 and 70.44 MeV respectively. Duty

factors for the injector are around 1 %, with the 200 – 240 µs long pulse delivered every 20 ms. Typical beam currents at the end of the linac are around 24 mA.

2.1.1.4 High-Energy Drift Space

Following the linac, the train of H^- micro-bunches is transported to the next accelerator stage via a High-Energy Drift Space (HEDS) beamline, see figure 2.7. This is made up of dipoles, quadrupoles, various diagnostic devices and a debuncher cavity (for momentum spread control), delivering a matched beam into the synchrotron.

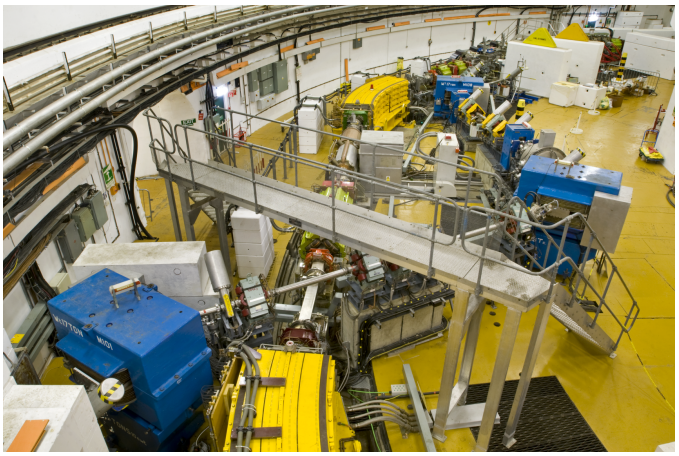


Figure 2.7: The ISIS HEDS as it crosses over the synchrotron for injection from the inside radius [30].

2.1.2 ISIS Synchrotron

The ISIS Rapid Cycling Synchrotron (RCS) is made up of ten superperiods, with each made up of a combined function dipole, quadrupole doublet and a quadrupole singlet, see figure 2.8. These are all powered by a 50 Hz resonant system called a White circuit [34]. Alongside these main magnets are forty correction magnets that are powered individually, allowing control of the betatron tune and closed orbit through the acceleration cycle. Between the repeating magnetic lattice are straight sections: one is devoted to the injection system, one to extraction and collimation and the others are occupied by radio-frequency (RF) cavities and a variety of beam diagnostic devices (see section 2.1.3). Some key ISIS synchrotron parameters are listed in table 2.1.

Table 2.1: Important ISIS synchrotron parameters.

Parameter	**Symbol**	**ISIS**
Energy range	E_k	70 – 800 MeV
Operational intensity	N	3×10^{13} ppp
Repetition frequency	f	50 Hz
Gamma transition	γ_t	5.034
Mean synchrotron radius	R	26.0 m
Dipole bend radius	ρ	7.003 m
Number of superperiods		10
Superperiod length		16.34 m
Dipole length		4.4 m
Dipole field minimum	$B_{\min}$	0.1764 T
Dipole field maximum	$B_{\max}$	0.697 T
Nominal betatron tune values	Q_x, Q_y	4.31, 3.83
Natural chromaticity	ξ_x, ξ_y	-1.4, -1.4
Number of RF cavities (1RF, 2RF)		6, 4
Machine acceptance (H, V)	(A_h, A_v)	540 π, 430 π mm mrad
Injection scheme		H^- charge-exchange
Extraction scheme		Fast, kicked, single turn

2.1.2.1 Injection

Injection into the 163.4 m, 800 MeV RCS [29] is via charge-exchange using a thin, carbon foil. This removes the two electrons of the H^- ions with around 98 % efficiency, leaving bare protons to accumulate in the RCS. The remaining unstripped and partially stripped beam is collected by dedicated beam dumps. The foil is mounted in the middle of a symmetric, four-dipole injection straight (superperiod 0 in figure 2.8) which creates an orbit bump during injection to bring the closed orbit of the machine close to the foil (see blue trace in figure 2.9).

The small transverse injected beam is spread across the acceptance of the synchrotron in a process known as painting. In high-intensity machines, such as ISIS, painting is primarily performed to minimise transverse space charge forces and create a well-defined beam distribution for efficient acceleration. As indicated in figure 2.10, the beam in ISIS is injected over the falling main dipole field leading to horizontal painting of the beam. This occurs as, with a constant energy injected beam, the dispersive closed orbit moves away from the stripping foil through the injection period.

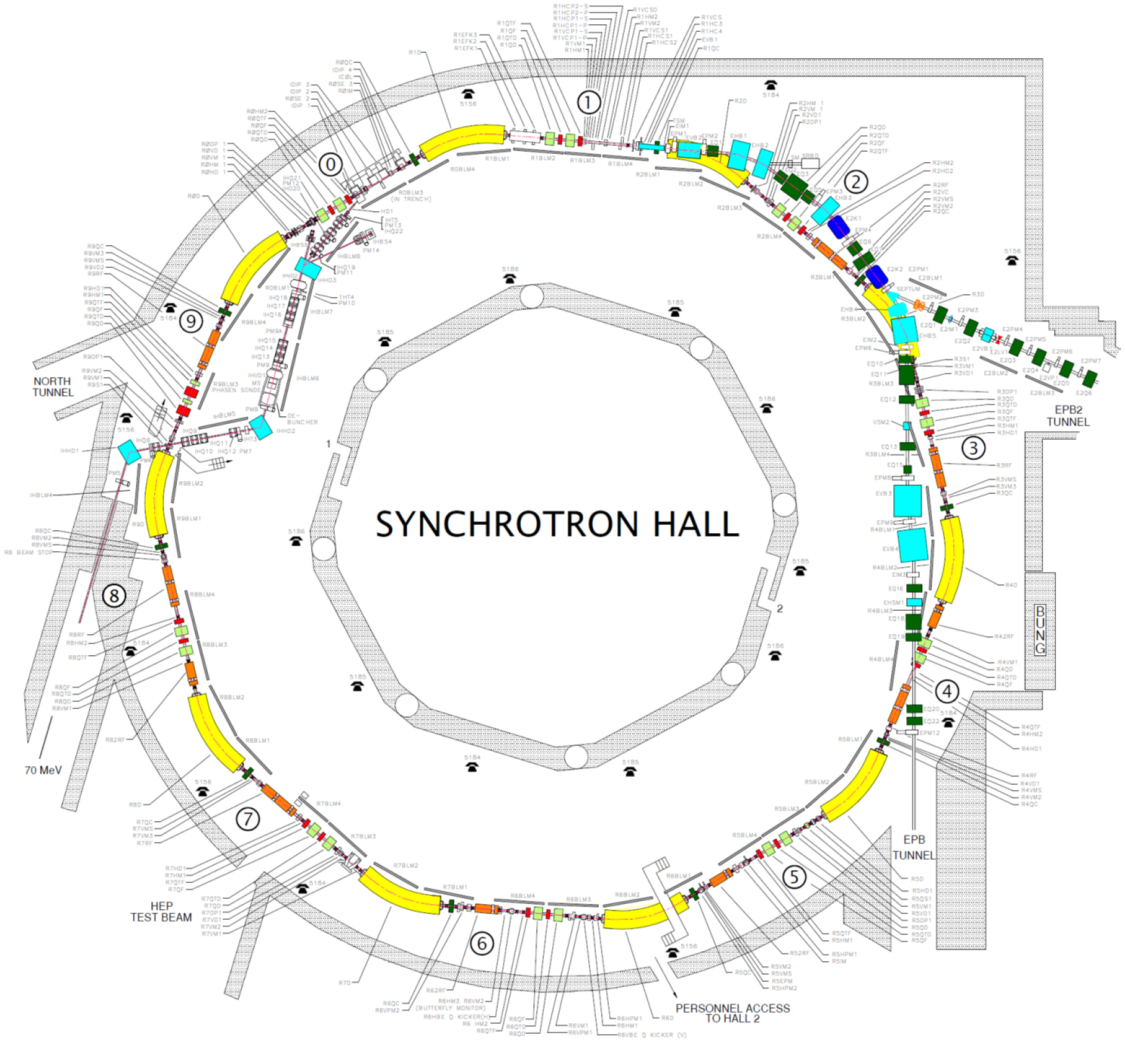


Figure 2.8: Schematic of the ISIS synchrotron [30].

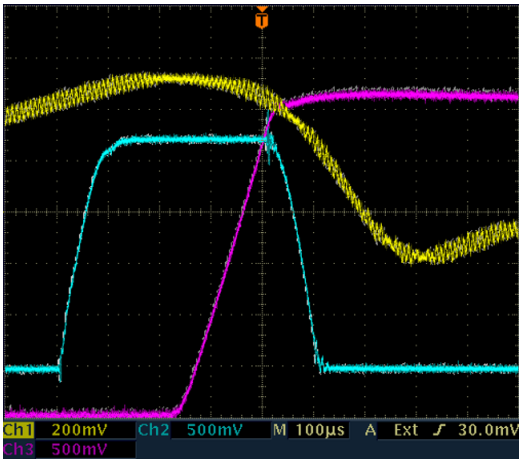


Figure 2.9: Oscilloscope traces of vertical sweeper current (yellow), injection dipole current (blue) and a ring IM (pink) over the injection period. The trigger point is at −0.2 ms and there are 100 µs per division.

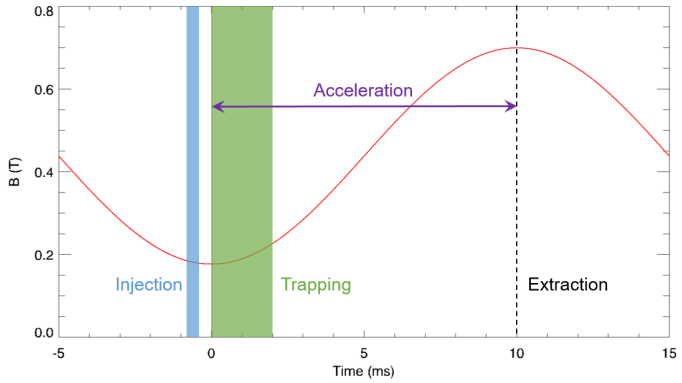


Figure 2.10: The ISIS cycle with reference to the main dipole field.

Vertically, the beam is painted with a specialised dipole magnet, known as the "vertical sweeper", in the injection line (see yellow trace in figure 2.9). Typically, the magnet current ramps up to full current prior to injection and falls at a constant rate (sweeps) as the beam is injected, thereby painting from large to small emittance in the synchrotron.

2.1.2.2 Acceleration and Trapping

There are ten dual-gap, ferrite-loaded, RF cavities in the synchrotron: six operating at a harmonic number (h) of two (twice the particle revolution frequency) known as 1RF cavities (see figure 2.11), and four operating at an harmonic number of four known as 2RF cavities. Collectively these are referred to as the Dual Harmonic RF (DHRF) system. The dominant 1RF harmonic leads to the formation of two proton bunches with the 2RF cavities used to elongate the bunches, reducing beam-losses and increasing capture area, allowing for higher beam intensities.

The RF cavities form the bunches of protons and accelerate them to 800 MeV on the 10 ms rising edge of the main dipole sinusoidal field. Due to the relatively low beam energies (in comparison to the proton's rest mass) the frequency of the RF cavities has to vary appreciably. During acceleration, the relativistic beta goes from 0.36 to 0.84, leading to an RF frequency range of 1.3 – 3.1 MHz for the 1RF ($h = 2$) and 2.6 – 6.2 MHz for the 2RF ($h = 4$). This is possible due to the ferrite in the cavities, which has a variable permeability dependent on an applied bias current which tunes the resonant frequency of the cavities. These harmonic numbers

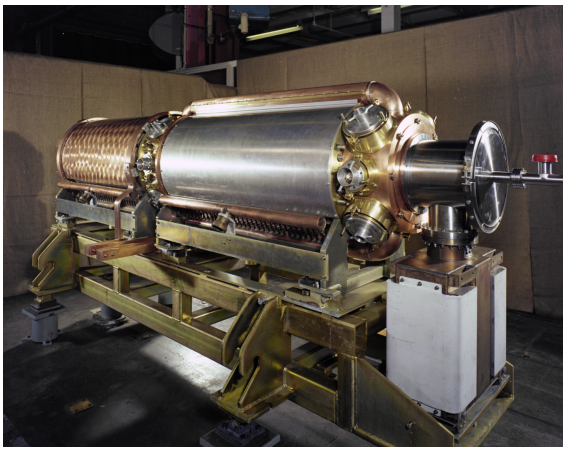


Figure 2.11: An ISIS 1RF ($h = 2$) cavity prior to installation [30].

were chosen to maximise the possible accumulated intensity in the synchrotron whilst allowing for efficient extraction to the targets.

The 200 – 240 µs long injected pulse of protons equates to around 140 revolutions of the synchrotron at injection energy. During injection RF voltage is applied to the cavities at a low level to begin the formation of two, long bunches and allow the linac microbunch structure to disperse. Once the beam is fully accumulated the RF voltage is increased rapidly. This leads to a capture process which, although non-adiabatic, is ∼97 % efficient. The beam is considered fully bunched by 1 ms with peak beam-losses associated with trapping occurring at 0.5 ms (figure 2.10). The RF voltage profile through acceleration is largely determined by the sinusoidal time variation of the main magnet fields, the desire to transport as many protons as possible within the synchrotron aperture constraints and the need for low beam-losses. On ISIS, this results in a peak accelerating voltage per turn of 160 kV for the 1RF system.

Control systems are utilised throughout the RF systems to ensure they are tuned to the required frequency, phase and voltage. Phase differences between the cavities are arranged such that the voltage in the cavity gaps adds together for the circulating bunches. Feedback loops are necessary to maintain the voltage and phases required. Signals from the bunches are also used to provide feed-forward beam compensation to stabilise radial position, bunch phase and bunch length as well as to take into account beam-loading effects.

2.1.2.3 Transverse Dynamics

The design of ISIS' magnetic lattice focussed on three key areas: the requirements of low beam-loss levels, particularly in the presence of high space charge; the need for long straights for injection, RF cavities and extraction; the constraints imposed by reusing an existing resonant magnet power supply and buildings. The nominal betatron tunes are $Q_x = 4.31$ and $Q_y = 3.83$, which are chosen to avoid resonances.

Each superperiod contains two trim quadrupoles, one located at a high horizontal beta and one at a high vertical beta position. These are independently powered and programmable through the acceleration cycle for control of the betatron tunes. Azimuthal harmonics can also be applied to the trim quadrupole currents to correct for harmonic errors in the machine. There are also fourteen programmable steering magnets, seven in each plane, distributed around the machine. These allow for correction of the closed orbit through acceleration and the vertical correctors aid in the extraction process (see section 2.1.2.5).

The ISIS synchrotron was originally constructed with families of sextupoles and octupoles for chromaticity correction (chromaticity is the spread in tune due to the spread in momentum) and Landau damping (a mechanism by which an instability is suppressed by the spread in particle frequencies [21]), respectively. However, most of these magnets have been removed in subsequent years as they were not required in routine operations and the synchrotron operates with no chromaticity control.

2.1.2.4 Collimation and Loss Control

As beam-loss is the primary limiting factor for high-intensity operation of the ISIS facility, minimising and localising that loss is a major focus of routine operations. Collimation systems are utilised to intercept beam before it is lost elsewhere, thereby controlling the loss to a specially designed, well-shielded region of the accelerator. On the ISIS synchrotron, the collimation system is located in superperiod one and is co-located with extraction from the ring (figure 2.8). The system itself consists of moveable graphite and copper blocks distributed in an upstream primary collimator and downstream secondary collimator and in both horizontal and vertical planes.

These are placed to deflect and absorb the lost particles efficiently, effectively cleaning the edge of the transverse distribution.

On ISIS, the collimation system is designed for the primary losses occurring around 100 MeV (peak trapping losses). It enables a minimisation of machine activation by not only localising loss, but by intercepting lost particles earlier in the acceleration cycle. These particles have lower energies and as such produce less activation. The primary collimators on ISIS are typically set at about ∼85 % of the machine acceptance.

2.1.2.5 Extraction

At the end of the 10 ms acceleration cycle, the proton beam is extracted vertically from the synchrotron in a single turn. This is non-trivial, as the two 800 MeV proton bunches are only separated by ∼200 ns so any components will have to activate on that timescale, and the beam must be precisely extracted into the extraction line to minimise high-energy beam-loss. At ISIS, the beam is prepared in the last millisecond by creating a vertical orbit bump in the extraction straight using the correction magnets.

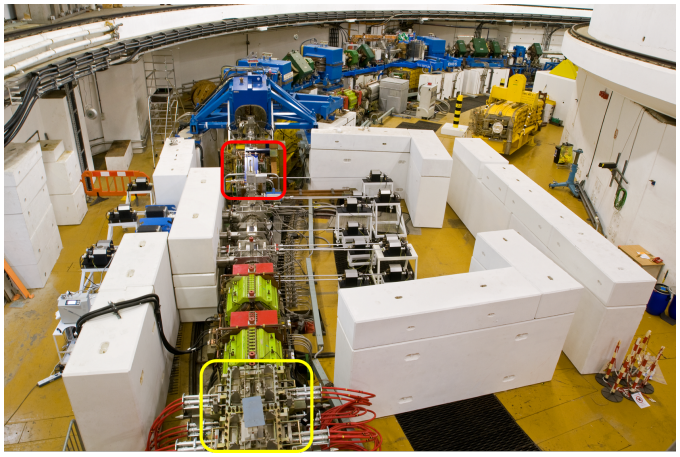


Figure 2.12: Extraction straight in the ISIS synchrotron (kickers highlighted in yellow and septum in red) [30].

Figure 2.12 shows the superperiod of ISIS that deals with extraction with kickers sited on the bottom and vertical extraction septum in the middle of the photograph just prior to a main dipole and extracted proton beamline (EPB). Extraction is

triggered by neutron user demand to enable proper synchronisation of time-of-flight neutron measurements. Three fast specialised vertical dipole magnets with single-turn coils are powered by pulse-forming networks to energise from 0 – 5000 A at a voltage of 35 kV in approximately 100 ns, between the two proton bunches. They are powered long enough to deflect both bunches by 14 mrad into the extraction aperture of a septum magnet 9 m downstream. This 1 T dipole bends the extracted beam 21.1° out of the synchrotron into the Extracted Proton Beamline (EPB). From there it is directed to either of the two target stations (see figure 2.3), or during machine setup can be sent to a beam dump in the synchrotron hall.

2.1.2.6 High-Intensity Operation

The ISIS synchrotron has been specifically designed with high-intensity operation in mind. Together with the programmable trim quadrupoles and steering magnets for flexibility in operational setting, the accelerator has large transverse acceptances to allow for increased beam sizes and, as such, reduced transverse space charge forces and associated losses. ISIS employs rectangular beam pipes, stainless steel in the majority of the ring and the ceramic beam pipe in fast ramping dipoles and quadrupoles. Rectangular RF screens (an array of thin wires) run between the beam and ceramic to conduct the image current through the magnets, with capacitative coupling to avoid eddy currents.

In order to minimise issues due to instabilities and their associated beam-losses, the rectangular vacuum vessel was constructed such that the aperture follows the shape of the beam envelope which the nominal magnetic lattice determines. This reduces both the longitudinal and transverse space charge impedances and provides benefits in suppressing electron-proton interactions.

2.1.2.7 Machine Physics Operation

During accelerator setup and dedicated machine physics experiments, the facility may be operated in a variety of different modes, enabling flexibility in fault diagnosis and experimentation. Central to this is the independent flexibility in repetition rate to each target station. Nominally the facility operates at 50 Hz, with four pulses out

of five going to Target Station 1 (TS1) and the fifth going to Target Station 2 (TS2). The control system enables operation at certain fractions of the nominal repetition rate ($50/2^n$ Hz where n is an integer between 0 and 7). As such, whilst the machine is in a high beam-loss state (as it may be during a fault or a dedicated accelerator experiment) the repetition rate may be lowered to investigate the machine state without risk to beam-loss related component damage or high activation.

ISIS also has the capability to operate many of its correction elements (trim quadrupoles, steering magnets, RF volts, *etc.*) in a pulsed mode. This enables switching operating parameters between two sets of values: "Normal" and "Experimental". Most of the 50 Hz pulses are "Normal", with typically 50/32 or 50/128 Hz being assigned the "Experimental" values. This flexibility allows for experimentation and diagnosis during routine operation as well as pulsing equipment at levels not normally feasible at full repetition rate.

2.1.2.8 Storage Ring Mode

During dedicated machine physics time, the synchrotron can be put into Storage Ring Mode (SRM), with the main magnets set at constant currents matching injection energy and the extraction system switched off. The RF systems can then be turned off to store a coasting beam, or operated at constant frequency (again matched to the injection energy) so the injected beam can be bunched and stored rather than accelerated.

2.1.3 Diagnostics on the ISIS Synchrotron

Diagnostic devices are an essential part of the accelerator framework and are key to efficient high-intensity operations. Regularly used diagnostics are non-intrusive to minimise disruption to the beam whilst it is in the synchrotron and also to prevent damage to any such device from the beam. The main devices employed are listed below:

2.1.3.1 Beam Intensity Monitor

In order to measure the beam current of the passing charged particles, intensity monitors (IMs) are used in an analagous way to transformers. The beam itself provides the primary winding and an inductive toroidal coil acts as the secondary. These devices are accurate to around 0.1 % and are regularly calibrated. On ISIS, several are installed throughout the injector, in the synchrotron and the extraction beamlines. Together with providing a measure of the beam intensity, the efficiency of beam transport through each section may be calculated. The IMs are also monitored as a key part of the machine protection system, automatically switching the beam off if the efficiency drops too low (indicating uncontrolled beam-loss). Figure 2.13 shows one of the ring beam intensity monitors *in situ*.

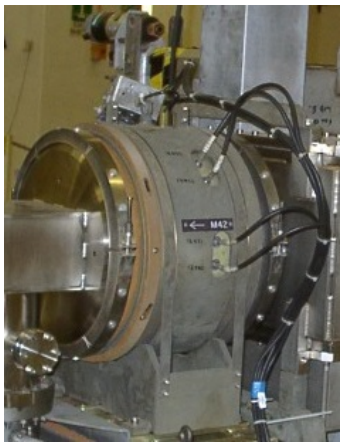


Figure 2.13: One of two beam intensity monitors in the ISIS synchrotron [30].

2.1.3.2 Beam-Loss Monitor

Measurement of beam-loss is essential for an high-intensity hadron accelerator. Lost beam can be measured in a number of ways; on ISIS two different methods are used: ionisation chambers and scintillators. The former are referred to as Beam-Loss Monitors (BLMs) [35] and are positioned along the accelerator: from the linac, around the synchrotron, and along the extracted proton beamlines to both target stations. The thirty-nine synchrotron BLMs are 3 m long, filled with argon and positioned around the inside radius of the accelerator, four to each superperiod (the injection superperiod has three), see figure 2.14. A proportion of the lost

particles that hit the beam pipe ionise nuclei which then relax producing neutrons isotropically which are then detected by the BLMs. They provide a good spatial as well as temporal resolution with a frequency response of 20 kHz. Unlike the intensity monitors, there is no absolute calibration for BLMs, however they are far more sensitive, with response down to the 0.01 % level. These are complementary to the intensity monitor signals and are also part of the machine protection system.

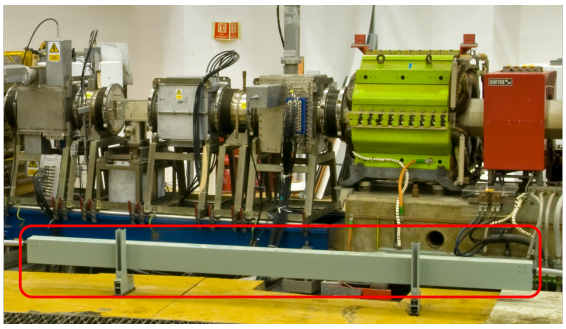


Figure 2.14: One of the synchrotron BLMs, highlighted in red [30].

Figure 2.15 shows typical beam intensity and sum beam-loss signals as a function of time for neutron user operations. The beam intensity signal comes from a calibrated resonant current transformer in the synchrotron, and the beam-loss trace is a sum of all 39 BLMs. Beam-losses can be loosely categorised by the time they occur in the acceleration cycle into those associated with injection (-0.4 – 0 ms), trapping (peaking at 0.5 ms), transverse space charge (0.5 – 2 ms), vertical instability (2 – 3 ms) and extraction (9.8 – 10 ms).

The second method of beam-loss detection at ISIS uses scintillators [36] that have been primarily installed in regions not covered by the BLMs, or where non-metallic loss monitors are required. Each main dipole covers a quarter of the superperiod and, as the yoke masks most of the beam-loss from the BLMs and the rapid-cycling magnets require non-metallic monitors, six scintillators have been installed in each dipole (see figure 2.16). They provide similar time-resolved information to the BLMs but are far more sensitive. Their small size and ease of installation means they are also useful for areas of ISIS where beam-loss has previously caused high activation levels or damage to the machine. The monitors are rectangular blocks of plastic scintillator BC-408 which are sensitive to a wide range of secondary

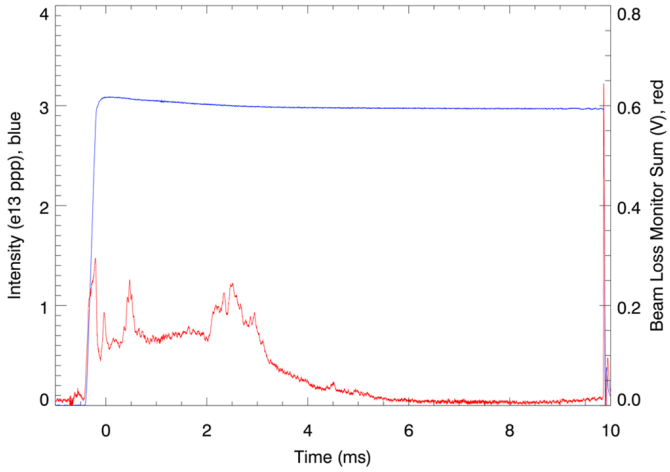


Figure 2.15: Beam intensity and sum beam-loss traces as a function of time through the injection and acceleration cycle.

particles generated by particles impinging on the beam pipe. They are connected to photomultiplier tubes by optical fibres and are calibrated prior to installation with a strontium-90 beta source.



Figure 2.16: Beam-loss monitoring scintillators within one of the ISIS main dipoles [30].

Together these two beam-loss monitoring systems are an essential part of attaining and maintaining high-intensity operation whilst ensuring protection of machine components. They provide invaluable information on the operational status and efficiency of the accelerator, enabling minimisation and control of beam-losses.

2.1.3.3 Beam Position Monitor

The transverse position of the beam within the beam pipe is measured using Beam Position Monitors (BPMs). On ISIS, the BPMs are circular cylindrical, split-electrode capacitive devices that are sensitive to changes in the beam field and as such require the beam to be bunched to operate (figure 2.17). The position of the

bunch centroid is proportional to the difference of the two beam induced voltages divided by the sum [37] (position $= R(V_1 - V_2)/(V_1 + V_2)$, where R is the radius of the electrodes). There are sixteen horizontal, and twenty vertical, monitors with ten at equivalent lattice points in each superperiod, where the beta function is at a maximum, close to the main focusing or defocusing quadrupole respectively.

BPMs provide information on the transverse alignment of the beam around the synchrotron (and in the extracted beamlines) and as a function of time through the acceleration cycle. The BPM difference signal is also of interest when investigating beam instabilities as it is the most sensitive measure of transverse motion. They have an accuracy of approximately 0.5 mm. The BPM sum signal provides a measure of the longitudinal line density (proton density along the bunch's length).

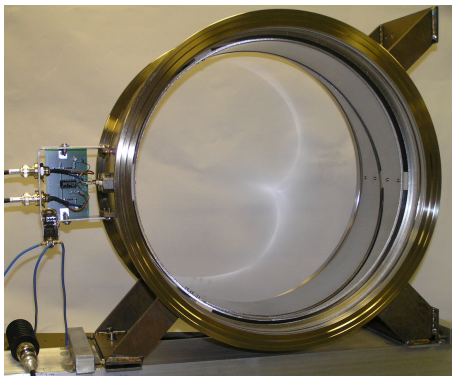


Figure 2.17: A synchrotron BPM being calibrated in the laboratory [30].

2.1.3.4 Beam Profile Monitor

The transverse profile of the beam is measured using residual gas ionisation profile monitors (IPMs). These operate by directing ions produced in the interaction between the circulating proton beam with the remaining gas (vacuum levels of around 10^{-7} mbar) in the beam pipe towards a detector. The ions are directed using static transverse electric fields in either the horizontal or vertical plane for a vertical or horizontal profile, respectively.

ISIS employs five profile monitors in the synchrotron, one in the EPB and one modified version in the HEDS. The unmodified design incorporates two transverse electric fields, the second to compensate for the deflection of the proton beam due to

the primary field. Single detector monitors take a few minutes to measure a profile as the detector is mechanically driven across the aperture, thus detecting an average beam profile over many pulses. Multi-channel profile monitors (one in the vertical and one in the horizontal) modify the design, making use of the compensating field to detect profiles. They each use a fixed array of 40 detectors across the aperture, enabling a profile measurement in a few microseconds. The existing single detector profile monitor is then utilised to calibrate the multichannel's 40 separate detectors, see figures 2.18 and 2.19.

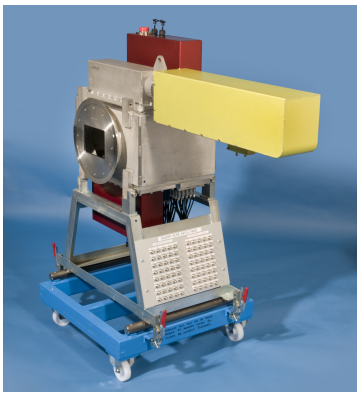


Figure 2.18: A horizontal multi-channel ionisation profile monitor [30].

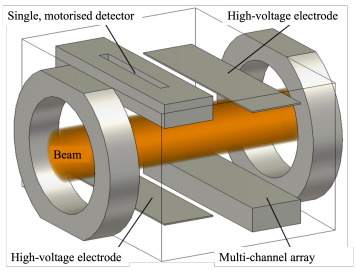


Figure 2.19: A schematic showing the inside of the ionisation profile monitor pictured in figure 2.18.

Intercepting wire profile monitors are also utilised in the HEDS and EPB. Beam particles interact with the wire (usually silicon-carbide coated carbon fibres), either knocking electrons from the wire or depositing charge, thereby inducing a current proportional to the flux of the beam passing through the wire. By measuring the relative current at several positions a beam profile can be obtained. The measurement is destructive, causing beam-loss and deterioration of the transverse beam emittance (the area occupied by the beam in $x, x' = dx/ds$ or $y, y' = dy/ds$ space). As such, these are only used at low repetition rates to prevent damage to the monitors and minimise beam-loss with its associated activation of the machine.

2.1.3.5 Other Diagnostics

There are several other diagnostic devices used in the ISIS accelerators as well as some that are under development. A beam chopper in the HEDS is used to create

short pulses of protons in the synchrotron for various beam and lattice measurements. A betatron exciter (also known as a "Q-kicker") is used to drive transverse beam frequencies and currently operates as part of a prototype instability damping system.

The synchrotron has an electron cloud monitor that uses a micro-channel plate (MCP) to detect electrons liberated through the interactions of the beam with the residual gas and beam pipe. Vacuum gauges are installed throughout the accelerator complex and, though slow, can be a diagnostic of beam-loss or accelerator component failure. Stripline monitors that are able to measure both beam position and envelope, as well as form part of a dedicated instability damping system, are under development at ISIS.

2.2 ISIS-II Concept

With the ISIS Facility successfully producing world-leading neutron and muon science for almost 40 years, studies are now underway to identify an optimal configuration for a next generation, short-pulse facility, "ISIS-II". The design and specification of the facility builds upon experience from existing machines and input from a wide variety of sources including neutron scientists, target and instrument experts as well as accelerator physicists. A roadmap defining the design work, feasibility and research required to identify and build ISIS-II has been established [38]. The roadmap includes a research and development (R&D), feasibility and design stage which, on completion in 2027, will define the proposed accelerator and target configuration. A full technical design will follow ready for construction to begin in ∼2031.

Design options currently being considered to supply the megawatt beam powers required include RCS, Accumulator Ring (AR) and Fixed Field Accelerator (FFA) machines [39]. The primary aim of the current phase of the project is to undertake the necessary feasibility, design and R&D studies to identify realistic options for an ISIS-II facility. Reference points for these studies are the operational machines listed in section 1.1.1 (particularly SNS and J-PARC) and ISIS (section 2.1).

Table 2.2: Comparison of main ISIS and ISIS-II synchrotron parameters.

Parameter	**Sym**	**ISIS**	**ISIS-II**
Energy range	E_k	0.07 – 0.8 GeV	0.4 – 1.2 or 1.2 GeV
Operational intensity	N	3×10^{13} ppp	1.3×10^{14} ppp
Repetition frequency	f	50 Hz	50 Hz
Mean synchrotron radius	R	26.0 m	26.0 or 45.0 m
Number of superperiods		10	3 or 4
Betatron tune values	Q_x, Q_y	4.31, 3.83	4.40, 4.32 or 6.40, 6.32
Injection scheme		H^- charge-exchange	H^- charge-exchange
Extraction scheme		Fast, kicked, single turn	Fast, kicked, single turn

2.2.1 ISIS-II Beam Specification

The working parameters for this study are for a 1.25 MW proton beam at a beam energy of 1.2 GeV. The ∼1 µs beam pulses are to be delivered to two targets, one receiving 10 Hz (0.25 MW) and the other 40 Hz (1 MW). It should be noted that these parameters may be revised following interaction between the various experts, although the values are correct at the time of writing. A summary of key synchrotron parameters for a potential ISIS-II is shown in table 2.2 [39], in comparison to current ISIS operating specifications.

The primary challenge of this design, as with similar high power accelerators, is to achieve low beam-loss (less than ∼0.1 %) such that machine activation is kept to a level at which hands-on maintenance of accelerator components remains possible. This limit is based on the well-established guidance to keep localised losses down to 1 W/m around the accelerator, thus ensuring activation remains low. Assuming that the collimation system is suitably efficient, a top beam energy of 1.2 GeV leads to loss limits of ∼0.1 % (inclusive of the collimation region) and ∼0.01 % uncontrolled (excluding the area around the collimators).

Figure 2.20 shows an example lattice design for a "green-field" ISIS-II [39]. Sextupoles and octupoles are planned for chromaticity correction and Landau damping respectively. Further designs have been produced for an ISIS-II to reuse the existing ISIS synchrotron hall. This entails decommissioning and removal of the existing synchrotron, however much of the current ISIS infrastructure may

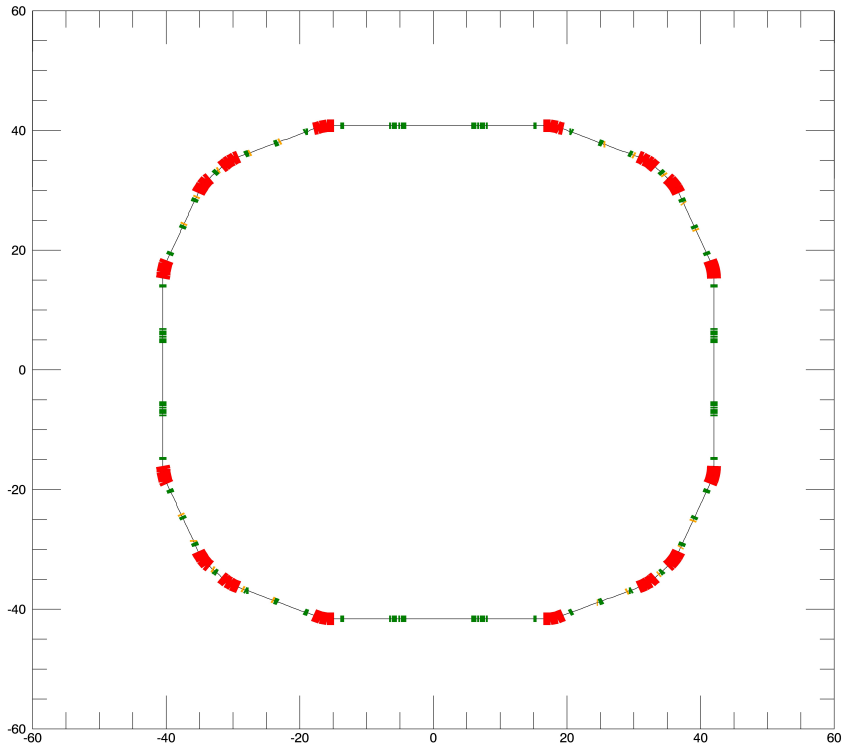


Figure 2.20: Example ISIS-II lattice design: dipoles in red, quadrupoles in green and sextupoles in orange [39].

be reused. Reusing the existing hall, however, limits the size of the synchrotron which has knock-on impacts on the beam energy and intensity achievable. The "green-field" designs are not limited by space constraints.

He [Frank Sacherer] was always extremely diffident about his accomplishments, bemoaning the fact that he couldn't accomplish more. The world accelerator community has lost an important colleague whose help we were counting on for many years to come.

— Lloyd Smith (LBNL), Frank J. Sacherer obituary, Physics Today, February 1979.

3 Head-Tail Instability Theory

3.1 Introduction

In this chapter the theory behind the head-tail instability mechanism is presented. This begins with the concept of wake functions and beam coupling impedances and their use in describing and quantifying the effect of the surroundings on beam dynamics. Following this, the established mechanism of the head-tail instability is discussed starting from the single-particle equations of motion and the definition of the coupling impedance. The instability growth rate is calculated for the model of Sacherer [22], given a number of assumptions, and the instability's distinguishing features are outlined. The head-tail model of Rees [40] is also presented. Finally the influence of space charge on the head-tail instability is discussed, with a review of the latest published theories and experimental findings.

3.2 Wakes and Impedances

When at rest a charged particle produces a static electric field whose strength is only dependent on the radial distance from the particle. As the particle moves this situation changes and a magnetic field is created. In the limiting case of a charged particle travelling near the velocity of light, c, the electric and magnetic fields become "pancake" like with a radial electric field and an azimuthal magnetic field. This

pancake has an opening angle of $\sim 1/\gamma$, where γ is the relativistic factor given by $\gamma = (1 - v^2/c^2)^{-1/2}$, see figure 3.1. This pancake is always perpendicular to the path of motion with the fields moving with the test particle without any lagging behind.

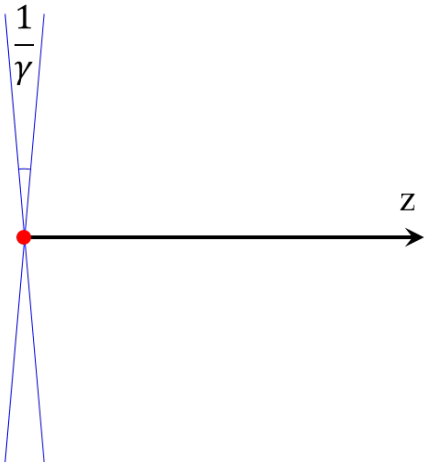


Figure 3.1: Schematic showing the "pancake" like electromagnetic fields emitted by a relativistic charged particle.

3.2.1 Wake Fields and Wake Functions

However, in realistic accelerator physics scenarios, this particle is travelling within a beam pipe and the pancake of fields is cut off by the pipe. For a positively charged particle, this creates a ring of negative charges on the wall of the beam pipe where the electric field intersects it. These are known as image charges and, if the beam pipe is perfectly conducting, these will travel at the same velocity as the positively charged particle, creating an image current. For the case of an imperfect conducting beam pipe, or one with discontinuities, as found in all realistic particle accelerators, these image charges are slowed and leave electromagnetic fields behind. These fields are known as *wake fields* and are key to examining the behaviour of particles following on from the positively charged source particle, in this example.

As stated in the introductory chapter (chapter 1), these wake fields are in addition to the numerous electromagnetic fields used in particle accelerators to guide, control and accelerate charged particles and can act on the particle in either (or both) the longitudinal or transverse planes. However, for the purposes of accelerator beam dynamics, these wake fields are much smaller than the external

fields from magnets, RF, *etc.* (*i.e.* $(\vec{E},\vec{B})_{\text{wake}} \ll (\vec{E},\vec{B})_{\text{external}}$). As such we can treat the wake fields as a perturbation to the particle dynamics.

Wake fields are often dependent on the test particle's position and time in complex ways. In order to calculate analytically the wake fields as a function of the distance between the source particle and a trailing test particle, two approximations are made. The *rigid-beam approximation* states that the beam is of high enough energy (ultra-relativistic) that it will pass discontinuities or wake resonating structures without a change in position, just a change in momentum. Even in the presence of synchrotron oscillations, the longitudinal distance between source and test particles varies very little in one turn in comparison to the bunch length. The second is the *impulse approximation*, and is related to the first in that the importance is placed on the change in momentum, the impulse, rather than the force experienced.

These simplifying approximations lead to the definitions of *wake functions*, $W_m(z)$ (where m is the azimuthal mode number, see section 1.4). They are essentially the accelerator component's (or source of the wake field's) response to a pulse excitation. This can be expanded in a power series in the offset of the source and test particle [41]. The dominant longitudinal wake function is $W_0(z)$ ($m = 0$) such that it is independent of the transverse offset of either the source or test particles, whilst the dominant transverse wake function, $W_1(z)$ ($m = 1$), is proportional to the transverse offset of the source particle. It should be noted that this behaviour only holds true if the structure is rotationally symmetric. Axially asymmetric structures, such as rectangular beam pipes, have an additional detuning (or quadrupolar) wake proportional to the transverse offset of the trailing particle.

3.2.2 Impedances

The definition of wake functions is useful for macroparticle simulations (see section 3.5) as it can relatively easily be implemented as extra terms in the equations of motion for single-particle dynamics. However, for some problems it is better (or easier) to treat the wake effects in the frequency domain using the definition of the *beam coupling impedance* (see section 1.4). For example, when dealing with a

imperfectly conducting beam pipe, the conductivity, permittivity and permeability of the material can depend on frequency. This lends itself to implementing impedances in macroparticle simulations rather than (or in combination with) wake functions.

Some important properties of coupling impedances are listed here:

1. As the wake function is a real quantity, if the impedance is known at frequency ω then it can be calculated at $-\omega$, $Z^{\perp}(-\omega) = -[Z^{\perp}(\omega)]^*$ and similarly for the longitudinal impedance, $Z^{\parallel}$. (Negative frequencies are included primarily to allow calculations using $e^{i\omega t}$ rather than trigonometric functions.)

2. With the convention we have used of $e^{i\omega t}$ rather than $e^{-j\omega t}$ in the definitions of impedances (equations 1.4 and 1.5) $Z^{\perp}(\omega)$ and $Z^{\parallel}(\omega)$ have poles in the lower half of the ω plane. This follows from the need to guarantee causality.

3. From the equation linking longitudinal and transverse wake functions (equation 1.3) and the Panofsky-Wenzel theorem [42], the longitudinal and transverse impedances are related by $Z^{\parallel}(\omega) = \frac{\omega}{c} Z^{\perp}(\omega)$.

4. To ensure the total energy of a particle (or bunch) does not increase after passage through a non-accelerating structure where the entrance and exit beam pipe cross-sections are the same, $\mathfrak{Re}\ Z^{\parallel}(\omega) \geq 0$. Due to the Panofsky-Wenzel theorem, $\mathfrak{Re}\ Z^{\perp}(\omega) \geq 0$ when $\omega > 0$.

5. As a consequence of the wake function being zero at $z = 0$, $\int_0^{\infty} \mathfrak{Im}\ Z^{\perp}(\omega)\, d\omega = 0$ and $\int_0^{\infty} \frac{\mathfrak{Im}\ Z^{\parallel}(\omega)}{\omega}\, d\omega = 0$.

3.2.3 Common Examples of Wake Functions and Impedances

Many components may be installed in a particle accelerator environment, leading to wakes and impedances that can act back on the beam. Often it is useful to model the effect of generalised wakes and impedances before the precise impedance is known through bench measurement, electromagnetic simulation or beam-based measurement. Below are a few common wake functions and impedances that apply in all accelerator environments and have particular relevance for high-intensity hadron beams.

3.2.3.1 Resistive Wall

Realistic beam pipes are not perfectly conducting and therefore present an impedance for the image current passing through the pipe, creating an electromagnetic wake. Assuming a cylindrical beam pipe, the longitudinal impedance for a length L of resistive beam pipe is:

$$Z^{\parallel}_{\mathrm{rw}}(\omega) = [1 \pm i]\frac{L}{2\pi b \sigma_c \delta_{\mathrm{skin}}} \,, \tag{3.1}$$

where the $+$ is taken for negative ω and the $-$ for positive ω, b is the beam pipe radius, σ_c is its conductivity and δ_{skin} is the skin depth at a given frequency. This is defined by:

$$\delta_{\mathrm{skin}} = \sqrt{\frac{2c}{Z_0 \mu_r \sigma_c |\omega|}} \,, \tag{3.2}$$

where μ_r is the relative magnetic permeability of the beam pipe. The transverse resistive wall impedance for a cylindrical beam pipe is similar and given by:

$$Z^{\perp}_{\mathrm{rw}}(\omega) = [1 \pm i]\frac{Lc}{\pi \omega b^3 \sigma_c \delta_{\mathrm{skin}}} \,, \tag{3.3}$$

where $Z^{\perp}_{\mathrm{rw}}(\omega) = 2cZ^{\parallel}_{\mathrm{rw}}(\omega)/b^2\omega$. It should be noted that the equation for the transverse resistive wall impedance no longer holds true at low frequencies, where the impedance asymptotically approaches infinity as ω approaches zero ($Z^{\perp}(\omega) \propto \omega^{-1/2}$). At these frequencies a different, thin wall (in comparison to the skin depth) model applies and a third model is also required at very high frequencies.

Moving into the time domain, the resistive wall wake functions are given by:

$$W^{\perp}_{\mathrm{rw}}(z) = \frac{\beta c L}{\pi b^3}\sqrt{\frac{Z_0 \beta \mu_r}{\pi \sigma_c |z|}} \tag{3.4}$$

$$W^{\parallel}_{\mathrm{rw}}(z) = \frac{\beta c L}{4\pi b z}\sqrt{\frac{Z_0 \beta \mu_r}{\pi \sigma_c |z|}} \,, \tag{3.5}$$

given the assumption that $b^{2/3}/(\sigma_c Z_0)^{1/3} \ll z \ll b^2 \sigma_c Z_0$ [43].

3.2.3.2 Resonator

An important source of impedances in accelerators is the resonator, not least because accelerating cavities are resonators by design and are an essential component of accelerators. Alongside this, diagnostic devices, vacuum ports and changes in beam pipe cross-section can act as resonant structures. A generalised form for a resonator impedance, approximating it to an RLC parallel circuit, is given by:

$$Z^{\parallel}_{\text{res}}(\omega) = \frac{R_s}{1 + iQ\left(\frac{\omega_r}{\omega} - \frac{\omega}{\omega_r}\right)} \ , \tag{3.6}$$

where $\omega_r/(2\pi)$ is the resonant frequency of the cavity ($1/\sqrt{LC}$, in terms of the RLC circuit comparison); R_s is the shunt impedance (R in the circuit comparison); Q is the quality factor of the cavity ($R\sqrt{C/L}$ in the circuit comparison). The transverse resonator impedance can readily be obtained from the Panofsky-Wenzel theorem [42] leading to:

$$Z^{\perp}_{\text{res}}(\omega) = \frac{c}{\omega}\frac{R_s}{1 + iQ\left(\frac{\omega_r}{\omega} - \frac{\omega}{\omega_r}\right)} \ . \tag{3.7}$$

The corresponding resonator wake functions are therefore given by:

$$W^{\perp}_{\text{res}}(z) = \frac{\beta R_s \omega_r^2}{Q\overline{\omega}} e^{-\alpha z/\beta c} \sin\left(\frac{\overline{\omega} z}{\beta c}\right) \tag{3.8}$$

$$W^{\parallel}_{\text{res}}(z) = \frac{\omega_r R_s}{Q} e^{-\alpha z/\beta c}\left[\cos\left(\frac{\overline{\omega} z}{\beta c}\right) - \frac{\alpha}{\overline{\omega}}\sin\left(\frac{\overline{\omega} z}{\beta c}\right)\right] \ , \tag{3.9}$$

where $\alpha = \omega_r/(2Q)$, $\overline{\omega} = \sqrt{\omega_r^2 - \alpha^2}$ and $W^{\perp}_{\text{res}}(z) = W^{\parallel}_{\text{res}}(z) = 0$ for $z > 0$.

3.2.3.3 Broadband impedances

The impedances due to changes in beam pipe cross-section, vacuum bellows and BPMs are often lumped together in a broadband impedance. This typically takes the same functional form as the resonator impedance (equation 3.7) but with a quality factor $Q \approx 1$ and the resonant frequency is often taken as the cut-off frequency of the beam pipe, $\omega_r \approx R\omega_0/b$ (where R is the mean accelerator radius and b is the beam pipe radius). The impedance due to space charge may also, in certain circumstances, be considered as a broadband impedance as it is independent of frequency (see section 3.4) over a particular frequency range.

3.3 Head-Tail Instability Theory

In general, collective instabilities (such as head-tail) are modelled theoretically using two approaches. The first begins with the single-particle equations of motion, while the other starts with the Vlasov equation and deals with a superposition of modes rather than a bunch of individual particles.

3.3.1 Sacherer's Theory

The Vlasov approach was utilised successfully by Sacherer [22] in the late 1970s to model the dynamics of the head-tail instability. The Vlasov equation is a differential equation that describes the evolution of a charged-particle distribution where long-range interactions are present (*e.g.* Coulomb). The equation is non-linear and can only be solved analytically for small perturbations, when the equation can be linearised. Studying solutions to the linearised Vlasov equation in the case of circular co-ordinate systems (in both longitudinal and transverse phase spaces) allows calculation of *Sacherer's Integral Equation* for instabilities. These lead to a description of what modes are unstable, given a set of initial conditions, and allows the calculation of each mode's growth rate.

In this section Sacherer's integral equation in the transverse plane is derived from the linearised Vlasov equation and the solution for radial modes is shown in detail. The solution for a selection of other excitation modes is also outlined. The formulation largely follows Ng [43] with details from [44], [45] and [46]. It is covered in more detail in [47].

3.3.1.1 Linearised Vlasov Equation

It is convenient to focus on one transverse dimension, y, and move from a rectangular co-ordinate system in phase space (y, p_y) to circular co-ordinates (r_β, θ) by defining:

$$\begin{aligned} y &= r_\beta \cos\theta \\ p_y &= r_\beta \sin\theta \ . \end{aligned} \tag{3.10}$$

Making the assumption that the perturbation due to the wake's interaction with the beam is small in comparison to the external field components and synchro-betatron coupling is avoided, the bunch distribution Ψ can be factorised in the longitudinal-transverse phase space:

$$\Psi(r, \phi; r_\beta, \theta; s) = \psi(r, \phi; s)\ f(r_\beta, \theta; s)\ , \tag{3.11}$$

where $\psi(r, \phi)$ is the longitudinal distribution and $f(r_\beta, \theta)$ is the transverse distribution. These distributions may then be separated into their unperturbed and perturbed parts:

$$\psi(r, \phi; s) = \psi_0(r) + \psi_1(r, \phi; s)\ , \tag{3.12}$$

$$f(r_\beta, \theta; s) = f_0(r_\beta) + f_1(r_\beta, \theta; s)\ . \tag{3.13}$$

The unperturbed distribution ψ_0 is the stationary longitudinal bunch distribution normalised by the number of particles in the bunch, and f_0 is the stationary transverse distribution normalised to unity. Substituting these into equation 3.11 results in four terms:

$$\Psi(r, \phi; r_\beta, \theta; s) = \Big(\psi_0(r) + \psi_1(r, \phi; s)\Big)\Big(f_0(r_\beta) + f_1(r_\beta, \theta; s)\Big) \tag{3.14}$$

$$= \psi_0(r)f_0(r_\beta) + \psi_0(r)f_1(r_\beta, \theta; s) + \psi_1(r, \phi; s)f_0(r_\beta) + \psi_1(r, \phi; s)f_1(r_\beta, \theta; s)\ . \tag{3.15}$$

The $\psi_1 f_0$ term describes only longitudinal excitations, without transverse, driven by longitudinal impedances. As such these can be neglected as we are only interested in a transverse instability. The $\psi_0 f_1$ term describes transverse excitation, without longitudinal, driven by transverse impedances. This may be encapsulated in the $\psi_1 f_1$ term if the azimuthal $m = 0$ longitudinal mode is retained. Therefore the bunch distribution is given by just two terms:

$$\Psi(r, \phi; r_\beta, \theta; s) = \psi_0(r)f_0(r_\beta) + \psi_1(r, \phi)f_1(r_\beta, \theta)e^{-i\Omega s/v}\ , \tag{3.16}$$

where $\psi_1(r, \phi)$ includes, in addition to that in equation 3.13, the longitudinal $m = 0$ mode. The coherent frequency Ω, and with it the dependence on s, is also separated from the $\psi_1 f_1$ term.

This leads to the linearised Vlasov equation, with only first-order terms

$$\left[-i\frac{\Omega}{v}f_1\psi_1 + \frac{\omega_s}{v}f_1\frac{\partial\psi_1}{\partial\phi} + \frac{\omega_\beta}{v}\psi_1\frac{\partial f_1}{\partial\theta}\right]e^{-i\Omega s/v} - \psi_0\frac{df_0}{dr_\beta}\sin\theta\frac{c}{E_0\omega_\beta\beta}\left\langle F_1^\perp(\tau;s)\right\rangle = 0\ , \tag{3.17}$$

where the transverse force $\left\langle F_1^\perp\right\rangle$ is dependent on the average transverse displacement of the beam and is also a function of the longitudinal co-ordinate τ.

Utilising the rigid-beam approximation (section 3.2.1), only rigid dipole mode excitations are considered in the transverse plane. Therefore the bunch will be displaced by a small amount δ from the centre of the transverse phase space and perform betatron oscillations, rotating as a rigid bunch around the phase space centre at ω_β anticlockwise. Assuming a small dipole moment, D, leads to a new linearised Vlasov equation:

$$\left[i(\Omega-\omega_\beta)\psi_1 - \omega_s\frac{\partial\psi_1}{\partial\phi}\right]De^{-i\Omega s/v} + \frac{ic^2}{2E_0\omega_\beta}\psi_0\left\langle F_1^\perp(\tau;s)\right\rangle = 0\ , \tag{3.18}$$

where the exponential expression for $\sin\theta$ has been used with the $e^{-i\theta}$ term dropped. This term corresponds to negative phase space rotations, and therefore the transverse betatron frequency $-\omega_\beta$. Provided the frequency shift due to the wake field is small, this is sufficiently far from the bunch frequency ω_β to be neglected.

3.3.1.2 The Wake Force

The vertical wake force on any given particle is

$$\begin{aligned}\left\langle F_1^\perp(\tau;s)\right\rangle = -\frac{e^2N_b}{C_0}\sum_{k=-\infty}^{\infty}\int d\tau'\Big\langle y\left(\tau';s-kC_0-v(\tau'-\tau)\right)\Big\rangle \\ \times\,\lambda\left(\tau';s-kC_0-v(\tau'-\tau)\right)W_1\left(kC_0+v(\tau'-\tau)\right),\end{aligned} \tag{3.19}$$

where C_0 is the accelerator circumference; $\langle y(\tau';s)\rangle$ is the average vertical displacement of the beam slice that has time advance τ' at a location s along the accelerator; and $\lambda(\tau';s)$ is the longitudinal distribution. The summation over k accounts for the contribution from wakes left on previous turns. Substituting in the phase space distribution from equation 3.16 one finds that the $\psi_0(r)f_0(r_\beta)$ term gives no contribution as there is no transverse displacement of the unperturbed

beam centre, $\langle y(\tau';s)\rangle = 0$. Therefore the vertical wake force, $\left\langle F_1^{\perp}(\tau;s)\right\rangle$, only receives contributions from the perturbed, dynamic part of the distribution.

Assuming M identical, equally spaced bunches, the wake force on a test particle in the n^{th} bunch, at time advance τ, can be calculated:

$$\left\langle F_{1,n}^{\perp}(\tau;s)\right\rangle = \frac{i\beta e^2 DMN_b\omega_0}{C_0} e^{-i\Omega s/v} \sum_{q=-\infty}^{\infty} \tilde{\lambda}_{1,n}(\omega_q) Z^{\perp}(\omega_q) e^{i\omega_q \tau} \ , \tag{3.20}$$

where N_b is the number of particles per bunch, $\tilde{\lambda}_{1,n}$ is the Fourier transform of the perturbed line density of the n^{th} bunch and $\omega_q = (qM + \mu + Q_y)\omega_0 + \Omega$, the frequencies of the bunch's line spectrum (where q takes any integer, the coupled bunch mode μ is a positive integer or zero, Q_y is the vertical betatron tune).

3.3.1.3 Sacherer's Integral Equation

Substituting the wake force of equation 3.20 into the linearised Vlasov equation (equation 3.18) leads to:

$$\left[i(\Omega - \omega_\beta)\psi_1 - \omega_s \frac{\partial \psi_1}{\partial \phi}\right] D e^{-i\Omega s/v} = \\ - \frac{ic^2}{2E_0\omega_\beta}\psi_0 \frac{i\beta e^2 DMN_b\omega_0}{C_0} e^{-i\Omega s/v} \sum_{q=-\infty}^{\infty} \tilde{\lambda}_{1,n}(\omega_q) Z^{\perp}(\omega_q) e^{i\omega_q \tau} \ . \tag{3.21}$$

First, expand the perturbed distribution ψ_1 in the longitudinal plane ($\psi_1(r,\phi) = \sum_m \alpha_m R_m(r) e^{im\phi}$) and express the unperturbed longitudinal distribution as

$$\psi_0(r)\, d\tau d\Delta E = \frac{\omega_s \beta^2 E_0}{\eta}\psi_0\, dx dp_x = N_b g_0(r) r\, dr d\phi \ . \tag{3.22}$$

With these and the projection of the perturbed distribution $\tilde{\lambda}_{1,n}(\omega_q)$ in the time domain:

$$\begin{aligned} \tilde{\lambda}_{1,n}(\omega_q) &= \frac{1}{2\pi}\int \lambda_{1,n}(\tau') e^{-i\omega_q\tau'} d\tau' \\ &= \frac{1}{2\pi}\int \psi_{1,n}(\tau', \Delta E') e^{-i\omega_q\tau'} d\tau' d\Delta E' \\ &= \frac{E_0\omega_s\beta^2}{2\pi\eta}\int \psi_{1,n}(r',\phi') e^{-i\omega_q\tau'} r' dr' d\phi' \\ &= \frac{E_0\omega_s\beta^2}{2\pi\eta}\sum_{m'} \alpha_{m'} \int R_{m'}(r') e^{im'\phi'} e^{-i\omega_q\tau'} r' dr' d\phi' \ , \end{aligned} \tag{3.23}$$

the linearised Vlasov (equation 3.21) can be expressed as

$$i(\Omega - \omega_\beta - m\omega_s)\sum_m \alpha_m R_m(r)e^{im\phi} = \frac{c^2\beta e^2 M N_b \omega_0}{4\pi E_0 \omega_\beta C_0} g_0 \sum_{q=-\infty}^{\infty}\sum_{m'} Z^\perp(\omega_q)\alpha_{m'}\int R_{m'}(r')e^{im'\phi'}e^{i\omega_q(\tau-\tau')}r'dr'd\phi' \ . \tag{3.24}$$

Rewriting in circular coordinates, utilising the smooth approximation ($\omega_\beta = \nu_\beta\omega_0 = \beta c/\beta_y$) and solutions in the form of Bessel functions results in Sacherer's integral equation in the transverse plane:

$$(\Omega - \omega_\beta - m\omega_s)\alpha_m R_m(r) = -\frac{i\pi e^2 M N_b}{\beta E_0 T_0^2} g_0 \sum_{q=-\infty}^{\infty}\sum_{m'} i^{m-m'}\beta_y Z^\perp(\omega_q)\alpha_{m'}\int R_{m'}(r')J_m(\omega_q r)J_{m'}(\omega_q r')r'dr' \ . \tag{3.25}$$

3.3.1.4 Solutions of Sacherer's Integral Equation

To solve Sacherer's integral equation in the transverse plane, for each azimuthal m, a complete set of orthonormal functions $g_{mk}(r)$ (where $k \in \mathbb{N}$) must be found such that

$$\int W(r)g_{mk}(r)g_{mk'}(r)rdr = \delta_{kk'} \ , \tag{3.26}$$

where $W(r) = g_0(r)$ is taken as a weight function, and the subscript k represents the radial modes associated with the azimuthal quantum number m. As the weight function $W(r)$ is independent of m, the orthonormal functions $g_{mk}(r)$ are not uniquely defined. However, examining a single azimuthal in equation 3.25 it may be seen that

$$R_m(r) \propto W(r)J_m(\omega_q r) \ , \tag{3.27}$$

and, therefore for small r

$$R_m(r) \sim r^m \lim_{r\to 0} W(r) \ . \tag{3.28}$$

In order to reduce the equation to an eigenvalue problem, the radial functions $R_m(r)$ are expanded using the orthonormal functions in equation 3.26:

$$\alpha_m R_m(r)e^{im\phi} = \sum_k a_{mk}W(r)g_{mk}(r)e^{im\phi} \ . \tag{3.29}$$

Since $g_{mk}(r)$ is an expansion of $R_m(r)$, the small r behaviour of $g_{mk}(r)$ will be constrained. As such the set of orthonormal functions become dependent on the azimuthal m and therefore unique.

Substituting the expansion in equation 3.29 into both sides of Sacherer's integral equation, multiplying both sides by $g_{mk}(r)$ and integrating over $r\,dr$ reduces the equation to

$$\begin{aligned}(\Omega - \omega_\beta - m\omega_s)a_{mk} = \\ - \quad \frac{i\pi e^2 M N_b}{\beta E_0 T_0^2} \sum_{q=-\infty}^{\infty} \sum_{m'} \sum_{k'} \beta_y Z^\perp(\omega_q) a_{m'k'}\ \tilde{\lambda}^*_{mk}(\omega_q)\tilde{\lambda}_{m'k'}(\omega_q)\ , \end{aligned} \quad (3.30)$$

where the $\tilde{\lambda}$ term has been defined

$$\tilde{\lambda}_{mk}(\omega) = \int i^{-m} W(r) J_m(\omega_q r) g_{mk}(r) r dr\ . \quad (3.31)$$

This is also the Fourier transform of the eigenmode $\lambda_{mk}(\tau)$ and the mk component of the perturbed density. Together this reduces the integral equation to a matrix equation

$$(\Omega - \omega_\beta - m\omega_s)a_{mk} = \sum_{m'k'} \omega_s M^\perp_{mk,m'k'} a_{m'k'}, \quad (3.32)$$

where the dimensionless interaction matrix has been defined,

$$M^\perp_{mk,m'k'} = -\frac{i\pi e^2 M N_b}{\beta E_0 T_0^2 \omega_s} \sum_{q=-\infty}^{\infty} \beta_y Z^\perp(\omega_q) \tilde{\lambda}^*_{mk}(\omega_q)\tilde{\lambda}_{m'k'}(\omega_q)\ . \quad (3.33)$$

Solutions to this reduced matrix form of Sacherer's integral equation are dependent on the assumed, unperturbed distribution as well as the impedance. In general, for most beam coupling impedances, the interaction matrix $M^\perp_{mk,m'k'}$ is not diagonal. Therefore, in order to solve the equation, the diagonalisation must be performed numerically. However, an estimate of the collective frequency can be found by computing just the diagonal elements of the interaction matrix. To help with this, equation 3.33 may be rewritten with a form factor given by,

$$F_{mk} = \frac{4\pi M\hat{\tau}}{T_0} \sum_q |\tilde{\lambda}_{mk}(\omega_q)|^2 = \frac{4\pi M\hat{\tau}}{T_0} \sum_q h_{mk}(\omega_q)\ , \quad (3.34)$$

$$M^\perp_{mk,m'k'} = -\frac{ie^2 N_b}{8\pi\beta E_0 \nu_s \hat{\tau}} \frac{\sum_q \beta_y Z_\perp(\omega_q)\tilde{\lambda}^*_{mk}(\omega_q)\tilde{\lambda}_{m'k'}(\omega_q)}{\sum_q |\tilde{\lambda}_{mk}(\omega_q)|^2} F_{mk}. \quad (3.35)$$

Taking only the diagonal elements this becomes

$$M^{\perp}_{mk,m'k'} = -\frac{ie^2 N_b \overline{\beta}_y}{8\pi\beta E_0 \nu_s \hat{\tau}} Z_{\perp}|^{mk}_{\text{eff}} F_{mk} \ , \tag{3.36}$$

where an effective impedance, $Z_{\perp}|^{mk}_{\text{eff}}$ is defined representing a weighted average of the impedance over the power spectrum $h_{mk}(\omega_q)$,

$$Z_{\perp}|^{mk}_{\text{eff}} = \frac{\sum_q [\beta_y Z_{\perp}(\omega_q)] h_{mk}(\omega_q)}{\overline{\beta}_y \sum_q h_{mk}(\omega_q)}. \tag{3.37}$$

The factor $\overline{\beta}_y$ maintains the dimensions of impedance and can be taken as the average value of the beta function, its value at a particular location or, using the smooth approximation, $\overline{\beta}_y = R/Q_y$.

3.3.1.5 Sacherer's Radial Modes

Head-tail excitations are observed to be sinusoid-like standing waves along the bunch length. Sacherer [22] discovered that, assuming that the perturbation is small enough such that only one azimuthal mode (m) is excited and that the transverse unperturbed distribution is a uniform or so-called "waterbag" distribution (constant number density within the 100 % beam size and zero elsewhere), the dominant radial mode (with $k = 0$) projected onto the time axis is approximately sinusoidal. As such, rather than solving the integral equation, Sacherer approximated $\lambda_{mk}(\tau)$ by a linear combination of sinusoidal modes,

$$\lambda_{m0}(\tau) = \begin{cases} \cos & \left[(m+1)\pi\frac{\tau}{\tau_b}\right] \ , \quad m = 0, 2, 4, \ldots \\ \sin & \left[(m+1)\pi\frac{\tau}{\tau_b}\right] \ , \quad m = 1, 3, 5, \ldots \end{cases} \tag{3.38}$$

where τ_b is the total bunch length. This model leads to m nodes along the bunch length, discounting the bunch's two ends, as well as all azimuthal modes being orthogonal to one another.

From these sinusoids the bunch power spectrum can be found from the square of the Fourier transforms of equation 3.38 [47]

$$\begin{aligned} h_m(\omega) &= |\tilde{\lambda}_{m0}(\omega)|^2 = |\mathcal{F}[\lambda_{m0}(\tau)]\,|^2 \\ &= (m+1)^2 \frac{\tau_b^2}{2\pi^4} \frac{1 \pm \cos\,\pi y}{\left[y^2 - (m+1)^2\right]^2} \ , \end{aligned} \tag{3.39}$$

where $y = \omega\tau_b/\pi$ and the plus sign is for even m while the minus sign is for odd m. Figure 3.2 shows $h_m(\omega)$ for m between 0 and 4 with zero chromaticity (no variation of tune with momentum offset).

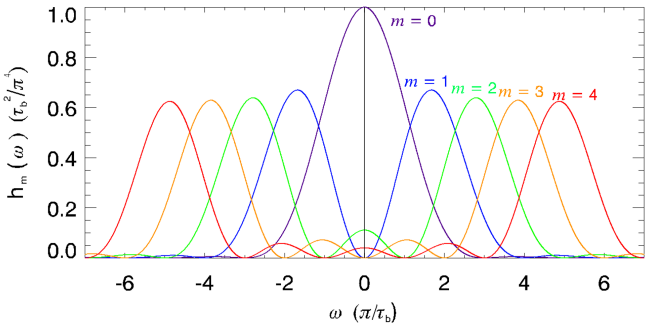


Figure 3.2: Frequency spectrum $h_m(\omega)$ for modes 0 to 4 with zero chromaticity.

For finite chromaticity ($\xi = (dQ/Q)/(dp/p)$), the betatron tune Q varies as the particle makes a synchrotron oscillation in longitudinal phase space (figure 3.3). This leads to a phase shift along the bunch reaching its maximum value between head and tail of

$$\chi = \frac{\xi}{\eta} Q\omega_0\tau_b = \omega_\xi Q\tau_b \ , \tag{3.40}$$

where ω_ξ is the shift in frequency due to chromaticity, which also provides the frequency of oscillations along the bunch.

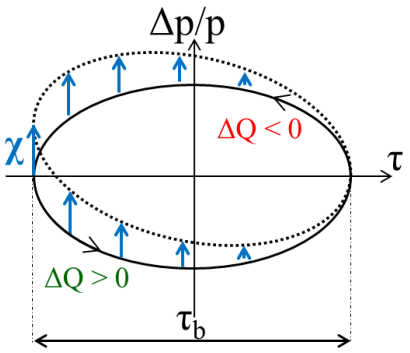


Figure 3.3: Longitudinal phase space showing the accumulated chromatic phase slip between the head and the tail of the bunch (assuming negative chromaticity).

Figure 3.4 illustrates some examples of head-tail mode structures as may be observed on a BPM difference signal $\propto \lambda_{m0}(\tau)e^{i\omega_\xi t}e^{2\pi ikQ}$. This figure is taken directly from Sacherer's paper [22].

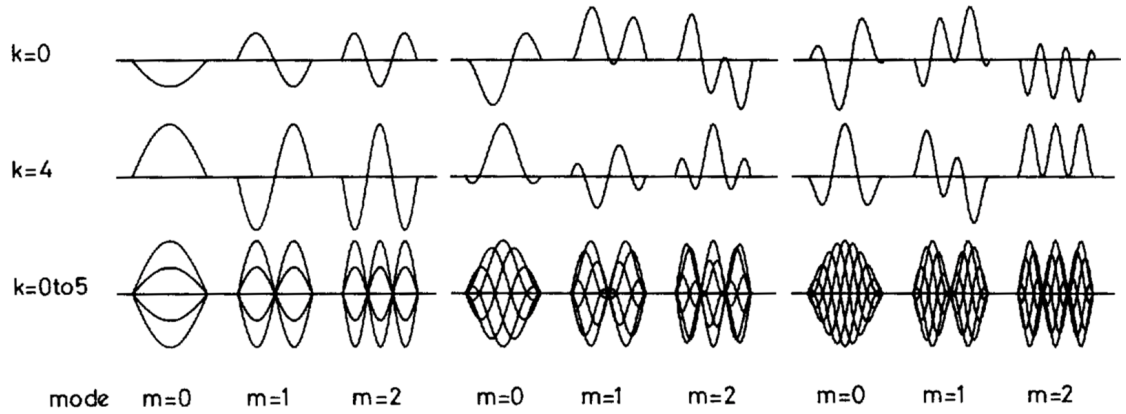


Figure 3.4: BPM difference signal of a single bunch on the k^{th} turn and six turns overlaid for $Q = 4.833$ and: $\chi = 0\,\text{rad}$ (left); $\chi = 5\,\text{rad}$ (middle) and $\chi = 9\,\text{rad}$ (right). Taken from figure 13 in [22].

With non-zero chromaticity, the bunch standing wave also has a travelling-wave component $e^{i\omega_\xi t}$ shifting the bunch power spectrum $h_m = h_m(\omega - \omega_\xi)$. However, it is noted that the power spectrum in equation 3.39 only represents an envelope to the bunch line spectrum defined by the sum of the individual particle's spectra. Figure 3.5 illustrates an example bunch spectrum with four bunches and a chromatic frequency shift.

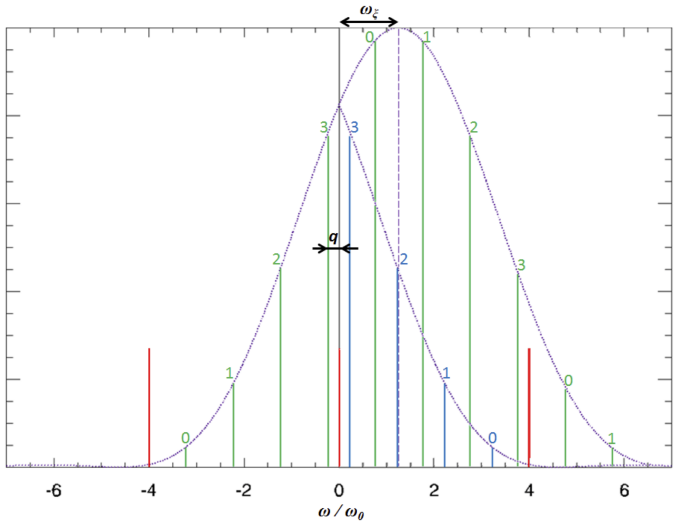


Figure 3.5: Fourier spectrum for four bunches and $Q = 3.75$ for different coupled-bunch modes $n = 0, 1, 2, 3$. The envelope is drawn for $m = 0$ head-tail mode and shifted by the chromatic frequency $\omega_\xi = 1.22\omega_0$. Green lines show the positive and negative frequencies, whereas a network analyzer "sees" the blue lines as reflected in the zero frequency line.

3.3.1.6 Growth Rate

The head-tail growth rate may be calculated from the interaction matrix (equation 3.36) with

$$\begin{aligned} \frac{1}{\tau} &= \mathfrak{Im}\, M^{\perp}_{m0,m'0}\, \omega_s \\ &= -\frac{1}{1+m}\, \frac{e^2 N_b \overline{\beta}_{\perp} \omega_s}{8\pi\beta E_0 \nu_s \hat{\tau}}\, Z_{\perp}|^{mk}_{\text{eff}}\,, \end{aligned} \tag{3.41}$$

where the form factor has been taken to be $F_{mk} = (1+m)^{-1}$, [48]. The impedance is integrated over the entire bunch spectrum to obtain the growth rate for each azimuthal mode m. Equation 3.41 is the general result and reduces to the single bunch head-tail growth rate in the limit of short-range wakes.

Figure 3.6 shows an example for a resistive wall impedance and a bunch spectrum with a positive chromatic frequency shift. Given that the effective impedance in equation 3.41 involves a sum over the impedance and bunch spectrum (equation 3.37), it shows that mode $m = 0$ is stable; however mode $m = 1$ may be unstable as the line spectrum may sample more negative $Z_{\perp}$ than positive. The precise growth rate depends on the full bunch line spectrum, ω_q (which depends on the betatron tune) and the impedance at those specific frequencies (see equation 3.37).

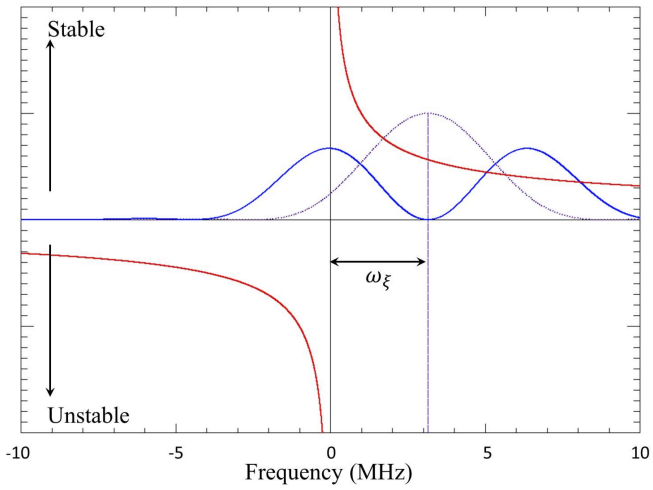


Figure 3.6: A resistive wall impedance (red) and azimuthal modes $m = 0$ (purple) and $m = 1$ (blue) in the case of a positive chromatic frequency ω_ξ.

3.3.2 Rees' Theory

An alteration to Sacherer's theory was proposed by Rees [40] in order to explain some observations on the ISIS synchrotron. The paper aims at explaining the discrepancy between the mode number predicted by Sacherer's theory (obtained from the head-tail phase shift assuming a resistive wall impedance) and the oscillation mode observed in accelerator operation.

Rees proposed that the upper and lower betatron sidebands are incorrectly treated in Sacherer's model as the standing-wave pattern is assumed to be a complex exponential ($\propto e^{i\omega_\xi \tau + i\pi kQ}$) rather than a real sinusoid. With the latter assumption, the displacement pattern along the bunch can be expanded in terms containing $\sin \omega_\xi \tau$ and $\cos \omega_\xi \tau$, each with their separate modulations. This leads to two separate Fourier transforms rather than the single one in Sacherer. As such, there are two amplitudes for each Fourier harmonic and the amplitude of each betatron sideband is given by half the sum or half the difference of the two Fourier harmonic amplitudes.

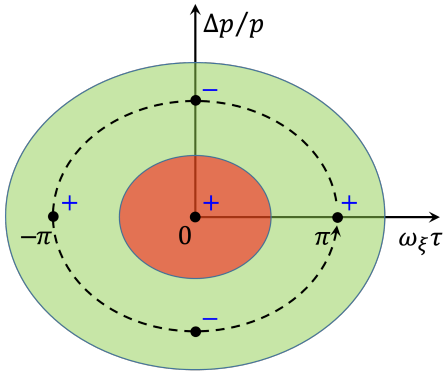


Figure 3.7: Longitudinal phase space indicating Rees' theory with cancellation between betatron motions of large and small synchrotron amplitude particles. In this $m = 1$ case, there is a single node in the bunch's differential signal.

Treating the differential signal in this way leads to large differences in lower and upper betatron sideband amplitudes. In the case of ISIS, which operates below transition and with natural chromaticity, this leads to large resistive wall forces for $(n + Q_y)$ sidebands rather than the generally associated $(n - Q_y)$ sidebands.

This finding, together with the measured head-tail phase shift, has led to a different proposed head-tail mechanism. Instead of coherent betatron motion cancelling between $+\Delta p/p$ and $-\Delta p/p$ particles to create nodes in the bunch differential signal, Rees proposed that the cancellation occurs between particles of small and large synchrotron amplitude, see figure 3.7. Similar pictures can be created for higher-order mode numbers.

3.3.3 Transverse Mode Coupling Instability, TMCI

As the bunch intensity increases, the different head-tail modes shift in frequency and may end up overlapping the neighbouring mode. Therefore, the modes can no longer be treated separately and a single perturbation distribution ($\lambda_{mk}(\tau)$, described after equation 3.31) no longer describes the mode. Instead, a linear combination of azimuthal modes may represent the dynamics. This phenomenon is most commonly referred to as mode coupling and, in the transverse plane, the instability is called the Transverse Mode Coupling Instability (TMCI, first described in terms of coupling modes, by Kohaupt [49]).

TMCI may be thought of as a transverse version of Sacherer's theoretical proposal to explain the longitudinal microwave instability as the coupling of coherent longitudinal modes. TMCI is a synchrotron version of a similar instability observed in linacs, beam break-up, although with a significant difference arising from the synchrotron oscillations, which stabilise the beam below a threshold intensity. The threshold is dependent on the synchrotron tune, beam energy, strength of impedance as well as the bunch length. Two regimes have been identified, when the bunch length is longer or shorter than the inverse of twice the resonant frequency of the impedance ($\tau_b >$ or $< 1/(2f_r)$) [50].

3.4 Influence of Space Charge

3.4.1 What is Space Charge?

Interactions between particles within a beam are generally referred to as collective effects. This includes the phenomena of wakes and impedances (see section 3.2),

which relate to the electromagnetic fields produced by the beam interacting with the environment (magnets, RF cavities, beam pipes, *etc.*) and acting back on the beam. This is also sometimes referred to as indirect space charge. Collective effects also encompasses self fields: electromagnetic fields produced by the particles in the beam directly interacting with other particles within the same beam, referred to simply as space charge or direct space charge.

Forces from direct space charge arise due to the combination of electric and magnetic fields created by the individual particles and are dependent on the distribution of particles within the beam. For example (following [51]), considering a uniform, continuous beam (charge per unit length, λ) of circular cross-section (radius, a) and coasting at a velocity of βc the electric and magnetic fields are

$$\vec{E}_r = \frac{\lambda}{2\pi\epsilon_0 a^2}\vec{r} \tag{3.42}$$

$$\vec{B}_\phi = = \frac{\beta\lambda}{2\pi\epsilon_0 c a^2}\vec{r}, \tag{3.43}$$

where ϵ_0 is the permittivity of free space, β the relativistic factor, c the speed of light in vacuum, $\vec{r}$ the radial vector and ϕ the radial angle. The combined effect of these fields on charged particles is the space charge force, derived using the Lorentz force equation

$$\vec{F} = q\left(\vec{E} + \vec{B}\times\vec{v}\right) = \frac{q\lambda}{2\pi\epsilon_0 a^2}\left(1-\beta^2\right)\vec{r}, \tag{3.44}$$

where $\vec{F}$ is the force on a particle with charge q and velocity $\vec{v}$. Using the relativistic factor $\gamma = (1-\beta^2)^{-1/2}$ this becomes

$$\vec{F} = \frac{q\lambda}{2\pi\epsilon_0 a^2\gamma^2}\vec{r}. \tag{3.45}$$

The space charge force (equation 3.45) is inversely proportional to γ^2, approaching zero as the particle velocity approaches c and becoming an increasingly important component in beam dynamics at lower energies. Replacing the radial coordinate $\vec{r}$ by the Cartesian transverse coordinates (x, y) results in the horizontal and vertical space charge forces (F_x and F_y) which are linear in x and y (more realistic non-uniform beam distributions feature non-linear terms)

$$F_x = \frac{q\lambda}{2\pi\epsilon_0 a^2\gamma^2}x\,, \qquad F_y = \frac{q\lambda}{2\pi\epsilon_0 a^2\gamma^2}y\,. \tag{3.46}$$

Comparing the space charge force with that of a quadrupole magnet (also linear in x and y), the quadrupole is focusing in one transverse plane and defocusing in the other; whereas space charge is defocusing in both planes. As such, the force opposes the transverse focusing provided by the quadrupoles in the accelerator and therefore modifies the beam's envelope around the accelerator.

3.4.1.1 Space Charge Tune Shift

Assuming uniform focusing (also known as the smooth focusing approximation), where the beta functions are constant and given by the average radius of the machine divided by the betatron tune $\beta_{x,y} \approx R/Q_{x,y}$, and the uniform, continuous, circular beam of before, an equation of motion without space charge may be derived (following [51]):

$$\frac{d^2y}{dt^2} + Q_y^2\omega_0^2 y = 0 \ . \tag{3.47}$$

Equation 3.47 includes the vertical betatron tune Q_y, the revolution frequency ω_0 and only shows the vertical equation of motion; horizontally the situation is identical with x replacing y. The presence of space charge forces adds a further acceleration term to the individual particles, leading to a modified equation of motion

$$\frac{d^2y}{dt^2} + \left(Q_y^2\omega_0^2 - \frac{q\lambda}{2\pi\epsilon_0 a^2 m_0\gamma^3}\right) y = 0 \tag{3.48}$$

$$\frac{d^2y}{dt^2} + Q_M^2\omega_0^2 y = 0 \ . \tag{3.49}$$

The bracketed term of equation 3.48 has been replaced with a modified tune $Q_M^2 = (Q_y + \Delta Q_y)^2$. Expanding the bracket, assuming that the space charge modification to the tune ΔQ_y is small with respect to Q_y, the ΔQ_y^2 term may be neglected leaving $Q_M^2 \approx Q_y^2 + 2Q_y\Delta Q_y$.

Therefore, given the assumptions, the incoherent space charge tune shift ΔQ_y is given by the formula

$$\begin{aligned} \Delta Q_y &= -\frac{q\lambda}{4\pi\epsilon_0 a^2 m_0\gamma^3\omega_0^2 Q_y} \\ &= -\frac{q\lambda R^2}{4\pi\epsilon_0 a^2 m_0 c^2\beta^2\gamma^3 Q_y} \ , \end{aligned} \tag{3.50}$$

where $\omega_0 = \beta c/R$, with R as the average accelerator radius. Expressing the charge per unit length λ in terms of the number of particles N and bunching factor B_F, $\lambda = qN/2\pi RB_F$ and amalgamating several terms using the classical radius $r_0 = q^2/2\pi\epsilon_0 m_0 c^2$

$$\Delta Q_y = -\frac{r_0 N R}{2\pi a^2 Q_y \beta^2 \gamma^3 B_F} \,. \tag{3.51}$$

As a smooth approximation was made, equation 3.51 may easily be expressed in terms of the 100 % vertical emittance $\varepsilon_y = a^2/\beta_y \approx Q_y a^2/R$:

$$\Delta Q_y = -\frac{r_0 N}{2\pi \varepsilon_y \beta^2 \gamma^3 B_F} \,. \tag{3.52}$$

Equation 3.52 is the incoherent space charge tune shift, and is often used as a figure-of-merit for comparisons between accelerators. It should be noted that the formula does not take into account coherent effects arising from image charges (*e.g.* [43, 44]), although these are typically smaller. Importantly, realistic, non-uniform beam distributions result in non-linear force terms and a corresponding space charge tune spread as well as a shift.

3.4.2 Role of Space Charge in Instabilities

Direct space charge (interaction of particles within a single beam) cannot, on its own, drive a beam unstable. As described in section 3.2, beam instability requires the presence of an external impedance, or interaction with the beam's environment. However, direct space charge can, and does, play a role in beam instability dynamics, and is still the subject of research at various sites [52].

The theory behind the head-tail instability in bunched beams has become well-established (see section 3.3.1), albeit with some discrepancy with regards to ISIS ([40], including a modified interpretation). However, perhaps due to the paucity of accelerators operating in the high-intensity regime where space charge plays an appreciable role, the interaction between space charge and the head-tail instability has only been studied sporadically since the 1990s.

3.4.2.1 Theoretical Treatments

Theoretical treatment of the influence of space charge on head-tail instability dynamics was first attempted by Blaskiewicz [53]. This analysed the effect of space charge on coherent head-tail modes and their growth rates in the presence of a square potential well, or "airbag" particle distribution, with short-range wake functions. No assumptions were made of the amplitude of space charge tune shift or its comparison with the synchrotron tune or wake induced tune shift, which became important in later theoretical studies. Simulations agreed well with the model and suggested space charge should damp the TMCI (section 3.3.3). The model predicts a tune shift due to space charge (without impedances) dependent on the head-tail mode as

$$\Delta Q = -\frac{\Delta Q_{\mathrm{SC}}}{2} \pm \sqrt{\frac{\Delta Q_{\mathrm{SC}}^2}{4} + k^2 Q_s^2}\,, \tag{3.53}$$

where ΔQ_{SC} is the space chare tune shift of equation 3.52 and + is used for integer modes $k \geq 0$.

A different approach was taken by Burov [23] and Balbekov [24], making no assumption of the bunch distribution or shape of the potential well but assuming that the space charge tune shift is large compared to the synchrotron tune and wake-induced tune shift. This assumption allows for a "rigid slice" approximation where each longitudinal slice of the beam oscillates as a rigid body, reducing the complexity of the problem. Solutions for a parabolic potential well and a 3D Gaussian distribution are given, although the method applies universally. The papers conclude that space charge itself increases the threshold for TMCI by 1 – 2 orders of magnitude by either Landau damping or because the mode coupling is shifted to higher intensities.

The "two-particle model" [44] was designed to illustrate the mechanism of TMCI. This theoretical description was extended by Ho Chin *et al.* to include space charge forces [54] and chromaticity effects [55]. In agreement with other theoretical studies, Ho Chin *et al.* found that, as the space charge force increases, the beam moves from an unstable region to a stable one. However, the new "two-particle model" predicts that further increases in the space charge make the beam unstable again creating a

series of stable and unstable regions. The inclusion of chromaticity may help to explain observations in machines with relatively short bunches, where increasing chromaticity has a negligible effect on mitigating TMCI.

A further theory, put forward in order to investigate the behaviour of instabilities in the presence of strong space charge, particularly TMCI, is that of convective instabilities [56]. In contrast to "absolute" instabilities, where an initial perturbation seeds unrestricted exponential growth everywhere, convective instabilities only have a spatial amplification and the perturbation eventually decays when any size of damping is added. This theory was partly presented to address the strange conclusion of TMCI in the presence of strong space charge [23] that a beam experiencing a TMCI, once stabilised by strong space charge, is then stable regardless of how much higher the beam intensity is taken. The author argues that some instabilities have been misattributed to TMCI when their attributes better fit that of convective instabilities.

A new description of the space charge interaction with TMCI has been introduced using a circulant matrix model [57]. This seems to confirm predictions of the convective instability described by Burov as well as possibly confirming the new two particle model proposed by Ho Chin *et al.*, with the mitigation of TMCI through space charge and the the generation of further mode couplings at increased space charge levels.

3.4.2.2 Simulations

Given developments in computing power, numerical simulations (see section 3.5) have become an invaluable tool in pursuing more accurate predictions of beam stability, particularly in the presence of space charge. The effect of space charge on the head-tail instability was studied using the macroparticle tracking PATRIC code [58] by Kornilov and Boine-Frankenheim [25, 59]. They found that Blaskiewicz's airbag model gave a good prediction of the head-tail mode frequencies (given by equation 3.53), even with Gaussian bunch distributions, especially in the case of strong space charge. The range of space charge strength where Landau damping was prominent was found to depend on the head-tail mode excited. Applications

to experimental data from CERN PS showed reasonable agreement. In order to characterise the impact of space charge on the head-tail instability a "space charge parameter" $q = \Delta Q_{\mathrm{SC}}/Q_s$ was introduced (the peak incoherent space charge tune shift divided by the synchrotron tune), although the ratio was utilised in Blaskiewicz's airbag model.

Simulations of the transverse dipole modes in the presence of space charge have also been performed [60] using the SYNERGIA program [61], with results comparing well with those of Kornilov and Boine-Frankenheim [25]. The study also estimated the threshold for the strong space charge regime first proposed by Burov [23] and found that Landau damping rates were very sensitive to the transverse particle distribution.

The studies of Balbekov have progressively been extended to model the variation of the TMCI threshold at high space charge levels for various potentials [62], and for different bunch distributions [63]. Also concluding, for a parabolic potential well, that the TMCI threshold increases with decreasing root-mean-square (RMS) bunch length, for a fixed total bunch length. Burov's work has included the development of a new Vlasov solver to analyse transverse oscillations of bunched beams with strong space charge [64, 65] and its application to TMCI [66] indicating the possibility of two types: one where the threshold value of the wake induced tune shift increases linearly with the space charge tune shift (when the latter is large enough), and one in the strong space charge case where the wake induced tune shift is asymptotically inversely propotional to the space charge tune shift.

Further studies of TMCI at high beam intensities have been made most recently by Métral and Migliorati [67] and by Métral where mode coupling occurs due to space charge (or impedance, beam-beam effects or e-cloud) in [68]. These studies predominantly used the Vlasov solver GALACTIC [69], but with comparisons to PyHEADTAIL [70] macroparticle simulations. A good agreement was found between the codes for a broadband resonator impedance for head-tail modes and growth rates. In the most recent study [68] Métral investigated the difficulty of non-linearities and higher order modes in TMCI, with particular reference to the

BPM intrabunch signal. Features of this signal are noted above and below the TMCI threshold, as well as after mode decoupling (when it exists).

3.4.2.3 Experiments

Few experimental studies have been performed to benchmark these space charge modified head-tail instability theories. Kornilov and Boine-Frankenheim's study [25], and a linked paper on the interpretation of measured transverse spectra [71], showed experimental observations of the transverse coherent spectra on the SIS18 synchrotron at GSI Darmstadt [72] matched well with a slightly modified version of Blaskiewicz's airbag model [53]. This modification was further extended to include the additional coherent tune shift due to image charges which could enhance Landau damping and was proposed in order to explain some observations on the ISIS synchrotron [59].

Studies have been ongoing at the J-PARC facility (see section 1.1.1.5) looking at the effect of space charge on a transverse beam instability induced by the impedance of their extraction kickers [73, 74]. Although the studies are focused on the coupled-bunch instability (characterised by whole-bunch, coherent, dipolar oscillations rather than intrabunch modes), the mechanisms are similar. Both papers show that space charge plays an important role in damping the instability with Shoduba *et al.* [73] producing a modified coupled-bunch instability theory to predict the growth rates. Saha *et al.* [74] used PyORBIT [75] with an enhanced impedance model to show the chromaticity dependence of the instability as well as the important role indirect space charge plays in stabilising the beam.

3.5 Instability Simulation

A number of methods can, and have been, used to assess beam stability in synchrotrons as well as evaluating instability mitigation techniques. There are predominantly two methods used to approach this stability assessment: solving the Vlasov equation [76] and macroparticle tracking simulations. Historically, instability dynamics was first investigated by finding solutions to the Vlasov equation using

perturbation theory (*e.g.* [22]). This considers the beam's phase space as a continuous medium and solutions to the equation represent eigenmodes of oscillation that develop on the action of impedances. This semi-analytical approach led to Sacherer's integral equation (3.3.1) and, more recently, computer codes such as DELPHI (Discrete Expension over Laguerre Polynomials and Head-tail modes to compute Instabilities, [77]), GALACTIC (GArnier-LAclare Coherent Transverse Instabilities Code, [69]), MOSES (MOde-coupling Single bunch instability in an Electron Storage ring, [78]) and NHTVS (Nested Head-Tail Vlasov Solver, [79]) have been used to find solutions.

The second main approach to beam stability assessment is the use of macroparticle tracking simulations. In these, the beam is treated as a collection of macroparticles (one macroparticle usually representing a large number of real particles) which are tracked through the accelerator. This particularly facilitates the study of multiple effects at once (*e.g.* space charge, interaction with electron cloud, effect of multiple impedances, *etc.*) and allows observation of the time evolution of the beam's longitudinal and transverse motion. A number of macroparticle tracking codes include the effects of beam coupling impedances, and as such assess beam stability, including BEAMBEAM3D (including counter-rotating beam effects in colliders, [80]), SBTRACK and MBTRACK (Single Bunch and Multi-Bunch TRACKing, respectively, for electron storage rings [81]), MUSIC (MUlti-bunch particle SImulation Code, [82]), PATRIC [58], PyHEADTAIL (including electron cloud effects, [70]) and PyORBIT (including direct space charge and tracking through individual lattice elements, [75]).

To study an instability effectively, the primary drivers of the beam dynamics must be determined (*e.g.* impedances, space charge, coupled bunch effects, *etc.*). A suitable code may then be chosen that incorporates many (if not all) of the desired physical processes and a systematic investigation of the beam stability may begin.

3.5.1 PyHEADTAIL

The macroparticle simulation code PyHEADTAIL [83] is an open source library written in Python, C and CUDA [84] and based on the HEADTAIL code [85]. It has been specifically designed to simulate collective effects in circular accelerators. It utilises a "drift-kick" model, treating the accelerator as a collection of segments, incorporating elements that modify a subset of the beam's attributes and drifts. At the end of each of these segments one or more collective effects may be simulated.

The tracking routines comprise linear transverse motion including models for dispersion and chromaticity, and linear or non-linear longitudinal motion with arbitrary RF harmonic combinations. Often a smooth focusing approximation is utilised which assumes a constant β-function equal to $\beta_{x,y} = R/Q_{x,y}$, hence $\alpha_{x,y} = 0$.

PyHEADTAIL includes functions to create several standard particle beam distributions or the code user can define a bespoke distribution. Standard beam distributions [86] include the Kapchinskij-Vladimirskij distribution (uniform density in real space and elliptical cross-section) [1], 4D waterbag distribution (uniform in 4D phase space), parabolic distribution (parabolic density in phase space) and Gaussian distribution.

3.5.1.1 Collective Effects

Collective effects are applied at the end of each segment and are typically correlated to the longitudinal position of the particle within the bunch. Calculating the effect of each macroparticle on every other macroparticle would be laboriously time consuming and computationally intensive, even assuming the electromagnetic fields (or wakes) only act on trailing particles. As such it is convenient to bin the macroparticles longitudinally using a 1D particle-in-cell (PIC) algorithm, slicing the bunch into longitudinal strips (usually of equal length or of equal charge). Then the collective effect may be calculated at each slice due to all preceding slices. This vastly increases the speed of the tracking but clearly reduces the resolution of the wake. Therefore care must be taken to ensure convergence and realistic particle dynamics.

With the bunch sliced longitudinally, the wake at a test particle (in its longitudinal slice) is calculated as a sum of all slices' wake functions forward of the test slice (as well as preceding bunches and previous turns' contributions if required). The momentum kick for the test particle (and all the other macroparticles within the test slice) is then,

$$\begin{aligned} \Delta p_y &= \frac{F_\perp}{E_0}\Delta s \\ &= \sum_n \frac{q^2 N_n W(z_t - z_n)\,\overline{y_n}}{E_0}\,, \end{aligned} \tag{3.54}$$

where N_n is the number of particles in the n^{th} slice, z_t and z_n are the longitudinal position of the test and n^{th} slices and $\overline{y_n}$ is the average y coordinate in the n^{th} slice. The momentum kick in the horizontal, x, plane is exactly analogous to equation 3.54 but with y replaced with x.

At the time of writing, PyHEADTAIL has implemented modules that cover multi-turn wakes, transverse dampers, feedback systems, electron clouds and space charge. The space charge models written into PyHEADTAIL include longitudinal indirect space charge and an estimate of the direct space charge contribution (see section 3.4), as well as the more involved transverse space charge models.

Space charge in the transverse planes is typically implemented through the use of either a "frozen" or a self-consistent PIC space charge model [87]. The former, "frozen" space charge model assumes a Gaussian transverse distribution. The Bassetti-Erskine [88] formula is then used to give the non-linear beam space charge field. This model is not truly "frozen" but rather it adapts to the beam's RMS size and centroid to produce a fixed-field map for each slice at each calculation. This model is not self-consistent, but is typically used when long simulations (1×10^5 turns or more) are required and PIC simulations are too computationally intensive.

The second, and more traditional, method for calculating the transverse space charge is to use a PIC algorithm to resolve the actual macroparticle distribution. This enables modelling of the space charge self-consistently [89], that is to say a Kapchinskij-Vladimirskij distribution [1] (uniform density and elliptical cross-section) does not change with time under space charge and linear periodic focusing

lattices. In order to compute the space charge kicks the macroparticles are interpolated to nodes on a regular grid. Then the beam's potential is found using the discrete Poisson equation in the rest frame of the beam (where the magnetic terms due to relative particle motion may be neglected). The electric field on the grid is calculated using a second-order finite-difference gradient of the potential. These fields are then interpolated to the macroparticle positions and Lorentz transformed to the lab frame to apply the space charge kicks to the macroparticles.

3.5.1.2 High Performance Computing

Multiparticle dynamics studies of collective effects have become increasingly complex with the addition of further physics processes and running with higher numbers of macroparticles for higher resolution. As such, high performance computing has become desirable, and in some cases necessary, in order to run simulations in a reasonable timeframe. PyHEADTAIL can be run using CUDA-enabled NVIDIA GPUs which enable appreciable hardware acceleration. Increases in speed of order 100 for transverse space charge calculations, and a few 10s for wake field simulations have been reported [70]. This is particularly useful when parameter scans are required and multiple simulations may be run in parallel, allowing full exploitation of the GPU.

Science and everyday life cannot and should not be separated. Science, for me, gives a partial explanation of life.

— Rosalind Franklin, letter to Ellis Franklin, 1940.

4 Head-Tail in ISIS Operations

4.1 Introduction

During ISIS high-intensity operations, the proton beam experiences a coherent vertical instability around 1 – 2.5 ms through the 10 ms acceleration process (typical accelerator parameters are shown in table 2.1). Measurements of this instability have been made at a range of beam intensities and with 1RF or DHRF acceleration [40, 90–92] with a view to characterising it and developing mitigation strategies.

Figure 4.1 shows typical beam intensity and sum beam-loss signals as a function of time for neutron user operations. The beam intensity signal comes from a calibrated resonant current transformer in the synchrotron, and the beam-loss trace is a sum of 39 argon gas-filled coaxial ionisation tubes distributed around the ring circumference (see section 2.1.2). Beam-losses can be loosely categorised by the time they occur in the acceleration cycle into those associated with injection (-0.4 – 0 ms), trapping (peaking at 0.5 ms), transverse space charge (0.5 – 2 ms), vertical instability (2 – 3 ms) and extraction (9.8 – 10 ms).

4.2 Categorisation of Instability

The coherent vertical motion exhibited by the bunches has been interpreted as a head-tail type instability. Head-tail is characterised by an approximately sinusoidal

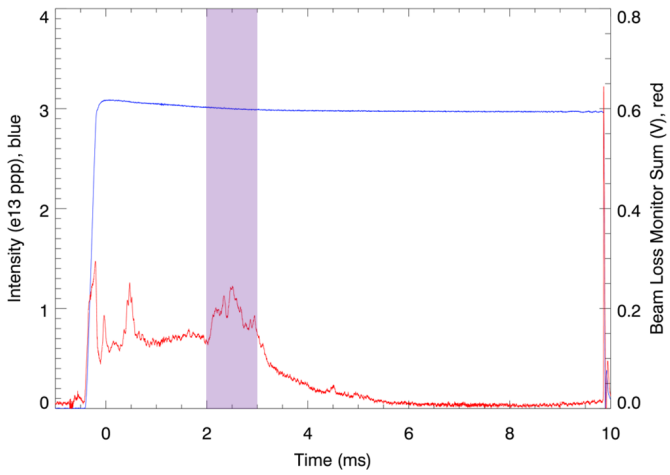


Figure 4.1: Beam intensity and sum beam-loss traces as a function of time through the cycle. Loss in the timeframe highlighted is associated with the beam instability.

mode structure in the beam centroid position along the bunch [22], recorded over a number of revolutions around the machine. The instability excites a standing wave between the bunch's head and tail with an envelope frequency given by the head-tail mode ($m = 0, 1, 2, \ldots$ indicating the number of nodes along the bunch) and an intrabunch frequency determined by the chromaticity.

Figure 4.2 shows the output of a vertical Beam Position Monitor (BPM) during typical high-intensity RCS operations (with DHRF). The BPM sum signal illustrates the longitudinal line density, or local beam intensity along the bunch length. The BPM difference signal provides the transverse (in this case vertical) coherent dipole offset along the bunch length. A zoomed-in view between 2 and 3 ms through acceleration is shown in figure 4.3. Despite well-controlled beam-losses (see figure 4.1), unstable behaviour can clearly be observed between these time points.

4.2.1 Mode Structure

Figures 4.4 and 4.5 are derived from the same vertical BPM signals as figure 4.3. Twenty consecutive turns of vertical BPM signals are overlaid at two time points (figure 4.4a at 2 ms and figure 4.5a at 2.6 ms). The corresponding FFT of the BPM signals (figures 4.4b and 4.5b) are calculated at the same timepoints but over a longer timeframe (0.125 ms, equating to just over 100 turns) to improve the frequency resolution. In these cases, head-tail motion with mode $m = 1$ and

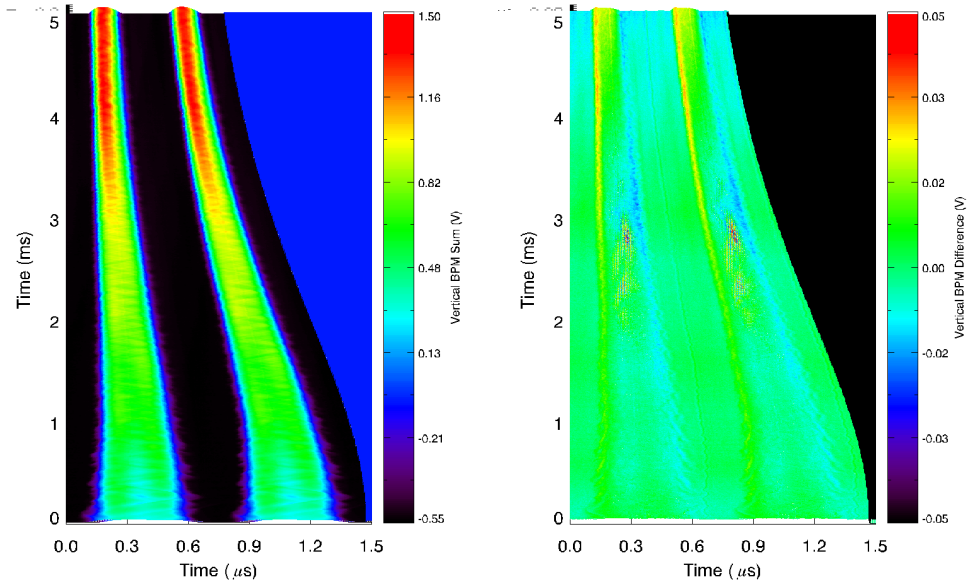


Figure 4.2: Turn-by-turn vertical BPM sum (left) and difference (right) signals from the end of injection (0 ms) to half-way through acceleration (5 ms).

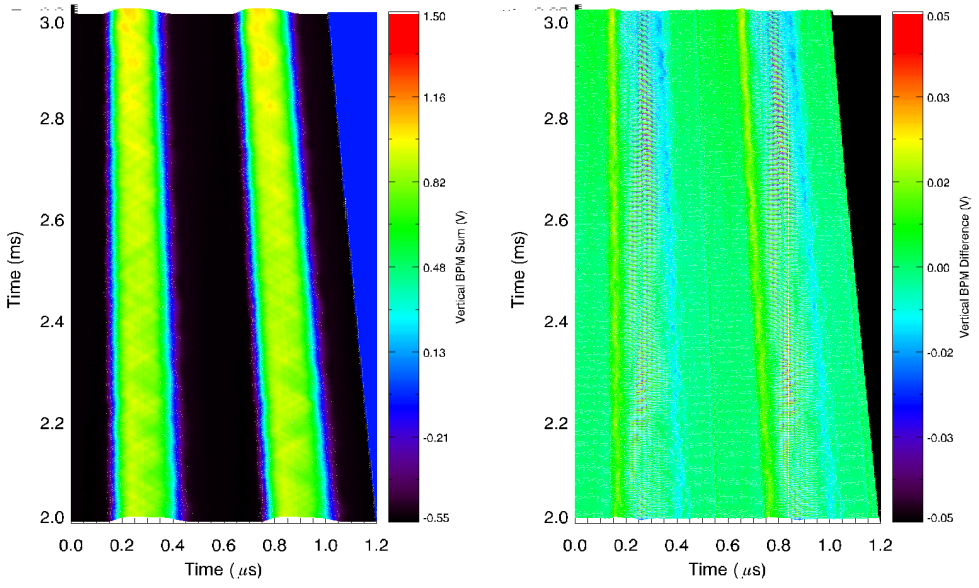
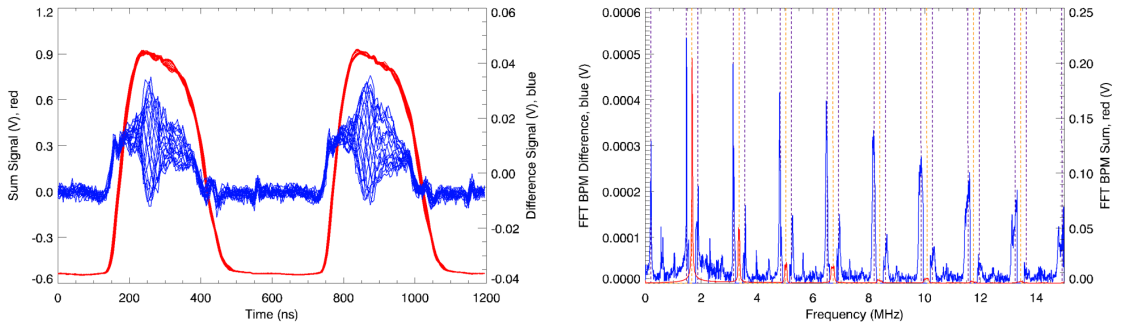


Figure 4.3: Zoomed-in version of figure 4.2. Turn-by-turn vertical BPM sum (left) and difference (right) signal, 2 – 3 ms through acceleration.

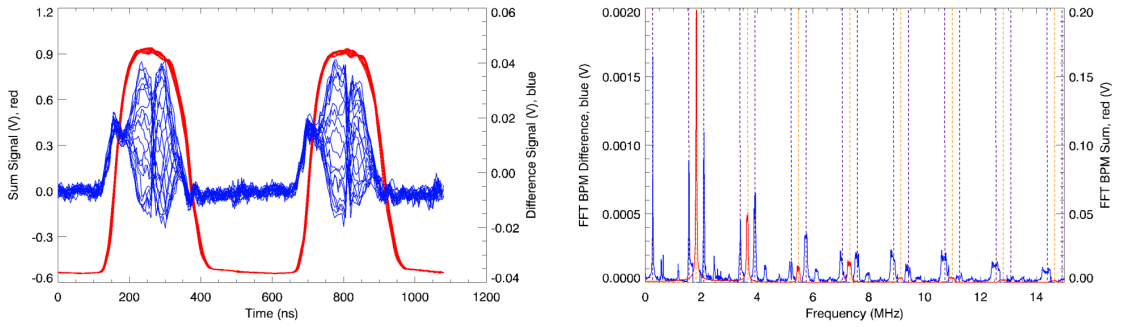
possibly $m = 0$ is observed, although the pure sinusoidal mode structure is likely to be distorted due to the addition of 2RF and the influence of space charge.

Measurements have also been made using only 1RF and lower intensity beams such that the effects of dual-harmonic synchrotron motion and space charge can



(a) **(b)**

Figure 4.4: a) BPM sum (red) and difference (blue) signals showing head-tail behaviour at 2 ms through acceleration. b) FFT of BPM sum and difference signals (red and blue respectively) at 2 ms. Dashed purple lines indicate the position of betatron sidebands.

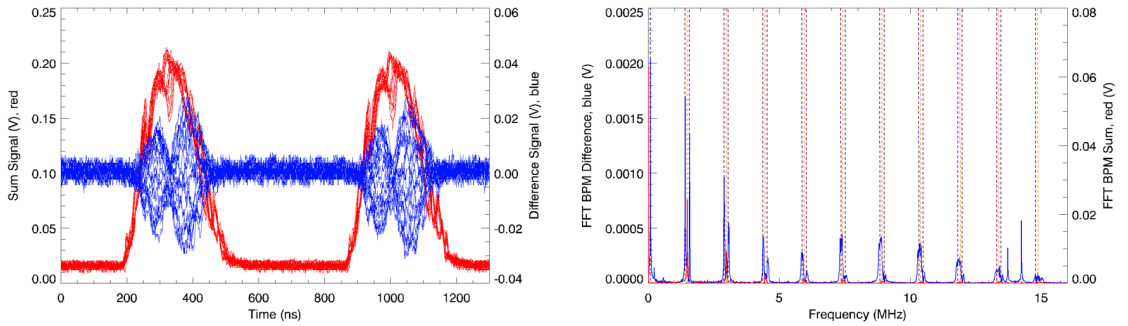


(a) **(b)**

Figure 4.5: BPM sum (red) and difference (blue) signal showing head-tail behaviour at 2.6 ms through acceleration. b) FFT of BPM sum and difference signals (red and blue respectively) at 2.6 ms. Dashed purple lines indicate the position of betatron sidebands.

be minimised [40, 90]. This enables a more direct comparison with Sacherer's theory [22]. Observations in this mode exhibit clear $m = 1$ mode head-tail motion for typical operational betatron tune settings and for a variety of initial transverse distributions [40, 90], *e.g.* figure 4.6 at a beam intensity of 2.5×10^{12} protons per bunch (ppb).

Figures 4.4 and 4.5 also illustrate that the vertical coherent motion does not occur over the full length of the bunch but only over a central portion of the bunch's length. The proportion of the bunch that is observed to oscillate is not consistent, varying between $\sim$40 – 80 % of the full bunch length, and there does not appear to be a local threshold in the longitudinal line density (BPM sum signal in red



(a) **(b)**

Figure 4.6: BPM sum (red) and difference (blue) signal showing head-tail behaviour at 1.2 ms through acceleration with 1RF only and low intensity (2.5×10^{12} ppb). b) FFT of BPM sum and difference signals (red and blue respectively) at 1.2 ms. Dashed purple lines indicate the position of betatron sidebands.

in the figures) at which instability occurs.

4.2.2 Instability Growth Rate

The instability grows from around 1 ms through the acceleration cycle, although (partly due to mitigation procedures, see section 4.3) beam-loss is usually observed from 2 – 3 ms. Figures 4.7 and 4.8 show how the vertical betatron sidebands sweep in frequency and particularly how the sidebands grow during the instability. The frequencies of the sidebands are dictated by the betatron tune (in this case the vertical tune) and the revolution frequency. The tune is controllable through the acceleration cycle by use of the trim quadrupoles and is empirically modified to minimise beam-losses. Therefore, the sidebands will move as a function of the revolution frequency due to changes in betatron tune, and the sidebands will increase in frequency due to acceleration and the increase in revolution and RF frequencies. In figure 4.7, between the vertical baseband (the lowest frequency betatron sideband) and the lower betatron sideband about the first RF harmonic, the sidebands about the revolution frequency may be distinguished (albeit with low amplitudes). There is also prominent fixed frequency noise on the BPM spectra at approximately 570 kHz which is induced on the BPM signals by nearby magnet power connections.

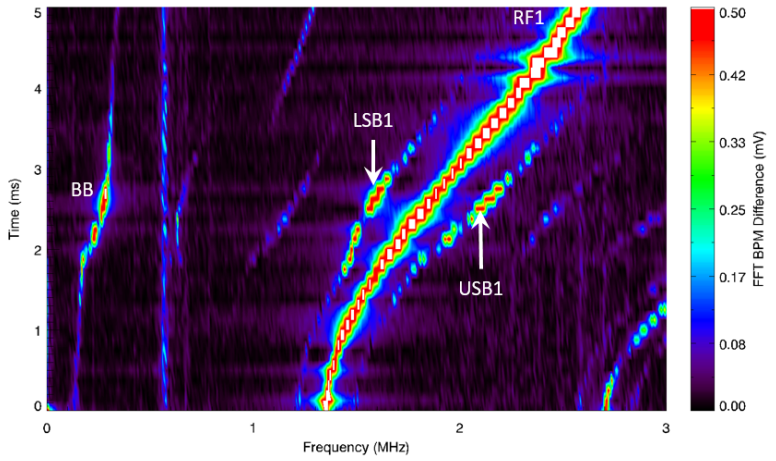


Figure 4.7: FFT of a typical vertical BPM difference signal from 0 – 5 ms. Vertical betatron baseband (BB), first RF harmonic (RF1) and upper and lower betatron sidebands about the first RF harmonic (USB1 and LSB1 respectively) are labelled.

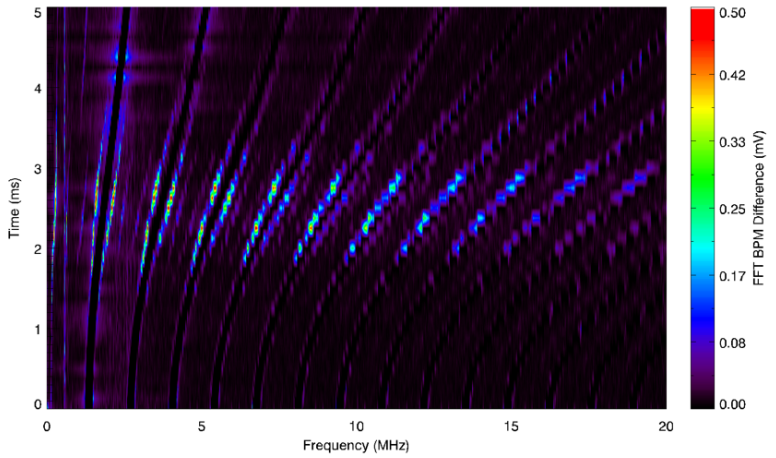


Figure 4.8: The same vertical BPM difference spectra as figure 4.7 but over a wider frequency range and with the RF harmonics removed for clarity.

Typically, the baseband has the largest amplitude, indicating a low frequency impedance is likely to be driving the instability. During the course of the instability, the revolution frequency is increasing and the betatron tunes are deliberately altered (see section 4.3) causing the baseband frequency to increase from 190 to 290 kHz (from 1 to 3 ms through acceleration). By 3 ms through the 10 ms acceleration cycle (at around 173 MeV) the vertical instability is no longer observed: the vertical betatron sidebands decrease in amplitude and no further associated beam-loss occurs.

Figure 4.9 illustrates one of two methods used to find the growth rate of the

instability. Fitting an exponential to the maximum value of the BPM difference signal (using the method of least squares regression) allows for fine temporal resolution of the growth rate although this method is complicated by the increase in amplitude over time due to BPM sum (*i.e.* longitudinal line density) information filtering through into the difference signal. Two different exponentials are shown which may relate to the two modes of instability observed in figures 4.4 and 4.5 at 2 and 2.6 ms respectively.

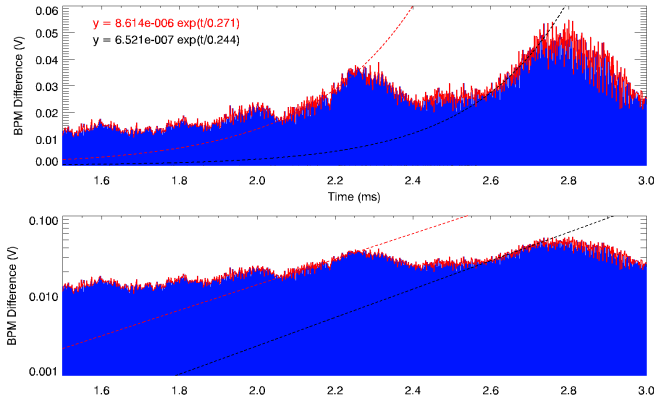


Figure 4.9: Absolute magnitude of the vertical BPM difference signal from 1.5 – 3.0 ms in blue with peaks picked out in red (top: linear vertical scale, bottom: logarithmic vertical scale). Two exponentials are fitted: red dashed from 2.05 – 2.25 ms and black dashed from 2.6 – 2.7 ms with the corresponding fitting equations shown.

However, figure 4.10 uses the amplitude of the fastest growing vertical betatron sideband to fit an exponential function (also using least squares regression) and has the benefit of focusing on a particular transverse mode, or subset of the full head-tail mode spectrum. It is noted that the spectrum of betatron sideband amplitudes is dependent on the longitudinal bunch distribution (see section 3.3.1 and equation 3.39) and it is assumed not to vary appreciably during the course of the exponential fit. However, to get the frequency resolution to be able to isolate the betatron sidebands from the revolution and RF frequencies, as well as the time resolution to fit an exponential over the course of the instability, is challenging. Figure 4.10 illustrates this challenge as the growth of the two instability modes observed in figures 4.4 and 4.5 merge into a single growth rate. However,

for increased clarity in frequency dependence, this method of determining the instability growth rate is utilised for the rest of the thesis.

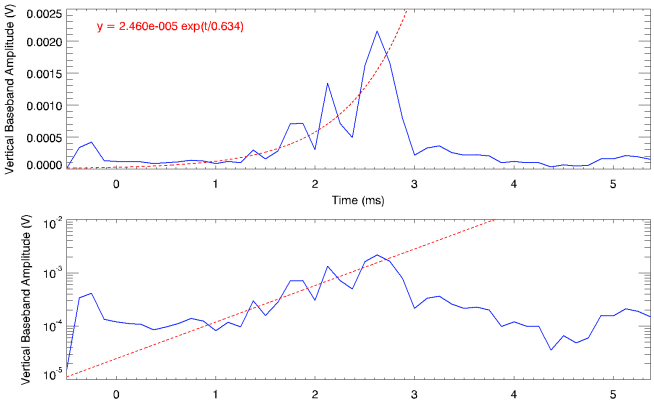


Figure 4.10: Vertical betatron baseband amplitude as a function of time in blue (top: linear vertical scale, bottom: logarithmic vertical scale). Exponential fit from 1 – 2.6 ms in red with fitted equation shown.

Growth rates during normal operations of 0.2 – 0.6 ms are typical, although the amount of beam-loss this causes is minimised as much as is reasonably practicable. If too much beam-loss occurs, the accelerator is either re-optimised or the beam intensity lowered until beam-losses are well controlled. Therefore, the head-tail instability often defines a limit to the beam intensity achievable on the ISIS synchrotron due to the need to have a reliable, maintainable accelerator.

4.2.3 Theoretical Interpretation

The head-tail theory developed by Sacherer (see section 3.3.1) allows the calculation of growth rates for each head-tail mode given the applied impedance. However, this theory assumes only 1RF and neglects space charge and, as yet, there is not an accepted model of head-tail which does not make these assumptions. However, it is still instructive to ascertain what Sacherer's model of head-tail predicts in the case of ISIS operations. The head-tail growth rate at ISIS is observed to increase as Q_y approaches 4, leading to the assumption that the dominant impedance is the resistive wall, possibly combined with a low frequency narrowband impedance, see section 5.2.

Using the beam and lattice parameters at 2 ms through acceleration, at the peak of instability related loss, the accumulated betatron phase shift along the

full bunch length, χ (equation 3.40) is calculated as:

$$\begin{aligned}\chi &= \frac{\xi}{\eta} Q\omega_0\tau_b \\ &= \frac{-1.4}{-0.757} \times 3.83 \times 2\pi \times 0.829 \times 10^6 \times 320 \times 10^{-9} \\ &= 11.8 \pm 0.4 \text{ rad.} \end{aligned} \tag{4.1}$$

Together with the resistive wall impedance, this leads to higher predicted growth rates for head-tail modes $m = 3$ and $m = 2$ than $m = 1$, while $m = 1$ is observed in 1RF operations. This discrepancy led Rees to put forward an alternative mechanism for head-tail [40] which predicts a higher growth rate for mode $m = 1$ (briefly summarised in section 3.3.2). It is noted, however, that this difference in predicted and observed head-tail mode has not been seen on other accelerators and Sacherer's theory rather than Rees' theory has been found to describe head-tail accurately (at low intensities and 1RF) on other machines.

4.3 Head-Tail Mitigation

The ISIS synchrotron is often described as "loss-limited", meaning that the beam intensity achievable is primarily constrained by the amount of beam lost as well as its temporal and spatial distribution (see section 2.1.3). As the beam-losses associated with head-tail are over a relatively long time period and later in the acceleration cycle (therefore at higher energy) than other losses (see figure 4.1), they currently define a key intensity limit of the ISIS synchrotron. On many other synchrotrons, head-tail instabilities are suppressed by control of the chromaticity, however ISIS operates without sextupole correction at the natural machine chromaticities measured as $\xi_x = \xi_y = -1.4$ (normalised) [93]. The instability is thus mitigated by other means, using a number of modifications to operational parameters.

4.3.1 Vertical Tune

ISIS has the capability of dynamically controlling the betatron tunes through the acceleration cycle through the use of trim quadrupoles (see section 2.1.2). Early on, during injection and trapping processes, the tunes are kept high to avoid space

charge depressing particle tunes onto the integer or half-integer. However, to mitigate the instability, the vertical tune is dropped rapidly at 2 ms, away from the integer (see figure 4.11). This increases the vertical betatron baseband frequency, moving it away from the peak in transverse impedance and lowers the growth rate of the instability, thereby reducing beam-losses. In comparison to the horizontal tune profile, also shown, the drop in tune by ∼0.09 in 0.5 ms is substantial.

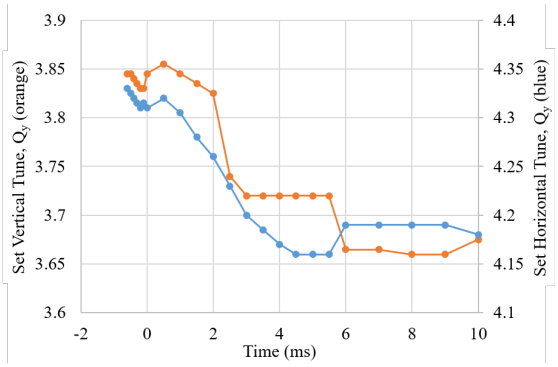


Figure 4.11: Typical vertical and horizontal tune settings as a function of time through the acceleration cycle.

4.3.2 Longitudinal Bunch Shape

Alongside the drop in vertical tune, the longitudinal bunch shape is altered during the instability, using the phase difference between the 1RF and 2RF systems. The bunch shape is deliberately shifted from a more symmetric, flatter bunch profile (expected to be optimal in reducing transverse space charge effects) to a far more asymmetric, peaked distribution. This change in longitudinal distribution has been observed to lower the growth rate of the instability and reduce the associated beam-losses. A typical measurement of the longitudinal distribution as a function of time is shown in figure 4.2 and specific profiles before and during the instability are shown in figure 4.12.

4.3.3 Injection Painting

The head-tail instability is also mitigated by empirical tuning of the longitudinal and vertical painting of the injected beam. The head-tail instability mechanism is, by definition, a combined effect of the transverse dipole motion (vertical in the case

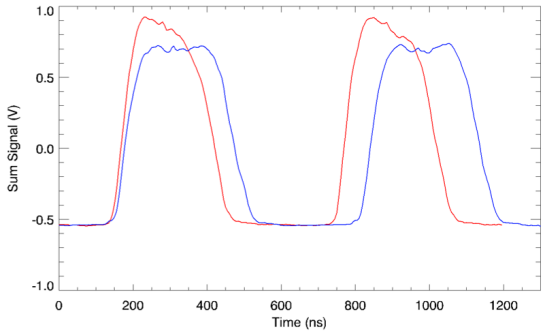


Figure 4.12: BPM sum signal at 1.4 ms (red) and 2 ms (blue) showing the deliberate longitudinal profile asymmetry.

of ISIS) with the longitudinal synchrotron motion. Therefore, it stands to reason that the distribution of particles in both those planes impacts on the instability growth rate. As described in section 2.1.2, on ISIS the unchopped, injected beam is accumulated over ∼140 turns with the ring RF on at low voltage. The RF voltage is then raised rapidly, capturing the protons in two long bunches. The resulting longitudinal distribution may be controlled by varying the RF voltage, but painting is also determined by the mean energy and energy spread of the injected beam, the magnetic field strength of the main dipoles and the frequency of the ring RF.

Vertically, the beam is painted during the injected pulse using a fast-ramping dipole magnet upstream of the stripping foil, together with the action of space charge. The deflection through the dipole is deliberately non-zero at the end of injection to create a hollow beam. For normal, high-intensity operation, the strong space charge forces act on the particles to fill in the hollow and create a centrally peaked distribution. Typically, larger beams are more stable with regards to the head-tail instability; however, these are then more susceptible to the non-linear magnetic fields within the magnets outside the good field regions and nearer to the collimated aperture limits. This can then lead to higher beam-losses through other effects such as resonances and closed-orbit distortions.

4.4 Current and Future Operations

Recent upgrades and modifications have led to an improved operational efficiency (consistent running with low beam-loss and high beam intensity on target).

These have included improved RF system control, re-optimised collimation, trim quadrupole power supply stability and improved beam-loss diagnostics. Since the beginning of 2020, the maximum beam current during 50 Hz RCS operation of 245 µA (currently limited by the targets at 205 µA to TS1 and 40 µA to TS2) has been achieved several times [94, 95].

Despite this fact, the head-tail instability is still present on the machine, causing beam-losses and associated machine activation. For regular, reliable operation beam-losses must be as low as reasonably achievable to minimise activation and associated dose rates for maintenance staff. Understanding the mechanisms of beam-loss will help optimise accelerator operation and make the highest beam currents achievable more regularly. Also, with possibilities of increased beam current limits on the neutron targets together with plans for a new machine, ISIS-II, understanding what drives the instability on ISIS, the influence of space charge and DHRF will have a demonstrable impact on instability mitigation strategies both on current high-intensity hadron machines, as well as future accelerators.

ISIS is uniquely placed to study many aspects of the physics of instabilities on high-intensity hadron accelerators. It experiences very high space charge levels, with peak incoherent tune shifts $\sim$0.5 (equation 3.52). ISIS operation is centred on an 800 MeV, 50 Hz proton RCS which, by its nature, is a complex environment with sweeping frequencies which can be both advantageous and challenging. ISIS is also noteworthy in its novel beam pipe geometry which is rectangular and follows the shape of the beam envelope defined by the nominal magnetic lattice.

Alongside the physics studies presented in this thesis, analysing the mechanism of the instability and producing an advanced simulation model of the influence of wakes and impedances on the ISIS beam, research and development is ongoing on active damping systems including an operational prototype [92]. Understanding the instability physics will aid in the development of these damping systems and may precipitate further mitigation methods, leading to higher-efficiency, safer operation of existing and proposed high-intensity hadron facilities.

An expert is a person who has found out by his own painful experience all the mistakes that one can make in a very narrow field.

— attributed to Niels Bohr, "Dr Edward Teller's Magnificent Obsession", Robert Coughlan, LIFE magazine, 6th September 1954.

5

SRM: Head-Tail Instability as a Function of Vertical Tune

5.1 Introduction

In order to understand better the instability mechanism observed during normal, high-intensity operation at the ISIS synchrotron, including the observed discrepancy with predictions from Sacherer's theory (section 4.2.3), a new, comprehensive series of experiments has been made in Storage Ring Mode (SRM). This involved removing the AC component of the main magnet fields and setting the DC component to injection values, and keeping the correction magnets constant throughout each test (steering magnets and trim quadrupoles). Initial experiments were performed with unbunched, coasting beams to obtain a measure of the effective impedance. SRM was a relatively recent operating mode for ISIS at the time, requiring careful planning, monitoring of the machine state and modifications to the setup method to ensure safe and consistent operation.

An important initial contribution of this research was to establish suitable beams in an entirely new operating mode for ISIS: Bunched Storage Ring Mode (BSRM). Like SRM, this involves operating with only the DC component of the main magnetic fields. However, in BSRM the RF system is powered and at a constant frequency matched to the incoming beam's revolution frequency ($f_{\mathrm{RF}} = hf_{\mathrm{rev}}$), providing

bunched beams stored at injection energy. The RF frequency is matched by monitoring the longitudinal line density, maximising intensity stored and minimising beam oscillations. The RF voltage in BSRM is fully controllable as in RCS mode but without the need for acceleration which allows for more flexibility in longitudinal painting and bunch manipulation. Key accelerator parameters are listed for RCS, SRM and BSRM ISIS operation in table 5.1.

Measurements in BSRM are complementary to those made in SRM and RCS modes, providing a "stepping stone" between the two. BSRM provides for a less complicated experimental environment than normal 50 Hz RCS operation and allows for closer study of the physics of bunched beams. It removes the fast sweeping beam frequencies experienced during acceleration and enables finer control of beam and lattice parameters and monitoring, albeit over a limited range due to being fixed at injection energy. For stable beam and lattice parameters it has been found that beam can be bunched and stored for 10 ms comfortably with negligible beam-loss. Storing beam for longer would require further modification to the RF controls and has not been necessary.

Table 5.1: ISIS synchrotron parameters for RCS, SRM and BSRM operations.

Parameter	**Symbol**	**RCS**	**SRM**	**BSRM**
Energy range	E_k	70 – 800 MeV	70 MeV	70 MeV
Main dipole field	B	0.176 – 0.697 T	0.176 T	0.176 T
RF frequency, $h = 2$	f_{RF}	1.3 – 3.1 MHz	n/a	1.3 MHz

5.2 Measurement of Effective Impedance Using Coasting Beams

Using the beam itself to measure the effective impedance of an accelerator, whether reactive or resistive, has become standard practice in the community. One method utilises unbunched, stored beams and monitors the growth rates of the coasting-beam instability as a function of betatron tune. These measurements have been made at ISIS [91], monitoring the vertical Beam Position Monitor (BPM) signals

as the vertical tune is changed. An example of one these measurements for an unstable tune is shown in figure 5.1.

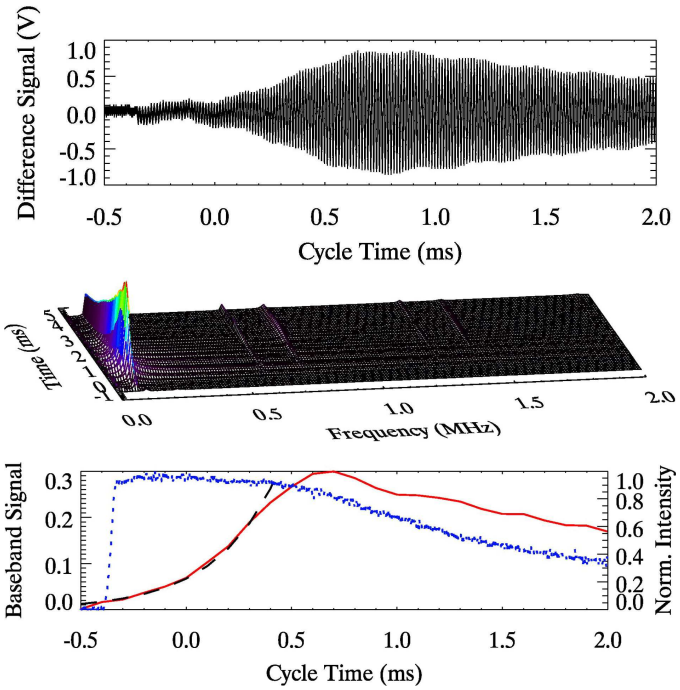


Figure 5.1: Vertical BPM difference signal, top; its Fourier transform as a function of time, middle; dominant betatron sideband (red), exponential fit (dashed black) and normalised beam intensity (dotted blue) as a function of time, bottom.

Coasting-beam theory [22] predicts the transverse growth rate is given by

$$\frac{1}{\tau} = -\mathfrak{Im}\left(i\frac{e\beta}{4\pi RQ\omega_0\gamma m_0}Z_{\perp\text{eff}}I\right), \tag{5.1}$$

where e is the elementary charge, β and γ are the relativistic parameters, R is the accelerator radius, Q is the betatron tune, ω_0 is the angular revolution frequency, m_0 is the rest mass, $Z_{\perp\text{eff}}$ is the transverse effective impedance and I is the beam current. The transverse effective impedance is the total transverse impedance experienced by the beam around the machine circumference. The growth rate, and hence the effective impedance, is evaluated at the betatron sideband frequency. Therefore, measuring the transverse growth rate (in this case vertical) at different betatron tunes moves the baseband betatron frequency and samples a different portion of the impedance spectrum (see equation 5.2, where Q_{frac} is the fractional part of the tune).

$$\begin{aligned}\text{Lower sidebands for } Q_{\text{frac}} > 0.5: \;\; f_\beta &= (n + Q_{\text{frac}})f_{\text{rev}} \text{ for } n = 0, 1, 2, \ldots \\ \text{Upper sidebands for } Q_{\text{frac}} > 0.5: \;\; f_\beta &= (n - Q_{\text{frac}})f_{\text{rev}} \text{ for } n = 1, 2, 3, \ldots\end{aligned} \tag{5.2}$$

An experiment was performed in SRM on ISIS to measure the growth rate of the vertical coasting-beam instability as a function of betatron frequency. A table of key experimental parameters is given in table 5.2. Using equation 5.1 the effective transverse impedance was calculated as a function of frequency, see figure 5.2. The error on the measured impedance is that from the exponential fit to the baseband amplitude and the frequency error from the measurement error on the baseband frequency. It is clear from figure 5.2 that there is an effective narrowband impedance at ∼85 kHz with a full width of 25 kHz and peaking around $3.71 \pm 0.35\,\mathrm{M\Omega\,m^{-1}}$. The position, width and height of this narrowband impedance has been found to be consistent between measurements.

Table 5.2: Key experimental parameters for measurements of effective impedance in coasting beams as a function of vertical tune, Q_y.

Parameter	Symbol	Value
Beam intensity	N	9.8×10^{12} ppp
Set betatron tunes	$Q_{x,\mathrm{set}}, Q_{y,\mathrm{set}}$	4.331, 3.730 – 3.860
Main dipole field	B	0.176 T
Revolution frequency	f_{rev}	677.4 ± 1.5 kHz
Relativistic beta	β	$0.369 \pm 8 \times 10^{-4}$
Relativistic gamma	γ	$1.076 \pm 4 \times 10^{-4}$
Slip factor	η	$-0.824 \pm 6 \times 10^{-4}$

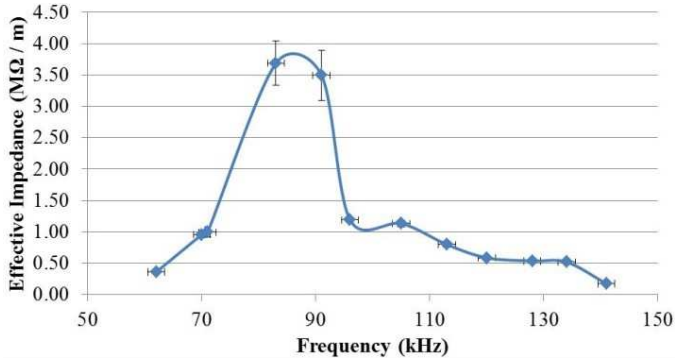


Figure 5.2: Measured transverse effective impedance as a function of baseband frequency, measured at a beam intensity of 9.8×10^{12} ppp [91].

Previous experimental observations have shown that both the growth rates of the head-tail and coasting beam instability increase rapidly as the vertical tune is moved up toward the integer ($Q_y = 4$) [40, 59, 90]. This has led to the

resistive wall impedance being cited as the most likely driving impedance. However, measurements shown in figure 5.2 indicate the picture is more complex with the vertical growth rate peaking at $Q_{y,\mathrm{set}} \sim 3.813$ (an integer tune corresponds to a baseband frequency of zero).

Simple calculations may be made to evaluate the approximate impedance due to resistive wall using the thick-wall formula (equation 3.3). At a frequency of 85 kHz, corresponding to the peak in the measured effective impedance, the formula estimates that for a full circumference ($C = 164\,\mathrm{m}$) of stainless steel beam pipe ($\sigma_c = 1.45\,\mathrm{MS\,m^{-1}}$) with an average half-height of 63.9 mm the resistive wall impedance is $54\,\mathrm{k\Omega\,m^{-1}}$. This is far less than the measured effective impedance which peaks at almost $4\,\mathrm{M\Omega\,m^{-1}}$. Therefore this simple model of resistive wall results in much lower growth rates than those observed. The origin of the observed vertical narrowband impedance is still under investigation and is a possible driving source for the head-tail instability seen in normal ISIS operation.

5.3 Overview of Measurements in BSRM

As noted in chapter 4, the head-tail instability observed on ISIS occurs over a period from 1 – 3 ms through the 10 ms acceleration cycle, during which time many parameters are changing due to the rapid-cycling nature of the machine. In order to understand the dynamics of the instability on ISIS better, a new, comprehensive set of experiments has been made by storing a bunched beam at injection energy (BSRM). As described in section 5.1, this alleviates difficulties with sweeping RF and betatron sideband frequencies during normal operation and gives finer control of beam parameters.

For the measurements shown in this section, the main dipole field was held constant at that required for the design injection energy (70 MeV), $B = 0.176\,\mathrm{T}$. A single 1RF cavity was powered whilst the others were set off-tune and with zero volts at the gap to minimise their contribution to the beam dynamics. The RF frequency was selected to match the injected beam energy and held constant. To maintain comparable longitudinal and horizontal painting to nominal RCS operation, the

RF voltage profile was kept the same as in RCS operation from injection until 1 ms but then held constant until 10 ms at 10.8 kV per turn (see figure 5.3). The beam distribution in the vertical plane was painted in exactly the same way as in the RCS and SRM cases using a specialised dipole (the "vertical sweeper") in the injection line (see section 2.1.2.1). Betatron tunes and steering functions were also held constant throughout each measurement.

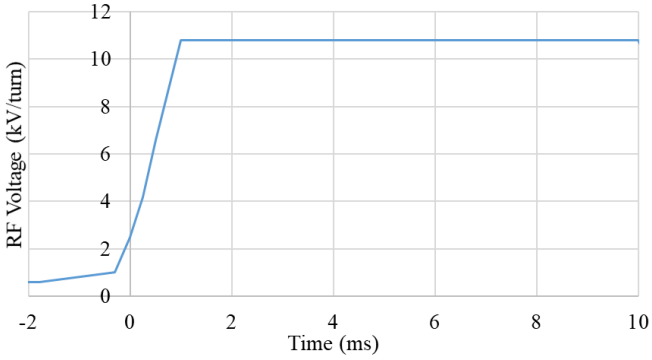


Figure 5.3: Total RF voltage per revolution as a function of time.

An intensity of 1.68×10^{12} protons per bunch (ppb) was injected, which is ∼10 % of a full-intensity beam. This intensity was selected as the lowest reasonable intensity where the instability is observable and the effects of space charge may be significantly reduced, but whilst maintaining a good signal-to-noise ratio on the BPM signals. Peak incoherent space charge tune shifts are reduced from ∼0.5 (using equation 3.52), experienced at full intensity during RCS operation, to ∼0.05 at the reduced intensity.

For each experimental setup, data was acquired from a ring intensity monitor (IM), a sum of all the 39 argon-filled ionisation beam-loss monitors (BLMs) and the individual electrode signals from one vertical and one horizontal BPM. The electrode signals allow easy access to the BPM sum and difference data required for instability analysis (as described in section 2.1.3). All the data were acquired at 200 MHz and, due to memory limits on the hardware, 1.6 million data points were recorded for each signal, equating to 8 ms of data. Measurements were triggered before injection, leading to around 6.5 ms of stored bunched beam recorded.

Key accelerator and beam parameters for measurements as a function of vertical tune are listed in table 5.3. Two sets of measurements are shown, focusing on different areas of vertical tune space and hence extending the baseband frequency range to include those excited during the head-tail instability during RCS operation (see section 4.2.2). The "vertical sweeper" current of 20 A was smaller than usually used for high-intensity RCS operation (typically 30 – 40 A) meaning the vertical beam size was smaller. This allows for more space for the vertical instability to drive emittance growth before beam-loss occurs. Further observations of the head-tail instability on ISIS as a function of vertical beam size are shown in chapter 6. The synchrotron tune, Q_s, and the vertical chromatic frequency, $f_{\xi,y}$ were calculated from the experimental parameters and nominal values from table 2.1 using the equations in the table (ϕ_s is the synchronous phase which is zero in this case and E_T is the total energy of the protons).

Table 5.3: Key experimental parameters for measurements of the head-tail instability in BSRM, as a function of vertical tune, Q_y.

Parameter	**Symbol**	**Value**
Bunch intensity	N	Set 1: 1.68×10^{12} ppb Set 2: 0.83×10^{12} ppb
RF voltage	V_{RF}	10.8 kV per turn
Vertical sweeper current	I_{VS}	20 A
Set betatron tunes	$Q_{x,\mathrm{set}}, Q_{y,\mathrm{set}}$	Set 1: 4.330, 3.670 – 3.870 Set 2: 4.330, 3.540 – 3.730
Main dipole field	B	0.176 T
Revolution frequency	f_{rev}	677.38 ± 0.06 kHz
Relativistic beta	β	$0.3691 \pm 3 \times 10^{-5}$
Relativistic gamma	γ	$1.076 \pm 1.6 \times 10^{-5}$
Slip factor	η	$-0.8243 \pm 2.6 \times 10^{-5}$
Synchrotron tune	$Q_s = \sqrt{\frac{V_{RF}\eta h \cos\phi_s}{2\pi\beta^2 E_T}}$	$0.00454 \pm 4 \times 10^{-7}$
Vertical chromatic frequency	$f_{\xi,y} = \xi_y f_{\mathrm{rev}} Q_y/\eta$	4.073 – 4.452 MHz

An example BPM measurement at an experimental setting with a head-tail instability is shown in figures 5.4 and 5.5. As may be observed in the RCS data shown in section 4.2, the sum signal (figure 5.4a) indicates the development of the longitudinal line density over the 8 ms of data and the difference signal (figure 5.4b) shows the coherent vertical dipole offset along the bunch length over

that time. Figure 5.5a reveals the frequency spectra of the BPM difference signal as a function of time, highlighting the growth of the sidebands due to the instability until significant beam-loss halts their growth (see figure 5.6b). Figure 5.5b shows selected spectra, just prior to significant beam-loss, with the first few RF harmonics and betatron sidebands labelled (BB refers to the baseband and LSB and USB the lower and upper sidebands either side of the RF harmonic). It should be noted that, as desired, the bunch length and frequencies are not changing over the measurement, unlike in the RCS case.

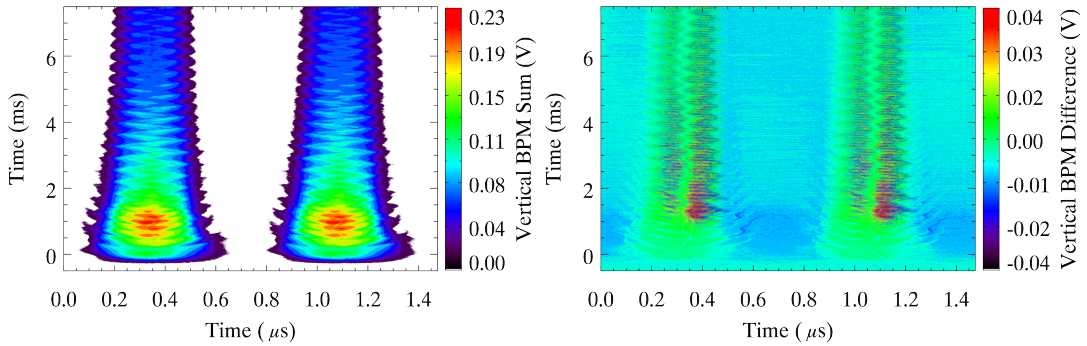


Figure 5.4: Vertical BPM sum signal (a) and difference signal (b) sliced to show each turn against time (measured $Q_y = 3.882$).

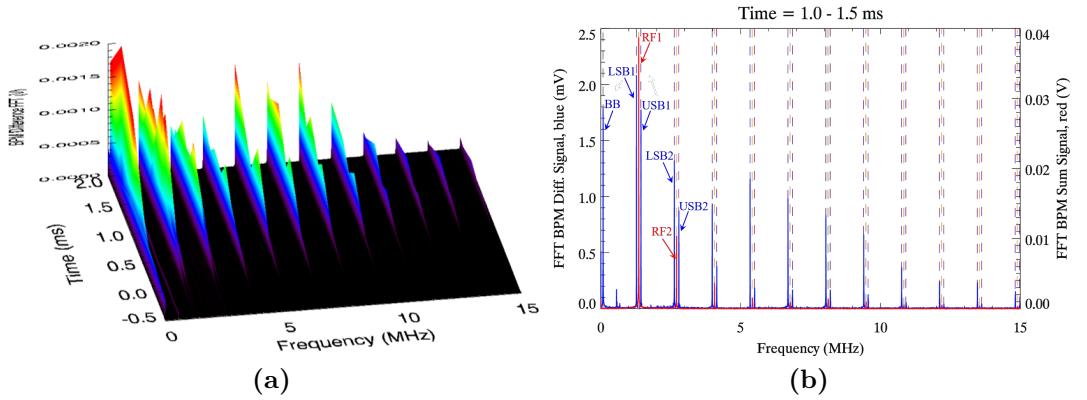


Figure 5.5: a) FFT of the difference signal from figure 5.4 over the first 2 ms illustrating sideband growth. b) Selected BPM sum and difference spectra with the first few betatron sidebands labelled.

Figure 5.6a is a 20-turn "snapshot" of the BPM signals in figure 5.4 at 1.2 ms after injection (before significant beam-loss occurs) with each turn overlaid to

highlight the head-tail mode structure. Figure 5.6b shows the IM and BLM signals which illustrate the beam-losses associated with the vertical instability, growing from ∼1 ms. Figures 5.4b and 5.6a reveal a persistent mode $m = 1$ head-tail instability (a single node in the vertical oscillations along the bunch length) in the BPM difference signal, beginning at ∼1 ms and lasting until the end of the measurement.

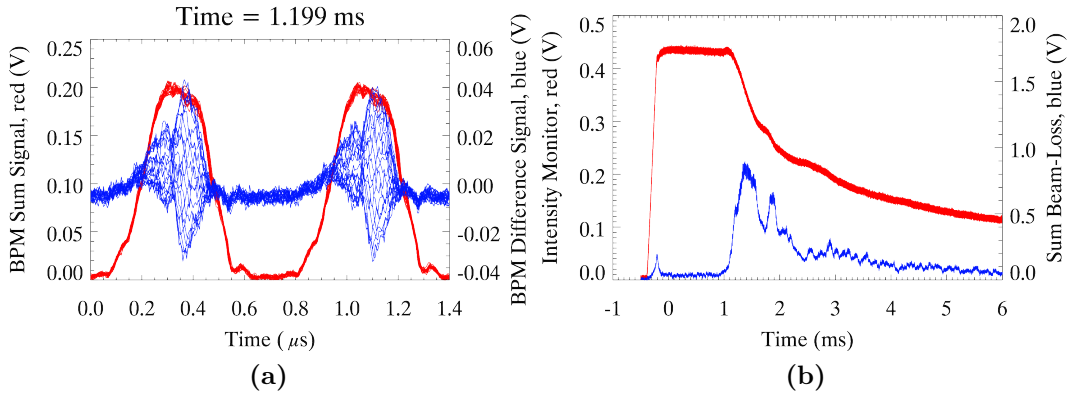


Figure 5.6: a) A 20-turn extract of the vertical BPM sum signal (blue) and difference signal (red) in figure 5.4, 1.2 ms after injection showing both bunches (head on the left, tail on the right). b) IM (red) and sum of all 39 ring BLMs (blue) versus time.

5.4 Head-Tail Instability as a Function of Vertical Tune

5.4.1 Introduction

The head-tail instability may be categorised by the intrabunch mode it excites, the bunch spectra in the frequency domain and the growth rate. Examining these characteristics in BSRM as a function of vertical tune (and in chapter 6 as a function of vertical beam size) aids in understanding of the dynamics of the instability and provides useful comparators to theoretical predictions (see chapter 7).

As introduced in section 4.2.2, by fitting exponential functions to the betatron sideband amplitudes as a function of time, growth rates may be determined for those sidebands, see figure 5.7. By changing the vertical tune, the frequency of the betatron sidebands shift and probe different parts of the impedance spectrum. Therefore, beam measurements were made for different vertical tunes to measure

the growth rate of the largest vertical betatron sidebands and examine the head-tail instability as a function of frequency.

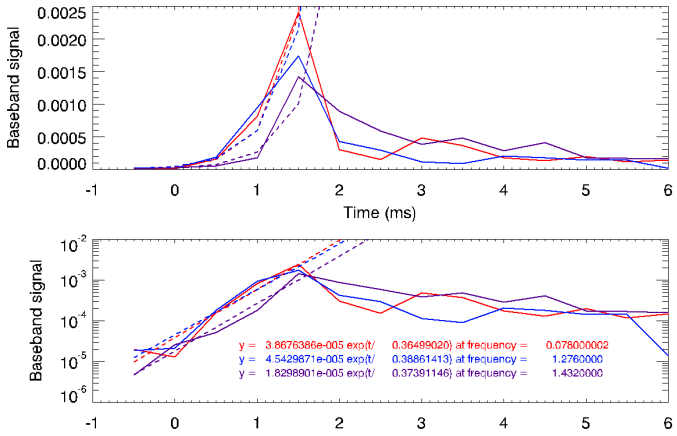


Figure 5.7: Vertical betatron sidebands from figure 5.5 (baseband in red and lower and upper sidebands around the first RF harmonic in blue and purple; top: linear vertical axis, bottom: logarithmic vertical axis). Exponential functions are shown in dashed lines with colour matching the sideband fitted and its equation also shown.

Figures 5.8 and 5.9 summarise measurements for vertical tunes that produced a vertical instability in "Set 1" (see table 5.4 for full dataset). Each column of graphs represents a single measurement for the given vertical tune with the aim being to characterise the head-tail instability. The intensity and beam-loss signals in figures 5.8(a – d) and 5.9(a – d) illustrate the timing and quantity of beam-losses associated with the head-tail instability at each tune. The BPM sum signals in figures 5.8(e – h) and 5.9(e – h) show the development of the longitudinal line density turn-by-turn. The BPM difference signals in figures 5.8(i – l) and 5.9(i – l) indicate the vertical coherent dipole offset along the bunch length turn-by-turn. These three graphs provide key background information, specifically the timings of when the head-tail instability develops (seen in the BPM difference signals) and when beam-loss occurs (in the IM and BLM signals).

The final three rows of graphs are fundamental to characterising the observed head-tail instability by the intrabunch mode, its frequency spectra and the associated growth rate (as is also shown for observations in RCS, section 4.2). The mode is observed in the BPM difference signal, figures 5.8(m – p) and 5.9(m – p), with 20 turns of BPM sum (red) and difference (blue) data overlaid at a time before peak

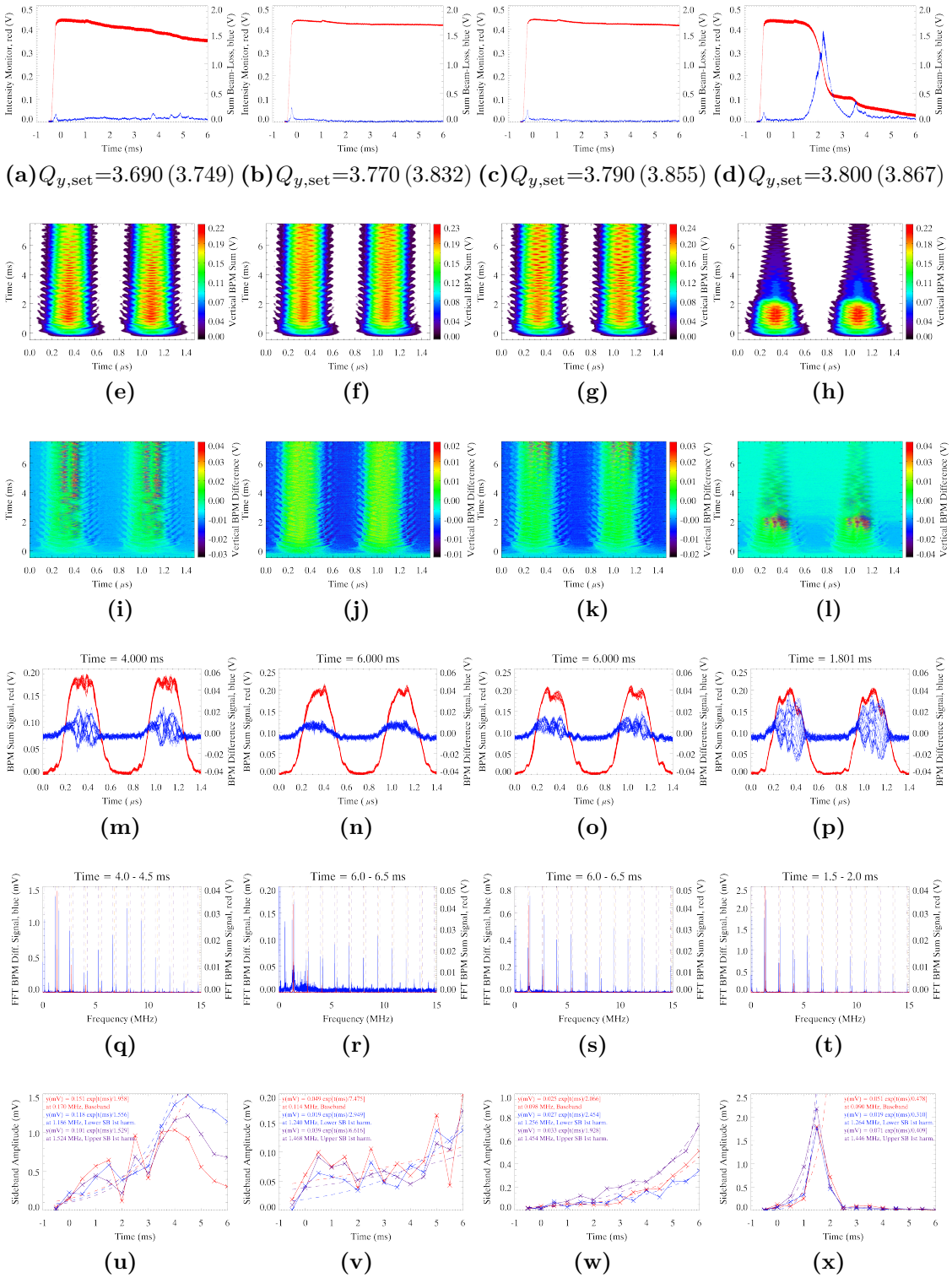


Figure 5.8: Experimental data from head-tail measurements at different vertical tunes (3.690 – 3.800, measured Q_y in brackets): intensity and beam-loss (a – d), vertical BPM sum signal over time (e – h), vertical BPM difference signal over time (i – l), BPM traces over 20 turns (m – p), FFT of BPM data around time of interest (q – t), growth rate fits to betatron sidebands (u – x).

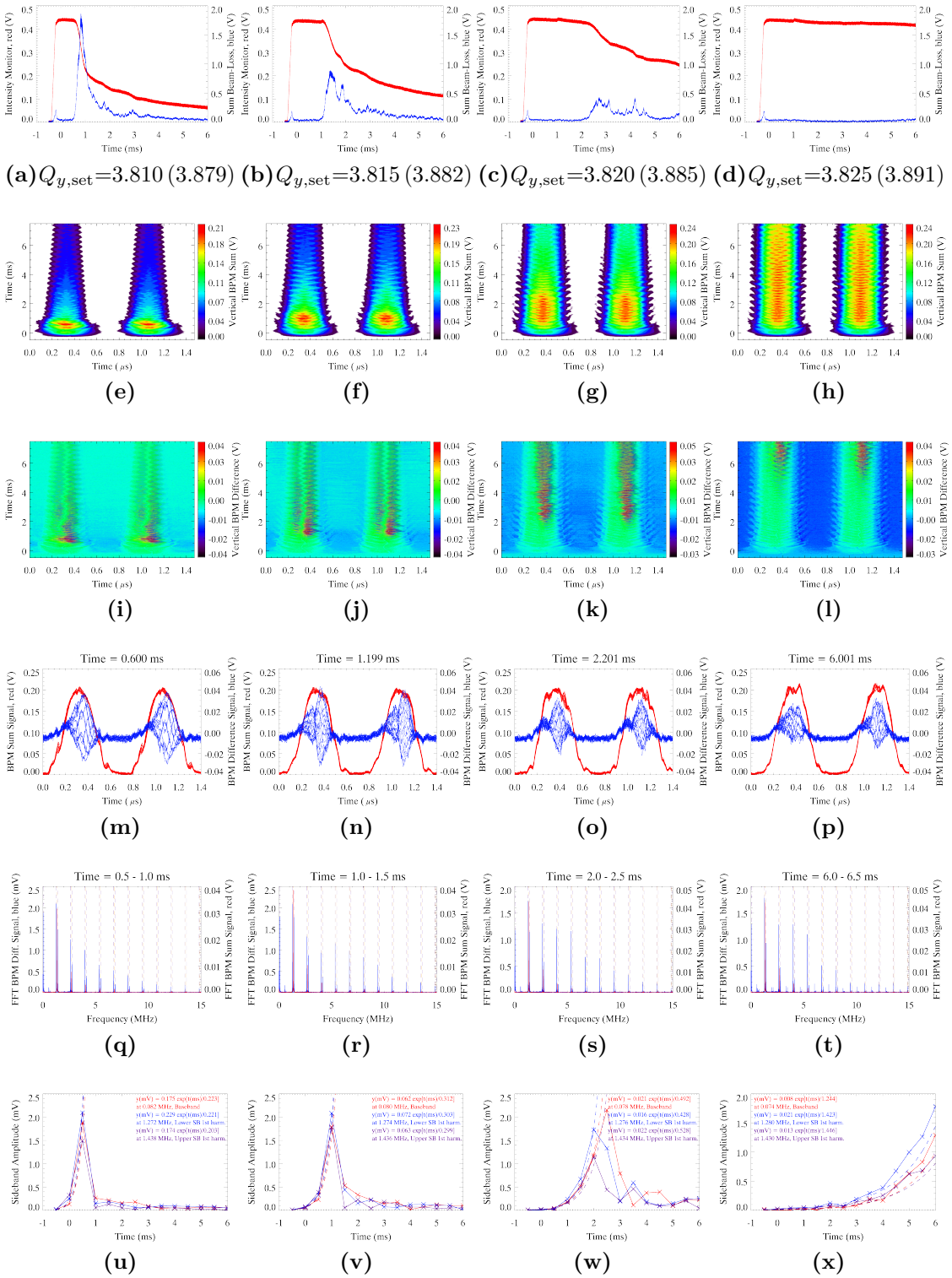


Figure 5.9: Experimental data from head-tail measurements at different vertical tunes (3.810 – 3.825, measured Q_y in brackets): intensity and beam-loss (a – d), vertical BPM sum signal over time (e – h), vertical BPM difference signal over time (i – l), BPM traces over 20 turns (m – p), FFT of BPM data around time of interest (q – t), growth rate fits to betatron sidebands (u – x).

Table 5.4: Summary of head-tail instability characteristics in BSRM on ISIS as a function of vertical tune for experiment "Set 1". $Q_{y,\mathrm{set}}$, $Q_{y,\mathrm{meas}}$ = set and measured vertical tunes, m = head-tail mode number, sideband = largest amplitude betatron sideband, f_{BB} = BB frequency, the growth rate is that of the BB, $\tau_{\mathrm{b,\,95\,\%}} = 95\,\%$ bunch length, τ_{e} = effective bunch length, a figure reference is given, if present.

$Q_{y,\mathbf{set}}$	$Q_{y,\mathbf{meas}}$	m	**Sideband**	$f_{\mathbf{BB}}$ **(kHz)**	**Growth Rate (turn^{-1})**	$\tau_{\mathbf{b,\,95\,\%}}$**(ns)**	$\tau_{\mathbf{e}}$**(ns)**	**Figure**
3.670	3.731	n/a	BB	182 ± 2	$(2.03 \pm 1.25)\times10^{-4}$	395	n/a	n/a
3.690	3.749	1	LSB1	170 ± 2	$(7.54 \pm 2.55)\times10^{-4}$	390	365	5.8a
3.710	3.770	n/a	BB	156 ± 2	$(3.30 \pm 0.80)\times10^{-4}$	375	n/a	n/a
3.730	3.793	n/a	BB	140 ± 2	$(1.80 \pm 0.71)\times10^{-4}$	385	n/a	n/a
3.750	3.811	n/a	BB	128 ± 2	$(1.06 \pm 0.77)\times10^{-4}$	375	n/a	n/a
3.770	3.832	n/a	BB	114 ± 2	$(1.97 \pm 0.83)\times10^{-4}$	395	305	5.8b
3.790	3.855	2	USB1	98 ± 2	$(7.15 \pm 0.43)\times10^{-4}$	405	305	5.8c
3.800	3.867	2	USB1	90 ± 2	$(3.09 \pm 0.67)\times10^{-3}$	365	360	5.8d
3.810	3.879	0	LSB1	82 ± 2	$(6.62 \pm 0.70)\times10^{-3}$	420	350	5.9a
3.815	3.882	1	LSB1	80 ± 2	$(4.27 \pm 0.36)\times10^{-3}$	385	340	5.9b
3.820	3.885	0	LSB1	78 ± 2	$(3.00 \pm 0.17)\times10^{-3}$	385	330	5.9c
3.825	3.891	0	LSB1	74 ± 2	$(1.19 \pm 0.12)\times10^{-3}$	375	305	5.9d
3.830	3.897	n/a	BB	70 ± 2	$(1.03 \pm 1.05)\times10^{-4}$	410	n/a	n/a
3.835	3.903	n/a	LSB4	66 ± 2	$(1.94 \pm 0.98)\times10^{-4}$	365	n/a	n/a
3.840	3.914	n/a	USB4	58 ± 2	$(6.69 \pm 6.94)\times10^{-5}$	380	n/a	n/a
3.850	3.917	n/a	BB	56 ± 2	$(0.62 \pm 1.26)\times10^{-4}$	375	n/a	n/a
3.870	3.941	n/a	BB	40 ± 2	$(1.32 \pm 0.77)\times10^{-4}$	380	n/a	n/a

Table 5.5: Summary of head-tail instability characteristics in BSRM on ISIS as a function of vertical tune for experiment "Set 2". $Q_{y,\mathrm{set}}$, $Q_{y,\mathrm{meas}}$ = set and measured vertical tunes, m = head-tail mode number, sideband = largest amplitude betatron sideband, f_{BB} = BB frequency, the growth rate is that of the BB, $\tau_{\mathrm{b,\,95\,\%}}$ = 95 % bunch length, τ_{e} = effective bunch length.

$Q_{y,\mathbf{set}}$	$Q_{y,\mathbf{meas}}$	m	**Sideband**	$f_{\mathbf{BB}}$ **(kHz)**	**Growth Rate (turn^{-1})**	$\tau_{\mathbf{b},\,95\,\%}$**(ns)**	$\tau_{\mathbf{e}}$**(ns)**
3.540	3.616	n/a	n/a	∼260	$<1 \times 10^{-4}$	330	n/a
3.550	3.627	n/a	n/a	∼253	$<1 \times 10^{-4}$	345	n/a
3.560	3.637	n/a	n/a	∼246	$<1 \times 10^{-4}$	335	n/a
3.570	3.652	n/a	n/a	∼236	$<1 \times 10^{-4}$	355	n/a
3.580	3.658	n/a	n/a	∼232	$<1 \times 10^{-4}$	365	n/a
3.590	3.663	n/a	n/a	∼228	$<1 \times 10^{-4}$	355	n/a
3.600	3.669	n/a	n/a	∼224	$<1 \times 10^{-4}$	345	n/a
3.610	3.687	n/a	n/a	∼212	$<1 \times 10^{-4}$	360	n/a
3.620	3.692	n/a	n/a	∼208	$<1 \times 10^{-4}$	365	n/a
3.630	3.692	n/a	n/a	∼208	$<1 \times 10^{-4}$	345	n/a
3.640	3.709	n/a	n/a	∼197	$<1 \times 10^{-4}$	355	n/a
3.650	3.727	n/a	n/a	∼185	$<1 \times 10^{-4}$	360	n/a
3.660	3.736	n/a	n/a	∼179	$<1 \times 10^{-4}$	355	n/a
3.670	3.737	n/a	BB	178 ± 2	$(2.50 \pm 1.84) \times 10^{-4}$	340	n/a
3.680	3.740	n/a	BB	176 ± 2	$(6.95 \pm 1.69) \times 10^{-4}$	335	n/a
3.690	3.752	1	BB	168 ± 2	$(4.41 \pm 1.42) \times 10^{-4}$	330	365
3.700	3.758	n/a	LSB3	164 ± 2	$(4.69 \pm 2.32) \times 10^{-4}$	360	n/a
3.710	3.786	n/a	n/a	∼145	$<1 \times 10^{-4}$	360	n/a
3.720	3.807	n/a	n/a	∼131	$<1 \times 10^{-4}$	355	n/a
3.730	3.804	n/a	n/a	∼133	$<1 \times 10^{-4}$	355	n/a

beam-loss occurs. An FFT of a 0.5 ms segment of the BPM sum (red) and difference (blue) signals produces the frequency spectra in figures 5.8(q – t) and 5.9(q – t), timed to include the 20-turn BPM "snapshot". Also indicated in the spectra are the positions of the RF harmonics (dashed orange) and the betatron sidebands (dashed purple). Finally, the growth rate of the instability at each tune is determined by exponential fits to betatron sideband amplitudes as a function of time, figures 5.8(u – x) and 5.9(u – x). For the fit, sideband amplitudes are included up until peak beam-loss occurs (which coincides with the peak in the sideband amplitude).

Key results of head-tail instability characteristics as a function of vertical tune are listed in table 5.4. This lists the set and measured vertical tune, the intrabunch head-tail mode number (m), the largest amplitude (dominant) betatron sideband, the frequency of the BB, the measured growth rate of the BB, the 95 % bunch length ($\tau_{\mathrm{b},95\,\%}$), the length of the oscillating portion of the bunch (hereafter referred to as the effective bunch length, τ_{e}) and the first figure associated with each vertical tune. The effective bunch length is determined by adding the absolute value of twenty turns of BPM difference signal for one bunch at the time of interest and calculating the interval between the minima closest to the head and closest to the tail. The fastest growth rates, and largest losses, occurred at $Q_{y,\mathrm{set}} = 3.810$ where it is noted that the RF had not reached its peak voltage at 1 ms before the instability had grown enough to cause large beam-losses.

The complete vertical tune range for the "Set 1" experiment was $Q_{y,\mathrm{set}} = 3.670$ – 3.870; it can be seen that instability was only present for a narrow range of tunes (3.770 – 3.825) as well as at $Q_{y,\mathrm{set}} = 3.690$. A further experiment, "Set 2", looked at lower vertical tunes ($Q_{y,\mathrm{set}} = 3.540$ – 3.720) in order to extend the BB frequency range above 170 kHz to include those excited during the head-tail instability during RCS operation (190 – 290 kHz, see section 4.2.2). A vertical set tune of $Q_{y,\mathrm{set}} = 3.540$ corresponded to a BB frequency of 260 kHz. A slightly reduced beam intensity of 1×10^{12} ppb was accumulated but no vertical instabilities were excited below the one observed at $Q_{y,\mathrm{set}} = 3.690$ (BB frequency of 170 kHz). Therefore only results from "Set 1" will be presented except when looking at the instability growth rate

as a function of BB frequency. Results from "Set 2" are summarised in table 5.5. For most vertical tunes in "Set 2" no betatron sidebands could be discerned from the noise. In these cases the peak in the FFT of the BPM difference signal closest to the expected BB frequency is given (signified by a "∼" beforehand).

5.4.2 Head-Tail Instability Mode Structure

A hallmark of head-tail instabilities is the mode structure. Figures 5.8(m – p) and 5.9(m – p) show 20-turn "snapshots" of the BPM difference signals prior to the peak of beam-loss which exhibit the head-tail mode structure, if present. The mode number observed (number of nodes along the bunch's length) for each vertical tune is listed in table 5.4. As the vertical tune was increased the intrabunch mode structure changed, with a general trend from higher mode number to lower, particularly for the contiguous set of unstable tunes between $Q_{y,\mathrm{set}} = 3.770$ to 3.825. Mode structures with two nodes, one node and no nodes ($m = 2, 1$ and 0) were observed within a narrow range of vertical tune (between $Q_{y,\mathrm{set}} = 3.800$ and 3.815 for example).

A key observation from these measurements is that the intrabunch oscillations, observed in the BPM difference signals, only occupy a fraction of the full bunch length. Typically, only the central portion of the bunch was observed to oscillate, with the extreme head and tail of the bunch showing little vertical deflection. The fraction of the bunch length that is observed to oscillate is consistent for repeat measurements with the same parameters. However, when the vertical tune is changed, the effective bunch length changes. The fraction of the bunch length that oscillates appears uncorrelated to the mode excited or the vertical tune, see figure 5.10.

Table 5.4 and figure 5.10 include the 95 % bunch lengths for each tune (as measured with the BPM sum signal) where the full, 100 % bunch length, is ∼450 ns. The table and figure also show the effective bunch length which varies between 305 – 365 ns. For example, figure 5.6a shows the mode structure for a vertical set tune of $Q_{y,\mathrm{set}} = 3.815$ with a full bunch length of ∼480 ns, a 95 % bunch length of 385 ns and an effective bunch length of ∼340 ns. For different vertical tunes that exhibit

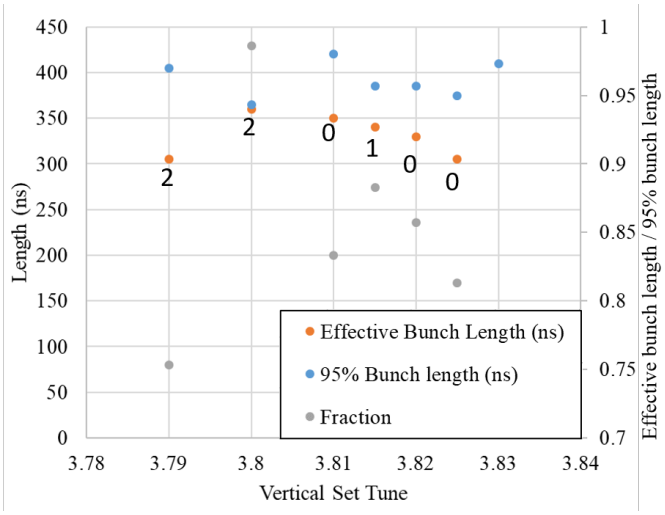


Figure 5.10: 95 % bunch length (blue), effective bunch length (orange) and oscillating fraction of the bunch (grey) versus tune. Head-tail mode number also indicated.

the same mode structure (*e.g.* mode $m = 0$ observed at $Q_{y,\mathrm{set}} = 3.810$, 3.820 and 3.825, figures 5.9(m, o and p) respectively) the fraction of the bunch that oscillates is inconsistent. There was no observed threshold of longitudinal line density at which the instability begins. As such, there appears to be no way of predicting the fraction of the bunch length that will exhibit head-tail motion.

Focusing on the BPM difference "waterfall" graphs in figures 5.8(i – l) and 5.9(i – l), mode structures can be seen to continue long after large portions of beam have been lost. For $Q_{y,\mathrm{set}} = 3.810$, a more complex scenario arose such that an $m = 0$ mode was excited with a fast growth rate, causing over half the beam to be lost. However, once the intensity dropped, a sustained, slow $m = 1$ mode was observed for the rest of the measurement.

5.4.3 Head-Tail Instability in Frequency Domain

Using a Fast Fourier Transform (FFT) on the BPM difference signal enables analysis of the bunches' transverse motion in the frequency domain through the betatron sidebands. The frequency and amplitude of these can be monitored and, by segmenting each BPM measurement into 0.5 ms portions, analysed as a function of time. Figures 5.8(q – t) and 5.9(q – t) show the spectra nearest the instability before significant beam-loss has occurred.

As the vertical tune was increased, the BB frequency decreased (see table 5.4). As detailed in equation 5.2, given the bunches' revolution frequency (which may be derived from an FFT of the BPM sum signal and is listed in table 5.3) the fractional part of the betatron tune may be determined by measuring the BB frequency. This is important as there were differences between the betatron tune set with the control system and that which was measured, particularly away from the design intensity of the accelerator. The measured and set vertical tunes are listed in table 5.4.

The amplitude of the measured betatron sidebands provides information on the amount of energy in particular oscillation frequencies. Generally, a stable beam will exhibit little to no transverse motion in a BPM difference signal and the associated FFT will show no, or very small, betatron sidebands. The largest betatron sideband, or that which grows fastest, is assumed to be dominant, providing information on the frequency dependence of the instability's driving impedance.

In the measurements shown in figures 5.8(q – t) and 5.9(q – t), the lowest frequency betatron sideband (the BB) was amongst the largest in amplitude during an instability. This indicates that the head-tail driving impedance dominated at low frequency (similar to that shown in the coasting-beam impedance measurements). The largest sideband for each vertical tune is listed in table 5.4.

The FFT of the BPM difference signals also show sidebands excited up to 15 MHz. The distribution of betatron sideband amplitudes is dependent on the mode excited (section 3.3.1.5) and therefore varies as a function of the vertical tune. The betatron sidebands decreased in amplitude with frequency until approximately the vertical chromatic frequency ($f_{\xi,y}$, see table 5.3). Above this frequency, the sidebands continued to decrease in amplitude for head-tail instabilities with mode zero ($m = 0$). However, for higher-order mode structures the betatron sidebands increased in amplitude above the vertical chromatic frequency, reaching a second peak whose frequency was dependent on the mode number excited. For mode one ($m = 1$) observed at $Q_{y,\mathrm{set}} = 3.690$, there was a second peak in betatron sideband amplitude around 8 MHz. Similarly for mode two ($m = 2$), observed at $Q_{y,\mathrm{set}} = 3.790$ and 3.800, the sidebands peaked at the BB as well as 9 and 12 MHz

respectively. This is expected as the higher-order mode structures oscillate at higher frequencies corresponding to standing waves along the bunch length.

It is noted that there was a small amount of noise on the BPM difference signal at specific frequencies which is particularly noticeable for small sidebands (low instability growth rates). The largest noise component was observed at approximately 560 kHz and was present with or without beam. This, and the peaks between 1.5 and 3.5 MHz, were due to pick-up from magnet power supplies in the synchrotron.

5.4.4 Head-Tail Instability Growth Rate Versus Frequency

The exponential growth time (τ, shown in figures 5.8(u – x) and 5.9(u – x)) for each vertical tune's BB was converted to a growth rate ($1/(\tau f_{\text{rev}})$) and is plotted as a function of the measured BB frequency, see figure 5.11. The error bars are the 1-sigma uncertainty estimates from the exponential fit to the BB growth and the frequency resolution of the FFT. Reference lines are shown for specific growth rates (one oscillation every 150, 250, 500 and 1000 turns) as well as the synchrotron tune, Q_s. The growth rates and associated errors are listed in table 5.4.

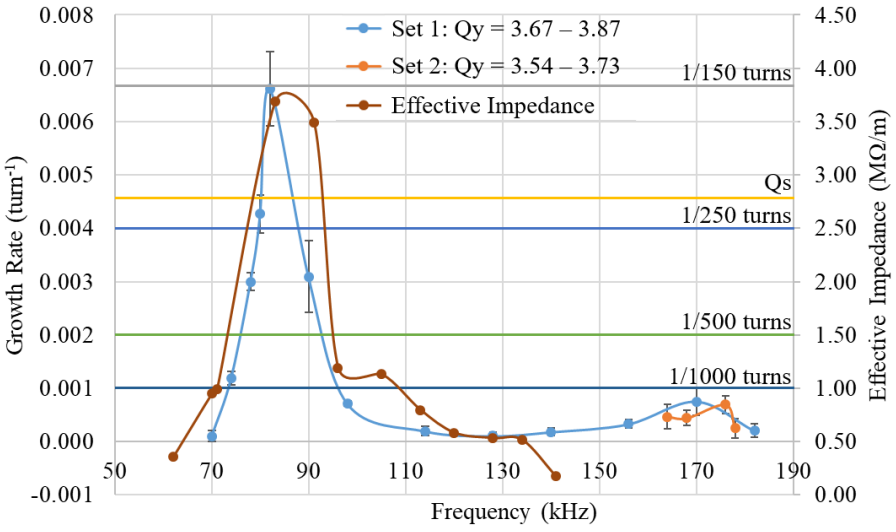


Figure 5.11: Growth rate versus betatron BB frequency for "Set 1" in blue and "Set 2" in orange. The effective impedance, as determined from beam-based measurements of coasting beams (figure 5.2), is also shown.

The growth rate as a function of BB frequency behaved very similarly to the coasting-beam instability measurements in section 5.2, with the result indicating the same low-frequency narrowband impedance (peaking around 80 kHz, corresponding to $Q_{y,\mathrm{set}} = 3.810$, with a quality factor of ∼10) drove both the head-tail instability in BSRM and the coasting-beam instability in SRM. It also confirmed the use of the betatron BB for the dependence of growth rate on frequency. The peak growth rate was $(6.62 \pm 0.70)\times10^{-3}$ turn^{-1} which equated to the BB growing by a factor of e (Euler's number) every ∼150 turns. It should be noted that this was faster than the synchrotron motion quantified by the synchrotron tune, $Q_s = 4.54 \times 10^{-3}$ turn^{-1}.

It should also be noted that there was another, much smaller, peak in growth rate at 170 kHz corresponding to the head-tail instability recorded at a set tune of $Q_{y,\mathrm{set}} = 3.690$ (see column of figures beginning with 5.8a). This indicates a further low-frequency narrowband impedance peaking at ∼170 kHz.

As stated in section 5.4, no head-tail instability was observed above a BB frequency of 176 kHz ($Q_{y,\mathrm{set}} = 3.680$). Betatron sidebands were almost undetectable and did not grow over the course of the measurement. This was despite experiment "Set 2" extending the BB frequency range up to 260 kHz in order to probe the BB frequencies excited during the head-tail instability in RCS operation (see section 4.2.2).

5.5 Simulations of Head-Tail Instability as a Function of Vertical Tune

5.5.1 Setup and Introduction

To understand the head-tail instability as observed on ISIS in BSRM better, a model of the synchrotron was built in PyHEADTAIL [70]. The results of simulations using PyHEADTAIL enable direct comparison between measurement and model, and allow for further comparisons to predictions from Sacherer's theory (presented in chapter 7). Discrepancies have already been noted between measurements in RCS mode and theoretical predictions (see section 4.2). PyHEADTAIL uses particle tracking and wake field calculations to simulate the effect of selected impedances on

beam dynamics, including instability (as outlined in section 3.5.1). It also includes models of space charge, enabling an assessment of its role in instability dynamics.

The simulations were set up to replicate, as close as practically possible, the synchrotron and beam parameters measured in the experiments above. Simulation specific parameters were chosen to give convergent behaviour whilst allowing for reasonable simulation time. Table 5.6 lists the main parameters that define the simulation and model parameters; other machine specific parameters (such as γ_t and machine radius) are included in table 2.1.

Table 5.6: Key simulation parameters for comparison with measurements of the head-tail instability on ISIS in BSRM as a function of Q_y.

Parameter	**Symbol**	**Value**
Bunch intensity	N	1.68×10^{12} ppb
RF voltage	V_{RF}	10.8 kV per turn
Betatron tunes	Q_x, Q_y	4.310, 3.840 – 3.920
Revolution frequency	f_{rev}	677.8 kHz
Relativistic beta	β	0.3694
Relativistic gamma	γ	1.0761
Slip factor	η	-0.8241
Synchrotron tune	$Q_s = \sqrt{\frac{V_{RF}\eta h \cos\phi_s}{2\pi\beta^2 E_T}}$	4.535×10^{-3}
Vertical chromatic frequency	$f_{\xi,y} = \xi_y f_{\mathrm{rev}} Q_y/\eta$	4.42 – 4.51 MHz
Machine aperture	$x_{\mathrm{aper}}, y_{\mathrm{aper}}$	± 81.6 mm, ± 63.9 mm
Horizontal emittance (RMS)	$\epsilon_{x,\mathrm{RMS}}$	50 π mm mrad
Vertical emittance (RMS)	$\epsilon_{y,\mathrm{RMS}}$	20 π mm mrad
Beam distribution	$\rho_{x,y}$, λ	4D waterbag, 2D parabolic
Bunch length (RMS)	$\sigma_{z,\mathrm{RMS}}$	10.5 m
Resonator frequency	f_{res}	82 kHz
Resonator quality factor	Q_{res}	10
Resonator shunt impedance	R_s	17.2 or 3.44 kΩ m^{-2}
Number of turns		2×10^3
Number of macroparticles		2×10^6
Number of PIC nodes (x, y, z)		$64 \times 64 \times 64$
Number of longitudinal slices		128
Number of wake turns		200

5.5.1.1 Beam and Lattice Parameters

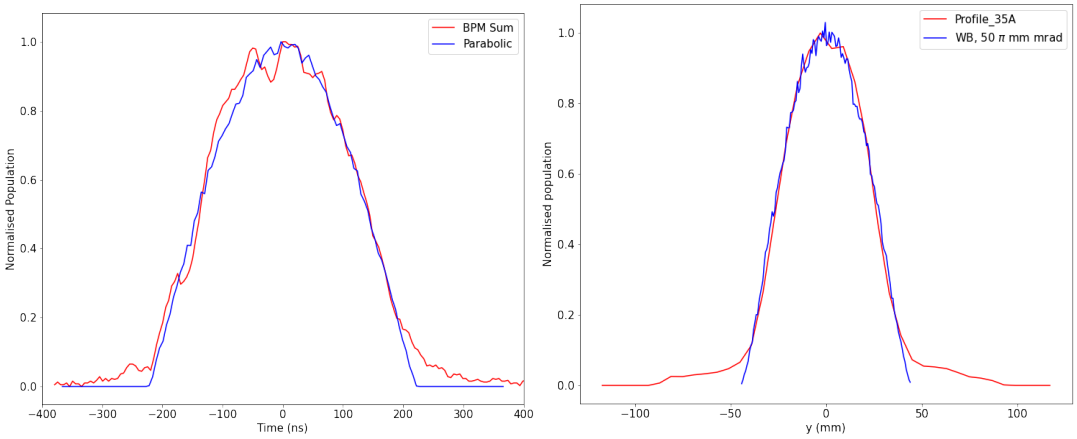
The bunch intensity, RF voltage and betatron tunes selected are those utilised in the measurements (table 5.3). The simulation begins with a fully formed bunch

distribution (injection processes are not simulated) to compare favourably with experimental measurements from ∼1 ms, after the RF voltage ramp. Hence, the RF voltage is held constant in the simulations. The betatron tunes are also held constant throughout, as they are during the experiment.

ISIS's mode of operation (BSRM) dictates the revolution frequency, relativistic parameters and slip factor. The synchrotron tune and chromatic frequency are calculated from the above values and were not directly measured in the experiment. A simulated machine aperture was included in order to compare measurements of beam-loss and intensity as a function of time. As described in section 2.1.2, the beam pipe aperture changes around the synchrotron, following the design beam envelope. To simplify simulations, the aperture was fixed at the average horizontal and vertical apertures. The smooth focusing approximation (see section 3.5.1) was also utilised.

The horizontal beam emittance used in simulations is nominal for ISIS. In the vertical plane, the beam emittance was measured using beam profiles as a function of the "vertical sweeper" current (see section 6.1.1.1). The simulated beam distributions (4D waterbag in the transverse and uncorrelated 2D parabolic in the longitudinal) and the bunch length were chosen by visual inspection to closely represent the measured distribution in the stored bunched beams. The longitudinal distribution was also deliberately mismatched to 75 % of the RF voltage, and a dipole shift of 2 m included, to give similar dipole and quadrupole bunch oscillations to those observed in the experiment.

Figure 5.12 shows comparisons between the simulated and measured longitudinal and transverse distributions. A parabolic distribution with a bunch length of 10.5 m was closest to the measured BPM sum signal. The vertical distribution was measured using an IPM (see section 2.1.3) and the resulting profile corrected against known drift field and space charge errors [96]. A waterbag distribution matched most closely to the measured vertical profile, with an RMS emittance of $20\,\pi$ mm mrad. The narrowband resonator characteristics (frequency, quality factor and shunt impedance) were selected to replicate the observed head-tail instability growth rate as a function of frequency (see figure 5.13).



(a) (b)

Figure 5.12: a) Simulated longitudinal parabolic distribution (blue) and a vertical BPM sum signal (red, $Q_{y,\mathrm{set}} = 3.820$, 2.3 ms). b) Simulated transverse waterbag distribution (blue) and a vertical IPM measurement ($I_{\mathrm{VS}} = 35$ A), corrected for drift field and space charge distortions (red).

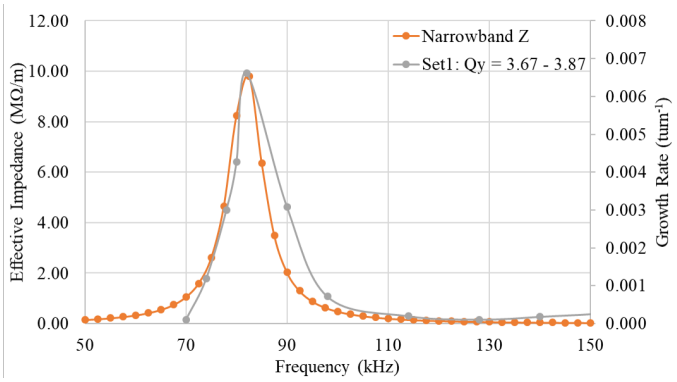


Figure 5.13: Narrowband resonator impedance (orange) as a function of frequency ($f_{\mathrm{res}} = 82$ kHz, $Q_{\mathrm{res}} = 10$ and $R_s = 17.2\,\mathrm{k\Omega\,m^{-2}}$). Growth rate as a function of frequency from instability measurements (grey) as a function of vertical tune (figure 5.11).

5.5.1.2 PyHEADTAIL Simulation Setup

The number of turns was selected to give enough time to allow for slower head-tail growth rates whilst also minimising the computation time. The number of macroparticles, number of PIC nodes and longitudinal slices were chosen in order to give convergent behaviour for space charge and wake field effects. As the simulations were only over 2000 turns a PIC space charge model could be used effectively. Although more computationally intensive than a "frozen" space charge model (see section 3.5.1), it is self-consistent and fully resolves the macroparticle distribution

at each turn. It has been found [89] that approximately ten macroparticles per cell reduces numerical fluctuations in PIC codes. Increasing the number of cells increases the resolution of space charge forces but necessitates a larger number of macroparticles, which increases simulation time. Convergence tests suggested that $64 \times 64 \times 64$ PIC nodes and two million macroparticles gave sufficient resolution to capture the intrabunch dynamics due to space charge effects whilst keeping the simulation time manageable.

Similarly, a convergence test with the number of longitudinal slices suggested 128 slices was optimum: providing sufficient resolution without unduly increasing the simulation time. The number of previous turns of accumulated wake to be included in the wake-force calculations is heavily dependent on the type of wake that is implemented. High-frequency impedances produce short-range wakes and low-frequency impedances produce long-range wakes. As the narrowband impedance implemented is low frequency, the wake spreads over many turns. A convergence test for the narrowband impedance implemented in these simulations suggested any more than 200 turns of accumulated wake gave little change in the head-tail instability behaviour.

5.5.2 Without Transverse Space Charge

To ascertain better the effect of space charge on the instability characteristics (growth rate, mode number, *etc.*), simulations were performed with longitudinal space charge but without the transverse PIC space charge solver. In order to compare favourably with the experimentally observed growth rates, the resonator shunt impedance (R_s) was set to $17.2\,\mathrm{k\Omega\,m^{-2}}$. An example output from a simulation with $Q_y = 3.880$ is shown in figures 5.14 and 5.15. The simulated BPM difference signal (figure 5.14b) illustrates that the mode number changes as the instability develops and as intensity is lost through collimation. As in the measurement data, figure 5.16 focuses on the BPM difference signal over 20 turns, before beam is lost (see beam intensity and loss, figure 5.15b) and the vertical emittance has grown beyond 2 %. At that time, the instability appears to be a clear mode $m = 2$ with

two nodes along the bunch's length. Betatron sidebands up to 15 MHz are shown as a function of time in figure 5.15a.

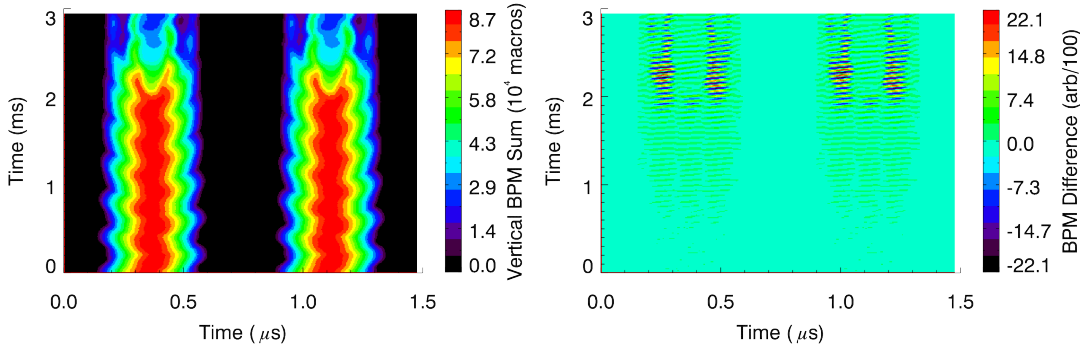


Figure 5.14: Simulated vertical BPM sum signal (a) and difference signal (b) sliced to show each turn against time for $Q_y = 3.880$.

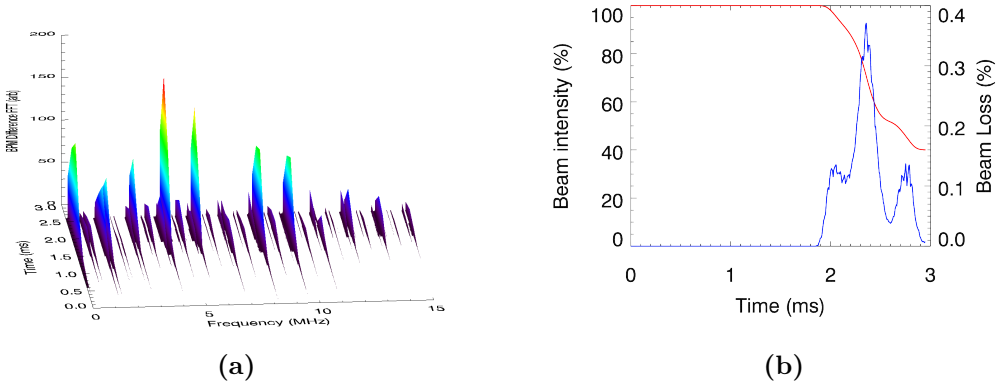


Figure 5.15: a) FFT of the difference signal from figure 5.14 versus time and b) intensity monitor and BLM sum signal versus time.

Figures 5.17 and 5.18 show PyHEADTAIL simulation results as a function of vertical tune for those that produced a vertical instability, in the same manner as those for the head-tail instability measurements as a function of vertical tune (figures 5.8 and 5.9). As indicated in table 5.6, the complete vertical tune range for these simulations was 3.840 – 3.920. The experiments indicated instability predominantly over a measured vertical tune range of 3.832 – 3.891 with the largest growth rates (and associated beam-loss) at $Q_{y,\mathrm{meas}} = 3.879$. The simulations show instability over a shorter range (3.860 – 3.895) although peaking at a similar tune of $Q_y = 3.880$ as expected. Key simulation results are listed in table 5.7.

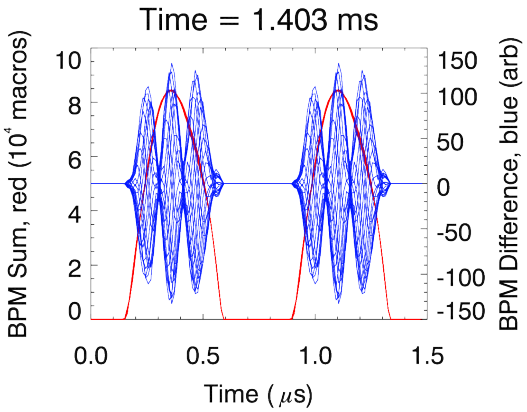


Figure 5.16: Simulated vertical BPM sum signal (blue) and difference signal (red) over 20 turns, after 1.4 ms of wakes.

5.5.2.1 Head-Tail Instability Mode Structure

The intrabunch mode structure is key in comparing simulation and measurement of the head-tail instability. Figures 5.17(m – p) and 5.18(m – p) show 20-turn "snapshots" of the simulated BPM difference signals when the vertical emittance had grown by 2 %, just prior to the beam hitting the vertical aperture and being lost. Intrabunch mode structures in the simulated BPM difference signal mostly showed two or three nodes ($m = 2$ or 3) over the tune range inspected. However, results from RCS mode (section 4.2.1) and the BSRM experiments presented in this chapter (section 5.4.2) indicated a dominant $m = 1$ head-tail mode with possible $m = 0$ and 2, dependent on the vertical tune. Variation of mode structure with vertical tune was observed in simulations as well as experimental measurements albeit at different mode ranges.

The simulated data suggested that, as the vertical tune was increased (and the corresponding BB decreased), the mode number decreased from $m = 3$ to 2 (see table 5.7). Though not distinct, the change in mode was present. In the experimental measurements, the trend of mode number with frequency was also present (see table 5.4), going from $m = 2$ to 0. Although, in the experiment, the change in observed mode was non-linear, with mode $m = 1$ observed at the lowest tune, $Q_{y,\mathrm{meas}} = 3.749$ and at $Q_{y,\mathrm{meas}} = 3.882$.

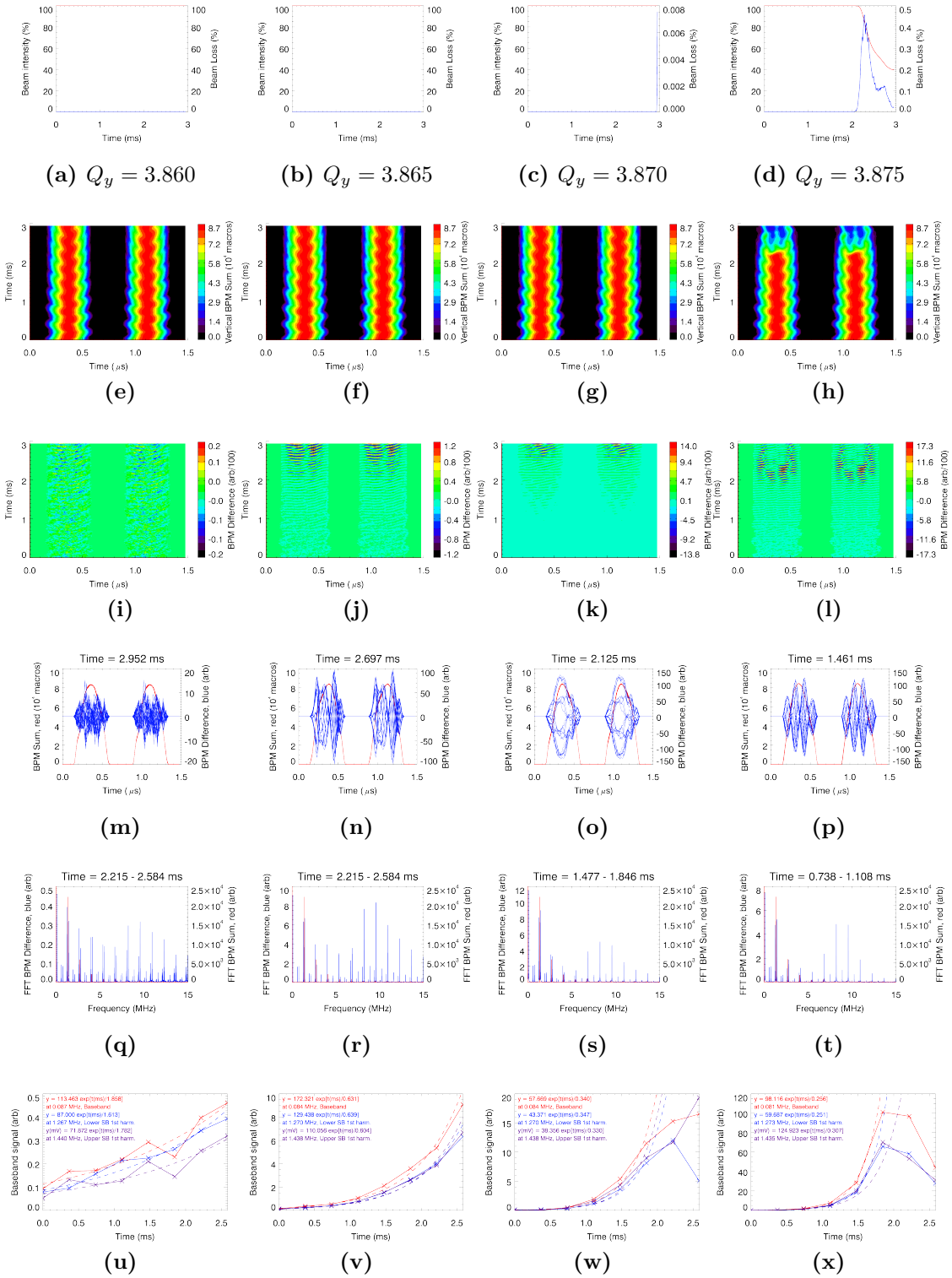


Figure 5.17: PyHEADTAIL output without transverse space charge for different vertical tunes (3.860 – 3.875): intensity and beam-loss (a – d), longitudinal bunch population over time (e – h), simulated vertical BPM difference over time (i – l), simulated vertical BPM traces over 20 turns (m – p), FFT of simulated BPM data around the time of interest (q – t), growth rate fits to betatron sidebands (u – x).

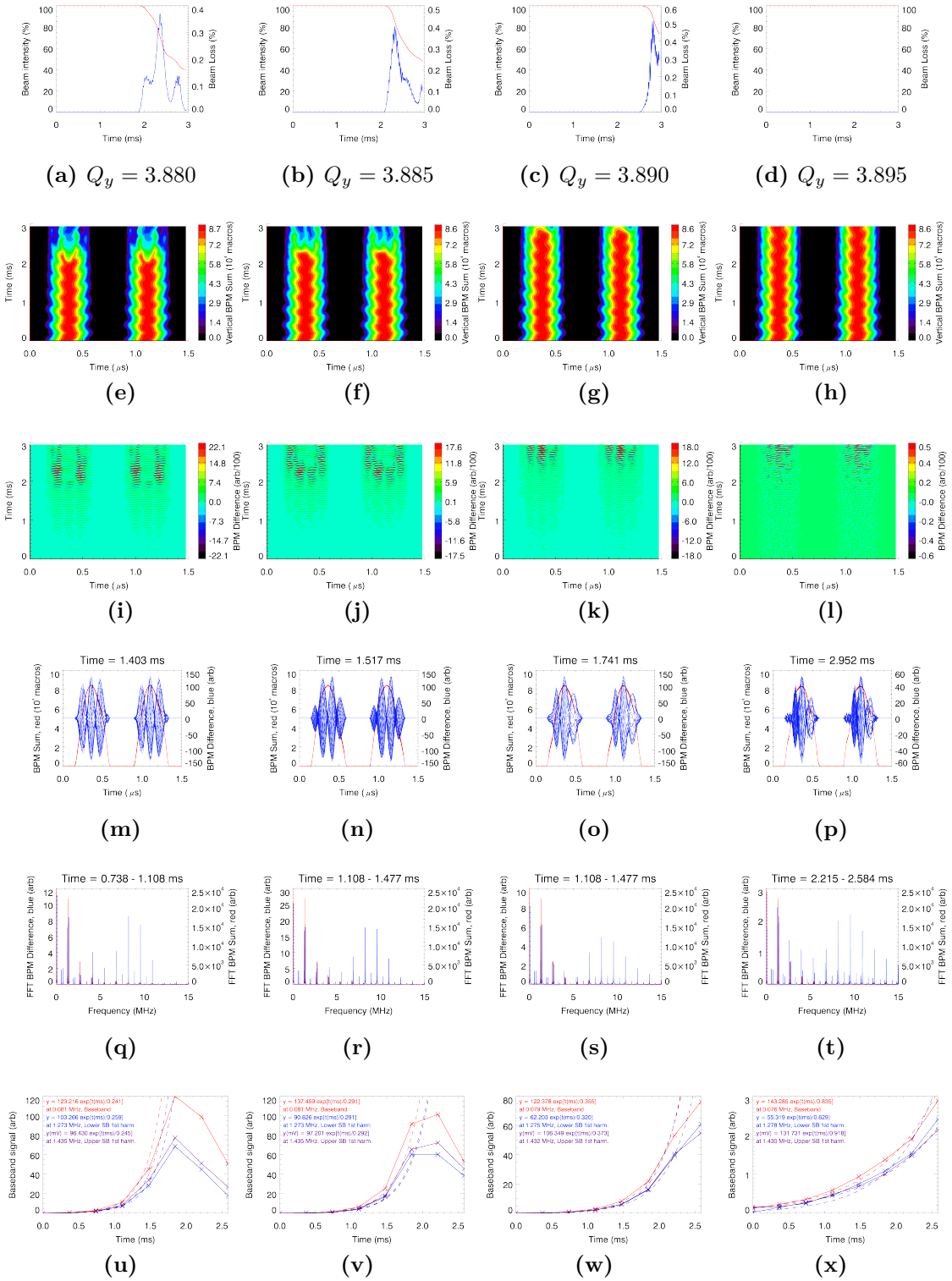


Figure 5.18: PyHEADTAIL output without transverse space charge for different vertical tunes (3.880 – 3.895): intensity and beam-loss (a – d), longitudinal bunch population over time (e – h), simulated vertical BPM difference over time (i – l), simulated vertical BPM traces over 20 turns (m – p), FFT of simulated BPM data around the time of interest (q – t), growth rate fits to betatron sidebands (u – x).

Table 5.7: Summary of head-tail instability characteristics in simulations of BSRM on ISIS as a function of vertical tune without transverse space charge. Q_y and $Q_{y,\mathrm{meas}}$ = set and measured vertical tunes respectively, m = head-tail mode number, sideband = largest amplitude betatron sideband, f_{BB} = BB frequency, the growth rate is that of the BB, τ_{b} = 95 % bunch length, a figure reference is given, if present.

Q_y	$Q_{y,\mathbf{meas}}$	m	**Sideband**	$f_{\mathbf{BB}}$ **(kHz)**	**Growth Rate (turn^{-1})**	$\tau_{\mathbf{b},\ 95\,\%}$**(ns)**	**Figure**
3.840	3.852	n/a	USB3	100 ± 2.7	(0.66 ± 3.12)×10^{-4}	348	n/a
3.845	3.856	n/a	USB3	97.5 ± 2.7	(-2.54 ± 2.98)×10^{-4}	348	n/a
3.850	3.852	n/a	USB4	100 ± 2.7	(8.39 ± 2.47)×10^{-4}	348	n/a
3.855	3.868	n/a	USB4	89.4 ± 2.7	(1.86 ± 5.10)×10^{-4}	348	n/a
3.860	3.872	n/a	BB	86.7 ± 2.7	(7.94 ± 1.10)×10^{-4}	348	5.17a
3.865	3.876	3	BB	84.0 ± 2.7	(2.42 ± 0.11)×10^{-3}	348	5.17b
3.870	3.876	0	BB	84.0 ± 2.7	(4.50 ± 0.58)×10^{-3}	351	5.17c
3.875	3.880	3	BB	81.3 ± 2.7	(5.79 ± 0.12)×10^{-3}	352	5.17d
3.880	3.880	2	BB	81.3 ± 2.7	(6.48 ± 0.25)×10^{-3}	347	5.18a
3.885	3.880	3	BB	81.3 ± 2.7	(4.79 ± 0.50)×10^{-3}	351	5.18b
3.890	3.884	2	BB	78.6 ± 2.7	(4.03 ± 0.36)×10^{-3}	350	5.18c
3.895	3.888	2	BB	75.8 ± 2.7	(1.77 ± 0.06)×10^{-3}	348	5.18d
3.900	3.892	n/a	BB	73.1 ± 2.7	(8.03 ± 0.74)×10^{-4}	348	n/a
3.905	3.900	n/a	USB4	67.7 ± 2.7	(3.34 ± 5.16)×10^{-4}	348	n/a
3.910	3.904	n/a	USB1	65.0 ± 2.7	(3.63 ± 2.16)×10^{-4}	348	n/a
3.915	3.908	n/a	USB3	62.3 ± 2.7	(2.01 ± 0.70)×10^{-4}	348	n/a
3.920	3.924	n/a	USB3	51.5 ± 2.7	(5.55 ± 1.78)×10^{-4}	348	n/a

The BPM difference "waterfall" graphs (i – l) clearly show that, as observed in the experiment, mode structures can continued long after large portions of beam had been lost. For $Q_y = 3.880$, an $m = 2$ mode was excited with a fast growth rate. Once part of the beam was lost, different modes became unstable (possibly $m = 1$ and $m = 3$, although the longitudinal bunch shape was much altered) and this was observed for the rest of the simulation period, causing further beam-loss.

Simulations produced oscillations along the full bunch length, unlike the measurements (section 5.4.2). This was independent of the vertical tune setting and the observed head-tail mode structure, consistent with theory (see section 7.2.2.1).

5.5.2.2 Head-Tail Instability in Frequency Domain

As in the experimental measurements, the simulated BPM difference signal may be observed in the frequency domain using an FFT, figures 5.17(q – t) and 5.18(q – t), showing the vertical betatron sidebands. The simulated data have been processed in the same way as the measured data, monitoring the frequency and amplitude of the sidebands as a function of time by dividing the simulated BPM data into 250-turn segments (equating to 0.37 ms each).

The fractional part of the betatron tune was determined by the lowest betatron sideband frequency divided by the revolution frequency (derived from an FFT of the simulated BPM sum signal, or directly from the revolution period output by the simulation). As the vertical tune was increased, the corresponding BB frequency decreased. As expected, unlike the experimental measurements, the simulated BPM data produced measured tune values far closer to those input into the simulation (see table 5.7). The increase in error on the tune measurement is due to the decreased frequency resolution in the simulation ($\pm$ 1.35 kHz in simulation compared to $\pm$ 1 kHz in experiment).

The betatron sidebands grew from nothing as the transverse distributions were matched at the start of each simulation. As stated above, the frequency spectra were recorded at 250-turn intervals. The spectra that included the time at which the vertical emittance had grown by 2 % is included in the figures. The largest betatron sideband at that interval is assumed to be dominant. As expected, for

those vertical tunes producing an instability, the largest sideband was the BB which is closest to the imposed driving impedance, the narrowband resonator at 82 kHz.

5.5.2.3 Head-Tail Instability Growth Rate Versus Frequency

As the FFT of the simulated BPM data was performed over 250-turn segments, the growth rate of each sideband could be determined. Figures 5.17(u – x) and 5.18(u – x) show the BB and the lower betatron sideband amplitudes around the first RF harmonic, together with an exponential fit up until the emittance had grown by 2 % or the end of the simulation.

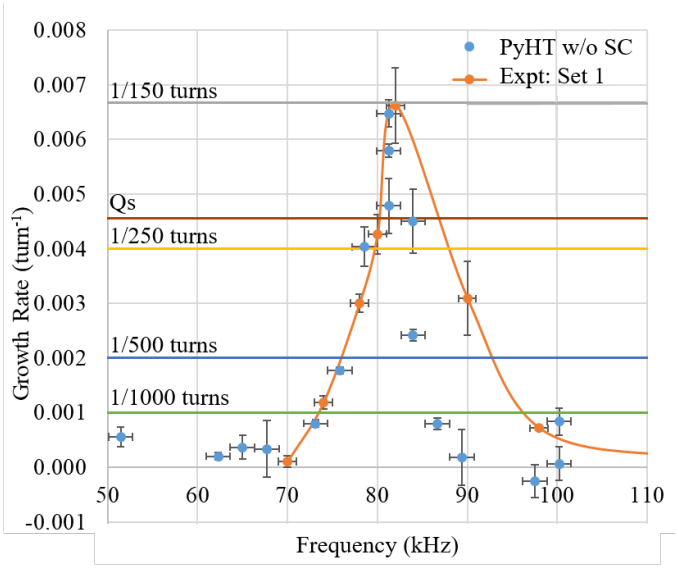


Figure 5.19: Growth rate versus betatron BB frequency for PyHEADTAIL simulations without transverse space charge.

The exponential growth time for each vertical tune's BB was converted to a growth rate ($1/(\tau f_{\mathrm{rev}})$) and is shown as a function of the measured BB frequency in figure 5.19 together with the measured growth rate from the experiment in BSRM on ISIS. The growth rates in simulation and associated errors are listed in table 5.7. The trend of growth rate with BB frequency was very similar between simulation and experiment. By design these are very close in peak amplitude and frequency, although the precise behaviour with frequency (betatron tune) is not the same. This is likely just a difference between an ideal narrowband resonator impedance and the real machine impedance as a function of frequency. The peak

growth rate was $(6.48 \pm 0.25) \times 10^{-3}$ turn^{-1} which equates to the BB growing by a factor of e (Euler's number) every $\sim$150 turns. As in the measured case, it should be noted that this was faster than the synchrotron motion quantified by the synchrotron tune, $Q_s = 4.54 \times 10^{-3}$ turn^{-1}.

5.5.3 With Transverse Space Charge

Despite operating the accelerator at approximately 10 % of its nominal beam intensity for the BSRM experiments (section 5.4) in an effort to reduce the complexities of space charge, these forces may still play a role in the dynamics of the beam and that of the head-tail instability. It may also go some way to explaining differences between the observed and simulated behaviour, in particular the different mode structures excited and only part of the bunch length becoming unstable.

To ascertain the degree to which space charge plays a role in the head-tail instability dynamics, the "space charge parameter", $q = \Delta Q_{\mathrm{SC}}/Q_s$ (the peak incoherent space charge tune shift, equation 3.52, divided by the synchrotron tune) may be calculated (see section 3.4.2). When this grows much larger than one, space charge is considered to be "strong" and plays a significant role in instability dynamics. The accepted theory of Sacherer assumes $q \ll 1$.

In the case of the experiments and associated simulations in this chapter, the incoherent space charge tune shift was 0.032 (using the values from table 5.6 and a calculated $B_f = 0.63$) and therefore the space charge parameter was $q = 7.06$ (the coherent space charge tune shift is $\sim$0.002 and can largely be ignored). Therefore, the effect of space charge on the tune is on a similar level to that of the chromaticity. Therefore, space charge is likely to play a role, even at 10 % of the nominal beam intensity. As stated in section 5.3, this intensity was selected in experiment as the lowest reasonable intensity where the instability was observable and BPM signals had a good signal-to-noise ratio. As transverse space charge is likely to affect instability dynamics, it was included in further PyHEADTAIL simulations using a 2.5D self-consistent PIC algorithm, solving the Poisson equation to evaluate space charge kicks slice by slice (see section 3.5 and chosen PIC simulation parameters in table 5.6).

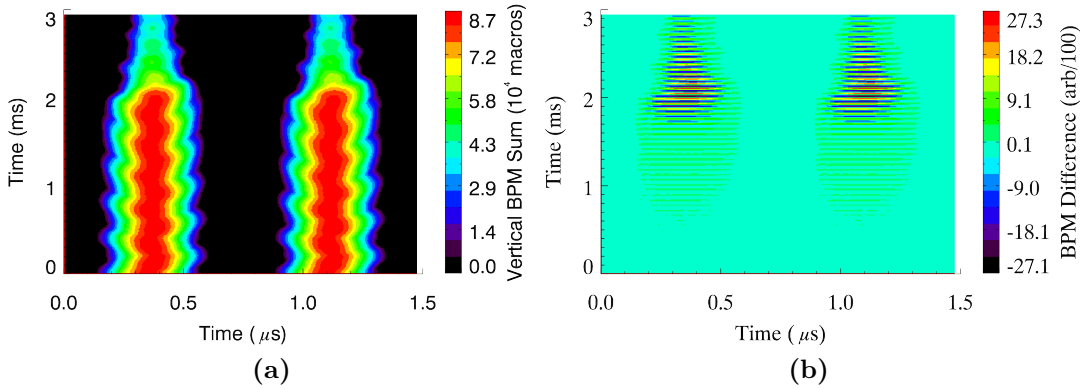
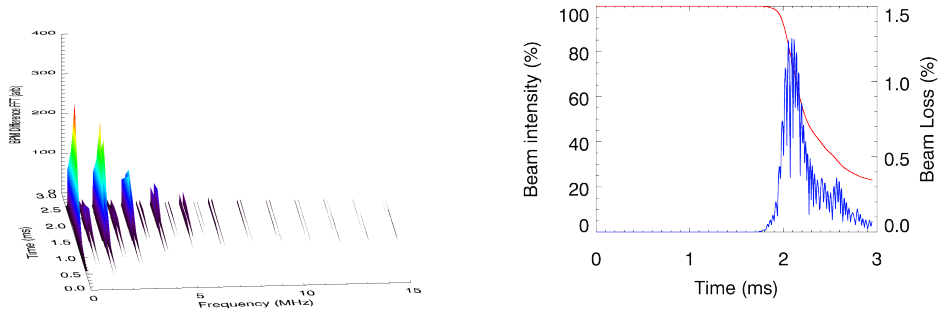


Figure 5.20: Simulated vertical BPM sum signal (a) and difference signal (b) sliced to show each turn against time for $Q_y = 3.880$.

To match the peak experimentally observed growth rate, the resonator shunt impedance was reduced 80 % to 3.44 kΩ m^{-2} (other resonator parameters are given in table 5.6). An example output from a simulation with $Q_y = 3.880$ is shown in figures 5.20 and 5.21. The simulated BPM difference signal (figure 5.20b) indicates a very different intrabunch mode structure from that without space charge (figure 5.14b). Figure 5.22 focuses on the BPM difference signal over 20 turns before beam was lost (beam intensity and loss versus time are shown in figure 5.21b) and the vertical emittance had grown beyond 2 %. At that time, and subsequently, the instability appears to be a clear mode $m = 0$ with no nodes along the bunch length. Betatron sidebands in figure 5.21a show a different situation from that without transverse space charge, figure 5.15, with the growth of low-frequency sidebands dominating the spectra and little growth observed in the 7 – 15 MHz range.

Figures 5.23 and 5.24 summarise the PyHEADTAIL simulation results including transverse space charge. The experiments indicated instability over a measured vertical tune range of 3.832 – 3.891 with peak growth rates at $Q_y = 3.879$. These simulations showed instability over a shorter range (3.860 – 3.895), although peaking at a similar tune of $Q_y = 3.88$, as also observed in simulations without transverse space charge. Key simulation results are also listed in table 5.8.



(a) (b)

Figure 5.21: a) FFT of the difference signal from figure 5.20 versus time and b) intensity monitor and BLM sum signal versus time.

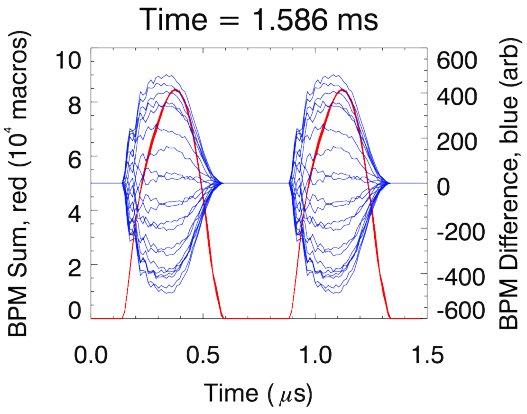


Figure 5.22: Simulated vertical BPM sum signal (blue) and difference signal (red) over 20 turns, after 1.4 ms of wakes.

5.5.3.1 Head-Tail Instability Mode Structure

Figures 5.23(m – p) and 5.24(m – p) show 20-turn overlays of the BPM sum and difference signals when the vertical emittance had grown by 2 % which exhibit the head-tail mode structure, if present. It may be clearly seen that the inclusion of transverse space charge has led to head-tail mode structures with no nodes ($m = 0$) and, where there was an instability, changing vertical tune had no effect on the observed mode. Observed head-tail mode numbers are also listed in table 5.8. However, simulations without transverse space charge (section 5.5.2.1) showed intrabunch mode structures in the BPM difference signal with two or three nodes, and experimental observations (section 5.4.2) showed one, two and occasionally zero nodes.

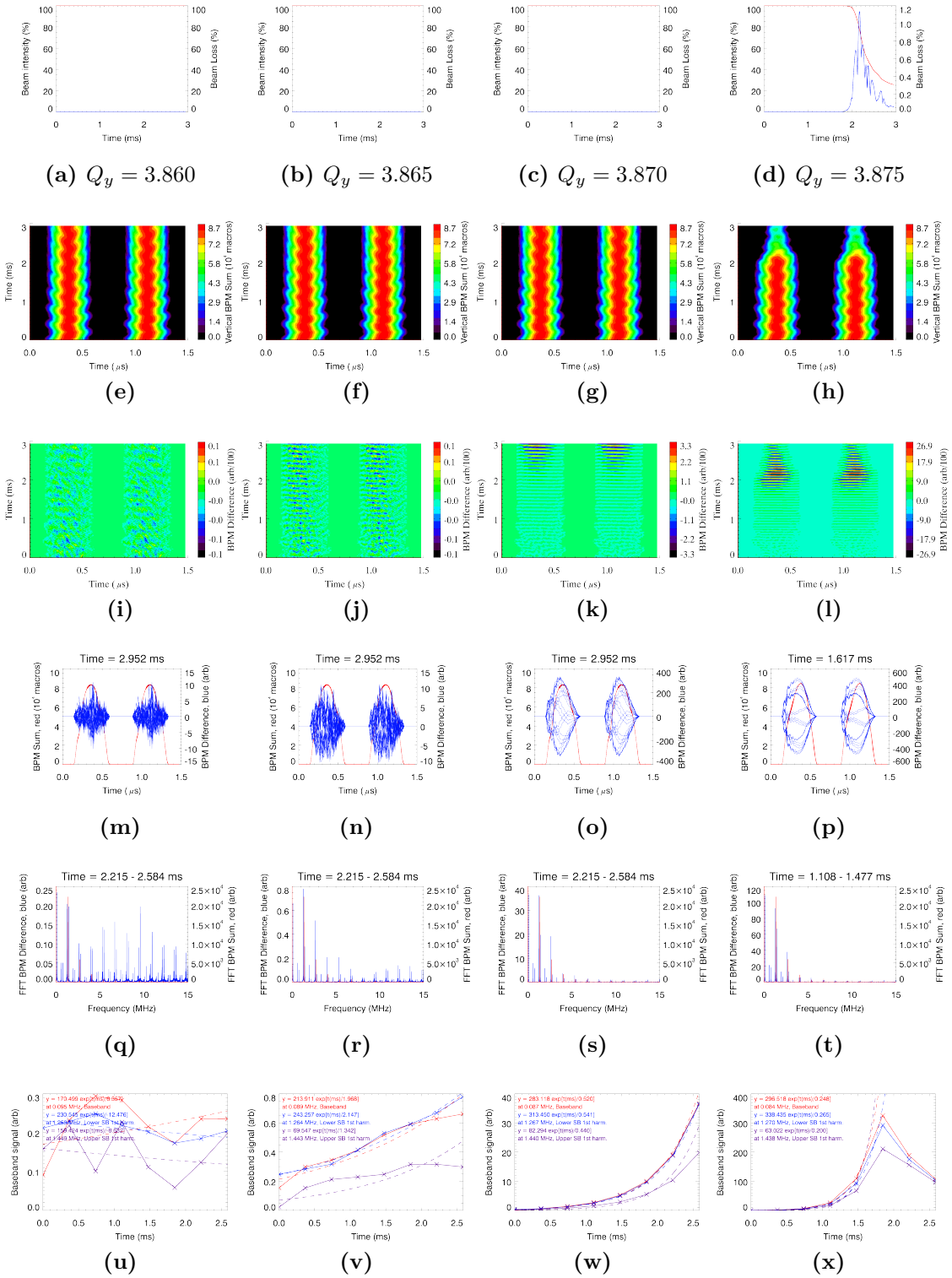


Figure 5.23: PyHEADTAIL output with transverse space charge for different vertical tunes (3.860 – 3.875): intensity and beam-loss (a – d), longitudinal bunch population over time (e – h), simulated vertical BPM difference over time (i – l), simulated vertical BPM traces over 20 turns (m – p), FFT of simulated BPM data around the time of interest (q – t), growth rate fits to betatron sidebands (u – x).

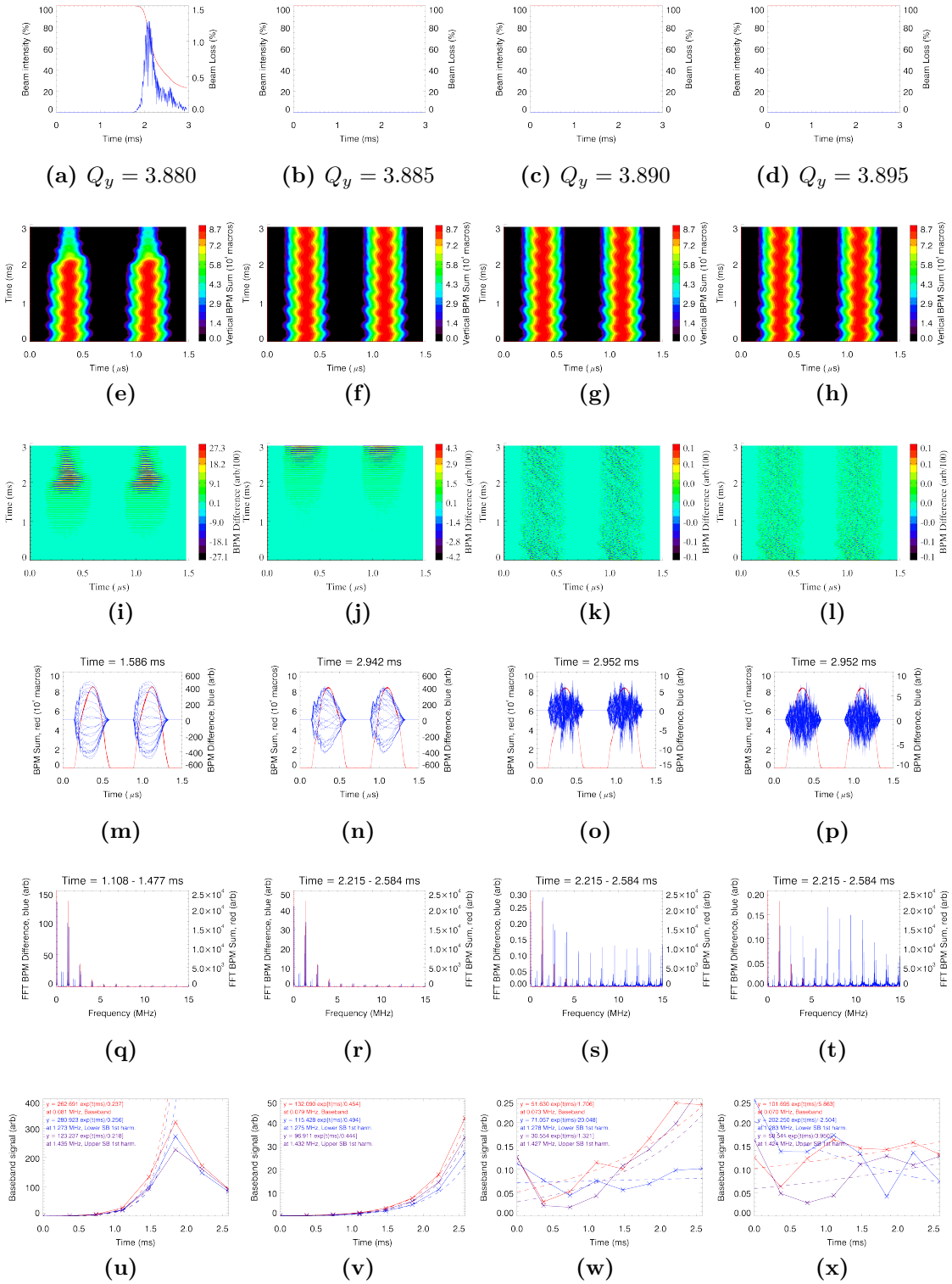


Figure 5.24: PyHEADTAIL output with transverse space charge for different vertical tunes (3.880 – 3.895): intensity and beam-loss (a – d), longitudinal bunch population over time (e – h), simulated vertical BPM difference over time (i – l), simulated vertical BPM traces over 20 turns (m – p), FFT of simulated BPM data around the time of interest (q – t), growth rate fits to betatron sidebands (u – x).

Table 5.8: Summary of head-tail instability characteristics in simulations of BSRM on ISIS as a function of vertical tune with transverse space charge. Q_y and $Q_{y,\mathrm{meas}}$ = set and measured vertical tunes respectively, m = head-tail mode number, sideband = largest amplitude betatron sideband, f_{BB} = BB frequency, the growth rate is that of the BB, τ_{b} = 95 % bunch length, a figure reference is given, if present.

Q_y	$Q_{y,\mathbf{meas}}$	m	**Sideband**	$f_{\mathbf{BB}}$ **(kHz)**	**Growth Rate (turn^{-1})**	$\tau_{\mathbf{b},\ 95\,\%}$**(ns)**	**Figure**
3.840	3.840	n/a	LSB1	108 ± 2.7	(-0.82 ± 3.64)×10^{-4}	348	n/a
3.845	3.848	n/a	LSB5	103 ± 2.7	(-2.23 ± 1.07)×10^{-4}	348	n/a
3.850	3.852	n/a	LSB2	100 ± 2.7	(-7.65 ± 2.41)×10^{-4}	348	n/a
3.855	3.856	n/a	BB	97.5 ± 2.7	(0.60 ± 1.64)×10^{-4}	348	n/a
3.860	3.860	n/a	BB	94.8 ± 2.7	(2.32 ± 2.32)×10^{-4}	348	5.23a
3.865	3.868	n/a	LSB1	89.4 ± 2.7	(7.50 ± 1.15)×10^{-4}	348	5.23b
3.870	3.872	0	BB	86.7 ± 2.7	(2.84 ± 0.10)×10^{-3}	348	5.23c
3.875	3.876	0	BB	84.0 ± 2.7	(6.08 ± 0.15)×10^{-3}	347	5.23d
3.880	3.880	0	BB	81.3 ± 2.7	(6.26 ± 0.04)×10^{-3}	344	5.24a
3.885	3.884	0	BB	78.6 ± 2.7	(3.22 ± 0.07)×10^{-3}	348	5.24b
3.890	3.892	n/a	USB1	73.1 ± 2.7	(8.66 ± 3.25)×10^{-4}	348	5.24c
3.895	3.896	n/a	USB5	70.4 ± 2.7	(2.52 ± 1.73)×10^{-4}	348	5.24d
3.900	3.900	n/a	USB2	67.7 ± 2.7	(-1.34 ± 2.23)×10^{-4}	348	n/a
3.905	3.908	n/a	LSB5	62.3 ± 2.7	(2.01 ± 2.32)×10^{-4}	348	n/a
3.910	3.912	n/a	USB4	59.6 ± 2.7	(-2.49 ± 0.80)×10^{-4}	348	n/a
3.915	3.916	n/a	LSB1	56.9 ± 2.7	(-0.80 ± 1.89)×10^{-4}	348	n/a
3.920	3.920	n/a	USB8	54.2 ± 2.7	(-1.08 ± 4.07)×10^{-4}	348	n/a

The shift to lower-order mode structures with the addition of transverse space charge was more consistent with the experimental observations. However, the variation of mode with vertical tune was not present in the simulations with space charge. Also, unlike simulations without transverse space charge and experimental data, the mode structures after beam had been lost were consistent with those excited before beam-loss occurred, see BPM "waterfall" figures 5.23(i – l) and 5.24(i – l).

As with the simulations without transverse space charge, the induced head-tail instability caused oscillations over the full bunch length. Once again, this was independent of the vertical tune setting and the observed head-tail mode structure.

5.5.3.2 Head-Tail Instability in Frequency Domain

Looking at the BPM difference signal in the frequency domain, figures 5.23(q – t) and 5.24(q – t), the vertical betatron sidebands may be observed around the time point when the vertical emittance had grown by 2 %. As in the case without transverse space charge, the BPM data were separated into 250-turn portions to allow enough resolution in both sideband frequency and the evolution of sideband amplitude through the simulation.

As in the previous simulations, the fractional part of the betatron tune was derived from the lowest betatron sideband frequency. As the vertical tune was increased, the corresponding BB frequency decreased. It is notable that, for vertical tunes with distinct head-tail motion (Q_y = 3.870 – 3.885), betatron sidebands were very small above ∼5 MHz. For simulations without transverse space charge (section 5.5.2.2), and experimental measurements (section 5.4.3), the frequency spectra for all vertical tunes showed betatron sidebands of appreciable amplitude up to, and beyond 10 MHz.

The largest betatron sideband at the time point of interest was assumed to be dominant and most often corresponded to the lowest frequency sideband (see table 5.8). This was in keeping with both simulations without transverse space charge and the experimental measurements; this is expected as it is closest to the narrowband driving impedance's frequency of 82 kHz.

5.5.3.3 Head-Tail Instability Growth Rate Versus Frequency

Using the regular FFTs of the BPM data (every 250 turns), the BB amplitude could be determined as a function of time, and an exponential function fitted to it up until the beam starts being lost. Figures 5.23(u – x) and 5.24(u – x) show the BB and the lower betatron sideband around the first RF harmonic, together with their exponential fits until the emittance had grown to 2 % or the end of the simulation (whichever occurs first).

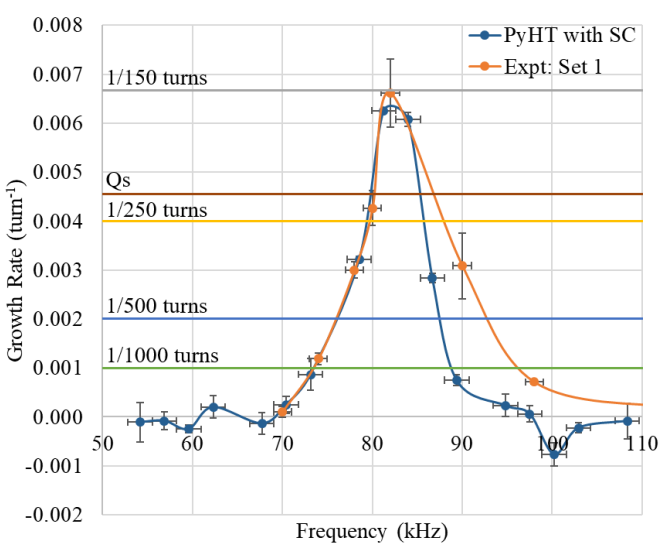


Figure 5.25: Growth rate versus betatron BB frequency for PyHEADTAIL simulations with transverse space charge.

Figure 5.25 shows the growth rate ($1/(\tau f_{\mathrm{rev}})$) as a function of the measured BB frequency as well as the measured growth rate from the experiments on ISIS in BSRM. The growth rates in simulations with transverse space charge, and associated errors, are listed in table 5.8. The trend of growth rate with BB frequency was very similar between simulation and experiment. As expected, due to the choice of narrowband shunt impedance (R_s), the peak growth rates in experiment and simulation were very close in amplitude and frequency. The behaviour with frequency showed good agreement between simulation and measurement up to the narrowband peak (82 kHz) but tailed off quicker above the peak in simulation. As in the simulations without transverse space charge, this was likely caused by a difference between an ideal narrowband resonator impedance and the real machine impedance as a

function of frequency. The peak growth rate was $(6.26 \pm 0.04) \times 10^{-3}$ turn^{-1} which equates to the BB growing by a factor of e (Euler's number) every $\sim$150 turns. As in the measured case, it should be noted that this was faster than the synchrotron motion quantified by the synchrotron tune, $Q_s = 4.54 \times 10^{-3}$ turn^{-1}.

5.6 Summary

The complications of studying the head-tail instability on ISIS in its normal operating mode (rapid cycling, high-intensity, DHRF) and comparing it to established theory, led to a suite of experiments in a new operating mode: BSRM. Initial beam-based measurements without RF (coasting beam) showed a low-frequency narrowband impedance in the vertical plane (section 5.2).

Measurements were made in the new operating mode to inspect the head-tail instability as a function of vertical tune (section 5.4) using a single 1RF cavity and 10 % of the nominal beam intensity. The results indicate the low-frequency narrowband impedance drives a head-tail instability characterised by mode numbers $m = 0$, 1 and 2. It was also noted that the mode structure, observed in the BPM difference signal, did not extend to the full bunch length but occupied as little as half the bunch length, leading to the concept of an effective bunch length.

Subsequent PyHEADTAIL simulations were performed to match the experimental setup, with the resulting data presented in the same format for ease of comparison (section 5.5). Initial simulations were performed with longitudinal space charge but without transverse space charge (section 5.5.2). The dependence of the instability growth rate on frequency matched well with the experimental data, however the observed mode structure differed. The simulations showed that the full bunch length was vertically unstable, in disagreement with the experimental measurements.

Further simulations were performed with a 2.5D PIC model of transverse space charge (section 5.5.3). Similarly, these reproduced the dependence of instability growth rate on vertical tune (BB frequency), however the mode structures differed from both simulations without transverse space charge and experiment. It was found that including transverse space charge had no effect on the portion of the

bunch length that became vertically unstable, still the full bunch length, differing from experimental measurements.

If the impedance is known then Sacherer theory (see section 3.3.1), together with knowledge of the chromaticity and bunch length, enables a prediction of the most unstable head-tail mode, the BPM difference frequency spectra (see figures 3.2 and 3.5) and instability growth rate. Comparisons between predictions from Sacherer's theory, experimental measurements and simulations are drawn in chapter 7.

Nothing in life is to be feared, it is only to be understood. Now is the time to understand more, so that we may fear less.

— Marie Curie, quoted in "Our Precarious Habitat", Melvin A. Benarde, 1973.

6

SRM: Head-Tail Instability as a Function of Vertical Beam Size

6.1 Introduction

The investigations of head-tail as a function of vertical tune in the new BSRM operating mode for ISIS (bunched beams, stored at injection energy) gave interesting insights into the development of the instability and the possible driving sources (chapter 5, particularly section 5.4). However, differences still remained between the experimentally observed behaviour and the new, complex simulations utilising PyHEADTAIL [70]. Experience in RCS operation suggests the vertical stability of the beam is sensitive to intensity, vertical tune, the longitudinal beam distribution and vertical beam size. In order to try and bridge the gap between observations and simulations, a further experiment was devised to establish the effect of the vertical beam size on the head-tail instability as present on ISIS.

The reasoning behind this is straight-forward: the head-tail instability is known to be a coupled effect between the transverse and longitudinal planes. As such, changing the painting in either plane might plausibly affect the development and characteristics of the head-tail instability. From the established theory (section 3.3) the vertical beam size, or emittance, only enters the growth rate formula through the impedance. If the impedance is a function of vertical beam size then the growth

rate of the head-tail instability will also be a function of vertical beam size. However, it should be noted that space charge forces are strongly dependent on the transverse beam size and the size of the beam pipe. Simulations in the previous chapter showed transverse space charge has an appreciable effect on the head-tail instability, even at much reduced beam intensities. Therefore, this experiment would be expected to probe transverse space charge's impact on the head-tail instability.

6.1.1 Experimental Setup

The ISIS synchrotron was set for stored bunched beams (BSRM) as described in section 5.3 (see table 5.1). A beam suitable for the experiment was established with key parameters listed in table 6.1.

Table 6.1: Key experimental parameters for measurements of the head-tail instability in BSRM as a function of vertical beam size.

Parameter	**Symbol**	**Value**
Bunch intensity	N	1.47×10^{12} ppb
RF voltage	V_{RF}	11.4 kV per turn
Set betatron tunes	Q_x, Q_y	4.330, 3.790 – 3.830
"Vertical sweeper" current	I_{VS}	14 – 35 A
RMS vertical emittance	$\epsilon_{y,\mathrm{RMS}}$	$10\,\pi$ – $50\,\pi$ mm mrad
Revolution frequency	f_{rev}	675.06 ± 0.06 kHz
Relativistic beta	β	$0.3679 \pm 3 \times 10^{-5}$
Relativistic gamma	γ	$1.0754 \pm 1.6 \times 10^{-5}$
Slip factor	η	$-0.8252 \pm 2.6 \times 10^{-5}$
Synchrotron tune	$Q_s = \sqrt{\frac{V_{RF}\eta h \cos\phi_s}{2\pi\beta^2 E_T}}$	$0.00468 \pm 4 \times 10^{-7}$
Vertical chromatic frequency	$f_{\xi,y} = \xi_y f_{\mathrm{rev}} Q_y/\eta$	4.318 – 4.398 MHz

As in the measurements of the head-tail instability as a function of vertical tune (section 5.4), the main dipole field was held constant at the level required for the design injection energy (70 MeV), $B = 0.176$ T. A single 1RF cavity was powered, whilst the others were set off-tune and with zero volts at the gap to minimise their contribution to the beam dynamics. The RF frequency was selected to match the injected beam energy and also held constant. To maintain comparable longitudinal and horizontal painting to nominal RCS operation, the RF voltage

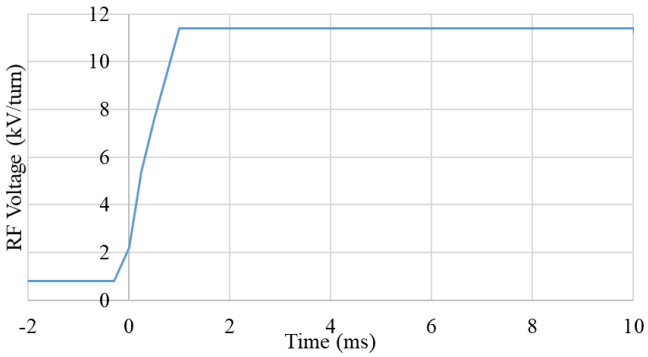


Figure 6.1: Total RF voltage per revolution as a function of time.

ramp was kept the same as in RCS operations up until 1 ms and then held constant until 10 ms at 11.4 kV per turn (see figure 6.1).

The vertical beam size is controlled during the injection process by a specialised, pulsed dipole magnet called the "vertical sweeper", situated in the injection line between the linac and the synchrotron (see section 2.1.2.1). In normal operation, beam is injected over the falling "sweeper" field to distribute the beam in vertical phase space. Typically, the beam experiences a current range of 40 – 20 A equating to kicks of 5 to 0.5 mrad. By reducing the peak "vertical sweeper" current, the painted vertical beam size is reduced. In this experiment the peak "vertical sweeper current", I_{VS}, was set between 14 and 35 A producing beams of different vertical size (see section 6.1.1.1). The timing of the "vertical sweeper" was selected such that the beam was almost all injected at the maximum emittance (determined by the "sweeper" current), producing a vertically hollow beam distribution at the end of injection.

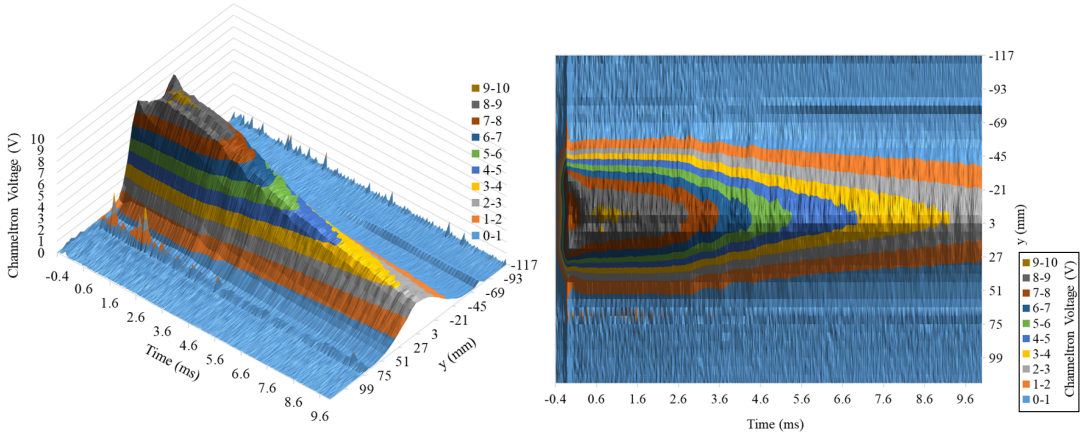
The vertical tune was held constant for each individual measurement and changed from 3.790 to 3.830 in steps of 0.01 to probe the previously measured low-frequency narrowband impedance (section 5.2). Therefore, for each vertical beam size a small vertical tune scan was performed over the unstable region. For each measurement, data were acquired from a ring IM, a sum of all the ionisation BLMs and the individual electrode signals from one vertical and one horizontal BPM. The electrode signals allow easy access to the BPM sum and difference data required for instability analysis (as described in section 2.1.3). These were acquired at 200 MHz and, due to memory limits on the hardware, 1.6 million data

points were recorded for each signal equating to 8 ms of data. Measurements were triggered before injection, leading to around 6.5 ms of stored bunched beam recorded. Each series of measurements over different vertical tunes was then repeated for a number of vertical beam sizes.

The synchrotron tune, Q_s, and the vertical chromatic frequency, $f_{\xi,y}$ listed in table 6.1 were calculated from the experimental parameters and nominal values from table 2.1 using the equations in the table (ϕ_s is the synchronous phase which is zero in this case and E_T is the total energy of the protons).

6.1.1.1 Vertical Beam Profile Measurement

As described in section 2.1.2, ISIS employs residual gas ionisation profile monitors (IPMs) to non-destructively measure the transverse profile of the proton beam. In this experiment, measurements of the vertical profile of the beam were taken at each peak "vertical sweeper" current setting. Nominal IPM measurements record the profile every 10 µs from -0.4 – 10 ms with each profile consisting of forty data points, corresponding to the forty ion detectors spread across the beam pipe aperture. The centre of each detector is 6 mm from the centre of its neighbour.



(a) **(b)**

Figure 6.2: Example vertical IPM measurement as a function of time ($I_{\mathrm{VS}} = 35$ A, $Q_{y,\mathrm{set}} = 3.810$, uncorrected).

For the purposes of this experiment, the profile at 0.6 ms, rather than at the end of injection, was compared for the different vertical sweeper settings. As can be seen in figure 6.2, the painted vertical distribution continues to change after

injection is complete (by $-0.2\,\mathrm{ms}$) and a fully formed and stable distribution is consistently created by around 0.6 ms. It should be noted that the RF voltage had not reached its flat-top value at this time (figure 6.1) and, therefore, the longitudinal distribution was still changing.

Studies into the measurement errors of the ISIS IPMs [96] have shown that the resulting profiles are distorted by the monitor's drift field and the beam's space charge. A simple correction (described in [96]) has been applied to the measured profiles and the results for each "vertical sweeper" current (normalised by the profile area) are shown in figure 6.3.

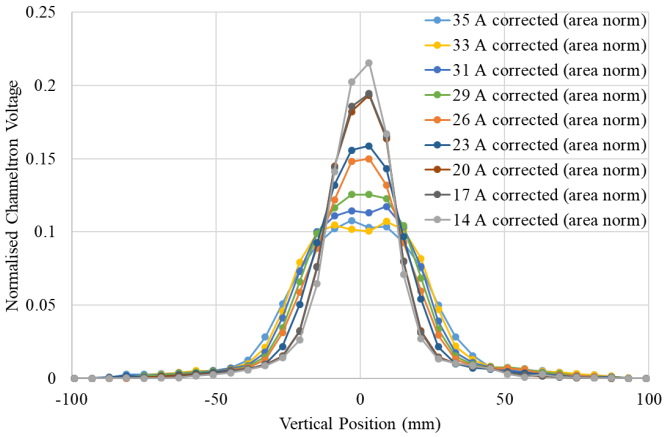


Figure 6.3: Corrected vertical IPM measurements at 0.6 ms, normalised by profile area, as a function of vertical sweeper current ($Q_{y,\mathrm{set}} = 3.810$).

The corrected profiles have been compared to standard bunch distributions and appear most closely represented by waterbag distributions (see example shown in figure 5.12). Figure 6.4 shows the fitted waterbag distributions' RMS vertical beam emittances as a function of the peak "vertical sweeper" current, I_{VS}. The RMS emittance varies between $10\,\pi$ and $50\,\pi\,\mathrm{mm\,mrad}$ (at "vertical sweeper currents" of 14 and 35 A respectively); a quadratic fit matches the data reasonably well and is shown in the figure. The error bars originate from uncertainty in the profile fitting process. These data are also given in tables 6.2 – 6.4.

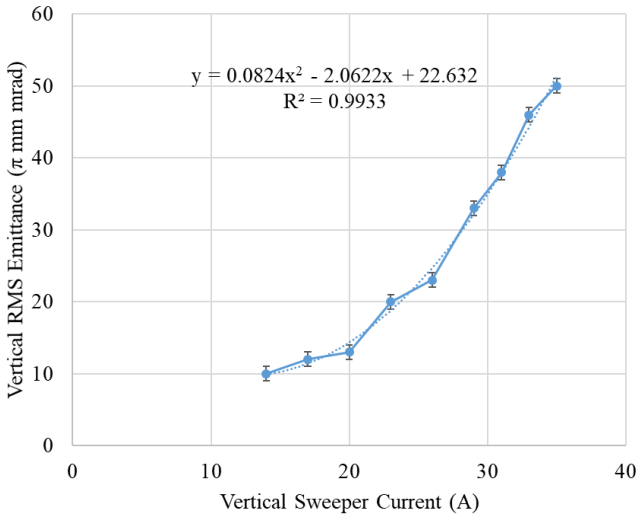


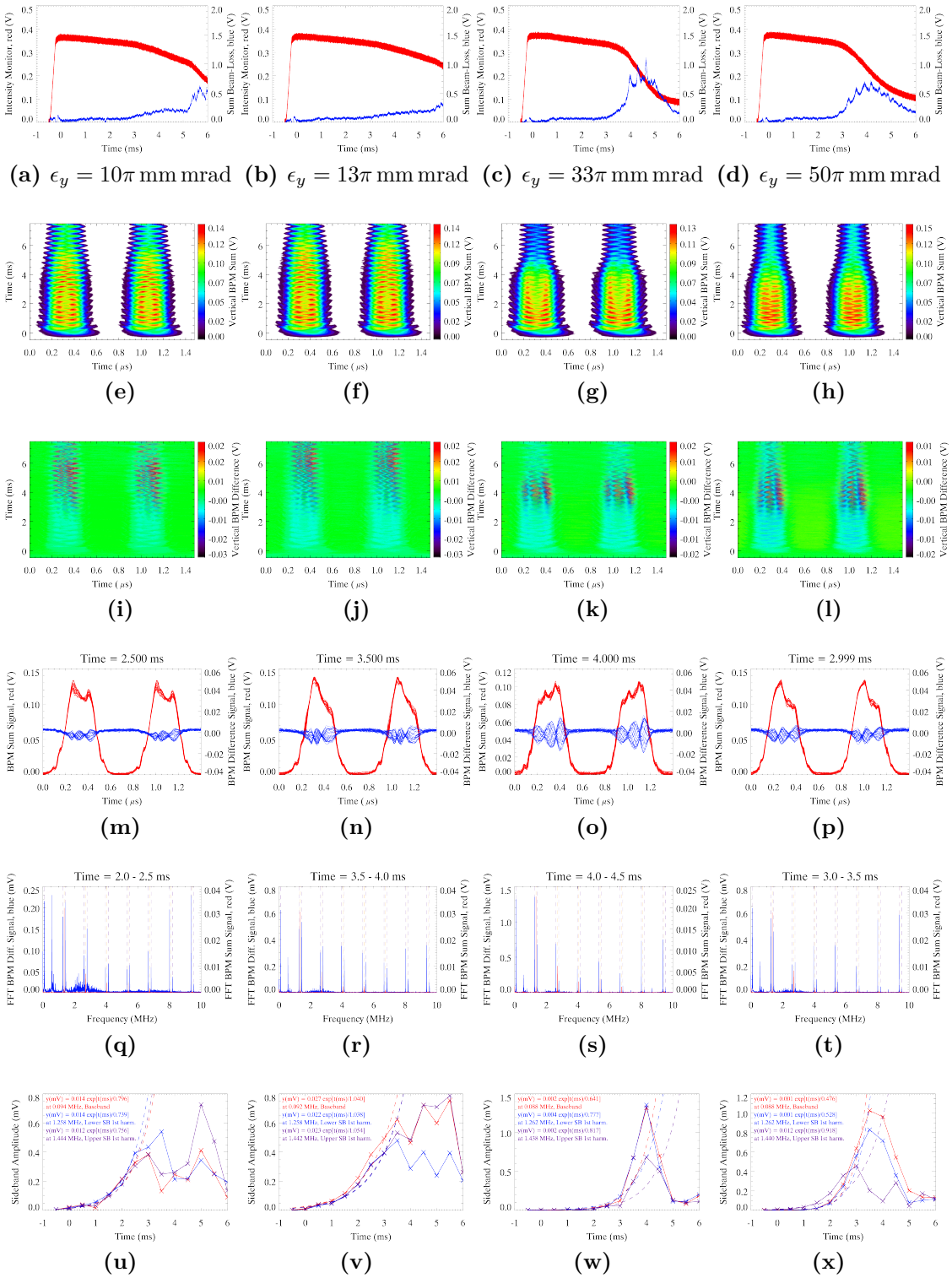
Figure 6.4: RMS vertical emittance of the painted beam as a function of the peak "vertical sweeper" current.

6.2 Head-Tail Instability as a Function of Vertical Beam Size

Each measurement is analysed in the same way as for the investigation into the head-tail instability as a function of vertical tune (section 5.4): categorising the instability by the intrabunch mode it excites, the bunch spectra in the frequency domain and the growth rate. Examining these characteristics in BSRM as a function of vertical beam size aims to deepen understanding of the instability dynamics and provides further comparators to theoretical predictions (see chapter 7).

As utilised in sections 4.2.2 and 5.4.4, by fitting exponential functions to the betatron sideband amplitudes as a function of time, growth rates may be determined for those sidebands. By changing the vertical tune, the frequencies of the betatron sidebands shift and probe different parts of the impedance spectrum. Therefore, beam measurements were made for different vertical tunes at each vertical beam size to measure the growth rate of the largest vertical betatron sidebands and examine the head-tail instability as a function of frequency as well as beam size.

Figures 6.5, 6.6 and 6.7 summarise these measurements for those vertical tunes and beam sizes that produced instability. Each figure illustrates four beam sizes spread across the measurement range for a fixed vertical tune. Each column of



(a) $\epsilon_y = 10\pi$ mm mrad (b) $\epsilon_y = 13\pi$ mm mrad (c) $\epsilon_y = 33\pi$ mm mrad (d) $\epsilon_y = 50\pi$ mm mrad

(e) (f) (g) (h)

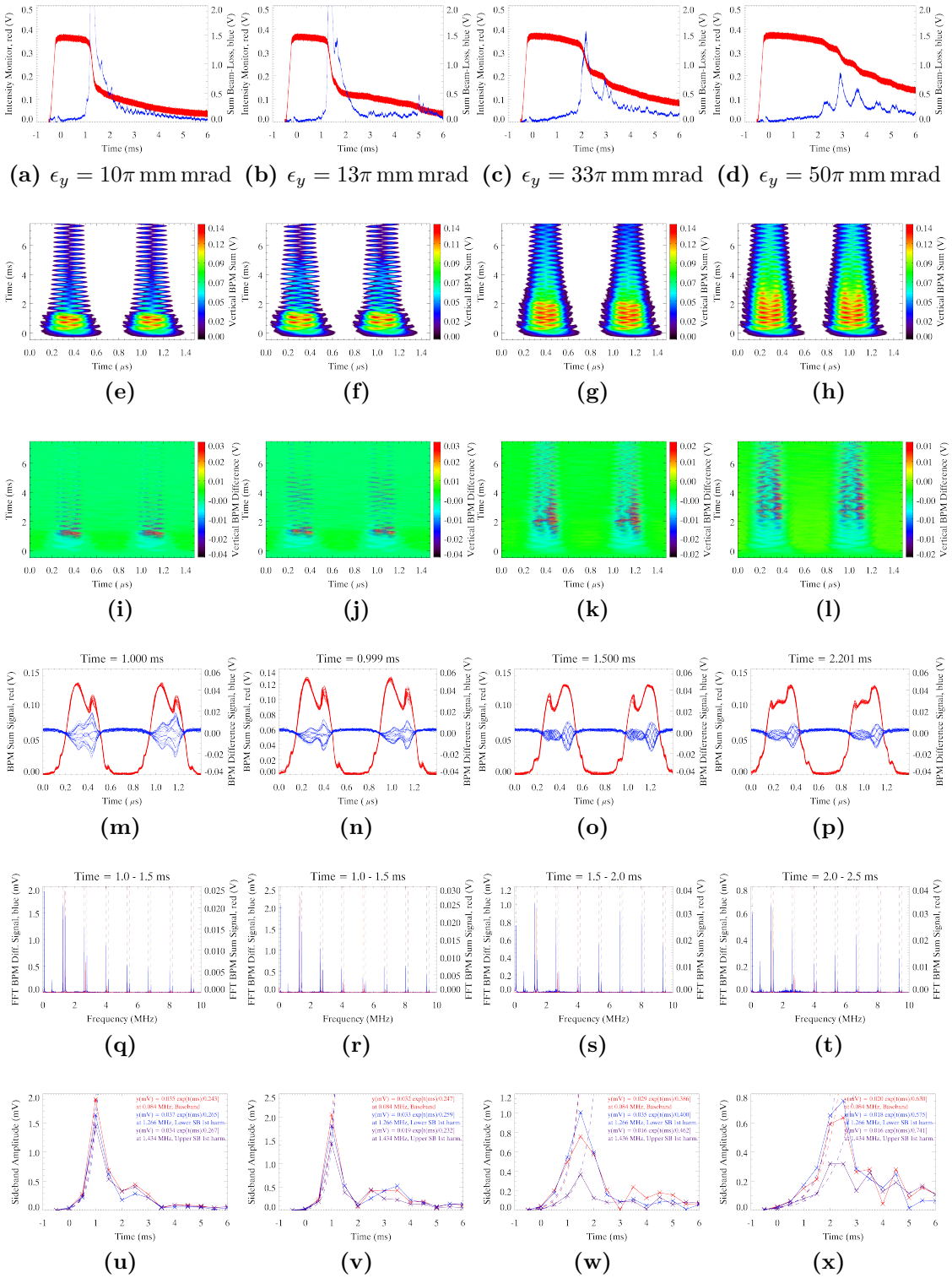
(i) (j) (k) (l)

(m) (n) (o) (p)

(q) (r) (s) (t)

(u) (v) (w) (x)

Figure 6.5: Experimental data from head-tail measurements with $Q_{y,\mathrm{set}} = 3.800$ ($Q_{y,\mathrm{meas}} = 3.867$) for different RMS vertical emittances (ϵ_y): intensity and beam-loss (a – d), vertical BPM sum signal over time (e – h), vertical BPM difference signal over time (i – l), BPM traces over 20 turns (m – p), FFT of BPM data around time of interest (q – t), growth rate fits to betatron sidebands (u – x).



(a) $\epsilon_y = 10\pi$ mm mrad **(b)** $\epsilon_y = 13\pi$ mm mrad **(c)** $\epsilon_y = 33\pi$ mm mrad **(d)** $\epsilon_y = 50\pi$ mm mrad

(e) **(f)** **(g)** **(h)**

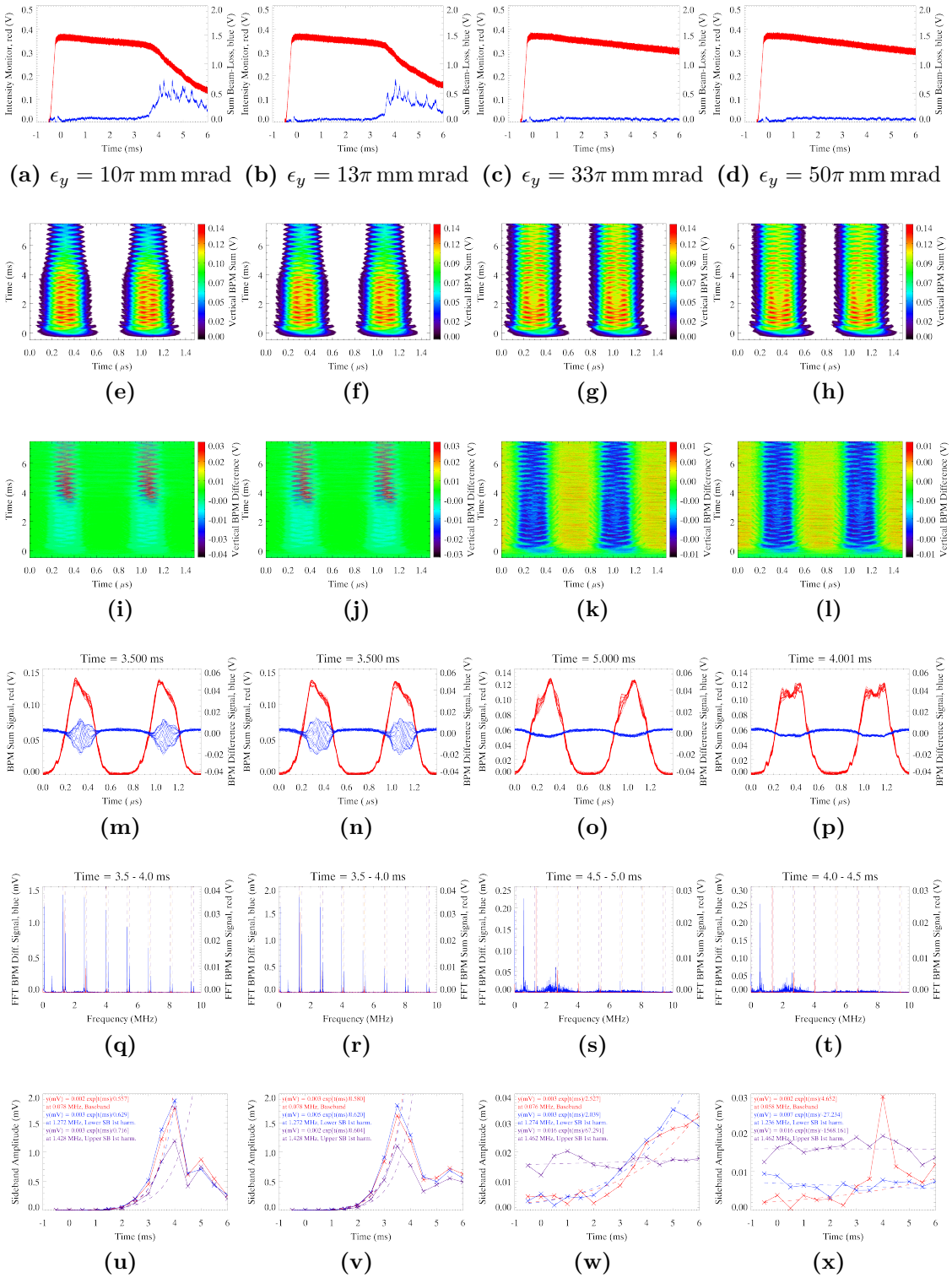
(i) **(j)** **(k)** **(l)**

(m) **(n)** **(o)** **(p)**

(q) **(r)** **(s)** **(t)**

(u) **(v)** **(w)** **(x)**

Figure 6.6: Experimental data from head-tail measurements with $Q_{y,\text{set}} = 3.810$ ($Q_{y,\text{meas}} = 3.876$) for different RMS vertical emittances (ϵ_y): intensity and beam-loss (a – d), vertical BPM sum signal over time (e – h), vertical BPM difference signal over time (i – l), BPM traces over 20 turns (m – p), FFT of BPM data around time of interest (q – t), growth rate fits to betatron sidebands (u – x).



(a) $\epsilon_y = 10\pi$ mm mrad **(b)** $\epsilon_y = 13\pi$ mm mrad **(c)** $\epsilon_y = 33\pi$ mm mrad **(d)** $\epsilon_y = 50\pi$ mm mrad

(e) **(f)** **(g)** **(h)**

(i) **(j)** **(k)** **(l)**

(m) **(n)** **(o)** **(p)**

(q) **(r)** **(s)** **(t)**

(u) **(v)** **(w)** **(x)**

Figure 6.7: Experimental data from head-tail measurements with $Q_{y,\mathrm{set}} = 3.820$ ($Q_{y,\mathrm{meas}} = 3.885$) for different RMS vertical emittances (ϵ_y): intensity and beam-loss (a – d), vertical BPM sum signal over time (e – h), vertical BPM difference signal over time (i – l), BPM traces over 20 turns (m – p), FFT of BPM data around time of interest (q – t), growth rate fits to betatron sidebands (u – x).

Table 6.2: Summary of head-tail instability characteristics in BSRM on ISIS as a function of vertical beam size for $Q_{y,\mathrm{set}} = 3.790$ and 3.800. $Q_{y,\mathrm{set}}$ and $Q_{y,\mathrm{meas}}$ = set and measured vertical tunes respectively, I_{VS} = peak "vertical sweeper" current, $\epsilon_{y,\ \mathrm{RMS}}$ = initial RMS vertical emittance, m = head-tail mode number, SB = largest amplitude betatron sideband, f_{BB} = baseband frequency, GR = growth rate of the baseband, $\tau_{\mathrm{b}} = 95\,\%$ bunch length, τ_{e} = effective bunch length and a figure reference for the data is given, if present.

$Q_{y,\mathbf{set}}$	$Q_{y,\mathbf{meas}}$	I_{VS} (A)	$\epsilon_{y,\ \mathrm{RMS}}$ (π mm mrad)	m	**SB**	$f_{\mathbf{BB}}$ **(kHz)**	**GR (turn^{-1})**	$\tau_{\mathbf{b}}$**(ns)**	$\tau_{\mathbf{e}}$**(ns)**	**Fig.**
3.790	3.861	14	10 ± 1	n/a	n/a	~94	$<1 \times 10^{-4}$	340	n/a	n/a
	3.861	17	12 ± 1	n/a	n/a	~94	$<1 \times 10^{-4}$	375	n/a	n/a
	3.861	20	13 ± 1	n/a	n/a	~94	$<1 \times 10^{-4}$	360	n/a	n/a
	3.861	23	20 ± 1	n/a	n/a	~94	$<1 \times 10^{-4}$	365	n/a	n/a
	3.861	26	23 ± 1	n/a	n/a	~94	$<1 \times 10^{-4}$	355	n/a	n/a
	3.861	29	33 ± 1	n/a	n/a	~94	$<1 \times 10^{-4}$	395	n/a	n/a
	3.861	31	38 ± 1	n/a	n/a	~94	$<1 \times 10^{-4}$	380	n/a	n/a
	3.861	33	46 ± 1	n/a	n/a	~94	$<1 \times 10^{-4}$	380	n/a	n/a
	3.861	35	50 ± 1	n/a	n/a	~94	$<1 \times 10^{-4}$	390	n/a	n/a
3.800	3.861	14	10 ± 1	2	LSB7	94 ± 2	$(1.86 \pm 0.31) \times 10^{-3}$	365	310	6.5a
	3.864	17	12 ± 1	2	BB	92 ± 2	$(2.47 \pm 0.25) \times 10^{-3}$	380	330	n/a
	3.864	20	13 ± 1	2	BB	92 ± 2	$(1.42 \pm 0.10) \times 10^{-3}$	365	360	6.5b
	3.867	23	20 ± 1	2	BB	90 ± 2	$(2.25 \pm 0.15) \times 10^{-3}$	340	355	n/a
	3.870	26	23 ± 1	2	BB	88 ± 2	$(2.11 \pm 0.23) \times 10^{-3}$	330	370	n/a
	3.870	29	33 ± 1	2	LSB1	88 ± 2	$(2.31 \pm 0.21) \times 10^{-3}$	345	380	6.5c
	3.867	31	38 ± 1	2	BB	90 ± 2	$(2.28 \pm 0.09) \times 10^{-3}$	365	345	n/a
	3.870	33	46 ± 1	2	BB	88 ± 2	$(2.12 \pm 0.28) \times 10^{-3}$	350	390	n/a
	3.870	35	50 ± 1	2	BB	88 ± 2	$(3.11 \pm 0.17) \times 10^{-3}$	350	340	6.5d

Table 6.3: Summary of head-tail instability characteristics in BSRM on ISIS as a function of vertical beam size for $Q_{y,\mathrm{set}} = 3.810$ and 3.820. $Q_{y,\mathrm{set}}$ and $Q_{y,\mathrm{meas}}$ = set and measured vertical tunes respectively, I_{VS} = peak "vertical sweeper" current, $\epsilon_{y,\ \mathrm{RMS}}$ = initial RMS vertical emittance, m = head-tail mode number, SB = largest amplitude betatron sideband, f_{BB} = baseband frequency, GR = growth rate of the baseband, $\tau_{\mathrm{b}} = 95\,\%$ bunch length, τ_{e} = effective bunch length and a figure reference for the data is given, if present.

$Q_{y,\mathbf{set}}$	$Q_{y,\mathbf{meas}}$	I_{VS} (A)	$\epsilon_{y,\ \mathrm{RMS}}$ (π mm mrad)	m	**SB**	$f_{\mathbf{BB}}$ **(kHz)**	**GR (turn^{-1})**	$\tau_{\mathbf{b}}$**(ns)**	$\tau_{\mathbf{e}}$**(ns)**	**Fig.**
3.810	3.876	14	10 ± 1	1	BB	84 ± 2	$(6.08 \pm 0.35)\times10^{-3}$	380	335	6.6a
	3.876	17	12 ± 1	1	BB	84 ± 2	$(6.40 \pm 0.41)\times10^{-3}$	400	325	n/a
	3.876	20	13 ± 1	1	BB	84 ± 2	$(6.01 \pm 0.21)\times10^{-3}$	370	340	6.6b
	3.873	23	20 ± 1	1	LSB1	86 ± 2	$(5.45 \pm 0.38)\times10^{-3}$	365	335	n/a
	3.879	26	23 ± 1	2	BB	82 ± 2	$(4.54 \pm 0.26)\times10^{-3}$	370	340	n/a
	3.876	29	33 ± 1	1	LSB1	84 ± 2	$(3.84 \pm 0.67)\times10^{-3}$	375	345	6.6c
	3.876	31	38 ± 1	1	LSB1	84 ± 2	$(4.54 \pm 0.27)\times10^{-3}$	360	325	n/a
	3.881	33	46 ± 1	1	LSB1	88 ± 2	$(3.28 \pm 0.36)\times10^{-3}$	355	350	n/a
	3.876	35	50 ± 1	1	LSB1	84 ± 2	$(2.35 \pm 0.27)\times10^{-3}$	360	350	6.6d
3.820	3.884	14	10 ± 1	0	LSB1	78 ± 2	$(2.66 \pm 0.18)\times10^{-3}$	360	310	6.7a
	3.884	17	12 ± 1	1	LSB1	78 ± 2	$(2.49 \pm 0.15)\times10^{-3}$	355	320	n/a
	3.884	20	13 ± 1	0	LSB1	78 ± 2	$(2.56 \pm 0.17)\times10^{-3}$	370	310	6.7b
	3.881	23	20 ± 1	0	LSB4	80 ± 2	$(1.08 \pm 0.06)\times10^{-3}$	330	300	n/a
	3.887	26	23 ± 1	1	LSB6	76 ± 2	$(1.20 \pm 0.08)\times10^{-3}$	375	315	n/a
	3.887	29	33 ± 1	1	LSB1	76 ± 2	$(5.86 \pm 1.31)\times10^{-4}$	365	310	6.7c
	3.887	31	38 ± 1	1	BB	76 ± 2	$(7.97 \pm 1.26)\times10^{-4}$	385	305	n/a
	3.887	33	46 ± 1	1	n/a	$\sim$76	$<1 \times 10^{-4}$	355	n/a	n/a
	3.887	35	50 ± 1	1	n/a	$\sim$76	$<1 \times 10^{-4}$	390	n/a	6.7d

Table 6.4: Summary of head-tail instability characteristics in BSRM on ISIS as a function of vertical beam size for $Q_{y,\mathrm{set}} = 3.830$. $Q_{y,\mathrm{set}}$ and $Q_{y,\mathrm{meas}}$ = set and measured vertical tunes respectively, I_{VS} = peak "vertical sweeper" current, $\epsilon_{y,\ \mathrm{RMS}}$ = initial RMS vertical emittance, m = head-tail mode number, SB = largest amplitude betatron sideband, f_{BB} = baseband frequency, GR = growth rate of the baseband, $\tau_{\mathrm{b}} = 95\,\%$ bunch length, τ_{e} = effective bunch length and a figure reference for the data is given, if present.

$Q_{y,\mathbf{set}}$	$Q_{y,\mathbf{meas}}$	I_{VS} (A)	$\epsilon_{y,\ \mathrm{RMS}}$ (π mm mrad)	m	**SB**	$f_{\mathbf{BB}}$ **(kHz)**	**GR (turn^{-1})**	$\tau_{\mathbf{b}}$**(ns)**	$\tau_{\mathbf{e}}$**(ns)**	**Fig.**
3.830	3.896	14	10 ± 1	n/a	n/a	~70	$<1 \times 10^{-4}$	355	n/a	n/a
	3.896	17	12 ± 1	n/a	n/a	~70	$<1 \times 10^{-4}$	380	n/a	n/a
	3.896	20	13 ± 1	n/a	n/a	~70	$<1 \times 10^{-4}$	370	n/a	n/a
	3.896	23	20 ± 1	n/a	n/a	~70	$<1 \times 10^{-4}$	350	n/a	n/a
	3.896	26	23 ± 1	n/a	n/a	~70	$<1 \times 10^{-4}$	355	n/a	n/a
	3.896	29	33 ± 1	n/a	n/a	~70	$<1 \times 10^{-4}$	375	n/a	n/a
	3.896	31	38 ± 1	n/a	n/a	~70	$<1 \times 10^{-4}$	365	n/a	n/a
	3.896	33	46 ± 1	n/a	n/a	~70	$<1 \times 10^{-4}$	380	n/a	n/a
	3.896	35	50 ± 1	n/a	n/a	~70	$<1 \times 10^{-4}$	385	n/a	n/a

graphs represents a single measurement for a given initial RMS vertical beam emittance with the particular aim to characterise the head-tail instability. The intensity and beam-loss signals, subfigures (a – d), illustrate the timing and quantity of beam-losses associated with the head-tail instability at each beam size. The BPM sum signals in subfigures (e – h) show the development of the longitudinal line density turn-by-turn. The BPM difference signals in subfigures (i – l) indicate the vertical coherent dipole offset along the bunch length turn-by-turn. These three graphs provide essential information, specifically regarding timings of when the head-tail instability develops (seen in the BPM difference signals) and when beam-loss occurs (in the IM and BLM signals).

The final three rows of graphs are key to characterising the head-tail instability by the intrabunch mode, its frequency spectra and the associated growth rate. The mode is observed in the BPM difference signal, subfigures (m – p), with 20 turns of BPM sum (red) and difference (blue) data overlaid at a time before peak beam-loss occurs. FFTs of 0.5 ms long segments of the BPM sum (red) and difference (blue) signals produce the frequency spectra in subfigures (q – t), timed to include the 20-turn BPM "snapshot". Also indicated in the spectra are the positions of the RF harmonics (dashed orange) and the betatron sidebands (dashed purple). Finally, the growth rate of the instability at each tune is determined by exponential fits to betatron sideband amplitudes as a function of time, subfigures (u – x). For the fit, sideband amplitudes are included up until peak beam-loss occurs which is also the peak in the sideband amplitude.

Although measurements cover the vertical tune range $Q_{y,\mathrm{set}} = 3.790 - 3.830$ (in 0.01 steps), figures 6.5, 6.6 and 6.7 only show results from the three vertical tunes that presented a head-tail instability. As in the vertical tune scan data (section 5.4), the fastest growth rates occurred at $Q_{y,\mathrm{set}} = 3.810$ for all beam sizes, apart from the largest at $\epsilon_{y,\mathrm{RMS}} = 50\pi$ mm mrad, where the growth rates for $Q_{y,\mathrm{set}} = 3.800$ and 3.810 are similar.

Key results of head-tail instability characteristics as a function of vertical tune are also listed in tables 6.2 – 6.4. This lists the set and measured vertical tune, the

peak "vertical sweeper" current and associated painted RMS vertical emittance, the intrabunch head-tail mode number (m), the largest amplitude (dominant) betatron sideband (BB is the baseband, LSB1 and USB1 are the lower and upper sidebands of the first RF harmonic, *etc.*), the frequency of the betatron baseband, the measured growth rate of the baseband, the 95 % bunch length ($\tau_{\mathrm{b},95\,\%}$), the length of the oscillating portion of the bunch (the effective bunch length, τ_{e}) and the first figure associated with each vertical tune. The effective bunch length is determined by adding the absolute value of twenty turns of BPM difference signal for one bunch around the time of interest and calculating the interval between the minima closest to the head and that closest to the tail. For some measurements no betatron sidebands could be discerned from the noise. In these cases the peak in the FFT of the BPM difference signal closest to the expected baseband frequency is given (signified by a "$\sim$" beforehand).

6.2.1 Head-Tail Instability Mode Structure

Figures 6.5(m – p), 6.6(m – p) and 6.7(m – p) show twenty turns of BPM sum and difference signals overlaid, taken just prior to instability induced beam-loss occurring. The envelope of the BPM difference signal illustrates the mode structure indicative of the head-tail instability. Consistent with previous measurements versus vertical tune (section 5.4.2), mode structures with two, one and zero nodes ($m = 2, 1$ and 0) were observed and the mode changed over a short tune range.

The mode structure appears consistent over the range of vertical beam sizes measured at $Q_{y,\mathrm{set}} = 3.800$ and 3.810. A head-tail mode $m = 2$ was observed at $Q_{y,\mathrm{set}} = 3.800$ (figure 6.5) and an asymmetric $m = 1$ at $Q_{y,\mathrm{set}} = 3.810$ (figure 6.6). Observed head-tail modes are listed in tables 6.2 – 6.4. At $Q_{y,\mathrm{set}} = 3.820$ (figure 6.7) the instability was only visible in the BPM difference signal at RMS vertical emittances below $33\,\pi$ mm mrad, and there described an $m = 0$ mode head-tail instability. Therefore, results at this tune suggest a threshold vertical beam size for stability: larger beams being stable.

As observed in measurements of the head-tail instability in BSRM as a function of vertical tune (section 5.4.2), the intrabunch oscillations only occupied a fraction of the full bunch length, leading to the concept of an effective bunch length. The fraction of the bunch length that was observed to oscillate was consistent if the lattice and bunch parameters are unchanged, however when the vertical tune or vertical beamsize was changed, the effective bunch length changed. Tables 6.2 – 6.4 include the 95 % bunch length (τ_b) and the effective bunch length (τ_e). There was also no observed threshold of longitudinal line density at which the instability began and therefore no way of predicting the fraction of the bunch length that will exhibit head-tail motion.

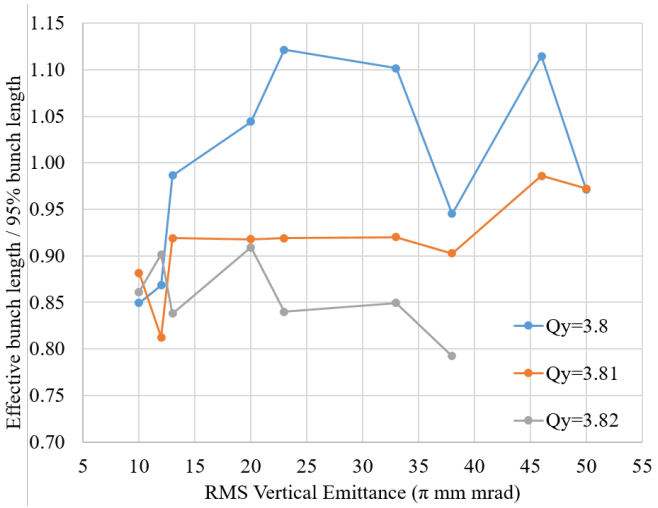


Figure 6.8: Ratio of the effective bunch length to the 95 % bunch length for $Q_{y,\mathrm{set}} = 3.800$ (blue), 3.810 (orange) and 3.820 (grey) versus RMS vertical emittance.

Figure 6.8 shows the ratio of the effective bunch length to the 95 % bunch length for the three tunes that exhibited a head-tail instability. Fractions of greater than one are possible because the full effective bunch length is used whereas the 95 % bunch length was chosen as it was a more reliable measure of bunch length than the full, 100 % length due to noise in the BPM signals. It is observed that higher-order structures exhibit intrabunch oscillations that make up a larger fraction of the bunch length and $m = 0$ head-tail instabilities show the lowest fraction of the bunch length oscillating.

6.2.2 Head-Tail Instability in Frequency Domain

Further information may be gained by looking at the BPM difference signal in the frequency domain using an FFT, as shown in figures 6.5(q – t), 6.6(q – t) and 6.7(q – t). This reveals the transverse frequencies present in the bunch, most notably the betatron sidebands. These data were analysed in the same way as for the vertical tune scan data (section 5.4), with the FFTs performed over 0.5 ms portions of the BPM data.

Measurement of the RF frequency from an FFT of the BPM sum signal, and the betatron sideband frequencies, allow the calculation of the fractional part of the betatron tune. As the vertical tune was increased, the baseband frequency decreased as anticipated. There was no dependence of baseband frequency on vertical beam size, as expected. As discovered in the vertical tune scan data, there were differences between the measured betatron tune and that set on the accelerator control system, particularly away from the design intensity of the accelerator. The measured and set vertical tunes are listed in tables 6.2 – 6.4.

Each betatron sideband's amplitude provides information about the amount of energy in that oscillation frequency. A stable, centred beam (in the chosen transverse plane) will exhibit little or no transverse motion on a BPM difference signal and the associated FFT will have no, or very small, betatron sidebands present. Typically, betatron sidebands are observed during the multiturn injection process as it is inherently non-linear, but will then damp out once the distribution has been painted and the beam aligned to the centre of the beam pipe. For the case of instabilities, the largest betatron sideband, or the fastest growing, is assumed to be dominant. By scanning the betatron tune (vertically in this case), the frequency dependence of the the head-tail driving impedance may be deduced.

In the majority of cases, the largest amplitude and fastest growing betatron sideband was at the lowest frequency (the baseband). In those cases where it was not, it was the second largest. The large, fast-growing baseband confirmed previous coasting beam and bunched beam, vertical tune scan measurements indicating a driving impedance that peaked at low frequency. The FFT of the BPM difference

signal showed sidebands excited up to 15 MHz in many cases. The betatron sidebands decreased in amplitude with frequency until approximately the vertical chromatic frequency listed in table 6.1. Above this frequency, the sidebands continued decreasing in amplitude for head-tail instabilities with mode zero ($m = 0$). However, for higher-order mode instabilities the betatron sidebands increased in amplitude above the vertical chromatic frequency, reaching a second peak whose frequency is dependent on the mode number excited.

For mode one, $m = 1$, observed at $Q_{y,\mathrm{set}} = 3.810$ (figure 6.6), there was a second peak in betatron sideband amplitude around 6.5 MHz, most noticeably for larger beam sizes. Similarly for mode two, $m = 2$, observed at $Q_{y,\mathrm{set}} = 3.800$ (figure 6.5), the sidebands peaked at baseband as well as around 9.5 MHz. This is expected, as the higher-order mode structures oscillate at higher frequencies, corresponding to standing waves along the bunch length.

It should be noted that there was a small amount of noise on the BPM difference signal at specific frequencies, noticeably at $Q_{y,\mathrm{set}} = 3.820$ and $\epsilon_{y,\mathrm{RMS}} = 33\,\pi$ and $50\,\pi$ mm mrad, figures 6.7(s, t). The largest noise component was observed at approximately 560 kHz and was present with or without beam. This, and the "forest" of peaks between 1.5 and 3.5 MHz, were due to pick-up from magnet power supplies in the synchrotron.

6.2.3 Head-Tail Instability Growth Rate Versus Frequency and Beam Size

The exponential growth time (shown in subfigures (u – x) of figures 6.5 – 6.7) for each baseband was converted to a growth rate ($1/(\tau f_{\mathrm{rev}})$ and is listed in tables 6.2 – 6.4) and plotted as a function of the measured baseband frequency for the four sample vertical beam sizes, see figure 6.9. The error bars are the one-sigma uncertainty estimates from the exponential fit to the baseband growth and the frequency resolution of the FFT. Reference lines are shown for specific growth rates (one oscillation every 150, 250, 500 and 1000 turns) as well as the synchrotron tune, Q_s.

Figure 6.9 shows that the instability growth rates for different vertical beam sizes were very similar functions of the baseband frequency. The figure also shows

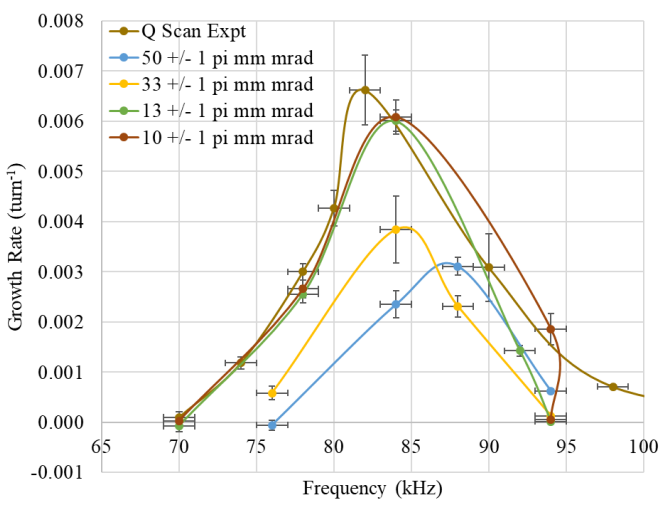


Figure 6.9: Instability growth rate versus betatron BB frequency for only those beam sizes shown in the previous figures ($\epsilon_{y,\,\mathrm{RMS}} = 10$, 13, 33 and $50\,\pi$ mm mrad). Previous vertical tune scan measurements (figure 5.11) are also shown in light brown.

the growth rate for "Set 1" of the vertical tune scan data (section 5.4.4), which was also a comparable function of the baseband frequency. It should be noted "Set 1" used I_{VS} =20 A (corresponding to $\sim$13 π mm mrad) and the bunch intensity was slightly higher (1.68×10^{12} ppb). The growth rate peaked between 80 and 90 kHz at a vertical tune of $Q_{y,\mathrm{set}} = 3.810$, further confirming a narrowband beam coupling impedance with a quality factor of around 10. However, the amplitude of the peak appeared to be a function of the vertical beam size, with the peak growth rate reducing as the vertical beam size was increased. Figure 6.10 illustrates this behaviour with 3D surface and contour graphs of the instability growth rate as a function of the vertical betatron tune and the RMS vertical emittance.

The variation of growth rate as a function of RMS vertical emittance at fixed vertical tunes is shown in figure 6.11. For $Q_{y,\mathrm{set}} = 3.810$ and 3.820 the growth rate was observed to reduce with increasing beam size, whereas at $Q_{y,\mathrm{set}} = 3.800$ (which was consistently mode $m = 2$) the growth rate was relatively flat as a function of vertical beam size. The decrease in growth rate with increasing vertical beam size appeared most notably at a vertical tune of 3.810, reducing from 6.4×10^{-3} turn^{-1} at $\epsilon_{y,\,\mathrm{RMS}} = 12\,\pi$ mm mrad to 2.4×10^{-3} turn^{-1} at $50\,\pi$ mm mrad.

The instability growth rate at $Q_y = 3.820$ was negligible above an emittance of $33\,\pi$ mm mrad. Below this emittance the growth rate increased from 1.2×10^{-3} to

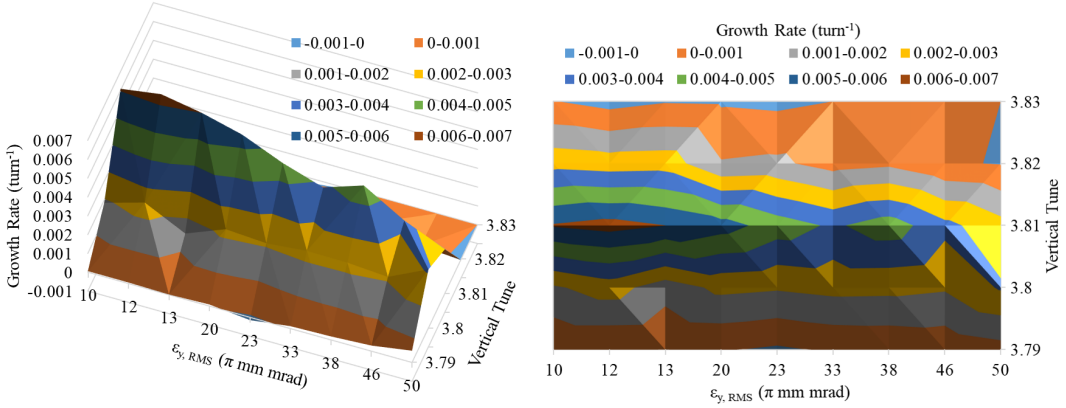


Figure 6.10: Instability growth rate versus RMS vertical emittance and vertical tune shown as (a) a 3D surface graph and (b) a contour graph.

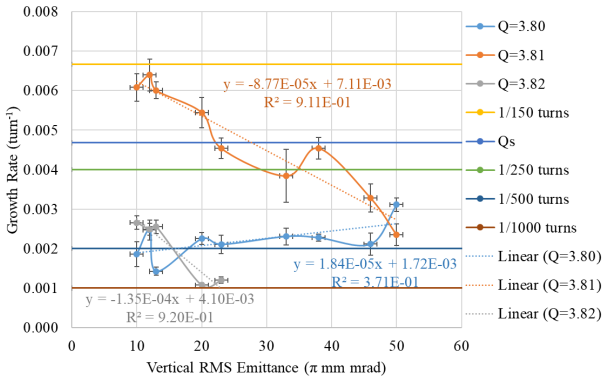


Figure 6.11: Instability growth rate as a function of RMS vertical emittance.

2.7×10^{-3} turn^{-1} as the emittance was reduced from $23\,\pi$ to $10\,\pi$ mm mrad. As shown in figure 6.11, a least-squares linear fit represented the change in growth rate with vertical beam size trend well for both $Q_{y,\mathrm{set}} = 3.810$ and 3.820, with R^2 values close to one. At both these tunes, the change in growth rate with emittance was approximately -1×10^{-4} turn$^{-1}(\pi\,\mathrm{mm\,mrad})^{-1}$. For $Q_{y,\mathrm{set}} = 3.800$ there was a small opposite trend (larger beams becoming more unstable) but the growth rates were still small in the range of beam sizes measured and the gradient much shallower at $\sim 2 \times 10^{-5}$ turn$^{-1}(\pi\,\mathrm{mm\,mrad})^{-1}$. The R^2 fitting parameter for this tune was also much lower suggesting the data was not well represented by a linear function. It was noted that the growth rate at $Q_{y,\mathrm{set}} = 3.810$ was above the synchrotron tune, Q_s, for vertical RMS emittances of $20\,\pi$ mm mrad and below.

6.3 Simulations of Head-Tail as a Function of Vertical Beam Size

6.3.1 Setup and Introduction

In order to study the head-tail instability dynamics observed on ISIS in more detail and, in particular, the instability's behaviour with vertical beam size, a model of the synchrotron was built in PyHEADTAIL [70]. As described in section 3.5.1, this code performs particle tracking and wake field calculations to simulate the effect of applied impedances on beam dynamics, including instability and models of transverse space charge.

As in the previous chapter, the simulations were built to replicate, as close as practically possible, the synchrotron and beam parameters as measured in the experiments. Many parameters were the same as in the previous chapter (section 5.5.1), including the driving impedance, beam distribution (transverse 4D waterbag and uncorrelated longitudinal 2D parabolic distributions) and simulation specific parameters which were chosen to give convergent behaviour whilst allowing for reasonable simulation time.

Table 6.5 lists the parameters that define the simulated beam, the accelerator and internal parameters chosen for convergence. ISIS specific parameters (such as the machine radius and γ_t) are included in table 2.1. The simulation specific parameters listed in table 6.5 were chosen for computational convergence, with details given in the previous chapter (section 5.5.1.2).

6.3.1.1 Beam and Lattice Parameters

The bunch intensity, RF voltage and betatron tunes selected were those utilised in the measurements shown above. As in PyHEADTAIL simulations for the previous chapter (section 5.5), simulations began with a fully formed bunch distribution (injection processes are not simulated) enabling favourable comparison with experimental measurements from $\sim$1 ms (after the RF voltage ramp, figure 6.1). Hence, the RF voltage was held constant in the simulations. The betatron tunes were also held constant throughout, as they were during the experiment.

Table 6.5: Key simulation parameters for comparison with BSRM measurements of the head-tail instability as a function of vertical beam size.

Parameter	**Symbol**	**Value**
Bunch intensity	N	1.47×10^{12} ppb
RF voltage	V_{RF}	11.4 kV per turn
Betatron tunes	Q_x, Q_y	4.31, 3.84 – 3.92
Revolution frequency	f_{rev}	677.8 kHz
Relativistic beta	β	0.3694
Relativistic gamma	γ	1.0761
Slip factor	η	-0.8241
Synchrotron tune	$Q_s = \sqrt{\frac{V_{RF}\eta h \cos\phi_s}{2\pi\beta^2 E_T}}$	4.659×10^{-3}
Vertical chromatic frequency	$f_{\xi,y} = \xi_y f_{\mathrm{rev}} Q_y/\eta$	4.42 – 4.51 MHz
Machine aperture	$x_{\mathrm{aper}}, y_{\mathrm{aper}}$	$\pm$ 81.6 mm, $\pm$ 63.9 mm
Horizontal emittance (RMS)	$\epsilon_{x,\mathrm{RMS}}$	$50\,\pi$ mm mrad
Vertical emittance (RMS)	$\epsilon_{y,\mathrm{RMS}}$	$10\,\pi$ – $50\,\pi$ mm mrad
Beam distribution	$\rho_{x,y}$, λ	4D waterbag, 2D parabolic
Bunch length (RMS)	$\sigma_{z,\mathrm{RMS}}$	10.5 m
Resonator frequency	f_{res}	82 kHz
Resonator quality factor	Q_{res}	10
Resonator shunt impedance	R_s	17.2 or 3.44 kΩ m^{-2}
Number of turns		2×10^3
Number of macroparticles		2×10^6
Number of PIC nodes (x, y, z)		$64 \times 64 \times 64$
Number of longitudinal slices		128
Number of wake turns		200

As the experiment was performed in BSRM, this dictated the revolution frequency, relativistic parameters and slip factor. The synchrotron tune and chromatic frequency were calculated from the values in table 6.5. As described in section 2.1.2, the beam pipe aperture changes around the synchrotron, following the design beam envelope. However, to simplify the simulations and try and replicate beam-loss and beam intensity as a function of time, a collimated aperture was fixed at the average horizontal and vertical apertures. The narrowband resonator impedance characteristics (frequency, quality factor and shunt impedance) were selected to replicate the observed head-tail instability growth rate as a function of frequency.

Residual gas ionisation monitor profiles were measured for each "vertical sweeper" setting. The profiles were corrected for drift field and space charge errors, and these corrected profiles were matched by visual inspection to represent the measured

distribution in the stored bunched beams closely. A 4D waterbag was found to correspond to the measured transverse profile (figure 6.12 shows comparisons between the simulated and measured transverse distributions for two example "vertical sweeper" settings). The RMS emittance of these distributions, and their variation with "vertical sweeper" setting, are given in tables 6.2 – 6.4 and shown in figure 6.4. Simulations covered the full range of measured RMS emittances ($10\,\pi$ – $50\,\pi$ mm mrad) in $5\,\pi$ mm mrad steps.

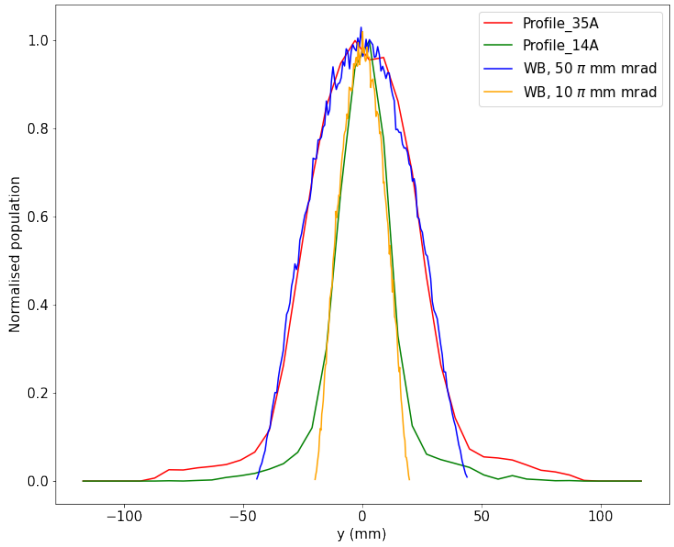


Figure 6.12: Simulated transverse waterbag distributions (blue, yellow for $50\,\pi$ and $10\,\pi$ mm mrad respectively) compared to vertical IPM measurements, corrected for drift field and space charge distortions (red, green at $I_{\mathrm{VS}} = 35$ and 14 A respectively).

In the longitudinal plane a parabolic distribution closely represented the measured distribution from the BPM sum signal. The longitudinal distribution was also deliberately mismatched to 75 % of the RF voltage, with a dipole shift of 2 m, to give similar dipole and quadrupole bunch oscillations to those observed in the experiment (simulated and measured longitudinal profiles are compared in figure 5.12).

6.3.2 Simulations Without Transverse Space Charge

In order to study the effect of space charge on head-tail instability characteristics (growth rate, mode number, *etc.*), simulations were performed with longitudinal space charge but without the transverse PIC space charge solver. It should be noted that the applied narrowband resonator impedance is independent of the beam size.

In order to compare better with the experimentally observed growth rates, the resonator shunt impedance was set to $17.2\,\mathrm{k\Omega\,m^{-2}}$. An example output from a simulation with $Q_y = 3.880$, and an initial $\epsilon_{y,\mathrm{RMS}} = 10\,\pi\,\mathrm{mm\,mrad}$ is shown in figures 6.13 and 6.14. Betatron sidebands up to 15 MHz are shown as a function of time in figure 6.14a.

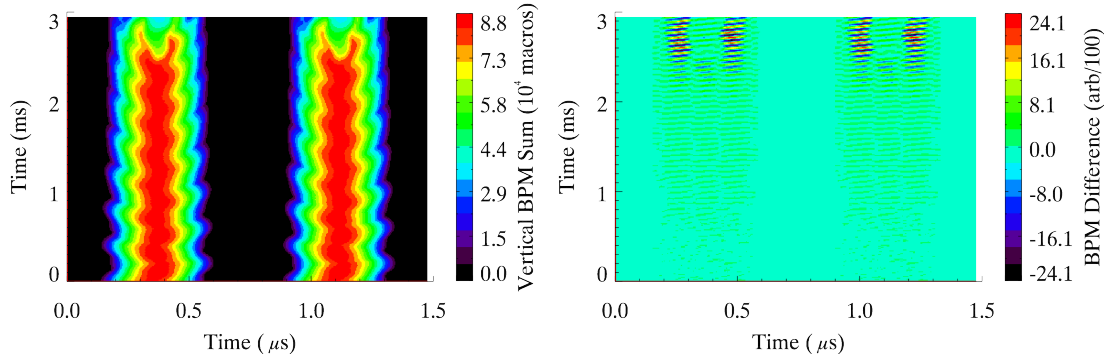


Figure 6.13: Simulated vertical BPM sum signal (a) and difference signal (b) sliced to show each turn against time ($Q_y = 3.880$, $\epsilon_{y,\mathrm{RMS}} = 10\,\pi\,\mathrm{mm\,mrad}$, without transverse space charge).

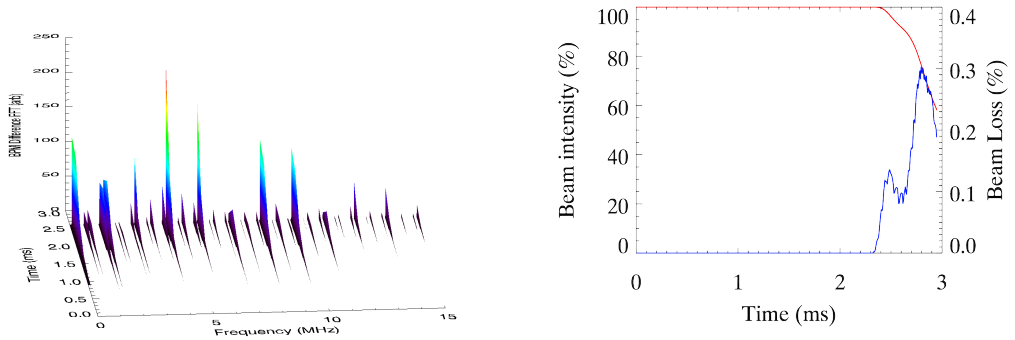


Figure 6.14: a) FFT of the simulated BPM difference signal from figure 6.13 versus time and b) simulated IM and BLM sum signals versus time ($Q_y = 3.880$, $\epsilon_{y,\mathrm{RMS}} = 10\,\pi\,\mathrm{mm\,mrad}$, without transverse space charge).

The simulated BPM difference signal (figure 6.13b) shows that the mode number changed as beam was lost through collimation. As in previous datasets, figure 6.15 focuses on the BPM difference signal over 20 turns before beam was lost and the vertical emittance had grown beyond 2 % (see beam intensity and loss, figure 6.14b).

At this time, the instability appears to be a mode $m = 3$ with three nodes along the bunch's length and an asymmetry with larger transverse motion toward the tail of the bunch.

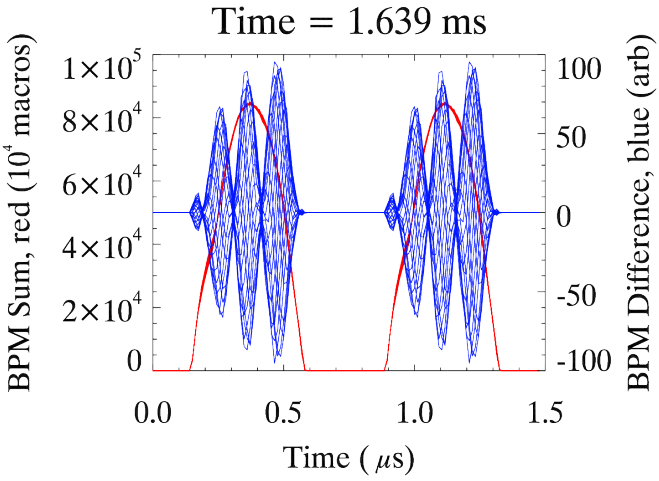
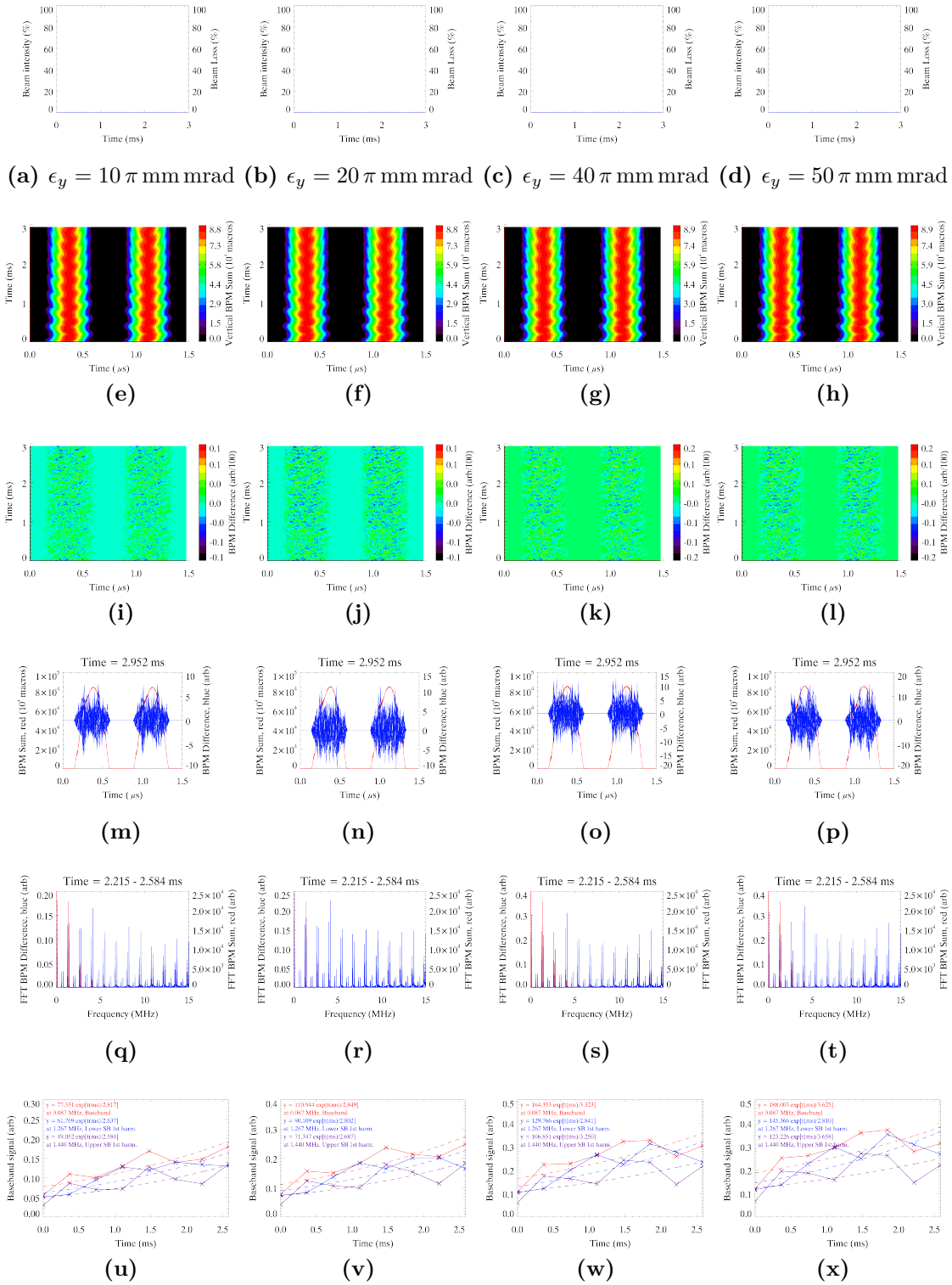


Figure 6.15: Simulated vertical BPM sum signal (blue) and difference signal (red) over 20 turns, after 1.64 ms of wakes showing both bunches (head on the left, tail on the right, $Q_y = 3.880$, $\epsilon_{y,\mathrm{RMS}} = 10\,\pi$ mm mrad, without transverse space charge).

Figures 6.16 – 6.20 summarise the PyHEADTAIL simulation results without transverse space charge for $Q_y = 3.860$ – 3.900 as a function of vertical emittance. The results are summarised in tables 6.6 – 6.8. The simulated data were processed in the same way as for the measurements presented in section 6.2. Simulations were also analysed for vertical tunes either side of this range ($Q_y = 3.840$ – 3.920) but resulted in far slower or negligible instability growth rates. The figures only show a representative sample of vertical beam sizes simulated with data produced for vertical emittances between $10\,\pi$ – $50\,\pi$ mm mrad in $5\,\pi$ mm mrad steps.

6.3.2.1 Head-Tail Instability Mode Structure

Figures 6.16 to 6.20 include a 20 turn overlay of the simulated BPM difference signals, subfigures (m – p), at the point when the vertical emittance had grown by 2 % for each vertical tune and emittance setting. The observed modes are listed in tables 6.6 – 6.8. These indicated a consistent mode structure for a given vertical tune as the vertical beam size was altered, in agreement with experiment (section 6.2.1).



(a) $\epsilon_y = 10\,\pi$ mm mrad **(b)** $\epsilon_y = 20\,\pi$ mm mrad **(c)** $\epsilon_y = 40\,\pi$ mm mrad **(d)** $\epsilon_y = 50\,\pi$ mm mrad

(e) **(f)** **(g)** **(h)**

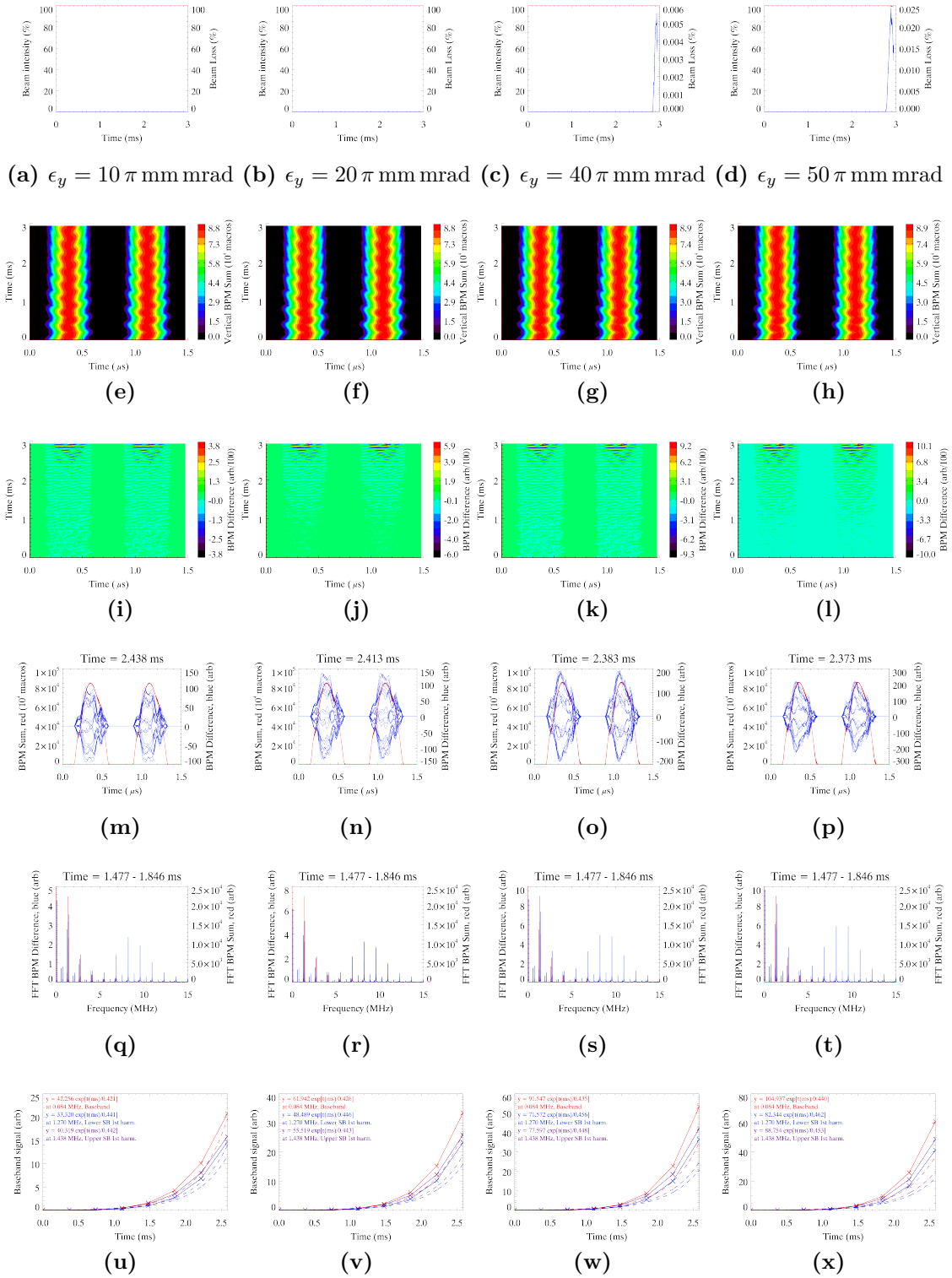
(i) **(j)** **(k)** **(l)**

(m) **(n)** **(o)** **(p)**

(q) **(r)** **(s)** **(t)**

(u) **(v)** **(w)** **(x)**

Figure 6.16: PyHEADTAIL simulation output without transverse space charge for different vertical beam emittances at $Q_y = 3.860$: intensity and beam-loss (a – d), longitudinal bunch population over time (e – h), simulated vertical BPM difference over time (i – l), simulated vertical BPM traces over 20 turns (m – p), FFT of simulated BPM data around time point of interest (q – t), growth rate fits to betatron sidebands (u – x).



(a) $\epsilon_y = 10\,\pi$ mm mrad (b) $\epsilon_y = 20\,\pi$ mm mrad (c) $\epsilon_y = 40\,\pi$ mm mrad (d) $\epsilon_y = 50\,\pi$ mm mrad

(e) (f) (g) (h)

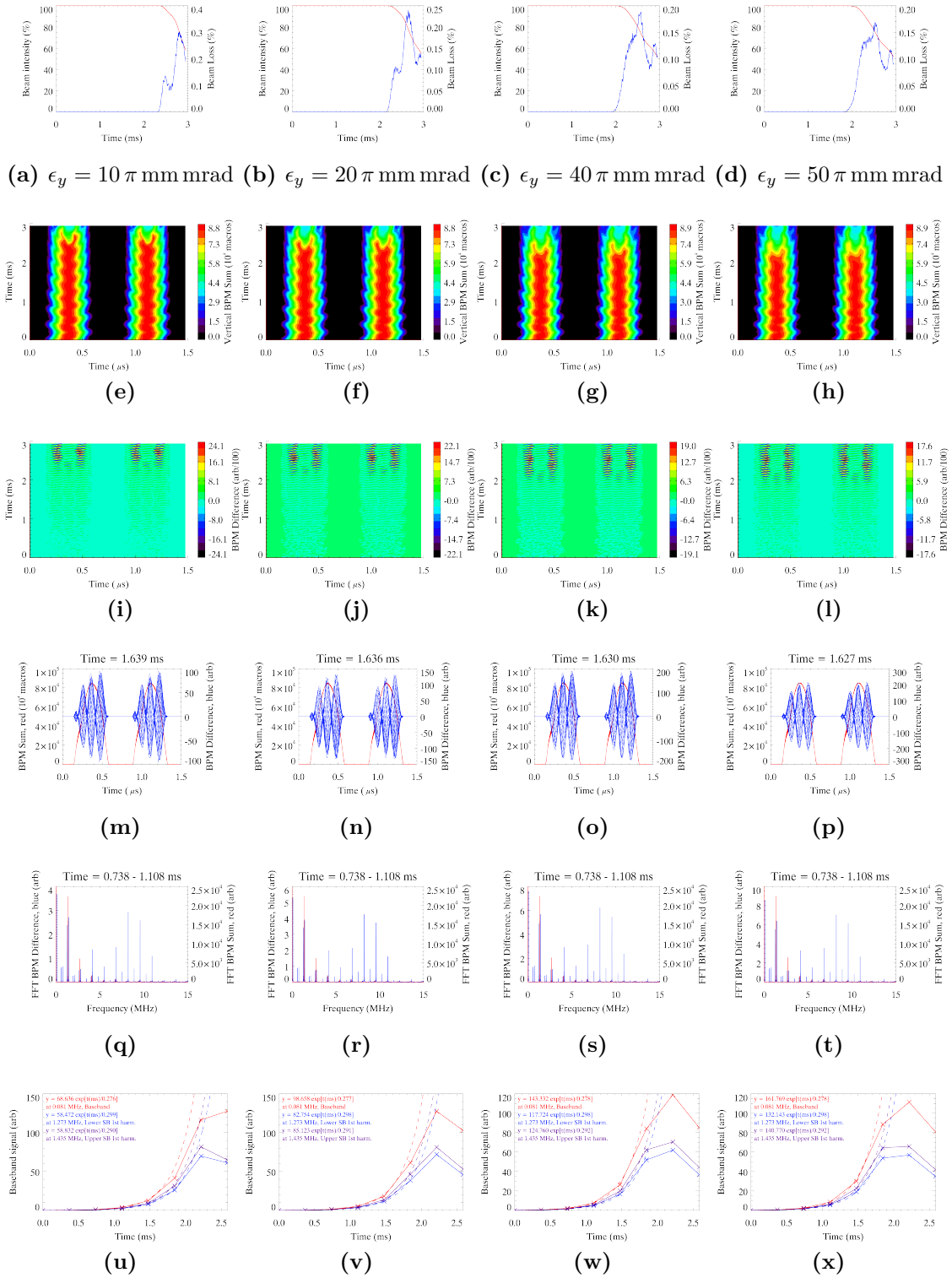
(i) (j) (k) (l)

(m) (n) (o) (p)

(q) (r) (s) (t)

(u) (v) (w) (x)

Figure 6.17: PyHEADTAIL simulation output without transverse space charge for different vertical beam emittances at $Q_y = 3.870$: intensity and beam-loss (a – d), longitudinal bunch population over time (e – h), simulated vertical BPM difference over time (i – l), simulated vertical BPM traces over 20 turns (m – p), FFT of simulated BPM data around time point of interest (q – t), growth rate fits to betatron sidebands (u – x).



(a) $\epsilon_y = 10\,\pi$ mm mrad **(b)** $\epsilon_y = 20\,\pi$ mm mrad **(c)** $\epsilon_y = 40\,\pi$ mm mrad **(d)** $\epsilon_y = 50\,\pi$ mm mrad

(e) **(f)** **(g)** **(h)**

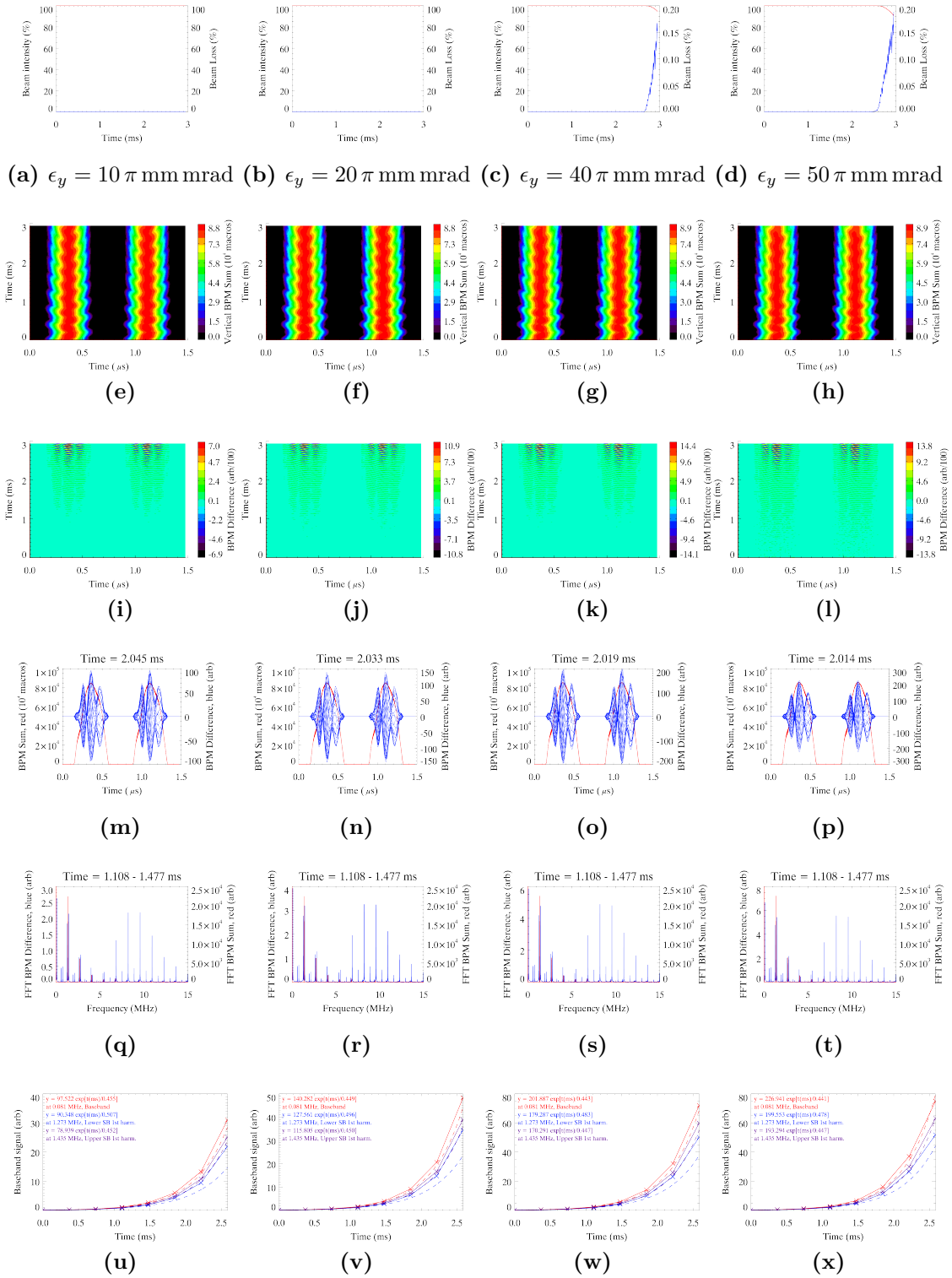
(i) **(j)** **(k)** **(l)**

(m) **(n)** **(o)** **(p)**

(q) **(r)** **(s)** **(t)**

(u) **(v)** **(w)** **(x)**

Figure 6.18: PyHEADTAIL simulation output without transverse space charge for different vertical beam emittances at $Q_y = 3.880$: intensity and beam-loss (a – d), longitudinal bunch population over time (e – h), simulated vertical BPM difference over time (i – l), simulated vertical BPM traces over 20 turns (m – p), FFT of simulated BPM data around time point of interest (q – t), growth rate fits to betatron sidebands (u – x).



(a) $\epsilon_y = 10\,\pi$ mm mrad **(b)** $\epsilon_y = 20\,\pi$ mm mrad **(c)** $\epsilon_y = 40\,\pi$ mm mrad **(d)** $\epsilon_y = 50\,\pi$ mm mrad

(e) **(f)** **(g)** **(h)**

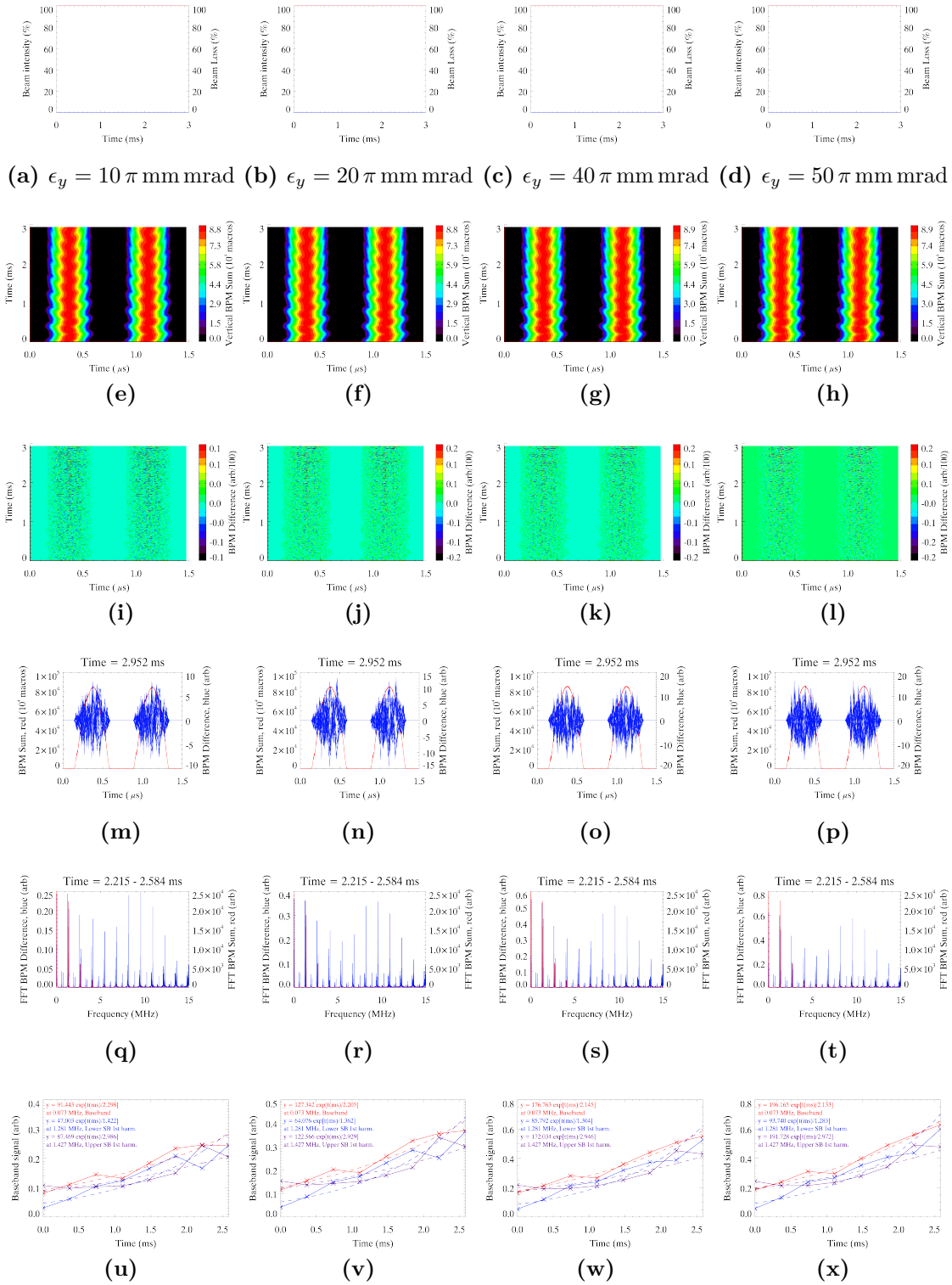
(i) **(j)** **(k)** **(l)**

(m) **(n)** **(o)** **(p)**

(q) **(r)** **(s)** **(t)**

(u) **(v)** **(w)** **(x)**

Figure 6.19: PyHEADTAIL simulation output without transverse space charge for different vertical beam emittances at $Q_y = 3.890$: intensity and beam-loss (a – d), longitudinal bunch population over time (e – h), simulated vertical BPM difference over time (i – l), simulated vertical BPM traces over 20 turns (m – p), FFT of simulated BPM data around time point of interest (q – t), growth rate fits to betatron sidebands (u – x).



(a) $\epsilon_y = 10\,\pi$ mm mrad **(b)** $\epsilon_y = 20\,\pi$ mm mrad **(c)** $\epsilon_y = 40\,\pi$ mm mrad **(d)** $\epsilon_y = 50\,\pi$ mm mrad

(e) **(f)** **(g)** **(h)**

(i) **(j)** **(k)** **(l)**

(m) **(n)** **(o)** **(p)**

(q) **(r)** **(s)** **(t)**

(u) **(v)** **(w)** **(x)**

Figure 6.20: PyHEADTAIL simulation output without transverse space charge for different vertical beam emittances at $Q_y = 3.900$: intensity and beam-loss (a – d), longitudinal bunch population over time (e – h), simulated vertical BPM difference over time (i – l), simulated vertical BPM traces over 20 turns (m – p), FFT of simulated BPM data around time point of interest (q – t), growth rate fits to betatron sidebands (u – x).

Table 6.6: Summary of head-tail instability characteristics in PyHEADTAIL simulation results as a function of vertical beam size for $Q_y = 3.860$ and 3.870, without transverse space charge. Q_y and $Q_{y,\mathrm{meas}}$ = set and measured vertical tunes respectively, $\epsilon_{y,\mathrm{RMS}}$ = RMS vertical emittance, m = head-tail mode number, SB = largest amplitude betatron sideband, f_{BB} = BB frequency, GR = BB growth rate, $\tau_{\mathrm{b}} = 95\,\%$ bunch length, a figure reference is given, if present.

Q_y	$Q_{y,\mathbf{meas}}$	$\epsilon_{y,\ \mathrm{RMS}}$ (π mm mrad)	m	**SB**	$f_{\mathbf{BB}}$ **(kHz)**	**GR (turn^{-1})**	$\tau_{\mathbf{b}}$**(ns)**	**Fig.**
3.860	3.872	10	n/a	BB	86.7 ± 2.7	$(5.24 \pm 1.31)\times10^{-4}$	345	6.16a
	3.872	15	n/a	BB	86.7 ± 2.7	$(5.31 \pm 1.33)\times10^{-4}$	345	n/a
	3.872	20	n/a	BB	86.7 ± 2.7	$(5.18 \pm 1.34)\times10^{-4}$	345	6.16b
	3.872	25	n/a	BB	86.7 ± 2.7	$(5.07 \pm 1.38)\times10^{-4}$	344	n/a
	3.872	30	n/a	BB	86.7 ± 2.7	$(4.93 \pm 1.44)\times10^{-4}$	344	n/a
	3.872	35	n/a	BB	86.7 ± 2.7	$(4.69 \pm 1.50)\times10^{-4}$	344	n/a
	3.872	40	n/a	USB3	86.7 ± 2.7	$(4.44 \pm 1.57)\times10^{-4}$	344	6.16c
	3.872	45	n/a	USB3	86.7 ± 2.7	$(4.27 \pm 1.64)\times10^{-4}$	342	n/a
	3.872	50	n/a	USB3	86.7 ± 2.7	$(4.07 \pm 1.70)\times10^{-4}$	342	6.16d
3.870	3.876	10	0	BB	84.0 ± 2.7	$(3.51 \pm 0.33)\times10^{-3}$	348	6.17a
	3.876	15	0	BB	84.0 ± 2.7	$(3.49 \pm 0.33)\times10^{-3}$	347	n/a
	3.876	20	0	BB	84.0 ± 2.7	$(3.47 \pm 0.34)\times10^{-3}$	347	6.17b
	3.876	25	0	BB	84.0 ± 2.7	$(3.45 \pm 0.34)\times10^{-3}$	345	n/a
	3.876	30	0	BB	84.0 ± 2.7	$(3.43 \pm 0.34)\times10^{-3}$	345	n/a
	3.876	35	0	BB	84.0 ± 2.7	$(3.41 \pm 0.34)\times10^{-3}$	344	n/a
	3.876	40	0	BB	84.0 ± 2.7	$(3.40 \pm 0.34)\times10^{-3}$	344	6.17c
	3.876	45	0	BB	84.0 ± 2.7	$(3.37 \pm 0.34)\times10^{-3}$	344	n/a
	3.876	50	0	BB	84.0 ± 2.7	$(3.36 \pm 0.34)\times10^{-3}$	342	6.17d

Table 6.7: Summary of head-tail instability characteristics in PyHEADTAIL simulation results as a function of vertical beam size for $Q_y = 3.880$ and 3.890, without transverse space charge. Q_y and $Q_{y,\mathrm{meas}}$ = set and measured vertical tunes respectively, $\epsilon_{y,\mathrm{RMS}}$ = RMS vertical emittance, m = head-tail mode number, SB = largest amplitude betatron sideband, f_{BB} = BB frequency, GR = BB growth rate, $\tau_{\mathrm{b}} = 95\,\%$ bunch length, a figure reference is given, if present.

Q_y	$Q_{y,\mathbf{meas}}$	$\epsilon_{y,\ \mathrm{RMS}}$ (π mm mrad)	m	**SB**	$f_{\mathbf{BB}}$ **(kHz)**	**GR (turn^{-1})**	$\tau_{\mathbf{b}}$**(ns)**	**Fig.**
3.880	3.880	10	3	BB	81.3 ± 2.7	$(5.35 \pm 0.08)\times10^{-3}$	350	6.18a
	3.880	15	3	BB	81.3 ± 2.7	$(5.34 \pm 0.07)\times10^{-3}$	350	n/a
	3.880	20	3	BB	81.3 ± 2.7	$(5.34 \pm 0.06)\times10^{-3}$	350	6.18b
	3.880	25	3	BB	81.3 ± 2.7	$(5.33 \pm 0.06)\times10^{-3}$	348	n/a
	3.880	30	3	BB	81.3 ± 2.7	$(5.33 \pm 0.06)\times10^{-3}$	350	n/a
	3.880	35	3	BB	81.3 ± 2.7	$(5.32 \pm 0.05)\times10^{-3}$	350	n/a
	3.880	40	3	BB	81.3 ± 2.7	$(5.32 \pm 0.05)\times10^{-3}$	350	6.18c
	3.880	45	3	BB	81.3 ± 2.7	$(5.31 \pm 0.05)\times10^{-3}$	348	n/a
	3.880	50	3	BB	81.3 ± 2.7	$(5.31 \pm 0.05)\times10^{-3}$	348	6.18d
3.890	3.880	10	2	BB	81.3 ± 2.7	$(3.25 \pm 0.06)\times10^{-3}$	348	6.19a
	3.880	15	2	BB	81.3 ± 2.7	$(3.27 \pm 0.06)\times10^{-3}$	348	n/a
	3.880	20	2	BB	81.3 ± 2.7	$(3.29 \pm 0.05)\times10^{-3}$	348	6.19b
	3.880	25	2	BB	81.3 ± 2.7	$(3.30 \pm 0.05)\times10^{-3}$	347	n/a
	3.880	30	2	BB	81.3 ± 2.7	$(3.31 \pm 0.05)\times10^{-3}$	347	n/a
	3.880	35	2	BB	81.3 ± 2.7	$(3.33 \pm 0.05)\times10^{-3}$	347	n/a
	3.880	40	2	BB	81.3 ± 2.7	$(3.33 \pm 0.05)\times10^{-3}$	348	6.19c
	3.880	45	2	BB	81.3 ± 2.7	$(3.34 \pm 0.04)\times10^{-3}$	347	n/a
	3.880	50	2	BB	81.3 ± 2.7	$(3.35 \pm 0.04)\times10^{-3}$	347	6.19d

Table 6.8: Summary of head-tail instability characteristics in PyHEADTAIL simulation results as a function of vertical beam size for $Q_y = 3.900$, without transverse space charge. Q_y and $Q_{y,\mathrm{meas}}$ = set and measured vertical tunes respectively, $\epsilon_{y,\mathrm{RMS}}$ = RMS vertical emittance, m = head-tail mode number, SB = largest amplitude betatron sideband, f_{BB} = BB frequency, GR = BB growth rate, $\tau_{\mathrm{b}} = 95\,\%$ bunch length, a figure reference is given, if present.

Q_y	$Q_{y,\mathbf{meas}}$	$\epsilon_{y,\ \mathrm{RMS}}$ (π mm mrad)	m	**SB**	$f_{\mathbf{BB}}$ **(kHz)**	**GR (turn^{-1})**	$\tau_{\mathbf{b}}$**(ns)**	**Fig.**
3.900	3.892	10	n/a	USB7	73.1 ± 2.7	$(6.43 \pm 0.77)\times10^{-4}$	345	6.20a
	3.892	15	n/a	BB	73.1 ± 2.7	$(6.58 \pm 0.70)\times10^{-4}$	345	n/a
	3.892	20	n/a	BB	73.1 ± 2.7	$(6.70 \pm 0.64)\times10^{-4}$	345	6.20b
	3.892	25	n/a	BB	73.1 ± 2.7	$(6.79 \pm 0.60)\times10^{-4}$	344	n/a
	3.892	30	n/a	BB	73.1 ± 2.7	$(6.86 \pm 0.56)\times10^{-4}$	344	n/a
	3.892	35	n/a	BB	73.1 ± 2.7	$(6.88 \pm 0.54)\times10^{-4}$	344	n/a
	3.892	40	n/a	BB	73.1 ± 2.7	$(6.88 \pm 0.51)\times10^{-4}$	344	6.20c
	3.892	45	n/a	BB	73.1 ± 2.7	$(6.92 \pm 0.49)\times10^{-4}$	342	n/a
	3.892	50	n/a	BB	73.1 ± 2.7	$(6.92 \pm 0.48)\times10^{-4}$	342	6.20d

The excited mode was similar to experimental observations in that modes $m = 0$ ($Q_y = 3.870$), $m = 2$ ($Q_y = 3.890$) and $m = 3$ ($Q_y = 3.880$) were observed. However, the experimentally observed $m = 1$ mode was not present in simulations. Results from RCS (section 4.2.1) and BSRM experiments (sections 5.4.2 and 6.2.1) showed low-order head-tail modes were excited ($m = 0$ – 2) with the dominant mode being $m = 1$. A change in mode with vertical tune was replicated in simulations, although the behaviour is reversed with higher mode numbers for higher tunes in simulations, whereas experiments show lower mode numbers with increasing tunes.

Specifically in the case of $Q_y = 3.880$ (figure 6.18), the BPM difference "waterfall" graphs (i – l) show that the mode number changed during the simulation, with the same initial setup. Initially an asymmetric, head-dominated, $m = 3$ mode instability was excited, and as beam was lost an $m = 2$ mode instability replaced it for a short while before a complex mode structure was observed from 2.1 ms onwards. However, by this time the longitudinal bunch shape, as can be seen in the BPM sum "waterfall" graphs (e – h), was very different than before beam-loss occurred.

As found in the PyHEADTAIL simulations varying only the vertical tune (section 5.5), the entire bunch length oscillated, whereas in the measured data less than the full bunch length oscillated and the fraction of bunch length that was observed to be unstable was inconsistent.

6.3.2.2 Head-Tail Instability in Frequency Domain

The simulated BPM signals have been processed in the same way as the measured data: segmenting the sum and difference signals into 250-turn segments (equating to 0.37 ms each) and using an FFT to show the RF frequency harmonics and vertical betatron sidebands as a function of time. From this, the fractional part of the betatron tune was determined by dividing the frequency of the lowest sideband by the revolution frequency. As the vertical tune was increased, the baseband frequency decreased. There was no dependence of baseband frequency on vertical beam size, as expected.

The betatron sidebands grew from numerical noise as the transverse distribution was matched at the start of the simulation. The specific BPM sum and difference

spectra shown in subfigures (q – t) of figures 6.16 – 6.20 were chosen when the vertical emittance had grown by 2 % (or at the end of the simulation, whichever came first). The largest sideband for each beam size and tune is listed in tables 6.6 – 6.8 and almost invariably the lowest frequency baseband (BB) was largest, as was expected as the imposed narrowband resonator was closest to this sideband.

In nearly all cases (in both experiment and simulation), the amplitude of the betatron sidebands decreased with increasing frequency until the chromatic frequency was passed (see table 6.5); the amplitudes subsequently increased again forming a second peak in sideband amplitude. In simulations, this was observed at around 8 MHz at $Q_y = 3.870$ and 3.880, 9 MHz at $Q_y = 3.890$ and 9.5 MHz at $Q_y = 3.900$, consistent with increasing mode number with vertical tune. At $Q_y = 3.860$ the sidebands only grew a small amount, indicating a slow instability, and interestingly the second highest betatron sideband was very close to the chromatic frequency.

6.3.2.3 Head-Tail Instability Growth Rate Versus Frequency and Beam Size

Subfigures (u – x) of figures 6.16 to 6.20 show the amplitudes of the vertical betatron basebands (and lower sideband of the first RF harmonic) as a function of time, and were derived from the FFTs of the simulated BPM difference signals. An exponential function was fitted to each sideband until the time at which the vertical emittance had grown by 2 % to give the e-folding growth time for each sideband at the corresponding vertical tune and beam size.

The growth time for each vertical tune and emittance was converted to a growth rate ($1/(\tau f_{\mathrm{rev}})$) and is listed in tables 6.6 – 6.8. The growth rates are shown as a function of the measured baseband frequency in figure 6.21. For comparison, the measured growth rate from experiment with an initial RMS vertical emittance of $13 \pm 1\pi$ mm mrad is shown. By design, the peak amplitudes were very close, although the behaviour with frequency, and as such betatron tune, was different.

The head-tail instability growth rate was unaffected by the initial vertical beam size, with the differences within the measurement error. This is to be expected as the applied impedance is independent of beam size and these simulations did not

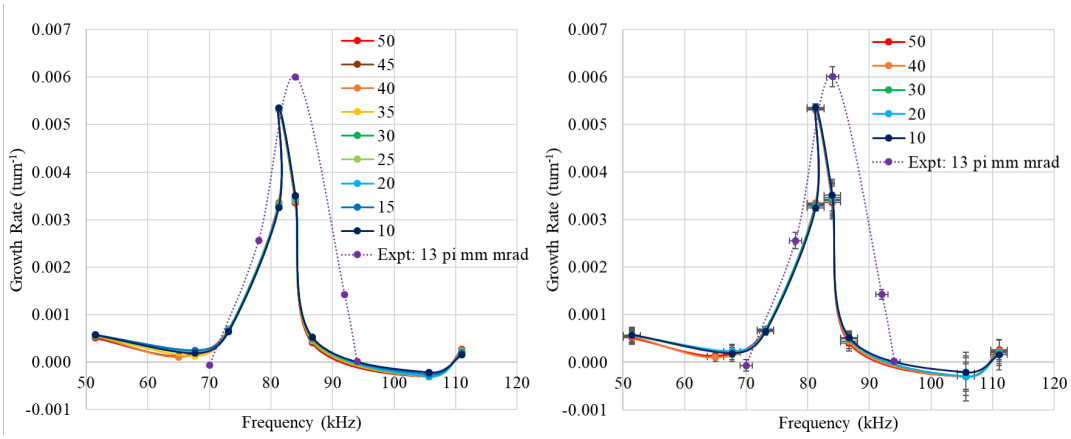


Figure 6.21: Growth rate versus betatron BB frequency for PyHEADTAIL simulations without transverse space charge as a function of vertical emittance: a) all emittances simulated, b) only those emittances shown in previous figures.

include transverse space charge, which is beam size dependent. The only aspect of the simulation that was beam size dependent was the fixed aperture, where larger initial beam sizes would encounter the aperture earlier in those simulations with an instability. This can be observed in subfigures (a – d) of figures 6.17 – 6.19 where loss happened earlier as beam size was increased. However, each growth rate was calculated from an exponential fit up until the time at which the emittance had increased by 2 %, which was still less than the aperture emittance in all the vertical beam sizes simulated.

6.3.3 With Transverse Space Charge

The experiment presented in this chapter was performed at approximately 10 % of typical beam intensities during operation (see tables 2.1 and 6.1) to reduce the effects of space charge on the beam. However, even at these reduced intensities, transverse space charge may play a role in the dynamics of the head-tail instability, not least as a function of vertical beam size. Simulations without transverse space charge have shown no effect of initial vertical emittance on the subsequent growth rate of the head-tail instability. Therefore, by adding transverse space charge, which is dependent on the beam size, a closer match with observed behaviour could perhaps be found.

As in the previous chapter (in particular section 5.5.3) the degree to which space charge impacts the head-tail instability dynamics has been quantified with the "space charge parameter", $q = \Delta Q_{\mathrm{SC}}/Q_s$ (the peak incoherent space charge tune shift divided by the synchrotron tune). A space charge parameter of much larger than one is considered to be "strong" space charge and therefore is expected to play a significant role in any head-tail instability dynamics.

In the experiments and simulations of this chapter (analysing the impact of initial vertical emittance on the head-tail instability as present on ISIS), the incoherent space charge tune shift (using equation 3.52 with the values from table 6.5 and a calculated $B_f = 0.63$) varies between $\Delta Q_{\mathrm{SC}} = 0.011$ and 0.056 (for $\epsilon_{y,\mathrm{RMS}} = 50\,\pi$ and $10\,\pi\,\mathrm{mm\,mrad}$ respectively). (The coherent space charge tune shift is $\sim$0.002 and can largely be ignored.) Therefore, as also stated in section 5.5.3, the effect of space charge on the tune was on a similar level to that of the chromaticity. When the incoherent space charge tune shift is combined with the synchrotron tune, this leads to space charge parameters of between 2.4 and 12.0. As these are greater than one, transverse space charge is likely to play a role in the head-tail instability dynamics and has been included in further PyHEADTAIL simulations using a 2.5D self-consistent PIC algorithm (see section 3.5.1).

To compare favourably with the experimentally measured peak growth rate as a function of baseband frequency, the resonator shunt impedance was reduced from 17.2 to $3.44\,\mathrm{k\Omega\,m^{-2}}$, as was done in the previous chapter (section 5.5.3). An example output from a simulation with $Q_y = 3.880$ and $\epsilon_{y,\mathrm{RMS}} = 10\,\pi\,\mathrm{mm\,mrad}$ is shown in figures 6.22 and 6.23. The simulated BPM difference signal (figure 6.22b) shows a very different intrabunch mode structure from that without space charge (figure 6.13b).

Figure 6.24 shows the BPM difference signal over 20 turns at the point where the vertical emittance had grown 2 % (before beam was lost, beam intensity and loss versus time shown in figure 5.21b), or the last 20 turns of the simulation if the vertical emittance has not grown that much. The instability appeared to be a clear mode $m = 0$ with no nodes along the bunch's length, and remained that way after

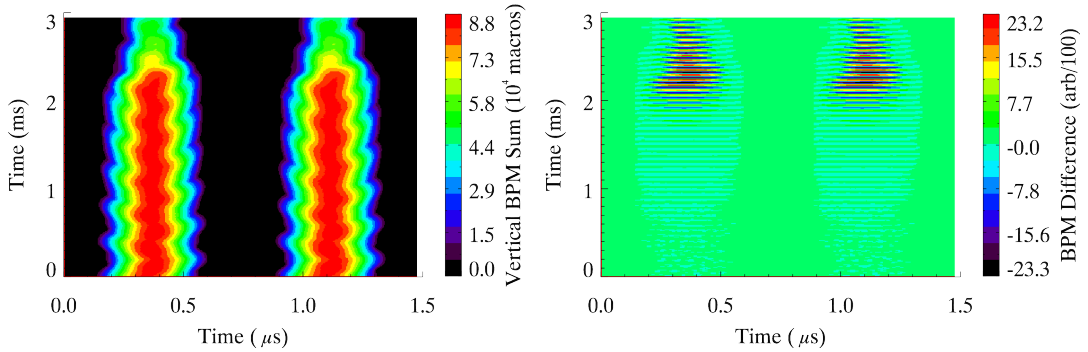


Figure 6.22: Simulated BPM sum signal (a) and difference signal (b) sliced to show each turn against time ($Q_y = 3.880$, $\epsilon_{y,\mathrm{RMS}} = 10\,\pi$ mm mrad, with transverse space charge).

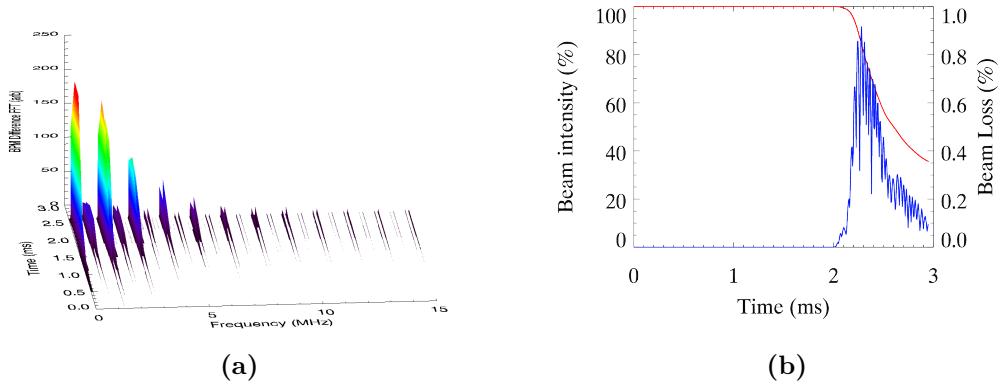


Figure 6.23: a) FFT of the simulated BPM difference signal from figure 6.22 versus time and b) simulated intensity monitor and beam-loss monitor sum signals versus time ($Q_y = 3.880$, $\epsilon_{y,\mathrm{RMS}} = 10\,\pi$ mm mrad, with transverse space charge).

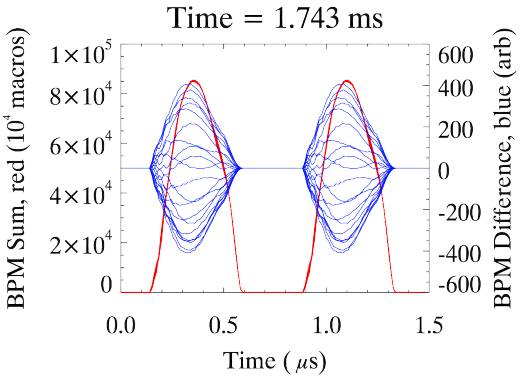


Figure 6.24: Simulated vertical BPM sum signal (blue) and difference signal (red) over 20 turns, after 1.74 ms of wakes ($Q_y = 3.880$, $\epsilon_{y,\mathrm{RMS}} = 10\,\pi$ mm mrad, with transverse space charge).

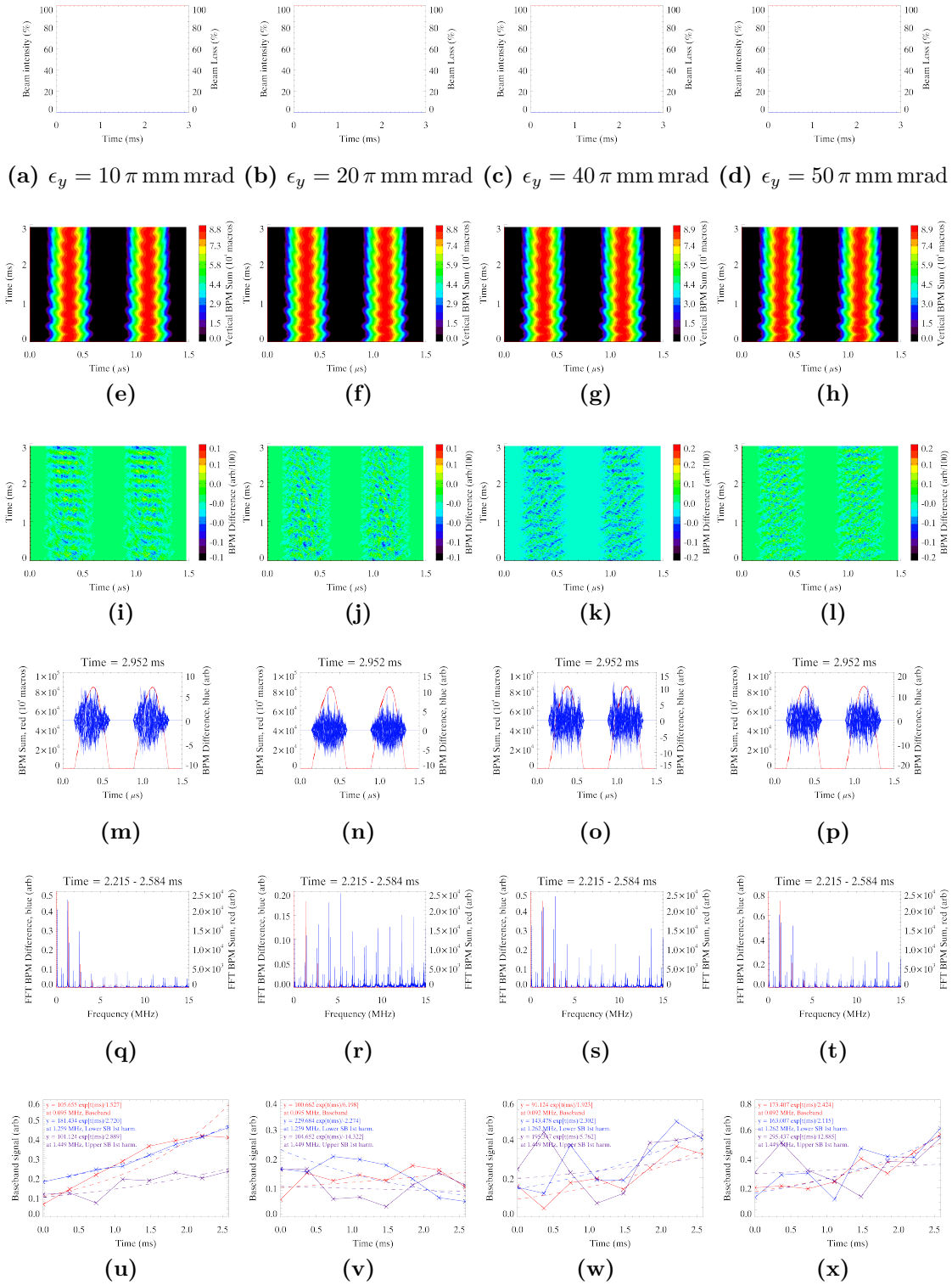
beam was lost. Betatron sidebands in figure 6.23a show a different distribution of amplitudes from that in the zero transverse space charge case (figure 6.14). The low-frequency sidebands have grown to dominate the spectra and little growth is observed above the vertical chromatic frequency.

Figures 6.25 – 6.28 show a summary of the simulation results complete with transverse space charge. As in previous figures, only those settings that caused a vertical instability are shown, and only a representative subset of the full vertical emittance range is shown. Key results are also summarised in tables 6.9 and 6.10.

6.3.3.1 Head-Tail Instability Mode Structure

Figures 6.25 – 6.28 include subfigures (m – p), which show 20-turn overlays of the simulated BPM sum and difference signals when the vertical emittance had grown by 2 % (or the end of the simulation, whichever occurred sooner) which exhibit the head-tail mode structure, if present. The observed modes are also listed in tables 6.9 and 6.10. It may be seen that including transverse space charge had made a number of differences to the observed intrabunch mode structure. BPM difference signals with zero, four, five and possibly six and seven nodes along the bunch's length were observed, whereas simulations without space charge produced zero, two and three nodes along the bunch (see section 6.3.2.1). The predominant experimentally observed mode numbers ($m = 1, 2$) were not found in the simulations. Results with little observed intrabunch mode structure but with betatron sideband growth are included (*e.g.* $Q_y = 3.860$ and 3.890). Performing these simulations for more turns is likely to bring out the mode structure. Unlike simulations without transverse space charge, there was no quantifiable betatron sideband growth, and hence no instability, at $Q_y = 3.900$.

Of particular note is the variation of mode number with initial vertical emittance as well as vertical tune. As simulations without transverse space charge showed no difference in instability dynamics with vertical beam size, it is clearly the impact of transverse space charge that is causing this effect. For $Q_y = 3.870$ and 3.880, there also appeared to be a threshold in observed mode as a function of vertical emittance, at which the mode structure goes from zero nodes to a much higher



(a) $\epsilon_y = 10\,\pi$ mm mrad (b) $\epsilon_y = 20\,\pi$ mm mrad (c) $\epsilon_y = 40\,\pi$ mm mrad (d) $\epsilon_y = 50\,\pi$ mm mrad

(e) (f) (g) (h)

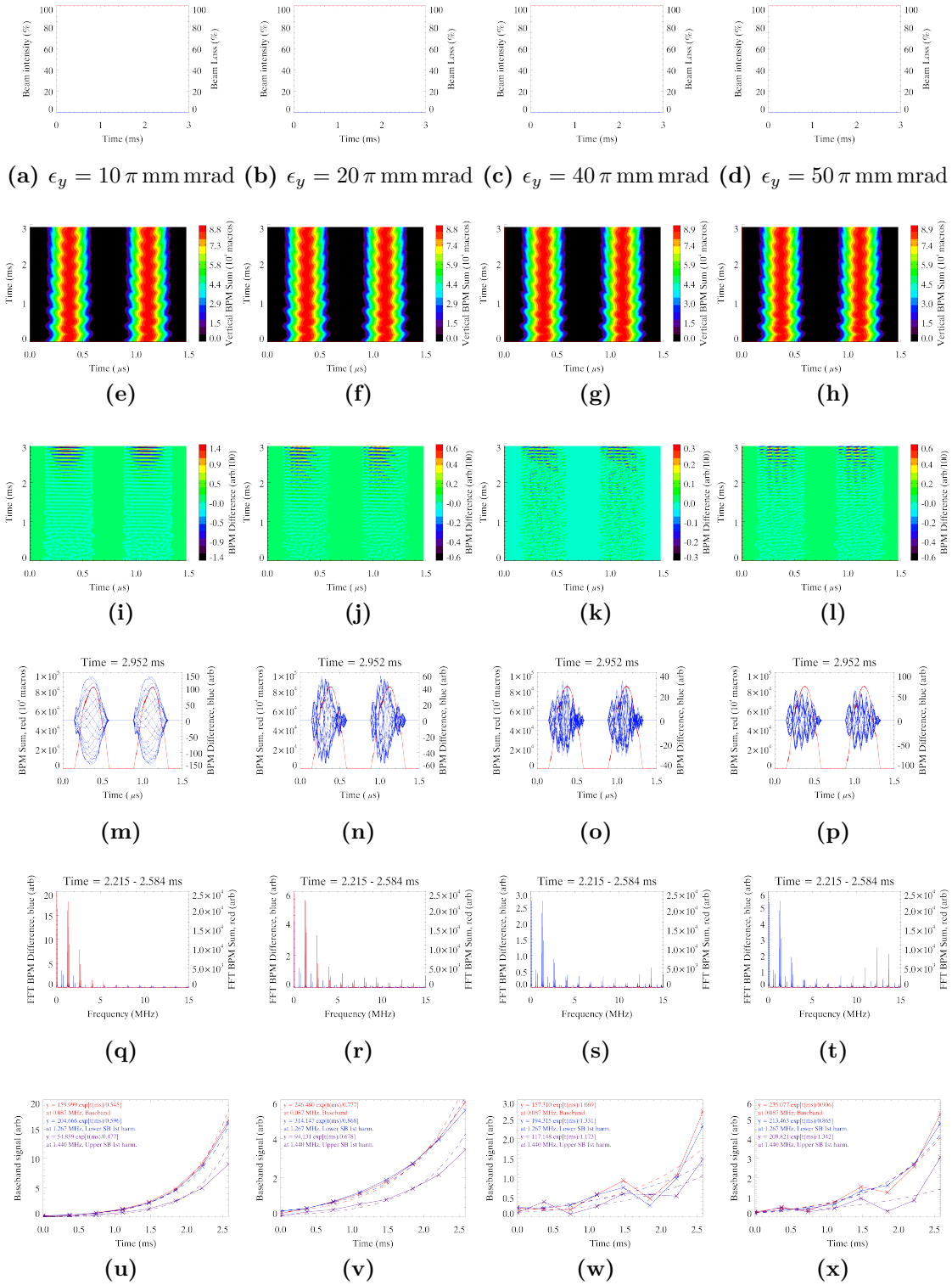
(i) (j) (k) (l)

(m) (n) (o) (p)

(q) (r) (s) (t)

(u) (v) (w) (x)

Figure 6.25: PyHEADTAIL simulation output with transverse space charge for different vertical beam emittances at $Q_y = 3.860$: intensity and beam-loss (a – d), longitudinal bunch population over time (e – h), simulated vertical BPM difference over time (i – l), simulated vertical BPM traces over 20 turns (m – p), FFT of simulated BPM data around time point of interest (q – t), growth rate fits to betatron sidebands (u – x).



(a) $\epsilon_y = 10\,\pi$ mm mrad **(b)** $\epsilon_y = 20\,\pi$ mm mrad **(c)** $\epsilon_y = 40\,\pi$ mm mrad **(d)** $\epsilon_y = 50\,\pi$ mm mrad

(e) **(f)** **(g)** **(h)**

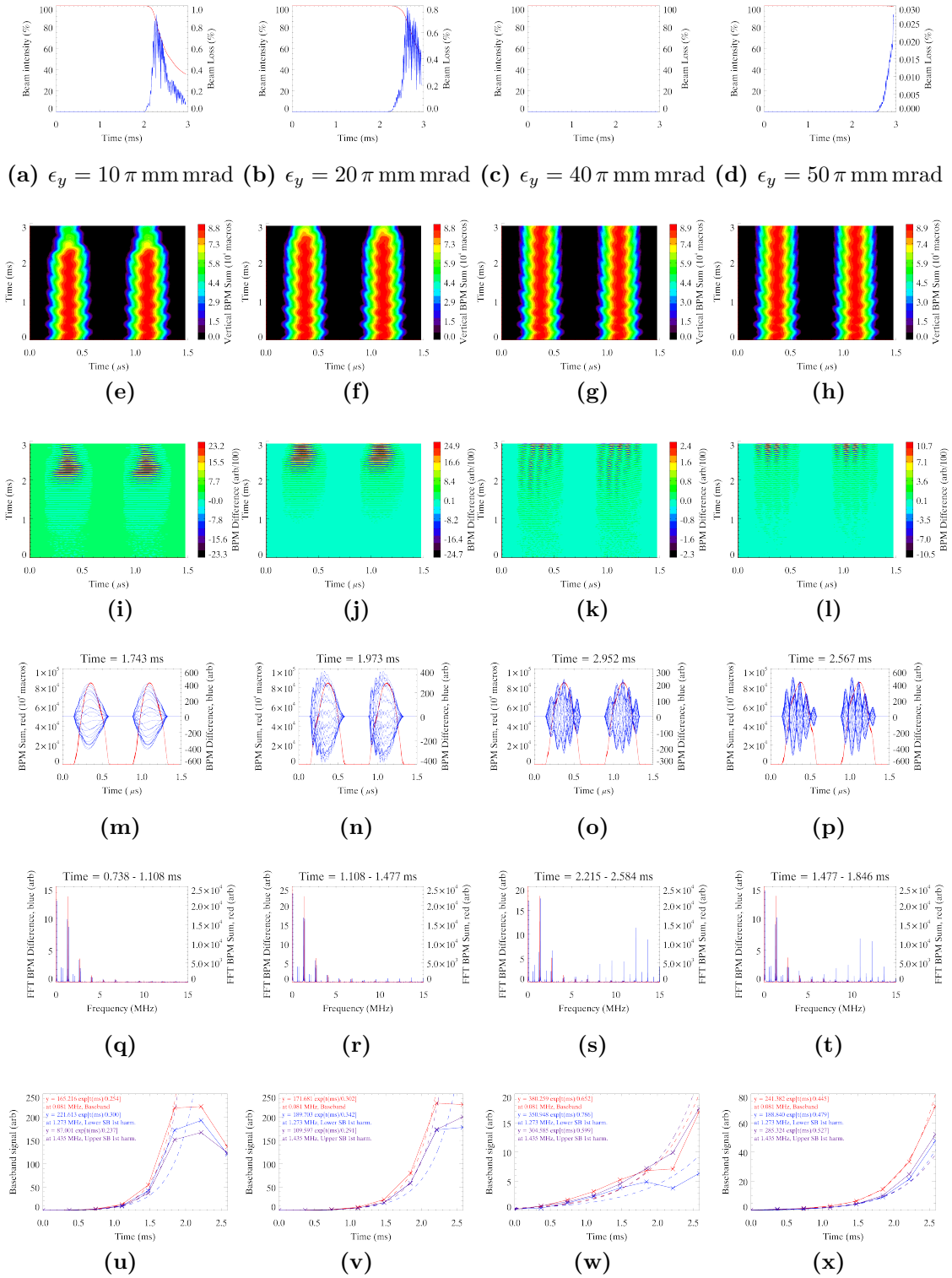
(i) **(j)** **(k)** **(l)**

(m) **(n)** **(o)** **(p)**

(q) **(r)** **(s)** **(t)**

(u) **(v)** **(w)** **(x)**

Figure 6.26: PyHEADTAIL simulation output with transverse space charge for different vertical beam emittances at $Q_y = 3.870$: intensity and beam-loss (a – d), longitudinal bunch population over time (e – h), simulated vertical BPM difference over time (i – l), simulated vertical BPM traces over 20 turns (m – p), FFT of simulated BPM data around time point of interest (q – t), growth rate fits to betatron sidebands (u – x).



(a) $\epsilon_y = 10\,\pi$ mm mrad (b) $\epsilon_y = 20\,\pi$ mm mrad (c) $\epsilon_y = 40\,\pi$ mm mrad (d) $\epsilon_y = 50\,\pi$ mm mrad

(e) (f) (g) (h)

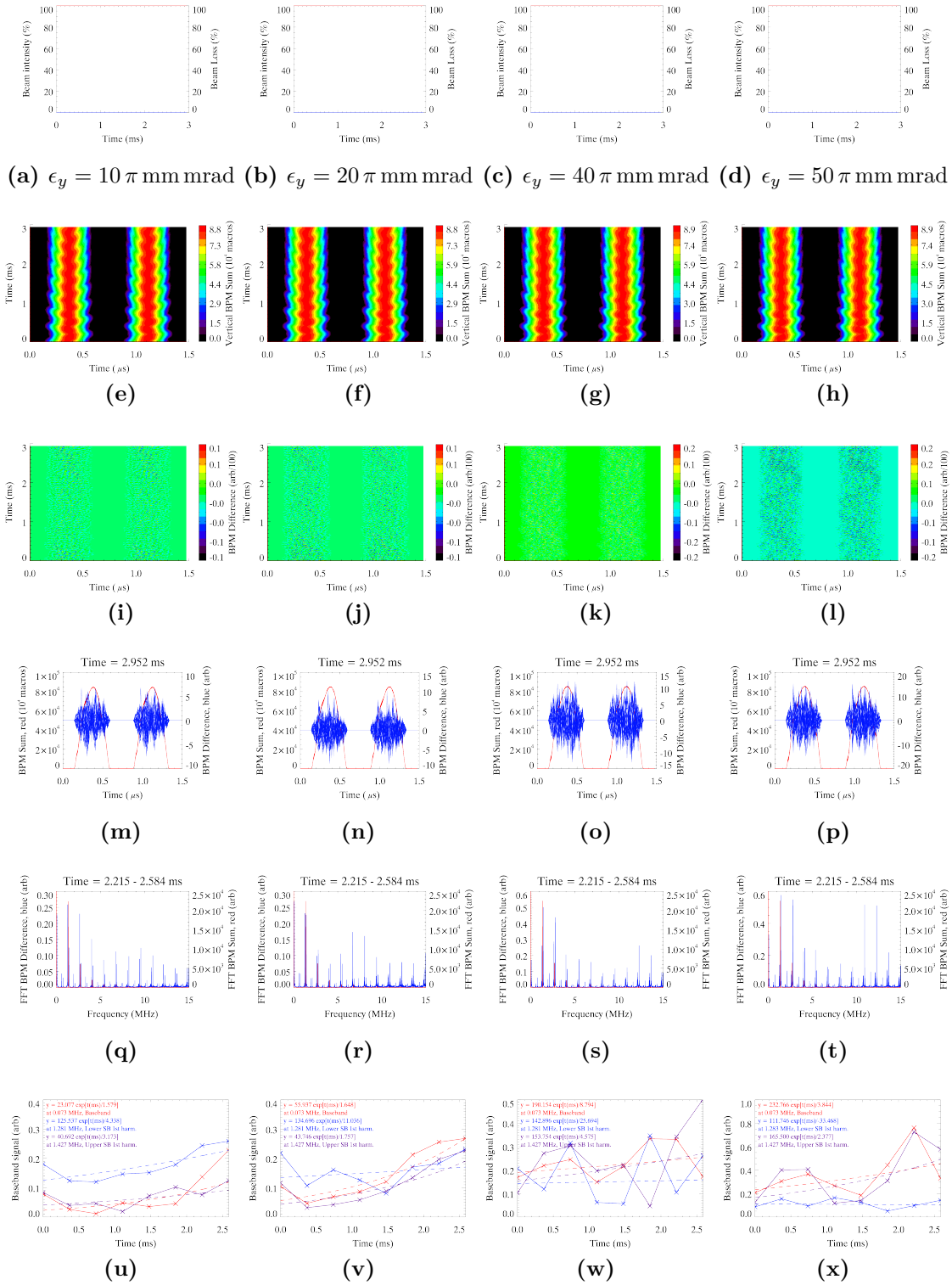
(i) (j) (k) (l)

(m) (n) (o) (p)

(q) (r) (s) (t)

(u) (v) (w) (x)

Figure 6.27: PyHEADTAIL simulation output with transverse space charge for different vertical beam emittances at $Q_y = 3.880$: intensity and beam-loss (a – d), longitudinal bunch population over time (e – h), simulated vertical BPM difference over time (i – l), simulated vertical BPM traces over 20 turns (m – p), FFT of simulated BPM data around time point of interest (q – t), growth rate fits to betatron sidebands (u – x).



(a) $\epsilon_y = 10\,\pi$ mm mrad **(b)** $\epsilon_y = 20\,\pi$ mm mrad **(c)** $\epsilon_y = 40\,\pi$ mm mrad **(d)** $\epsilon_y = 50\,\pi$ mm mrad

(e) **(f)** **(g)** **(h)**

(i) **(j)** **(k)** **(l)**

(m) **(n)** **(o)** **(p)**

(q) **(r)** **(s)** **(t)**

(u) **(v)** **(w)** **(x)**

Figure 6.28: PyHEADTAIL simulation output with transverse space charge for different vertical beam emittances at $Q_y = 3.890$: intensity and beam-loss (a – d), longitudinal bunch population over time (e – h), simulated vertical BPM difference over time (i – l), simulated vertical BPM traces over 20 turns (m – p), FFT of simulated BPM data around time point of interest (q – t), growth rate fits to betatron sidebands (u – x).

Table 6.9: Summary of head-tail instability characteristics in PyHEADTAIL simulation results as a function of vertical beam size for $Q_y = 3.860$ and 3.870, with transverse space charge. Q_y and $Q_{y,\mathrm{meas}}$ = set and measured vertical tunes respectively, $\epsilon_{y,\mathrm{RMS}}$ = RMS vertical emittance, m = head-tail mode number, SB = largest amplitude betatron sideband, f_{BB} = BB frequency, GR = BB growth rate, $\tau_{\mathrm{b}} = 95\,\%$ bunch length, a figure reference is given, if present.

Q_y	$Q_{y,\mathbf{meas}}$	$\epsilon_{y,\mathrm{RMS}}$ (π mm mrad)	m	**SB**	$f_{\mathbf{BB}}$ **(kHz)**	**GR (turn^{-1})**	$\tau_{\mathbf{b}}$**(ns)**	**Fig.**
3.860	3.860	10	n/a	LSB1	94.8 ± 2.7	(9.67 ± 1.93)×10^{-4}	345	6.25a
	3.860	15	n/a	LSB1	94.8 ± 2.7	(2.69 ± 2.58)×10^{-4}	345	n/a
	3.860	20	n/a	LSB4	94.8 ± 2.7	(2.38 ± 2.07)×10^{-4}	345	6.25b
	3.860	25	n/a	USB4	94.8 ± 2.7	(-0.42 ± 3.29)×10^{-4}	344	n/a
	3.864	30	n/a	LSB1	92.1 ± 2.7	(7.73 ± 5.32)×10^{-4}	344	n/a
	3.864	35	n/a	USB3	92.1 ± 2.7	(-6.56 ± 4.32)×10^{-4}	344	n/a
	3.864	40	n/a	USB2	92.1 ± 2.7	(7.68 ± 2.98)×10^{-4}	344	6.25c
	3.864	45	n/a	LSB1	92.1 ± 2.7	(1.42 ± 1.84)×10^{-4}	342	n/a
	3.864	50	n/a	LSB1	92.1 ± 2.7	(6.09 ± 1.11)×10^{-4}	342	6.25d
3.870	3.872	10	0	BB	86.7 ± 2.7	(2.71 ± 0.08)×10^{-3}	345	6.26a
	3.872	15	0	LSB1	86.7 ± 2.7	(2.23 ± 0.12)×10^{-3}	345	n/a
	3.872	20	7	BB	86.7 ± 2.7	(1.90 ± 0.12)×10^{-3}	345	6.26b
	3.872	25	0	BB	86.7 ± 2.7	(1.07 ± 0.16)×10^{-3}	344	n/a
	3.872	30	0	BB	86.7 ± 2.7	(9.76 ± 2.29)×10^{-4}	344	n/a
	3.872	35	6	LSB1	86.7 ± 2.7	(1.60 ± 0.08)×10^{-3}	344	n/a
	3.872	40	5	BB	86.7 ± 2.7	(1.38 ± 0.28)×10^{-3}	344	6.26c
	3.872	45	5	BB	86.7 ± 2.7	(1.68 ± 0.08)×10^{-3}	342	n/a
	3.872	50	5	BB	86.7 ± 2.7	(1.63 ± 0.19)×10^{-3}	342	6.26d

Table 6.10: Summary of head-tail instability characteristics in PyHEADTAIL simulation results as a function of vertical beam size for $Q_y = 3.880$ and 3.890, with transverse space charge. Q_y and $Q_{y,\mathrm{meas}}$ = set and measured vertical tunes respectively, $\epsilon_{y,\mathrm{RMS}}$ = RMS vertical emittance, m = head-tail mode number, SB = largest amplitude betatron sideband, f_{BB} = BB frequency, GR = BB growth rate, $\tau_{\mathrm{b}} = 95\,\%$ bunch length, a figure reference is given, if present.

Q_y	$Q_{y,\mathbf{meas}}$	$\epsilon_{y,\ \mathrm{RMS}}$ (π mm mrad)	m	**SB**	$f_{\mathbf{BB}}$ **(kHz)**	**GR (turn^{-1})**	$\tau_{\mathbf{b}}$**(ns)**	**Fig.**
3.880	3.880	10	0	BB	81.3 ± 2.7	$(5.80 \pm 0.01)\times10^{-4}$	344	6.27a
	3.880	15	0	BB	81.3 ± 2.7	$(5.59 \pm 0.10)\times10^{-4}$	344	n/a
	3.880	20	0	BB	81.3 ± 2.7	$(4.89 \pm 0.04)\times10^{-4}$	345	6.27b
	3.880	25	0	BB	81.3 ± 2.7	$(4.81 \pm 0.11)\times10^{-4}$	345	n/a
	3.880	30	5	BB	81.3 ± 2.7	$(4.49 \pm 0.19)\times10^{-4}$	348	n/a
	3.880	35	5	BB	81.3 ± 2.7	$(3.89 \pm 0.07)\times10^{-4}$	344	n/a
	3.880	40	4	USB1	81.3 ± 2.7	$(2.26 \pm 0.28)\times10^{-4}$	344	6.27c
	3.880	45	4	BB	81.3 ± 2.7	$(3.42 \pm 0.20)\times10^{-4}$	344	n/a
	3.880	50	4	BB	81.3 ± 2.7	$(3.32 \pm 0.20)\times10^{-4}$	344	6.27d
3.890	3.892	10	n/a	LSB1	73.1 ± 2.7	$(9.35 \pm 5.01)\times10^{-4}$	345	6.28a
	3.892	15	n/a	BB	73.1 ± 2.7	$(2.39 \pm 4.54)\times10^{-4}$	345	n/a
	3.892	20	n/a	BB	73.1 ± 2.7	$(8.96 \pm 2.20)\times10^{-4}$	345	6.28b
	3.892	25	n/a	BB	73.1 ± 2.7	$(4.36 \pm 2.13)\times10^{-4}$	344	n/a
	3.892	30	n/a	BB	73.1 ± 2.7	$(6.85 \pm 3.17)\times10^{-4}$	344	n/a
	3.892	35	n/a	LSB1	73.1 ± 2.7	$(4.95 \pm 1.54)\times10^{-4}$	344	n/a
	3.892	40	n/a	USB1	73.1 ± 2.7	$(1.68 \pm 1.89)\times10^{-4}$	344	6.28c
	3.892	45	n/a	BB	73.1 ± 2.7	$(5.33 \pm 3.16)\times10^{-4}$	342	n/a
	3.892	50	n/a	USB1	73.1 ± 2.7	$(3.84 \pm 2.54)\times10^{-4}$	342	6.28d

mode ($m = 6$ or 7 at $Q_y = 3.870$ and $m = 5$ at $Q_y = 3.880$). Once above this threshold, increasing the initial vertical emittance resulted in progressively lower mode numbers (fewer nodes along the bunch's length).

As observed in simulations with transverse space charge in the previous chapter (section 5.5.3), the mode structures excited before beam was lost remained in place afterwards, as seen in the BPM "waterfall" subfigures (i – l). This was in contrast to the simulations without transverse space charge, which sometimes showed different mode structures once beam had been lost.

Simulations for initial RMS vertical emittances greater than $\sim 30\,\pi$ mm mrad showed a change in mode number with vertical tune (see tables 6.9 and 6.10). However, variation of observed mode with vertical tune was observed in experiment at all beam sizes measured (see section 6.2.1). Simulations with initial RMS vertical emittances greater than $\sim 30\,\pi$ mm mrad also showed the opposite behaviour to results without transverse space charge in that the mode number decreased with increasing tune. This matches more closely with the experimentally observed behaviour, albeit at higher-order modes ($m = 5, 6$ at $Q_y = 3.870$ to $m = 4, 5$ at $Q_y = 3.880$ compared with the experimentally observed m=2 at $Q_{y,\mathrm{set}} = 3.800$ to $m = 1$ at $Q_{y,\mathrm{set}} = 3.810$ seen in tables 6.2 and 6.3).

As in all the PyHEADTAIL simulation results presented in this thesis, with or without transverse space charge, the head-tail instability was observed along the full bunch length. This was independent of the initial vertical emittance or the vertical tune, and in contrast to the experimentally observed behaviour of effective bunch lengths.

6.3.3.2 Head-Tail Instability in Frequency Domain

Observing the simulated BPM data in the frequency domain (see subfigures (q – t) in figures 6.25 – 6.28) allows for further comparison between experiment and simulation, and simulations with and without transverse space charge. As the vertical tune was increased, the baseband frequency decreased. There was no dependence of sideband frequency on vertical beam size, as expected.

The betatron sidebands grew from numerical noise as the transverse distribution was matched at the start of the simulation. The largest betatron sideband at the time of interest (once the vertical emittance had grown by 2 % or the end of the simulation, whichever was soonest) was, in most cases, the betatron baseband (see tables 6.9 and 6.10). This was consistent with the driving impedance in the simulation being a narrowband resonator at a low frequency of 82 kHz.

The amplitude of the betatron sidebands as a function of frequency was different from those in the simulations without transverse space charge. For those simulations with transverse space charge that produced a mode $m = 0$ instability, the amplitude of the sidebands decreased with frequency, whereas for the simulations with higher-order modes excited, there was an increase in betatron sideband amplitude at higher frequencies. As expected, the higher the mode number, the higher the frequency of the excited betatron sidebands. Mode $m = 4$ instabilities had a peak in betatron sideband amplitude around 12 MHz, $m = 5$ around 13 MHz and $m = 6$ around 15 MHz. Therefore, the behaviour in the frequency domain reflected that in the time domain, with a threshold above which higher frequency betatron sidebands were excited.

Despite little to no mode structure being observable in the simulated BPM difference signal at vertical tunes of 3.860 and 3.890, there were clearly betatron sidebands growing under the influence of the narrowband resonator impedance. Therefore, from the distribution of sidebands in frequency, particularly at frequencies above the chromatic frequency, it was likely possible to be able to predict which mode would be excited if the simulation were extended, allowing for more growth.

6.3.3.3 Head-Tail Instability Growth Rate Versus Frequency and Beam Size

In the same way as previous simulation and experimental data, an exponential function was fitted to the amplitude of the vertical betatron sidebands as a function of time until the vertical beam emittance had grown by 2 %. Subfigures (u – x) of figures 6.25 – 6.28 show the amplitude variation of the BB and LSB around the first RF harmonic as a function of time together with their exponential fits.

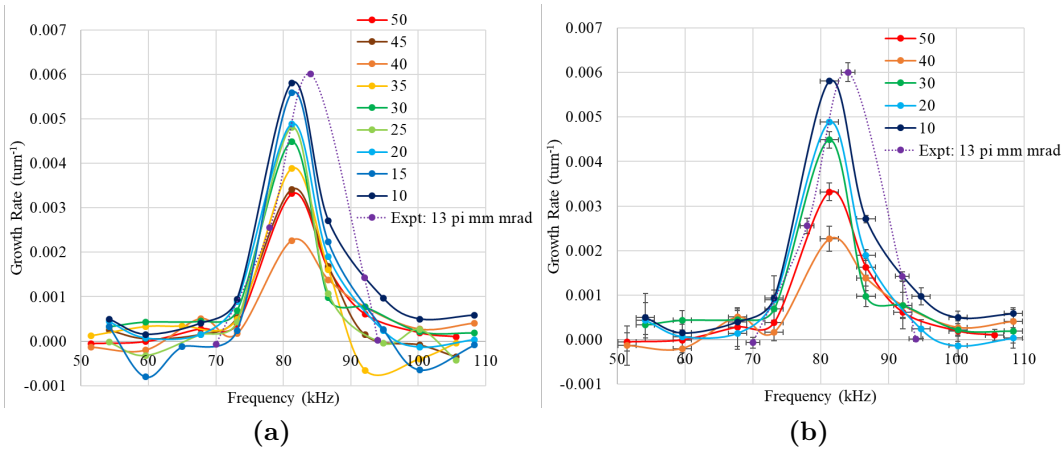
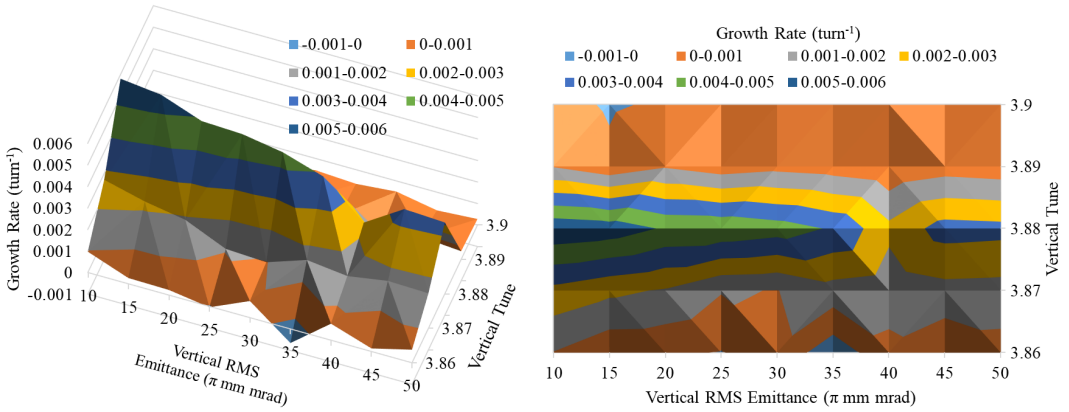


Figure 6.29: Growth rate versus betatron BB frequency for PyHEADTAIL simulations with transverse space charge as a function of vertical emittance: a) all emittances simulated, b) only those emittances shown in previous figures.

The e-folding time of the exponential fit to the baseband was converted to a growth rate ($1/(\tau f_{\text{rev}})$) for each vertical tune and emittance and is listed in tables 6.9 and 6.10. This is shown as a function of the measured baseband frequency in figure 6.29. Also shown, for comparison, is the measured growth rate from experiment with an initial $\epsilon_{y,\text{RMS}} = 13 \pm 1\,\pi\,\text{mm mrad}$.

A key difference with the simulations without transverse space charge was the variation in the growth rate with vertical emittance. The peak growth rate, at $Q_y = 3.880$ (and its corresponding baseband frequency of 81 kHz), was negatively correlated with the initial vertical emittance. This was the same behaviour observed in the experimental data (see section 6.2.3). Figure 6.30 illustrates this behaviour with 3D surface and contour graphs of the instability growth rate as a function of the vertical betatron tune and the initial RMS vertical emittance.

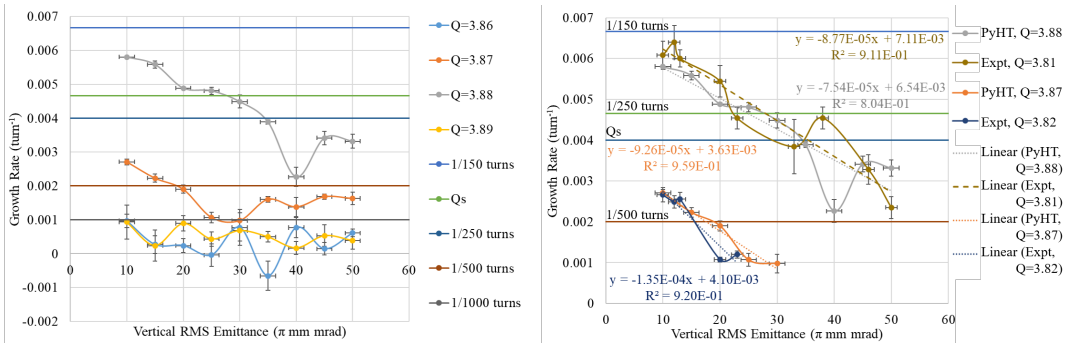
The growth rate peak at 81 kHz in figure 6.29 was expected, as the applied narrowband impedance had a resonant frequency of 82 kHz. The peak amplitudes were very close to those measured in experiment, as expected as the narrowband resonator shunt impedance was chosen for this. However, the precise behaviour with vertical baseband frequency was different from that measured experimentally. A modification of the narrowband resonator quality factor, Q, and resonant frequency, f_{res}, may address this. It should be noted that there was an anomalous dip in



(a) (b)

Figure 6.30: Instability growth rate versus initial RMS vertical emittance and vertical tune for PyHEADTAIL simulations with transverse space charge: (a) a 3D surface graph and (b) a contour graph.

growth rate at $Q_y = 3.880$ for an initial vertical emittance of $40\,\pi$ mm mrad. The instability growth rate for these conditions was far lower than the trends predict. At neighbouring vertical tunes, the growth rates also fell, but not to the same extent.



(a) (b)

Figure 6.31: Instability growth rate as a function of RMS vertical emittance for a) PyHEADTAIL simulations including transverse space charge and b) comparison between simulations at $Q_y = 3.870$ and 3.880 with experiment at $Q_{y,\mathrm{set}} = 3.810$ and 3.820.

The variation of growth rate as a function of RMS vertical emittance at fixed vertical tunes is shown in figure 6.31a. The increase in growth rate with reduction in vertical beam size appeared most notably at a vertical tune of 3.880, rising approximately linearly across the whole emittance range simulated. This was very similar to the behaviour seen in experiment at a set vertical tune of

$Q_{y,\mathrm{set}} = 3.810$ ($Q_{y,\mathrm{meas}} = 3.876 \pm 0.002$) as shown in figure 6.31b. The fitted linear gradient (minimising χ^2 statistic) of growth rate against vertical emittance was measured as $(-8.77 \pm 1.03) \times 10^{-5}$ turn$^{-1}(\pi\,\mathrm{mm\,mrad})^{-1}$ for experiment and for simulation the gradient was $(-7.54 \pm 1.41) \times 10^{-5}$ turn$^{-1}(\pi\,\mathrm{mm\,mrad})^{-1}$, as shown in figure 6.31b. As such, the two gradients were the same within the one-sigma uncertainty estimate on the fit.

At a vertical tune of 3.870, just below the instability growth rate peak at $Q_y = 3.880$, the trend was still for growth rate to increase with decreasing initial emittance (orange trace on figure 6.31a). However, the variation was not linear and there appeared to be a turning point at an emittance of around $30\,\pi$ mm mrad. Above this value, the instability was definitely present (see figure 6.26), although the growth rate held relatively constant between $35\,\pi$ and $50\,\pi$ mm mrad. The simulations with space charge showed the growth rate rising approximately linearly between $30\,\pi$ and $10\,\pi$ mm mrad.

This linear behaviour at low initial vertical emittances was very similar to that just above the peak growth rate at $Q_{y,\mathrm{set}} = 3.820$ in the experimental data ($Q_{y,\mathrm{meas}} = 3.885 \pm 0.002$), see figure 6.11b. Although this was the other side of the peak in instability growth rate, it is noteworthy that similar behaviour was observed. The gradients were also similar: $(-1.35 \pm 0.23) \times 10^{-4}$ turn$^{-1}(\pi\,\mathrm{mm\,mrad})^{-1}$ for experiment and $(-9.26 \pm 0.87) \times 10^{-5}$ turn$^{-1}(\pi\,\mathrm{mm\,mrad})^{-1}$ for simulation as shown in figure 6.31b. The gradients are consistent at the one-sigma level.

Instability growth rates at the other tunes ($Q_y = 3.860$ and 3.890) showed no significant variation with the initial vertical emittance. For both tunes, regardless of emittance, the growth rate remained below 1×10^{-3} turn^{-1}. The error on these measured growth rates was also an appreciable portion of the measured value, making interpretations or identification of trends in behaviour difficult.

6.4 Summary

Having studied the effect of vertical betatron tune on the head-tail instability in the new operating mode (BSRM) at low beam intensity and with 1RF only (chapter 5),

this chapter reported on an extended experimental program to probe the effect of vertical beam size on the head-tail instability. Measurements were made of beam-loss and beam intensity, together with longitudinal (BPM sum) and vertical (BPM difference and IPM profiles) beam signals as a function of both vertical tune as well as vertical beam size, through the action of the "vertical sweeper" (section 6.2). These measurements were, again, performed at reduced beam intensities (10 % of the nominal beam intensity) and using a single 1RF cavity at constant voltage.

The results confirmed the behaviour with vertical tune, indicating a low-frequency narrowband impedance driving a head-tail instability with variable mode structure dependent on the tune. Mode numbers $m = 0$, 1 and 2 were observed in the BPM difference signal, and the coherent vertical oscillations did not extend to the full bunch length. The mode structure was largely consistent for a given vertical tune across all the vertical beam sizes measured, and the mode number decreased with increasing tune: $m = 2$ at $Q_{y,\mathrm{set}} = 3.800$, $m = 1$ at $Q_{y,\mathrm{set}} = 3.810$ and $m = 0$ at $Q_{y,\mathrm{set}} = 3.820$.

The growth rate peaked at $Q_{y,\mathrm{set}} = 3.810$, corresponding to a vertical BB frequency of 83.5 kHz at all vertical beam sizes apart from the largest, when the peak shifted down in tune (up in frequency) to $Q_{y,\mathrm{set}} = 3.800$ (BB frequency, 90.0 kHz). Importantly, the peak instability growth rate was found to be negatively correlated to the vertical beam size.

PyHEADTAIL simulations were performed to match the new experimental setup and the resulting output presented in the same format for ease of comparison (section 6.3). Simulations were performed with longitudinal space charge but without transverse space charge (section 6.3.2). The results matched the variation in growth rate, however the intrabunch mode structures were different from experiment with the full bunch length vertically unstable, whereas experiments showed a shorter, effective bunch length. The simulations without transverse space charge showed no variation with vertical beam size.

Further simulations were performed including a 2.5D PIC model of transverse space charge (section 6.3.3). Again, the growth rate variation closely matched the

experimental measurements, however the intrabunch mode structures differed from both the experiment and simulations without transverse space charge. The full bunch length was vertically unstable, again unlike the experimental measurements. The simulations showed a very similar variation in instability growth rate with initial vertical emittance to those measured. This seems to confirm that transverse space charge is causing this dependence. Further comparisons between simulation, experiment and predictions from Sacherer's theory will be made, and conclusions drawn, in the following chapter (chapter 7).

Progress in science comes when experiments contradict theory.

— attributed to Richard P. Feynman

7 Comparison with Theory

7.1 Introduction

Following the description of the campaign of measurements aiming to characterise the head-tail type instability present on the ISIS synchrotron (chapters 4 to 6) and the most advanced simulations available using a new PyHEADTAIL model of ISIS including space charge (sections 5.5 and 6.3), this chapter focuses on their comparison both with established theory and recent theoretical proposals. In this introductory section, the relation between nominal, ISIS RCS operational data and predictions from Sacherer's theory [22] are summarised. Section 7.2 compares Sacherer's theory predictions of the head-tail instability as a function of vertical betatron tune with measurements and simulations and section 7.3 focuses on the variation of the head-tail instability as a function of vertical beam size. The impact of space charge on the instability dynamics will also be discussed and conclusions drawn. Finally, the conclusions are summarised in section 7.4.

7.1.1 Head-Tail in ISIS RCS Operations

Chapter 4 detailed observations and mitigation of the head-tail instability in normal, high-intensity operations on the ISIS synchrotron. This is characterised by coherent vertical dipolar oscillations with an intrabunch mode structure with modes $m = 1$

and possibly $m = 0$ (one or no nodes along the bunch's length). The growth rate of the instability is minimised by a series of beam manipulations: dynamic control of the vertical tune, deliberate asymmetry of the longitudinal bunch distribution and empirical tuning of the longitudinal and vertical painting over injection. Despite these, e-folding growth times at nominal beam intensities ($\sim 3 \times 10^{13}$ ppp, see table 2.1) are around 0.2 – 0.6 ms for vertical baseband (BB) frequencies between 190 and 290 kHz. Observations also show that the intrabunch motion does not occur over the full bunch length, but only over the central $\sim$40 – 80 % of the bunch.

Given beam and lattice information and an assumed impedance, Sacherer's theory enables prediction of the dominant head-tail mode structure and its growth rate. Using the vertical tune, natural chromaticity and the slip factor leads to an accumulated betatron phase shift along the bunch of $\chi = 11.8$ rad (see equation 4.1). In this case, with a low-frequency narrowband (or resistive wall) impedance assumed, the theory predicts a dominant head-tail instability of mode $m = 2$ rather than $m = 1$ or 0. Also, the fact that the instability is observed to increase in severity as the vertical tune is increased toward the integer (nominal $Q_y = 3.83$, increasing toward 4) is a strong indication that the driving impedance is resistive wall. However, such an assumption leads to predicted growth times ($\tau \sim 10$ ms) far longer than those observed. A further impedance, or impedances, at the appropriate frequency may go some way to explaining the growth rate discrepancy.

A second-harmonic RF (2RF) is not included in the theory and clearly plays a role in the longitudinal dynamics with a variation of synchrotron tune with longitudinal position and thereby modification to the head-tail instability mechanism. As such, the introduction of 2RF is likely to alter the mode structure and growth rate of these instabilities. However, observations using only 1RF also show the same discrepancy between measurement and theory (lower-order modes observed and faster growth rates, [40, 90]).

The theory of Rees (section 3.3.2, [40]) suggests an alternative instability mechanism to that of Sacherer and predicts the correct dominant mode excitation, $m = 1$. However, Rees' theory is still not the complete picture as it does not

predict the correct growth rate or the effective bunch length (the length of the bunch observed to exhibit vertical oscillations). Like Sacherer's theory, Rees' theory also does not take into account the effects of transverse space charge. It is worth noting that Rees' theory has not been required to explain observations at other facilities, therefore a study would be required to see if it applied equally well to head-tail observations at other accelerators.

7.1.1.1 Role of Space Charge

At nominal beam intensities (3×10^{13} ppp and 1.5×10^{13} ppb), ISIS is clearly a high-intensity machine with peak incoherent space charge tune shifts exceeding ∼0.5. The "space charge parameter" (see section 3.4.2.2) may be used to assess the degree to which transverse space charge plays a role in the mechanics of the observed head-tail instability. For ISIS, at nominal intensities, $q = \Delta Q_{\mathrm{SC}}/Q_s \gg 1$ throughout the acceleration cycle, implying the "strong" space charge regime. When the instability is present (around 1 – 3 ms), the "space charge parameter" is in the range $q \sim 20$ – 100 dependent on the precise longitudinal and transverse distribution.

Proposed head-tail instability theories including space charge (section 3.4.2) all agree that space charge predominantly acts to damp the instability through Landau damping. However, the two-particle approximation, adapted to include space charge [54], also predicts a series of stopbands and passbands (unstable and stable regions, respectively) as the space charge force is increased. If this model is applicable, given that the instability is observed at such intensities and space charge parameters, it may be concluded that ISIS nominal operation sits in one of these stopbands.

Preliminary studies by the author and Kornilov [59] show that this may be the case, as increasing the beam intensity led to two observed thresholds: a lower threshold, indicating the start of unstable bunches with associated intrabunch motion and beam-losses, and an upper threshold, with stabilised beams exhibiting no head-tail instability and lower associated beam-losses. That study went on to suggest that Landau damping was enhanced on the ISIS synchrotron due to the additional effect of a coherent tune shift related to image charges.

7.2 Head-Tail Instability as a Function of Vertical Tune

7.2.1 Introduction

In order to analyse better the possible discrepancies observed between predictions using Sacherer's theory and experimental observations in ISIS RCS high-intensity operations, a comprehensive series of experiments were performed in storage ring mode (SRM). Amongst the first was investigating the effect of vertical betatron tune on bunched beams in SRM (BSRM). This allowed for a great deal of simplification in the setup and a shrinking of the available parameter space with only 1RF operating, no acceleration and a much reduced beam intensity (10 % of nominal).

The measurements and associated simulations from this experiment were presented in chapter 5. In this section, comparisons are made between predictions from Sacherer's theory and experimental data (section 7.2.3) as well as results of PyHEADTAIL simulations [70] (section 7.2.4). The effect of transverse space charge on the observed coherent intrabunch instability is also discussed with reference to recent head-tail models with space charge (section 3.4.2).

7.2.2 Predictions from Sacherer's theory

Sacherer's theory of the head-tail instability (see section 3.3.1) has been chosen as a model for comparison with the experimental and simulation measurements as it has been used succesfully in explaining observations on many accelerators, including accelerators with similar beam energies and intensities to ISIS (*e.g.* [26, 97]). Sacherer's theory assumes 1RF and makes no allowance for space charge. Therefore, only 1RF was used in experiments in BSRM and a much lower intensity beam than nominal was used ($\sim 1.5 \times 10^{12}$ ppb), where space charge is less dominant. The detuning, or quadrupolar, impedance contribution due to ISIS' rectangular beam pipes has been neglected for simplicity. It should be noted that Sacherer's theory, and the more general wake and impedance theory from which it is partly derived, also assumes that the beam is travelling close to the speed of light, $\beta \approx 1$ (see section 3.2.1). However, ISIS operates in the range $0.36 < \beta < 0.84$ when

in RCS mode, and for beams in BSRM β was constant at 0.3691 (table 5.3). At these much lower velocities, the wakes can no longer be treated as only travelling backwards, but also travel forwards toward the head of the bunch. Also the rigid-beam approximation does not strictly hold, in that the beam particles can change both position and momentum when interacting with a wake. Hence the distance between particles, and thereby the size of the wake, can vary during the interaction. The relative importance of these effects in comparison to errors in the impedance model, space charge effects and systematic errors has not been studied in detail. Despite numerous approximations and limitations that may compromise its predictions, Sacherer's theory has been successfully used to model the head-tail instability in similar accelerators and, therefore, the predictions it forecasts are the selected reference to assess observations in this thesis.

7.2.2.1 Head-Tail Instability Mode Structure

Figure 7.1 shows an example bunch power spectrum $h_m(f - f_\xi)$ (see equation 3.39 of section 3.3.1) for the bunch and lattice parameters used in the experiment as a function of tune (table 5.3) and a measured full bunch length of 450 ns. This spectrum represents the beam frequencies that can interact with a suitable impedance to produce an instability. It should be noted that the head-tail instability growth rate (equation 3.41) is proportional to the impedance and that a real, negative impedance is required for an instability, whereas a positive impedance produces damping and the imaginary part (capacitive or inductive) results in a frequency shift rather than growth or damping.

Assuming the narrowband impedance from beam-based impedance measurements (section 5.2, $f_{\mathrm{res}} = 82\,\mathrm{kHz}$, $Q_{\mathrm{res}} = 10$, $R_s = 7\,\mathrm{k\Omega\,m^{-2}}$) whose resonant frequency is close to the lowest betatron sideband, the theory predicts a dominant (highest growth rate) head-tail mode of $m = 3$, at $Q_y = 3.880$. This can be seen in figure 7.2a, where a negative, real impedance coincides with the betatron sideband at a point where $h_m(f - f_\xi)$ is largest for $m = 3$ (predicted BPM difference signal using $e^{i\omega_\xi t}e^{2\pi ikQ}$ in section 3.3.1.5 is given in figure 7.2b).

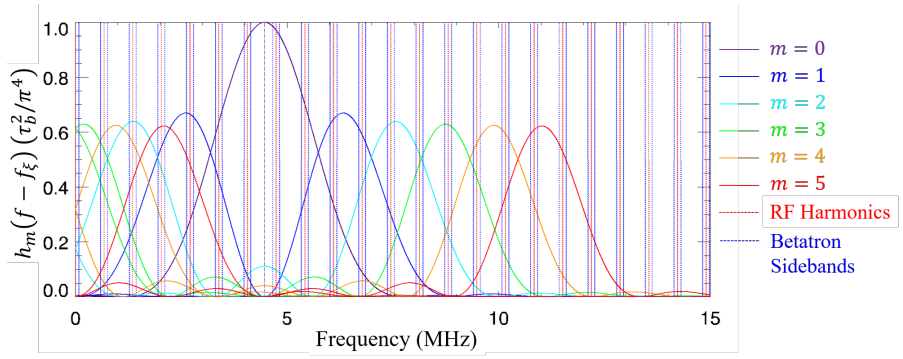
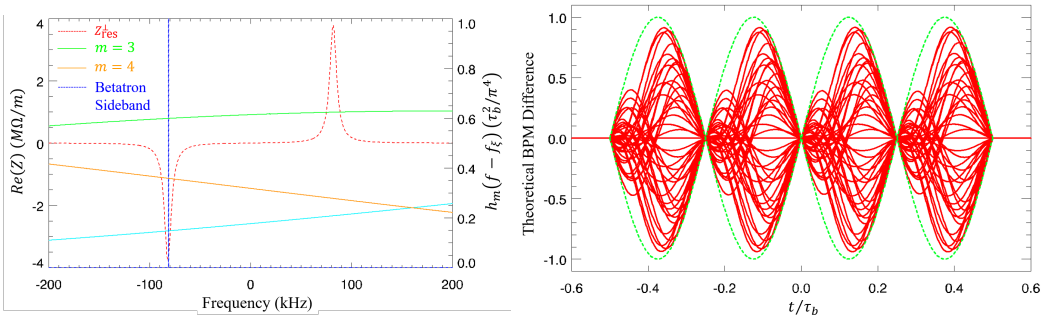


Figure 7.1: Sacherer's $h_m(f - f_\xi)$ function for the parameters listed in table 5.3, a vertical tune of $Q_y = 3.880$ and a full bunch length of 450 ns.



(a) **(b)**

Figure 7.2: a) Zoomed-in bunch power spectrum at $Q_y = 3.880$ with narrowband resonator impedance and betatron sideband overlaid. b) Predicted BPM difference signal (red) and envelope (dashed green) for one bunch over 40 turns for a head-tail mode $m = 3$ at $Q_y = 3.880$ with bunch and lattice parameters used in section 5.4.

Scanning the betatron tune moves the frequency of the betatron sidebands (see equation 5.2) and also shifts the bunch power spectrum. However, the movement in $h_m(f-f_\xi)$ over the range of betatron tunes used in this experiment ($Q_{y,\mathrm{meas}} = 3.606$ – 3.936) is relatively small. A larger effect is observed when the bunch length is changed. Sacherer's theory assumes unstable transverse oscillations occur along the full bunch length. Increasing the bunch length decreases the widths of each mode in frequency space (width $\sim 1/\tau_b$), and conversely decreasing the bunch length increases the size of the spectra. Experimental measurements of 100 % bunch length are noise-limited, especially at these lower beam intensities leading to a pulse-to-pulse standard deviation of more than 10 %.

Assuming that the narrowband resonator impedance identified in section 5.2

is the only driving impedance of the head-tail instability, the calculated spectrum envelope ($h_m(f - f_\xi)$) suggests that the dominant head-tail mode should not change as a function of vertical tune. Incorporating the measurement error on the bunch length, the theoretical bunch power spectrum could feasibly predict a dominant head-tail mode $m = 2$ or $m = 4$ as the width of the spectra changes (see section 7.2.2.2).

7.2.2.2 Head-Tail Instability in Frequency Domain

Sacherer's radial modes solution to his integral equation begins with the assumption that the head-tail instability eigenmodes are sinusoidal (equation 3.38) leading to the bunch spectrum $h_m(f - f_\xi)$. This actually represents an envelope for the bunch line spectrum (dependent on which head-tail mode is excited). With a dominant head-tail instability mode $m = 3$, the betatron sideband spectrum is predicted to peak around both zero frequency and 8.7 MHz, as shown in figure 7.3 (negative frequencies are not observed directly in network analyzers, but are reflected about zero frequency into the positive frequency domain producing the other betatron sideband around each RF harmonic).

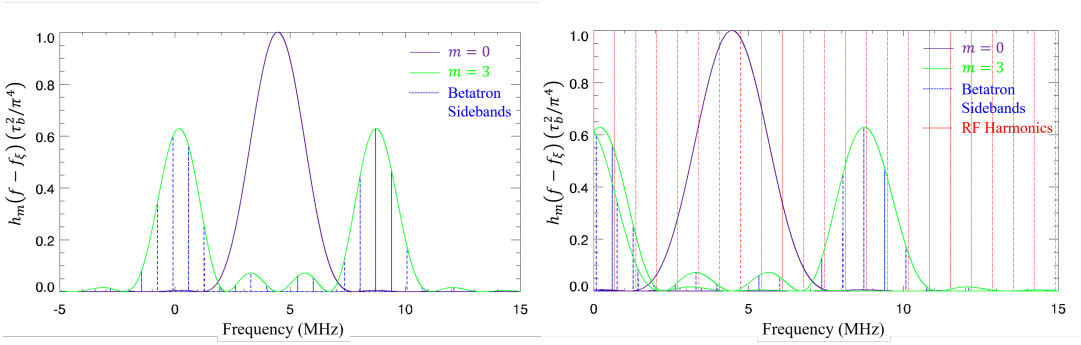
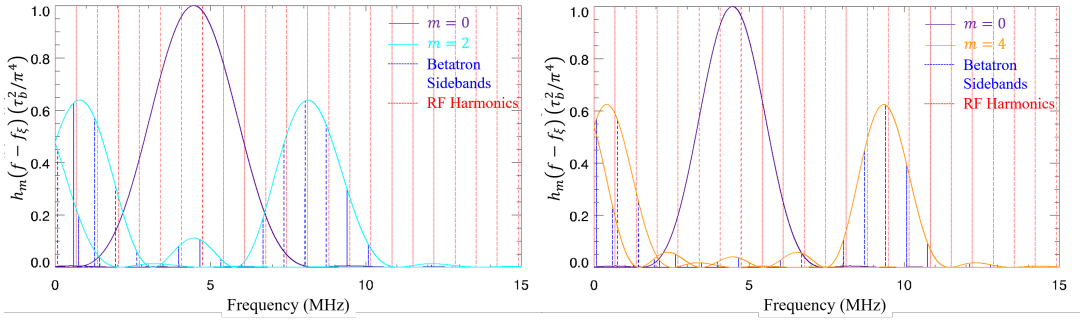


Figure 7.3: Sacherer's h_m function for a vertical tune of $Q_y = 3.880$ and a bunch length of 450 ns, indicating the betatron sideband envelope for a dominant $m = 3$ mode instability: a) with negative frequencies, b) expected observation on a network analyser.

As previously stated, changing the vertical betatron tune on its own shifts the bunch line spectrum and h_m spectrum by only a small amount, and does not produce a change in predicted mode number. However, the variability in the bunch length could produce a change in dominant mode structure. Two example possibilities are

outlined in figure 7.4. Reducing the bunch length from 450 ns to 380 ns (figure 7.4a) widens the bunch power spectra such that h_2 now has the largest value at the peak of the assumed low-frequency narrowband (close to zero frequency on this scale). Similarly, increasing the bunch length to 500 ns narrows the spectra such that h_4 has the largest value at the peak of the impedance.



(a) **(b)**

Figure 7.4: Sacherer's h_m function for a vertical tune of $Q_y = 3.880$ and a bunch length of a) 380 ns and b) 500 ns indicating the betatron sideband envelope for a dominant $m = 2$ and $m = 4$ mode instability respectively.

7.2.2.3 Head-Tail Instability Growth Rate Versus Baseband Frequency

Although changing the vertical tune on its own is not predicted to change the observed mode in Sacherer's theory, the growth rate will change as the betatron sideband samples a different part of the applied impedance spectrum. Figure 7.5 shows the range of BB frequencies probed in the measurements made of the head-tail instability as a function of vertical tune (in BSRM) together with the assumed narrowband impedance and the dominant h_m. The trough in impedance is only over a relatively narrow range of frequencies (vertical tunes), so high growth rates are only expected over that range, peaking at the resonator frequency of -82 kHz, which equates to the BB frequency for a vertical tune of $Q_y = 3.879$. It should be noted that negative frequency sidebands are reflected about zero frequency when viewed by network analysers (equation 5.2).

Applying equation 3.41 for the range of tunes (and associated sideband frequencies) in the experiment, the predicted growth rate as a function of vertical

BB frequency is shown in figure 7.6. As expected, the growth rate peaks at the resonator frequency (minimum of the real part of the impedance) and tails off quickly either side due to the quality factor of the resonator impedance.

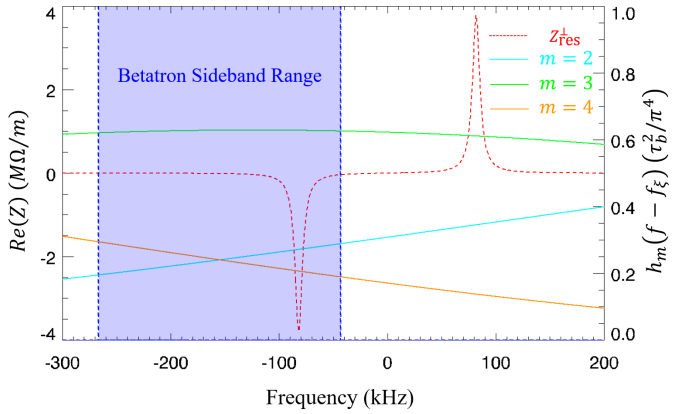


Figure 7.5: Narrowband impedance, Sacherer's h_m function for $m = 2 - 4$ and range of vertical BB frequencies in the measurements as a function of vertical tune.

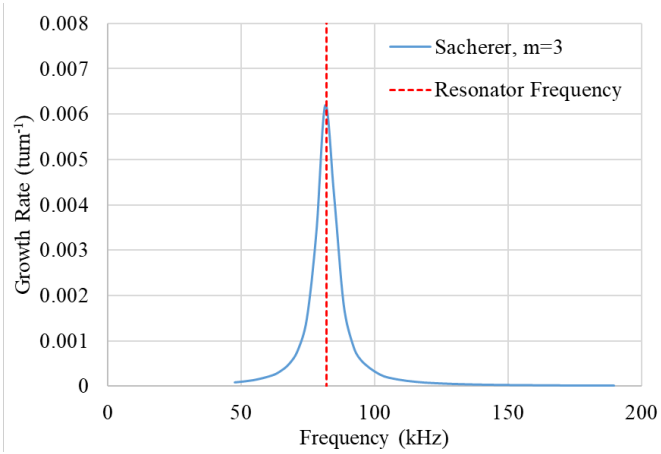


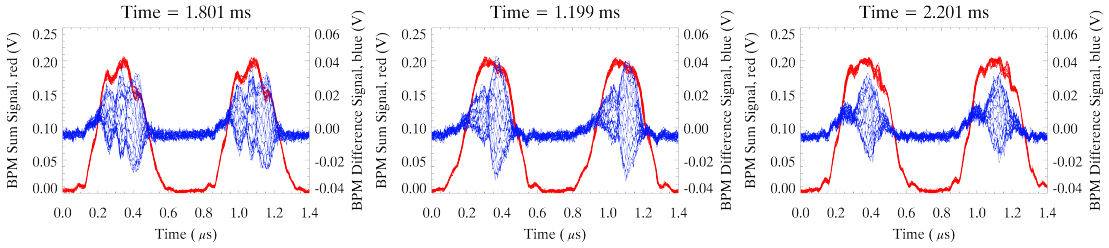
Figure 7.6: Predicted growth rate of the $m = 3$ head-tail mode as a function of vertical BB frequency.

7.2.3 Comparison Between Theory and Experiment

7.2.3.1 Head-Tail Instability Mode Structure

The experimental observations of the head-tail instability in BSRM on ISIS show a variation of mode structure as a function of vertical tune (section 5.4.2). Mode numbers $m = 2$, 1 and 0 were observed over a relatively narrow range of tune and BB frequency, as summarised in figure 7.7. This is in contrast to the prediction

that the mode number is unlikely to change. Accepting the fact that the bunch length could vary allows for a possible change of mode between measurements, however the mode was consistent between repeated observations at marginally different bunch lengths but the same tune.



(a) $Q_{y,\mathrm{set}} = 3.800$ (3.867) **(b)** $Q_{y,\mathrm{set}} = 3.815$ (3.882) **(c)** $Q_{y,\mathrm{set}} = 3.820$ (3.885)

Figure 7.7: BPM sum and difference signals over 20 turns, before beam was lost, for three selected vertical tunes ($Q_{y,\mathrm{meas}}$ in brackets).

The mode predicted from theory is $m = 3$, however this was not observed experimentally at any of the selected tunes. Only lower-order modes ($m < 3$) were observed. Another feature of the measurements may go some way to qualitatively explaining this behaviour: the effective bunch length (see section 7.2.3.2).

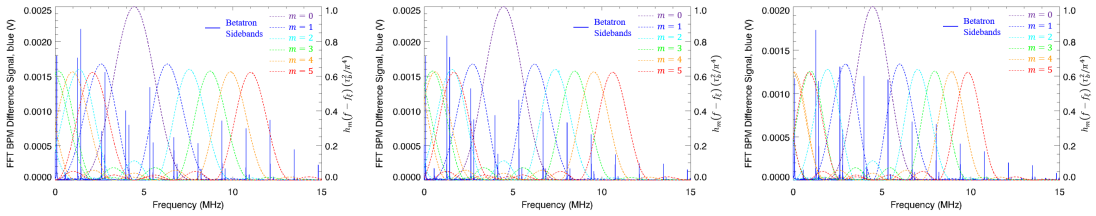
The theory of Rees [40] (section 3.3.2) typically predicts a lower mode than Sacherer, however it does not predict a change in mode with tune. Nor does it explain the observed effective bunch length. Hence, neither Sacherer's nor Rees' theory provides an accurate prediction of head-tail instability mode as a function of betatron tune in the case of ISIS in BSRM.

As noted in the observations, there was no observed threshold of the longitudinal line density at which the intrabunch oscillations begin. This means there is currently no way to predict the effective bunch length and hence what mode will be excited for a given set of bunch and lattice parameters.

7.2.3.2 Head-Tail Instability in Frequency Domain

Looking at the instability in the frequency domain, by using an FFT on the BPM difference signal allows the experimentally observed betatron sideband spectrum to be compared with predictions from Sacherer's theory. Using the measured vertical

tune (from the BB frequency), the nominal chromaticity, revolution frequency and an estimate of the full bunch length from the BPM sum signal, the bunch power spectra (h_m) may be calculated for each measurement. These provide a prediction of the envelope of betatron sideband amplitudes as a function of frequency for a given mode, m (*e.g.* figures 7.3 and 7.4).



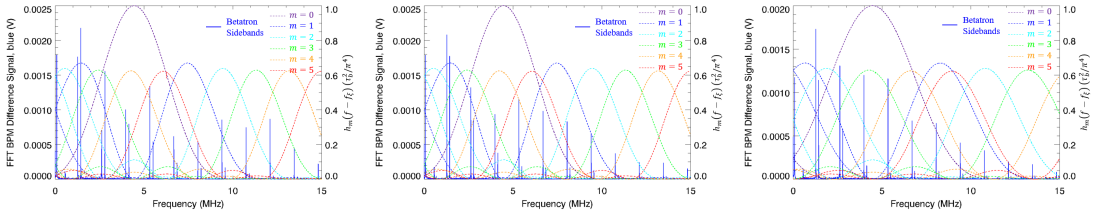
(a) $Q_{y,\mathrm{set}} = 3.800$ (3.867) **(b)** $Q_{y,\mathrm{set}} = 3.815$ (3.882) **(c)** $Q_{y,\mathrm{set}} = 3.820$ (3.885)

Figure 7.8: FFT of BPM difference signals at time point of interest and a calculated h_m overlaid (dotted lines) for three selected vertical tunes ($Q_{y,\mathrm{meas}}$ in brackets). Measured full bunch lengths are a) $\tau_b = 450\,\mathrm{ns}$, b) $\tau_b = 480\,\mathrm{ns}$ and c) $\tau_b = 550\,\mathrm{ns}$.

Figure 7.8 shows the FFTs of the BPM difference signals for the same measurements selected in figure 7.7, showcasing head-tail modes $m = 0$, 1 and 2. As expected, due to the discrepancy between predicted and observed mode structures, together with the effective bunch length feature, there was no correlation between each predicted sideband envelope (figure 7.3) and the measured betatron sidebands.

Sacherer's theory assumes that the full bunch length oscillates, and this length is the primary indicator of what mode is excited. The shorter the bunch length, the wider the mode power spectrum, h_m. So, for a fixed narrowband type impedance, a shorter bunch length (the effective bunch length) can result in a lower-order mode becoming dominant. Utilising the length of the observed mode structure (the effective bunch length, τ_e) instead of the full bunch length in the predicted sideband envelope calculations results in figure 7.9.

The expectation from the BPM difference observations (figure 7.7) would be that the betatron sideband amplitudes would follow the h_2 (cyan) envelope for $Q_{y,\mathrm{set}} = 3.800$ (figure 7.9a), the h_1 (blue) envelope for $Q_{y,\mathrm{set}} = 3.815$ (figure 7.9b) and the h_0 (purple) envelope for $Q_{y,\mathrm{set}} = 3.820$ (figure 7.9c). Although there were clearly large sidebands within these envelopes, particularly at low frequencies, the



(a) $Q_{y,\mathrm{set}} = 3.800$ (3.867) **(b)** $Q_{y,\mathrm{set}} = 3.815$ (3.882) **(c)** $Q_{y,\mathrm{set}} = 3.820$ (3.885)

Figure 7.9: FFT of BPM difference signals at time point of interest and a calculated h_m overlaid (dotted lines) for three selected vertical tunes ($Q_{y,\mathrm{meas}}$ in brackets). Effective bunch lengths are a) $\tau_\mathrm{e} = 280\,\mathrm{ns}$, b) $\tau_\mathrm{e} = 280\,\mathrm{ns}$ and c) $\tau_\mathrm{e} = 220\,\mathrm{ns}$.

picture was far from clear. There were appreciable sidebands under the h_0 mode envelope in all cases (where the predicted mode envelope, h_3, is close to zero), even for those cases where a higher-order mode was excited, and sidebands of significant amplitude at higher frequencies than are expected from the envelopes suggested by the mode observed in the BPM difference signal.

The h_m spectra were produced assuming a vertical chromaticity of $\xi = -1.4$, which is taken from previous measurements [93] and has an associated error of ± 0.09. This results in a chromatic frequency error (an error on the centre of the h_m spectra) of approximately $\pm$ 0.28 MHz (although dependent on the precise value of the vertical tune). There is also an error on the h_m spectra associated with the measured effective bunch length (affecting the width of the power spectrum), which is of the order of 10 % primarily due to the difficulty in determining the beginning and end of the oscillation.

It should be noted that the h_m spectra were produced assuming sinusoidal modes, whereas other oscillatory modes that are also solutions to Sacherer's equations, such as Legendre and Hermite modes (determined by the bunch distribution), give different power spectra [43]. These spectra have similar "lobe" widths (for each mode either side of the chromatic frequency) but have different peak positions in comparison to sinusoidal modes. These errors may provide enough flexibility to reconcile some betatron sideband spectra observations with theoretical predictions.

All predicted spectra are symmetric about the chromatic frequency (indicated by the peak of the purple h_0 curve in each figure) whereas there were clearly

assymmetries in the measured betatron spectra, with more power in lower frequency sidebands than in the higher frequency ones. This may arise due to the implicit assumption of symmetric oscillatory structures along the bunch length, whereas the BPM difference observations often showed asymmetry between the head and the tail of the bunch (a possible explanation for the mode assymetry is given in [68]).

It may be concluded that the predicted h_m envelope did not fit the experimental observations even when using the effective bunch length instead of the full bunch length. Therefore, without foreknowledge of the effective bunch length, the head-tail mode and its power spectra cannot be predicted. At best, Sacherer's theory provided an upper limit of mode number that may be excited (as the effective bunch length cannot exceed the 100 % observed bunch length) and the frequency range of sidebands with appreciable amplitude either side of the chromatic frequency (f_ξ): between the narrowband resonator frequency (f_{res}) and $\sim 2f_\xi + f_{\text{res}}$.

7.2.3.3 Head-Tail Instability Growth Rate Versus Baseband Frequency

Figure 7.10 shows a comparison of the head-tail instability growth rate as a function of betatron BB frequency between the prediction from Sacherer's theory (figure 7.6) and the measured growth rate of the BB (figure 5.11). The predicted growth rate as a function of tune matches very well with the observed growth rate despite the mode and spectra discrepancies outlined between prediction and observation. The growth rate peak was at the same frequency and the peak widths were close. The predicted width of the peak in growth rate can be adjusted with the resonator impedance's quality factor, however the growth rate is symmetric about the resonator frequency whereas the measured growth rate was asymmetric. This asymmetry may be due to further impedances not accounted for, or due to differences between the ideal bunch distribution used in theory and that which was produced experimentally.

The peak growth rate is notable in that it was above the synchrotron tune ($Q_s = 0.00456$ turn^{-1}), *i.e.* the instability e-folding time was faster than a synchrotron oscillation. This suggests the individual modes of head-tail should no longer be treated separately but together in the mode coupled instability of TMCI. Therefore, at this specific tune, Sacherer's model of head-tail is likely no longer the correct

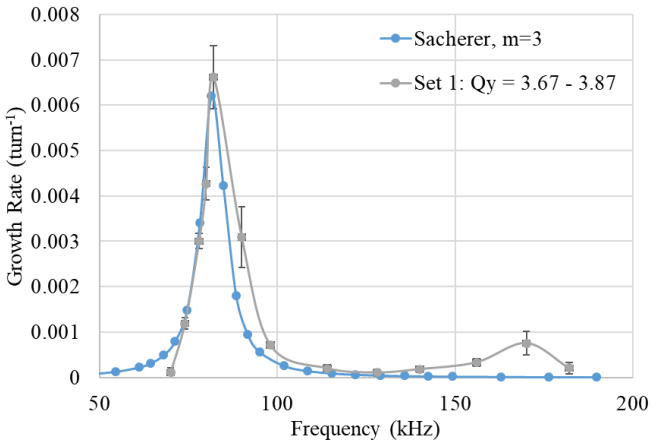


Figure 7.10: Growth rate versus vertical betatron BB frequency for experimental results in grey ("Set 1" in figure 5.11) and that predicted from Sacherer's theory for a head-tail mode $m = 3$ in blue.

theoretical framework, as it assumes separate modes of excitation. Despite this, the predicted growth rate from Sacherer's theory matched very well with measurements.

It should be noted that the experimental data showed a further, smaller peak in growth rate at around 170 kHz which was not predicted. The beam-based impedance measurements from studies of coasting beams only went up to a frequency of 140 kHz and other impedances modelled only show appreciable real parts above 6 MHz [98]. Therefore the head-tail measurement data suggest a second, smaller narrowband impedance at 170 kHz. This is closer to the frequency of the excited BB during the head-tail instability observations in RCS mode (190 – 290 kHz, see section 4.2.2) although still lower in frequency, and covering a smaller bandwidth. Better predictions may be obtained with this second narrowband impedance included together with modifications to the ideal resonator impedance to produce the observed growth rate asymmetry with frequency.

7.2.3.4 Summary and Effect of Transverse Space Charge

There are several discrepancies between predicted behaviour from Sacherer's theory and that which was measured experimentally. Firstly, the predicted head-tail mode is $m = 3$ when the observed instability was $m = 0$, 1 or 2. The mode is predicted to be constant as a function of vertical tune if the bunch length is constant, whereas the experiment showed variation of mode structure over a

relatively narrow range of tune. The measured bunch length had an associated error which was enough to predict neighbouring modes $m = 2$ and 4, however repeated measurements indicated that the mode structure for a given tune was unaffected by pulse-to-pulse variations in bunch length.

These two observed discrepancies may be partially explained by a third difference between prediction and experiment: only a fraction of the full bunch length was vertically unstable. This fraction was approximately consistent for a given tune but varied as the tune was changed. This "effective bunch length" can only be shorter than the full bunch length, therefore Sacherer's theory only predicts the upper limit of what mode may be excited for a given narrowband impedance at ISIS.

The mechanism that causes the extreme head and tail of the bunch to be damped, or not experience oscillations is still an area of active research with plans for future study (see sections 8.2.2 and 8.3.2). One possibility is the variation of synchrotron tune along the bunch length.

During injection, ISIS accumulates a continuous proton beam over many turns (section 2.1.2.1). This is then bunched by the synchrotron RF system which leads to very long bunches. These bunches are compressed in RCS operation as the bunches are accelerated, whereas in BSRM the bunches almost fill the RF bucket. Therefore, the assumption of a constant synchrotron tune is inaccurate. Particles near the centre of the RF bucket perform simple harmonic oscillations at a constant frequency, whereas particles at larger amplitudes oscillate more slowly, with the synchrotron tune decreasing to zero at the RF separatrix (the edge of the RF bucket). This could interfere with the head-tail instability mechanism that relies on the resonant effect of transversely oscillating particles swapping between the head and the tail of the bunch at a constant rate.

Space charge and image forces may have complicated impacts on the head-tail instability, not least on ISIS at injection energy. Even at 10 % of operational beam intensity, the effect of transverse space charge cannot be neglected. Also, previous studies have shown that image forces play a role in particle dynamics at ISIS [37] and specifically in relation to the head-tail instability [59]. These are particularly present

at ISIS due to the synchrotron's rectangular beam pipe, whose aperture varies to follow the beam envelope. The impedance these apertures present to the beam, and how they relate to the head-tail instability, is an active area of research [92, 98].

A TMCI could also help explain the effective bunch length. Modes of oscillation could couple in such a way as to give destructive interference at the head and tail of the bunch (for example [68, 99], which may also explain the asymmetric modes observed). However, this was not observed in the simulations (see sections 5.5.2.1 and 5.5.3.1). Further study is required to determine whether mode coupling plays a role in the head-tail instability observed on ISIS.

The frequency spectra bore little resemblance to the predicted betatron sideband envelope, even when the observed mode and effective bunch length were taken into account. Prior knowledge of the excited mode structure does enable prediction of the frequency range for which the betatron sidebands have an appreciable amplitude (symmetric about the chromatic frequency), however, without previous measurement, Sacherer's theory (with knowledge of the driving impedance) only provides upper limits to the frequency of appreciable vertical betatron sidebands.

The predicted growth rate for the $m = 3$ mode matched surprisingly well with experiment. However, it should be noted that the beam-based impedance measurements utilised the same theoretical derivation to extract the effective beam impedance as was used to predict the growth rate for the head-tail instability [22]. The instability dynamics are different: coasting beam for the impedance measurements, and bunched beam for the investigation of head-tail instability as a function of tune, but it is still intrinsically an interaction between an impedance and the beam. The growth rate formula for coasting beam [22] is similar to that for the head-tail instability (equation 3.41) with the beam current per bunch divided by the bunch length replaced by the total current divided by the ring circumference.

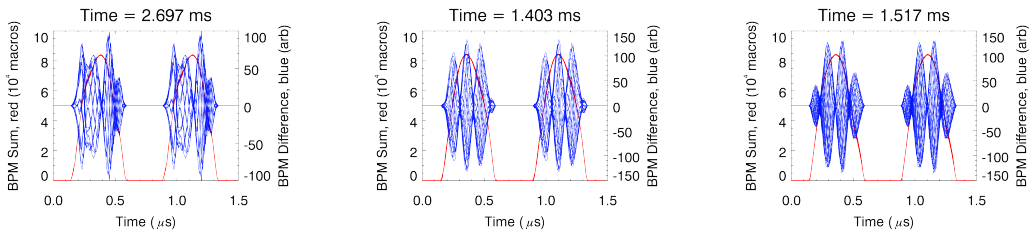
The effect of transverse space charge is difficult to determine at this stage. Further studies are planned to investigate the intensity dependence of the head-tail instability in BSRM although it should be noted that lower intensities would be challenging due to the signal-to-noise-ratio on the BPM measurements. The

differences in behaviour between theory and experiment could still be attributable to space charge, although references related to the head-tail instability with space charge (section 3.4.2) typically only refer to its damping of the instability rather than changes in mode structure or an effective bunch length. However, simulation results presented in this thesis indicate that transverse space charge does play a role in the head-tail instability, even at the reduced beam intensities (10 % nominal beam intensity) used in these experiments.

7.2.4 Comparison Between Theory and Simulations

7.2.4.1 Head-Tail Instability Mode Structure

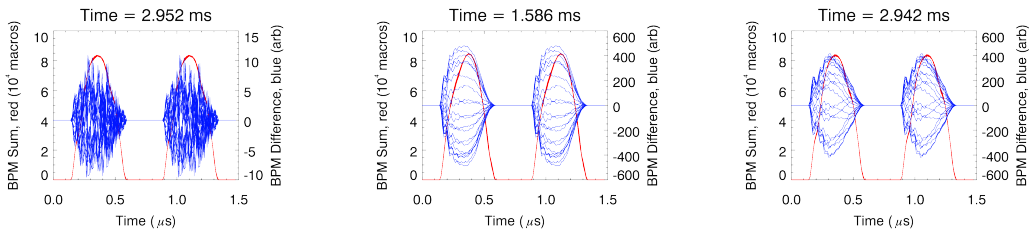
PyHEADTAIL simulations of the head-tail instability as a function of vertical tune were performed without (section 5.5.2) and with transverse space charge (section 5.5.3). Results without the effect of transverse space charge showed intrabunch $m = 2$ and $m = 3$ mode structures (two or three nodes along the bunch's length) in the simulated BPM difference signal (for example see figure 7.11).



(a) $Q_y = 3.865$ **(b)** $Q_y = 3.880$ **(c)** $Q_y = 3.885$

Figure 7.11: Simulated BPM sum and difference signals (without transverse space charge) over 20 turns, before beam was lost, for three selected vertical tunes.

Without transverse space charge, simulations showed the mode changing as a function of tune whereas sinusoidal modes in Sacherer's theory predict a consistent $m = 3$ mode. This mode was observed at three of the selected simulated vertical tunes ($Q_y = 3.865$, 3.875 and 3.885), but an $m = 2$ mode was excited in simulations with $Q_y = 3.880$, 3.890 and 3.895 (see table 5.7). Also, a possible $m = 0$ mode was observed at $Q_y = 3.870$.



(a) $Q_y = 3.865$ **(b)** $Q_y = 3.880$ **(c)** $Q_y = 3.885$

Figure 7.12: Simulated BPM sum and difference signals (with transverse space charge) over 20 turns, before beam was lost, for three selected vertical tunes.

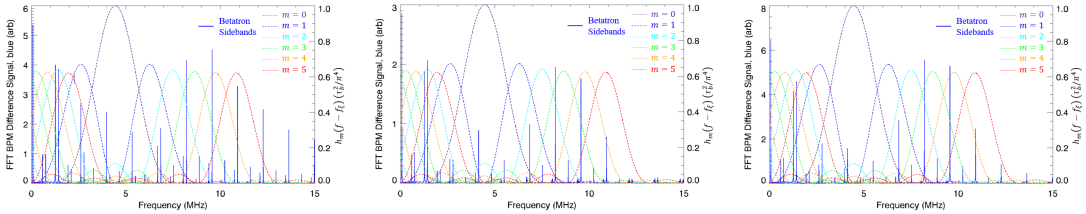
With transverse space charge, the resulting head-tail mode structures were very different, with a consistent $m = 0$ mode for those vertical tunes that exhibited an instability (examples shown in figure 7.12). Clearly, the addition of transverse space charge to the simulations caused the change, although it should be noted that the resonator shunt impedance had to be reduced to match the peak growth rate observed in experiment. This was unexpected, as most proposed theories of the head-tail instability with space charge (see section 3.4.2) suggest a damping effect due to space charge and do not predict changes in mode structure with tune or space charge except perhaps [54, 57].

The simulations, both with and without transverse space charge, showed vertical oscillations along the full bunch length as expected from theory. This suggests that direct space charge, on its own, does not cause the experimentally observed behaviour of a shorter, effective bunch length. However, the effects of indirect space charge and images were not included in these simulations.

The PyHEADTAIL simulations presented in this thesis included the full non-linear longitudinal calculations for each macroparticle's longitudinal dynamics; as such, the macroparticles do not all oscillate at the synchrotron frequency. This indicates that the effective bunch length is unlikely to be due to the variation in synchrotron motion with longitudinal amplitude. Possible further avenues of investigation include the effect of images, the low relativistic β which breaks the assumptions of Sacherer's theory and the effect of the precise longitudinal and transverse beam distribution on the predicted mode (see section 8.3.2).

7.2.4.2 Head-Tail Instability in Frequency Domain

As in the comparison between theory and experiment, the sideband spectra envelope, h_m, may be calculated for each simulation. The chromaticity, slip factor (η), revolution frequency and bunch length were all the same between simulation runs, with the only difference being the vertical tune. This had a very small effect on the bunch power spectra through the chromatic frequency shift derived from equation 3.40, $\omega_{\xi,y} = \xi_y Q_y \omega_0 / \eta$.



(a) $Q_y = 3.865$ **(b)** $Q_y = 3.880$ **(c)** $Q_y = 3.885$

Figure 7.13: FFT of simulated BPM data without transverse space charge, prior to beam-loss, for three selected vertical tunes with h_m overlaid ($m = 0 - 5$, dotted lines).

Figure 7.13 shows the FFT of the simulated BPM difference signals, without transverse space charge, for the same tunes as selected in figure 7.11, together with the predicted sideband envelopes, h_m, for head-tail modes $m = 0 - 5$. These spectra are the same as presented in figures 5.17 and 5.18. The theoretical spectra, h_m, do not define a distinct envelope within a given mode m for the simulated betatron sideband spectra. Sidebands with appreciable amplitudes are spread across several modes.

From the predicted spectra envelope and the applied narrowband impedance at 82 kHz (close to zero frequency and the BB in figure 7.13), it may be seen why a mode $m = 3$ is predicted, with the largest value of h_m for $m = 3$ around this frequency. As expected, the vertical sideband closest to the frequency of the minimum in the real part of the impedance (the vertical BB) is the largest. The expectation would then be that the betatron sideband amplitudes would follow the envelope described by the h_3 (green) function. The simulated spectra (without space charge) resembled the predictions for several tunes ($Q_y = 3.865, 3.875, 3.885$) with peak sideband amplitudes near the resonator frequency as well as a second peak

coinciding with the higher frequency peak in the h_3 function (above the chromatic frequency, $f_{\xi,y}$, indicated by the peak of the purple h_0 curve). However, it should be noted that sidebands of appreciable amplitude were also present where $h_3 \approx 0$ (for example see figure 7.13a above 11 MHz for example) and the variation in betatron sideband spectra with vertical tune was not predicted.

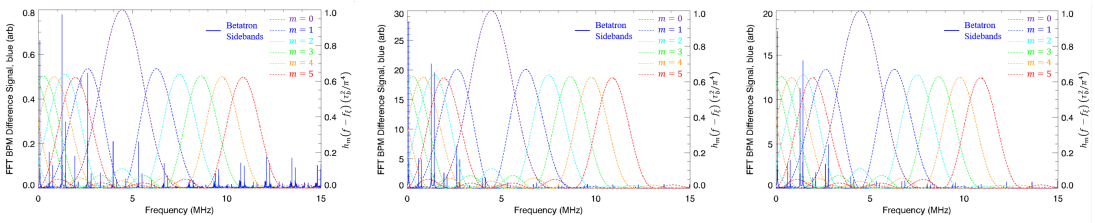
Unlike the experimental measurements, the 100 % bunch lengths of the simulations could be determined exactly as there was no noise on the signals. Although the longitudinal distribution was deliberately mismatched to reproduce the bunch length oscillations observed in the experiment more accurately, this change in bunch length is not enough to predict a change in mode number with tune.

Theoretically the bunch length could be modified such that the peak of the resonator impedance gives the same h_m for both $m = 2$ and $m = 3$, thereby predicting an increase in mode number ($m = 2$ to 3) as the vertical tune is increased (BB frequency reduced). This is because the h_m functions are relatively constant against small changes in tune whilst the vertical BB shifts from a higher h_2 to h_3 value. However, with the predicted spectra from the 100 % bunch lengths in simulation, the movement of the vertical sidebands was too small to predict a mode change on its own. It is noteworthy that the simulated behaviour, without transverse space charge, did the opposite ($m = 3$ to 2), which is not well understood.

As noted in the comparison with experiment, the theoretical predictions presented (section 7.2.2) assume pure sinusoidal modes, whereas the oscillations seen in both simulated and experimental data were not pure sinusoids. Other solutions to Sacherer's integral equation result in different predicted sideband envelopes (see section 7.2.3.2). Research into other distributions and mode solutions may provide a closer match to the simulated spectra.

As distinct from the experimental data (as exemplified in figures 7.8 and 7.9), the simulated betatron sideband spectra were symmetric about the chromatic frequency (indicated by the peak in h_0) both in peak frequency and sideband amplitude. This suggested a clear difference between the experimental and simulated BPM data.

Further research is required to determine if this difference is due to beam dynamics processes not accounted for in the simulation.



(a) $Q_y = 3.865$ **(b)** $Q_y = 3.880$ **(c)** $Q_y = 3.885$

Figure 7.14: FFT of simulated BPM data with transverse space charge, prior to beam-loss, for three selected vertical tunes with h_m overlaid ($m = 0 - 5$, dotted lines).

With transverse space charge, PyHEADTAIL simulations revealed very different betatron sideband spectra compared to the predicted power spectra (as summarised in figure 7.14) with none of the sideband amplitudes following the predicted h_m envelopes. The largest sideband was still the BB as expected, but there was little to no sideband growth above the chromatic frequency which differed from the theoretical prediction of figure 7.3. If the chromaticity were corrected, shifting the chromatic frequency and therefore the centre of the h_m functions, the $m = 0$ envelope would match more closely to the simulated spectra. Further study is required to ascertain whether the inclusion of indirect transverse space charge (image effects), or variations in beam distribution would bring the spectra closer to the experimental observations. However, it should be noted that agreement with Sacherer's theory predictions is not expected with the addition of space charge.

7.2.4.3 Head-Tail Instability Growth Rate Versus Baseband Frequency

A comparison between the predicted head-tail instability growth rate as a function of betatron BB frequency from Sacherer's theory (figure 7.5) and the growth rate of the BB from simulations (figures 5.19 and 5.25) is shown in figure 7.15. Despite the differences already noted between theory and simulation, the growth rate as a function of BB frequency (and vertical tune) compared favourably between simulations and theoretical predictions. The growth rate functions peaked at the same frequency and the peak widths were similar. The peak heights were similar as

the resonator's shunt impedance (R_s) was modified for this purpose. The predicted and simulated (with space charge) growth rate peaks were symmetric about the narrowband resonator frequency, whereas the simulations without transverse space charge showed some asymmetry.

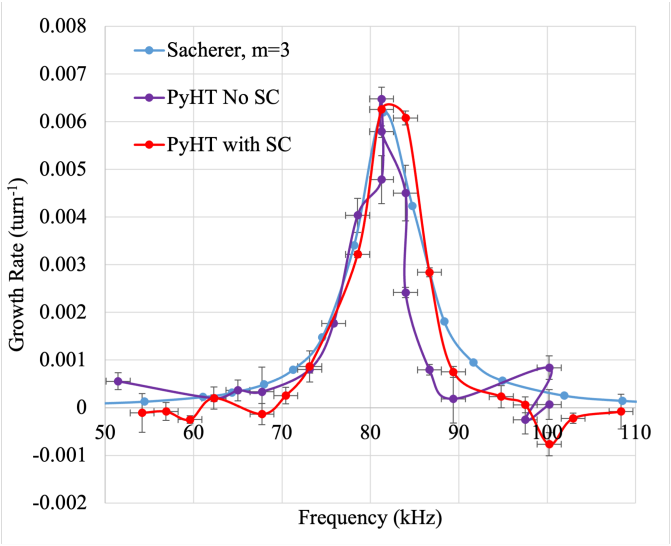


Figure 7.15: Growth rate versus vertical betatron BB frequency for simulated data with and without transverse space charge (red and purple respectively) and that predicted from Sacherer's theory for a head-tail mode $m = 3$ (blue).

In the PyHEADTAIL simulations presented, transverse space charge had increased the growth rate across the tune range, thus necessitating a reduction in the narrowband resonator shunt impedance from 17.2 to 3.44 $\mathrm{k\Omega\,m^{-2}}$ to bring the resulting growth rates down to those seen in figure 7.15. For comparison, the shunt impedance used in the predicted $m = 3$ growth rate is 7 $\mathrm{k\Omega\,m^{-2}}$. Changing the shunt impedance only results in a change in growth rate in Sacherer's theory, with no change in predicted sideband spectra or expected mode, until the growth rate is too high for the modes to be considered separately (*i.e.* TMCI).

Once again, the peak growth rate is notable as it was above the synchrotron tune ($Q_s = 0.00456$ turn^{-1}) suggesting that the head-tail modes may no longer be considered separately. Instead the mode-coupled instability, TMCI, was the more likely mechanism. However, even with this difference, the predicted growth rate matched very well with simulations.

7.2.4.4 Summary and Effect of Transverse Space Charge

PyHEADTAIL simulations without transverse space charge produced head-tail modes that matched reasonably well with those predicted from Sacherer's theory: a predominant $m = 3$ mode. However, the results also showed a change in the observed mode structure with vertical tune with both $m = 3$ and $m = 2$ modes identified. The addition of transverse space charge to the simulations altered the situation with only $m = 0$ modes excited across the tune range. Sacherer's theory does not include the effects of space charge, so full agreement was not expected. The difference in behaviour leads to the conclusion that space charge plays a role in the head-tail instability on ISIS, even at the reduced beam intensities used in these simulations and a new, or modified theory is required.

All the head-tail instability modes simulated, with or without transverse space charge, occurred over the entire bunch length. Therefore, the experimentally observed effective bunch length was likely neither due to direct transverse space charge nor the relatively full RF buckets (long bunches) noted previously. There are many elements that were not included in either the theory or simulation, including the effects of images (suggested by Kornilov to have an influence on head-tail [59]) and the relatively low relativistic beta ($\sim$0.36 at ISIS injection) where the theory implicitly assumes $\beta = 1$ (section 3.2.1). Simulations assume a simple scaling of the kicks due to the wake ($\propto 1/(\beta c)^2$).

The simulated bunch spectra without transverse space charge broadly matched those predicted for the observed mode in terms of where the betatron sideband amplitudes were greatest. However, the spread in frequency of appreciable betatron sidebands was larger than expected from theory, covering several h_m envelopes of modes neither observed nor predicted. This may be due to the inaccurate assumption of sinusoidal modes. With transverse space charge, the spectra did not match those which are expected from theory or from the observed mode ($m = 0$) for the value of chromaticity used ($\xi_y = -1.4$).

Finally, the PyHEADTAIL simulations produced head-tail growth rates as a function of tune (and vertical BB frequency) that matched very well with

theory. This was expected as the impedance parameters were chosen to match the experimentally observed peak amplitude, with the resonator shunt impedance increased for simulations without transverse space charge and decreased for those with transverse space charge (in comparison to the theoretical fit to beam-based impedance data). This illustrates how much of an effect transverse space charge can have on beam dynamics, even at lower operating intensities (10 % of nominal beam intensities), and its necessity in these and future simulations. It was notable that the head-tail growth rate increased with the inclusion of transverse space charge whereas theories propose that it should damp the instability (section 3.4.2).

7.3 Head-Tail Instability as a Function of Vertical Beam Size

7.3.1 Introduction

To probe further the observed discrepancies between predictions from Sacherer's theory and experimental observations, a second investigation was completed looking at the effect of vertical beam size on the head-tail instability in BSRM. This reused the simplified setup, with only 1RF operating, no acceleration and a much reduced beam intensity ($\sim 1.5 \times 10^{12}$ ppb). A series of measurements was made as a function of vertical beam size (varying the vertical injection painting) as well as vertical tune. The measurements and associated simulations from this experiment were presented in chapter 6.

In this section, predictions from Sacherer's head-tail instability theory are compared with experimental data (section 7.3.3) as well as results of PyHEADTAIL [70] simulations (section 7.3.4) as a function of beam size. The effect of transverse space charge on the instability is also discussed with reference to recent head-tail models including space charge (section 3.4.2).

7.3.2 Predictions from Sacherer's Theory

Predictions using Sacherer's theory have been chosen as a comparison to the experiment and simulation measurements as it is a well established model that has

been used succesfully to explain observations on many accelerators. However, as noted in the previous section (particularly section 7.2.2), Sacherer's theory may have limited validity in the case of the experiments presented in this thesis. It is also clear, from PyHEADTAIL simulations of the effect of vertical tune on the head-tail instability, that transverse space charge plays a role in the dynamics, even at the lower beam intensities used in the experiments (section 7.2.4.4). However, space charge is not included in Sacherer's theory and recent models aimed at including its effects have yet to be benchmarked and accepted by the community. Predictions from Sacherer's theory are, however, still instructive and form the baseline for the study of head-tail instability and its key characteristics.

Unlike betatron tune, transverse beam size is not an explicit factor in Sacherer's head-tail theory (see section 3.3.1). The only way it may impact the instability is through the transverse impedance (see equation 3.41), if this is a function of the transverse beam size. It should be noted that this is not the case for the resonator impedance (see equation 3.7) nor the resistive wall impedance (equation 3.3), which was originally considered the driver for the vertical head-tail instability observed on ISIS [40]. However, the space charge impedance (outlined in [43, 44] and elsewhere) is dependent on the transverse beam size. It is known that this cannot drive an instability on its own, as it is purely imaginary, only producing a frequency (or tune) shift rather than exponential growth. (In this experiment an incoherent space charge shift of between 0.011 and 0.056 and coherent space charge tune shift, due to indirect space charge, of $\sim$0.002, was calculated.)

Experimental observations as a function of vertical beam size may help to characterise what type of impedance is driving the head-tail instability on ISIS. Furthermore, PyHEADTAIL simulations will aid in interpreting observations, with particular reference to the impact of transverse space charge.

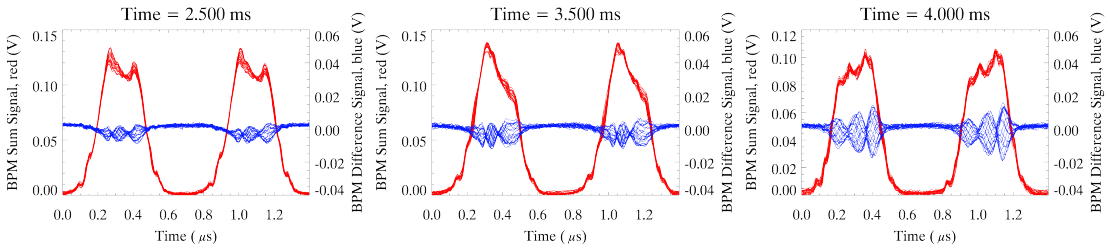
With the assumption of a narrowband resonator impedance, the head-tail mode, frequency spectra and growth rate predictions are the same as for the tune scan case (section 7.2.2), reduced in scale by the ratio of the different bunch intensities for the two experiments (equation 3.41, 1.47×10^{12} ppb for the beam size scan and

1.68×10^{12} ppb for the tune scan). If, however, an impedance is assumed with the same variation with frequency, but with a dependence on transverse beam size, theory predicts the same mode ($m = 3$) and frequency spectra (figure 7.3) as before but with a growth rate that now depends on the beam size in the same way as the impedance.

7.3.3 Comparison Between Theory and Experiment

7.3.3.1 Head-Tail Instability Mode Structure

Mode numbers $m = 0, 1$ and 2 were experimentally observed over a narrow range of tune (or BB frequency). There was little or no variation in the experimentally observed mode structure as the vertical beam size was altered for tunes $Q_{y,\text{set}} = 3.800$ and 3.810 (see example BPM difference signals over 20 turns for $Q_{y,\text{set}} = 3.800$ in figure 7.16 and the original figures 6.5 and 6.6). For a tune of $Q_{y,\text{set}} = 3.820$, the situation was different in that there appeared to be a threshold beam size, below which mode $m = 0$ was observed (figure 6.7). Therefore, the theoretical prediction that the mode structure is independent of vertical beam size appeared to hold true provided the growth rate was large enough for the mode to be distinguished on the BPM difference signal. It should be noted that the mode structures were not always clearly defined and a mixture of two modes could be possible. As experimentally observed in the study of the head-tail instability as a function of vertical tune on ISIS (section 5.4.2), the mode structure varied as the vertical tune was changed.



(a) $\epsilon_{y,\text{RMS}} = 10\pi$ mm mrad **(b)** $\epsilon_{y,\text{RMS}} = 13\pi$ mm mrad **(c)** $\epsilon_{y,\text{RMS}} = 33\pi$ mm mrad

Figure 7.16: BPM sum and difference signals over 20 turns, before beam was lost, for three selected initial vertical beam RMS emittances with $Q_{y,\text{set}} = 3.800$.

The unusual feature seen in the experimental vertical tune scan data, the effective bunch length, was also present in the BPM difference measurements as a

function of vertical beam size (see figure 6.8, tables 6.2 and 6.3). Sacherer's theory assumes the full bunch length oscillates and, given knowledge of the impedance as a function of frequency, is a primary driver in determining which head-tail instability mode is predicted to grow. The effective bunch length was observed to take up a larger fraction of the bunch length for higher-order mode structures (section 6.2.1). The experimentally observed effective bunch length was largely uncorrelated to the vertical beam size.

7.3.3.2 Head-Tail Instability in Frequency Domain

Observing the instability in the frequency domain, using an FFT on the BPM difference signal, allows a comparison between the measured betatron sideband spectrum and that predicted by Sacherer's theory. The predicted spectra envelope, h_m, may be calculated for the given mode m for each measurement using the vertical tune (measured from the BB frequency), the chromaticity [93], the measured revolution frequency and an estimate of the full bunch length from the BPM sum signal. However, as already noted, only part of the full bunch length oscillated. The measured betatron sideband spectra with the h_m envelopes overlaid, calculated using the full bunch length (τ_b), is shown in figure 7.17a and calculated using the effective bunch length (τ_e) instead, in figure 7.17b.

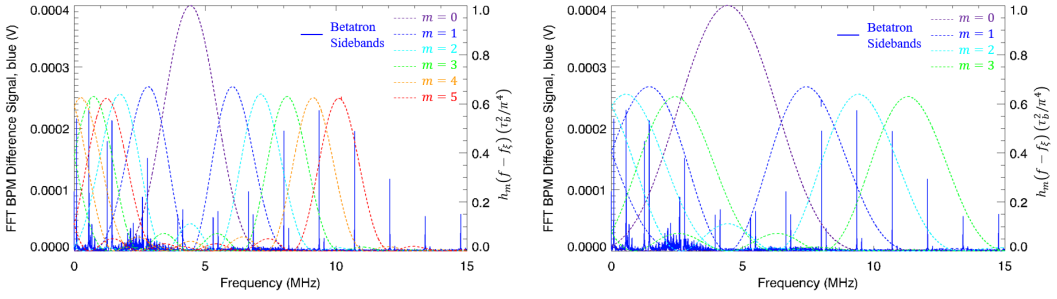


Figure 7.17: FFT of BPM difference signal around time point of interest for $Q_{y,\mathrm{set}} = 3.800$ ($Q_{y,\mathrm{meas}} = 3.867$) and initial $\epsilon_{y,\mathrm{RMS}} = 10\,\pi\,\mathrm{mm\,mrad}$. Calculated h_m overlaid for a) full bunch length $\tau_b = 520\,\mathrm{ns}$ and b) effective bunch length $\tau_\mathrm{e} = 280\,\mathrm{ns}$.

The expectation from the observed mode structure (figure 7.16a) would be that the betatron sideband amplitudes would follow the h_2 (cyan) envelope for

$Q_{y,\mathrm{set}} = 3.800$ for the full bunch length. Although there were clearly large sidebands within this envelope, there were also appreciable sidebands under the $m = 1, 3, 4$ and 5 mode envelopes. However, when the shorter, effective bunch length was utilised in the power spectra calculations, the measured betatron sidebands followed the predicted envelope for $m = 2$ far more closely (figure 7.16b). The precise shape of the predicted spectrum envelope is given by the sinusoidal mode assumption. It should be noted, however, that other oscillatory solutions to Sacherer's integral equation (from different assumed bunch distributions) exist and result in different spectra envelopes [43].

For other measurements, at different tunes and vertical beam sizes, the case was less clear, with many asymmetric spectra around the chromatic frequency, whereas the predicted spectra envelope is always symmetric. The effective bunch length was also variable. As in the tune scan comparison between experiment and theory, Sacherer's theory's predictions for spectra only reliably provide the frequency range of appreciable sidebands, between the resonator frequency, $\sim f_{\mathrm{res}}$, and $\sim 2f_{\xi} + f_{\mathrm{res}}$.

7.3.3.3 Head-Tail Instability Growth Rate Versus Baseband Frequency and Beam Size

Figure 7.18 shows a comparison of the head-tail instability growth rate as a function of betatron BB frequency between the prediction from Sacherer's theory (figure 7.5) and the experimentally measured growth rate of the BB for four example beam sizes covering the full range measured (tables 6.2 – 6.4).

The primary conclusion from these data is that the instability growth rate was dependent on the vertical beam size with smaller beam sizes driving faster growth rates, whereas the theory predicts no dependence. Therefore, the results suggested there was a beam size dependent impedance present. It should be noted that Sacherer's theory does not include the effects of space charge, which is expected to vary appreciably with beam size, and the impedance used in the predicted growth rate is independent of beam size, so full agreement was not expected.

Despite the discrepancies already mentioned between predictions and observations, the growth rate as a function of tune (BB frequency) matched well with

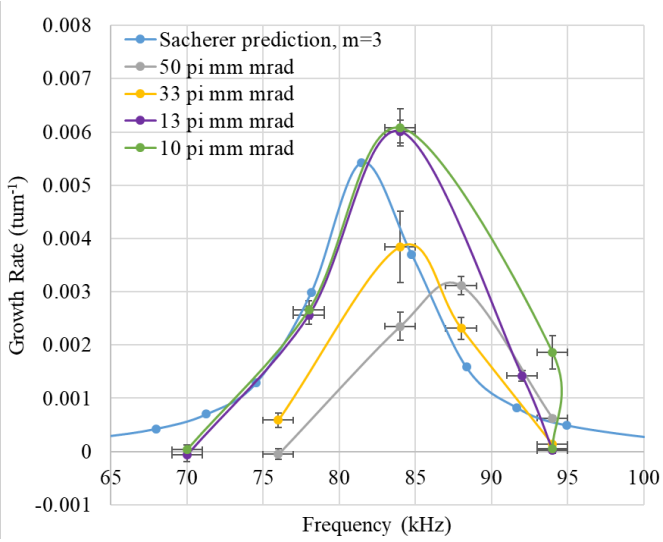


Figure 7.18: Growth rate versus vertical betatron BB frequency for selected vertical beam sizes (dictated by the peak "vertical sweeper" current) and that predicted from Sacherer's theory for a head-tail mode $m = 3$ in blue.

the observed growth rate in the peak's frequency and width. The frequency of the measured growth rate peak varied slightly between 80 and 88 kHz over the vertical beam sizes investigated with a modal average of 84 kHz. This was slightly different to the predicted peak of 82 kHz but within the error of the resonator fit to the beam-based impedance measurements. The observed peak was also slightly broader and often asymmetric, although the asymmetry was not consistently either to a higher or lower frequency than that of the peak. The resonator impedance's quality factor may be altered to fit the observed peak width better. However, assuming one ideal narrowband resonator impedance the predicted growth rate is symmetric about the resonator frequency.

7.3.3.4 Summary and Effect of Transverse Space Charge

The discrepancies already outlined between the experimentally observed head-tail instability and that predicted from Sacherer's theory in its variation with vertical tune (see section 7.2.3.4) were still present as the vertical beam size was modified. The measured mode and resultant sideband spectra remained different to predictions and vertical beam size was observed to have minimal effect on these (apart from the instability onset as the beam size was reduced at $Q_{y,\mathrm{set}} = 3.820$,

figure 6.7). This leads to a conclusion that vertical beam size played a negligible role in the mode observed but may include a beam size threshold for when an instability may be observed.

A primary difference between experiment and theory was that only a fraction of the full bunch length was vertically unstable. The measurements showed little variation in the effective bunch length with beam size (apart from where there ceased to be an instability). The fraction of bunch that oscillated was, however, linked to the mode excited and the vertical tune (as the mode changed with tune). Neither Sacherer's theory, nor the various models of the head-tail instability with space charge, directly predict this type of behaviour. These elements mean that there is little predictive power for the observed ISIS head-tail instability in the Sacherer model. Without prior knowledge of the effective bunch length, the head-tail mode structure and associated sideband spectra cannot be predicted.

The growth rate for the head-tail instability, as measured from the growth of the vertical betatron BB indicated a strong correlation with the vertical beam size, contrary to theoretical predictions. The larger the beam size, the slower the growth rate of the head-tail instability, with the mode number remaining unaffected. The growth rate prediction from Sacherer's theory (assuming sinusoidal modes and a narrowband impedance and a dominant $m = 3$ mode) lies in the middle of the spread of peak amplitudes for the different beam sizes. It is likely that the measured variation in growth rate with beam size was due to an impedance that varies in the same way with beam size (the space charge impedance increases with decreasing beam size).

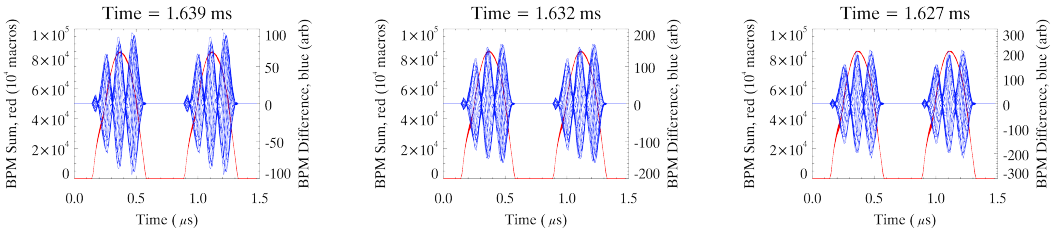
Although space charge on its own may not drive an instability, models of the head-tail instability with transverse space charge indicate that it has an impact on pre-existing head-tail instability dynamics (section 3.4.2). Blaskiewicz's model [53] predicts that head-tail modes will shift as a function of the space charge strength (or more particularly the "space charge parameter", $q = \Delta Q_{\mathrm{SC}}/Q_s$); and for "strong" space charge ($q \gg 1$), the various models predict Landau damping driven by the space charge tune spread. However, it should be noted that these models

typically refer to TMCI rather than the uncoupled modes of the head-tail instability. Space charge's role in the head-tail instability on ISIS requires further investigation including analysis of the instability as a function of beam intensity and simulation (see next section, 7.3.4).

7.3.4 Comparison Between Theory and Simulations

7.3.4.1 Head-Tail Instability Mode Structure

PyHEADTAIL simulations of the head-tail instability as a function of vertical beam size were performed without (section 6.3.2) and with transverse space charge (section 6.3.3). Results without the effect of transverse space charge showed intrabunch $m = 0$, 2 and $m = 3$ mode structures (for $Q_y = 3.870$, 3.890 and 3.880 respectively, figures 6.17 – 6.19) in the simulated BPM difference signal. The change in mode with tune was not expected from Sacherer's theory (section 7.2.2). Figure 7.19 illustrates the general finding that, without tranverse space charge, the head-tail mode structure was unaffected by changes to the vertical beam size. This was expected in this case as the impedance applied in PyHEADTAIL (a narrowband resonator) has no beam size dependence. The only dependence on beam size in the simulations (without transverse space charge) was the fixed aperture which resulted in earlier simulated beam-loss for larger beam sizes, but made no change to the instability dynamics.

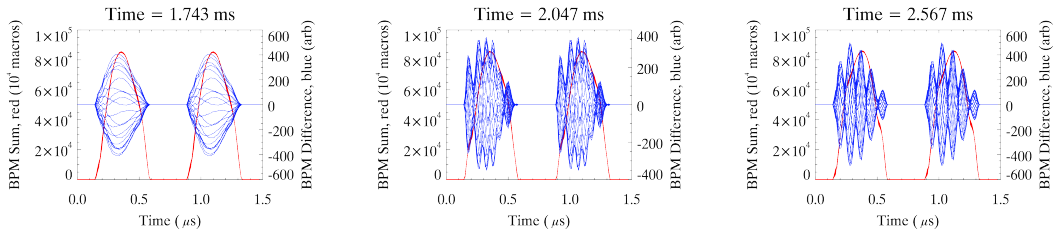


(a) $\epsilon_{y,\mathrm{RMS}} = 10\,\pi$ mm mrad **(b)** $\epsilon_{y,\mathrm{RMS}} = 30\,\pi$ mm mrad **(c)** $\epsilon_{y,\mathrm{RMS}} = 50\,\pi$ mm mrad

Figure 7.19: Simulated BPM sum and difference signals (without transverse space charge) over 20 turns, before beam was lost, for three selected vertical RMS emittances at $Q_y = 3.890$.

The inclusion of transverse space charge in PyHEADTAIL simulations altered the head-tail mode excited for several beam sizes and betatron tunes. Unlike the

simulations with transverse space charge for the tune scan case (section 5.5.3) which only showed mode $m = 0$ intrabunch motion, these simulations showed mode numbers $m = 4, 5$ and possibly 6 and 7 as well as the dominant $m = 0$ mode (for example, figure 7.20). The variability of intrabunch motion with beam size appeared to be due to the inclusion of transverse space charge.



(a) $\epsilon_{y,\mathrm{RMS}} = 10\,\pi$ mm mrad **(b)** $\epsilon_{y,\mathrm{RMS}} = 30\,\pi$ mm mrad **(c)** $\epsilon_{y,\mathrm{RMS}} = 50\,\pi$ mm mrad

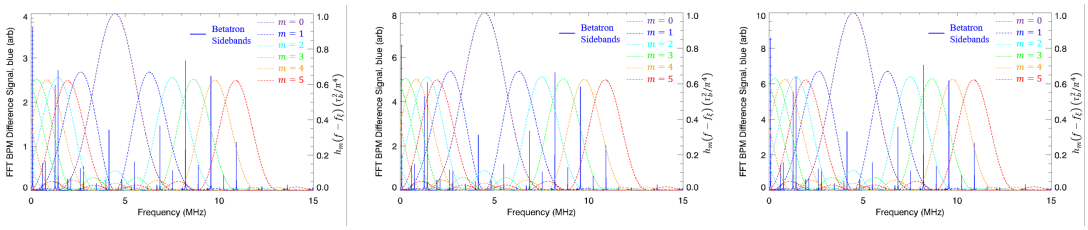
Figure 7.20: Simulated BPM sum and difference signals (with transverse space charge) over 20 turns, before beam was lost, for three selected vertical RMS emittances at $Q_y = 3.880$.

The change in mode structure with beam size in simulation was important as it illustrated the significance of including transverse space charge in the model of the head-tail instability on ISIS, even if it did not directly correlate to experimental findings. Recent theoretical models of head-tail including space charge do not explicitly predict the variation of mode with beam size (section 3.4.2) except perhaps [54, 57].

7.3.4.2 Head-Tail Instability in Frequency Domain

As shown previously, the spectra envelope (defined by h_m) may be calculated for each simulation and compared to the simulated BPM difference spectra. The chromaticity, slip factor (η), revolution frequency and bunch length were all constant between simulation runs, with the only difference being the vertical tune and beam size as they were scanned. The vertical tune changed the chromatic frequency shift ($\omega_{\xi,y} = \xi_y Q_y \omega_0/\eta$, equation 3.40), thus shifting the spectra slightly in frequency. The vertical beam size, however, had no effect on h_m.

Figure 7.21 shows the FFT of the simulated BPM difference signals, without transverse space charge, for the same tune and beam sizes as selected in figure 7.19.

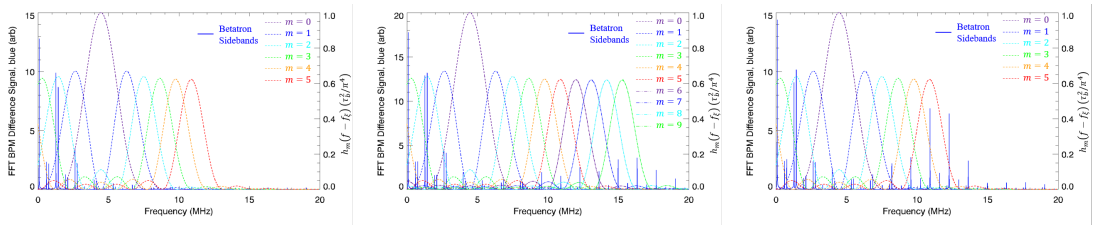


(a) $\epsilon_{y,\mathrm{RMS}} = 10\,\pi$ mm mrad **(b)** $\epsilon_{y,\mathrm{RMS}} = 30\,\pi$ mm mrad **(c)** $\epsilon_{y,\mathrm{RMS}} = 50\,\pi$ mm mrad

Figure 7.21: FFT of simulated BPM data without transverse space charge, prior to beam-loss, for three selected vertical RMS emittances at $Q_y = 3.880$, with h_m overlaid ($m = 0$ – 5, dotted lines).

The predicted sideband envelopes, h_m, for head-tail modes $m = 0$ – 5 are also shown. The betatron sideband spectra were very similar, as expected from the similar intrabunch structures observed in figure 7.19. The theoretical power spectra, h_3, defined a reasonable envelope for the betatron sidebands, which also matched with the observed intrabunch mode structure ($m = 3$).

From the predicted power spectra envelope and the applied narrowband impedance close to zero frequency (at 82 kHz), it may be seen why a mode $m = 3$ is predicted, with a large value of h_3 around the resonator frequency and lowest frequency sideband. As expected, the vertical sideband closest to the frequency of the minimum in the real part of the impedance (the vertical BB) was the largest (figure 7.2a). For PyHEADTAIL simulations without transverse space charge, the betatron sideband spectra matched well with predictions from Sacherer's theory.



(a) $\epsilon_{y,\mathrm{RMS}} = 10\,\pi$ mm mrad **(b)** $\epsilon_{y,\mathrm{RMS}} = 30\,\pi$ mm mrad **(c)** $\epsilon_{y,\mathrm{RMS}} = 50\,\pi$ mm mrad

Figure 7.22: FFT of simulated BPM data with transverse space charge, prior to beam-loss, for three selected vertical RMS emittances at $Q_y = 3.880$, with h_m overlaid ($m = 0$ – 5, dotted lines).

With transverse space charge, PyHEADTAIL simulations revealed very different betatron sideband spectra as exemplified in figure 7.22, together with the predicted

sideband spectra envelope. The predicted envelopes no longer matched with the observed spectra. For small vertical beam sizes, the simulated spectra were centred around zero frequency whereas the predicted spectra are centred around the vertical chromatic frequency. As the beam size was increased and the transverse space charge reduced, the spectra matched more closely with the predicted h_m bunch power spectra for the mode observed in figure 7.20.

For an initial RMS vertical beam emittance of $30\,\pi$ mm mrad, the betatron sidebands were of appreciable amplitude under the mode envelopes for $m = 2$ and 3 at low frequency and $m = 9$ at high frequency. As such, it was very asymmetric about the chromatic frequency. Also, the observed intrabunch mode structure exhibited five intrabunch nodes ($m = 5$, figure 7.20b) which does not tie in with the predicted spectra for that mode (h_5, red). At the largest vertical beam emittance simulated ($\epsilon_{y,\mathrm{RMS}} = 50\,\pi$ mm mrad), the betatron spectra were still asymmetric about the chromatic frequency, but with appreciable sidebands under $m = 2$ and 3 at low frequency and $m = 5$ at higher frequencies. The observed intrabunch structure was an $m = 4$ head-tail mode.

It is clear that the prediction no longer matched the simulations when transverse space charge was included. As space charge is not included in Sacherer's theory of the head-tail instability, a match was not likely to be expected. As the vertical beam size was reduced, thereby increasing the transverse space charge, the predicted spectra differed more and more from the simulated betatron sideband spectra. It may be possible that transverse space charge was shifting the chromatic frequency. It should also be noted that there was no coherent tune shift in the simulations as there were no boundaries in the space charge calculations. The incoherent tune will vary along the bunch, modulated by the line density which would alter the chromatic frequency. Further research would be needed to confirm this.

7.3.4.3 Head-Tail Instability Growth Rate Versus Baseband Frequency and Beam Size

A comparison between the predicted head-tail instability growth rate from Sacherer's theory and that deduced from the growth of the vertical BB in PyHEADTAIL

simulations without transverse space charge is shown in figure 7.23, as a function of vertical betatron BB frequency and initial RMS vertical beam emittance. Despite minor differences in the observed mode as a function of tune, the amplitude, frequency and width of the peak in growth rate matched reasonably well with that predicted from the simplified Sacherer model. As expected, the growth rate was entirely unaffected by the initial vertical beam size as there was nothing in the PyHEADTAIL simulation that was beam size dependent apart from the fixed beam pipe aperture. However, as the growth rate was determined before the beam encountered the aperture, this played no role in the beam dynamics.

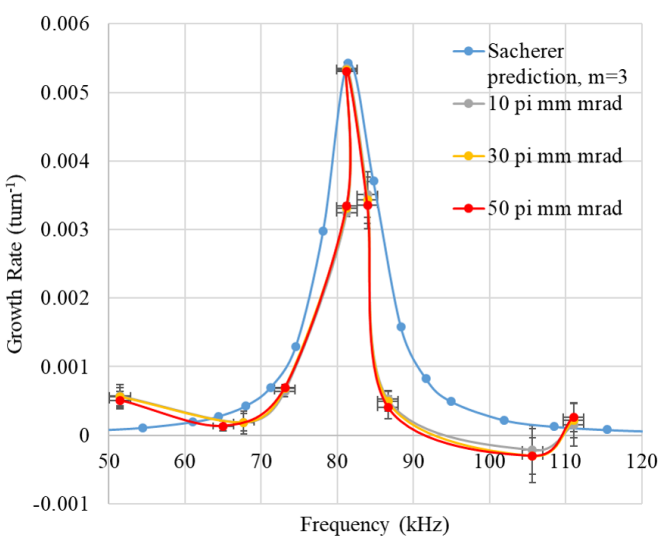


Figure 7.23: Growth rate versus betatron BB frequency for PyHEADTAIL simulations without transverse space charge for selected initial RMS vertical emittances and that predicted from Sacherer's theory for a head-tail mode $m = 3$ in blue.

When transverse space charge was added to the PyHEADTAIL model of ISIS in BSRM, the head-tail instability growth rate became dependent on the vertical beam size, as shown in figure 7.24. The peak's amplitude was a function of the initial beam emittance, unlike the peak's frequency and its width (which were largely unchanged). As vertical beam emittances were reduced, head-tail growth rates at $Q_y = 3.880$ increased approximately linearly over the range of emittances simulated (see figure 6.30). At $Q_y = 3.870$, the growth rate increases linearly but only below $30\,\pi$ mm mrad; above this threshold emittance the growth rate was flat.

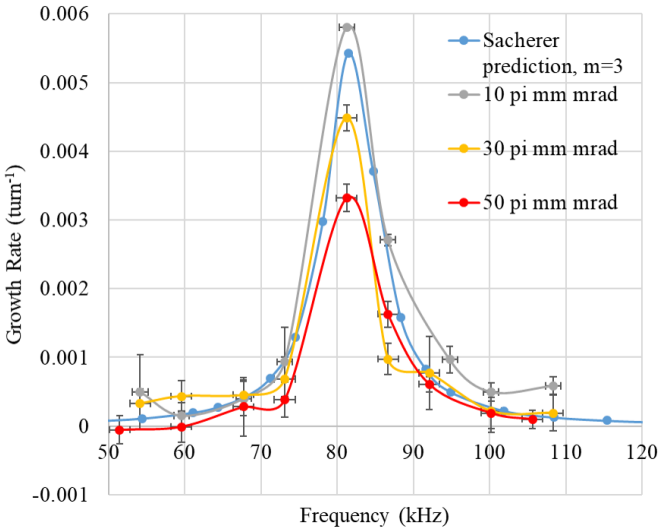


Figure 7.24: Growth rate versus betatron BB frequency for PyHEADTAIL simulations including transverse space charge for selected initial RMS vertical emittances and that predicted from Sacherer's theory for a head-tail mode $m = 3$ in blue.

This trend in head-tail instability growth rate with vertical beam size is not predicted in Sacherer's model if a resonator impedance is assumed and clearly arises due to the addition of space charge in simulations. Models of the head-tail instability with space charge (see section 3.4.2) mostly suggest a decrease in growth rate with space charge due to increased Landau damping. However, particularly in the model of Ho Chin *et al.* [54], a series of stable and unstable regions is predicted as transverse space charge is increased (specifically increasing the incoherent space charge tune shift whilst holding the wake strength, and hence intensity, constant).

It should be noted that this model assumes a constant wake potential, independent of the distance between the particles, whereas the resonator wake potential is not. However, the example presented by Ho Chin *et al.* (particularly figure 4 of [54] reproduced here as figure 7.25) is illustrative in its prediction of the behaviour of TMCI with space charge, especially its expectation of a series of pass and stopbands.

At $Q_y = 3.880$ and large vertical emittance, one can imagine sitting just above a passband (the black regions in the figure with zero head-tail growth). As the vertical emittance is reduced, the space charge tune shift and "space charge parameter", q, are increased whilst the wake strength remains constant. This results in larger

growth factors over a narrow range of q. Increasing q yet further results in passing over the peak in growth rate and into a region of lower growth rates.

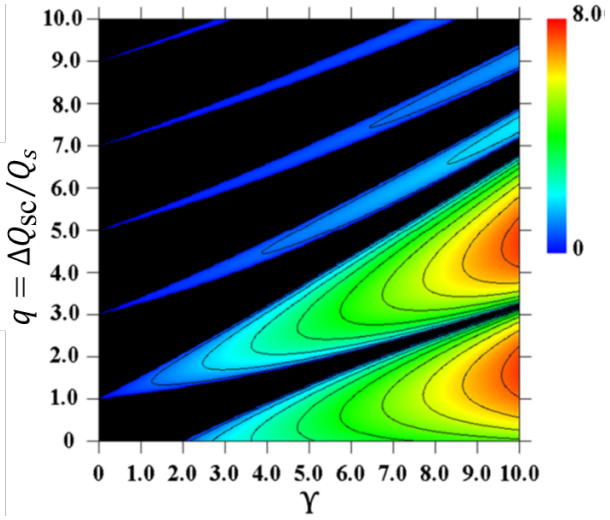


Figure 7.25: Reproduction of figure 4 of [54]: 2D contours of the head-tail growth factor as a function of wake strength, Υ, and space charge parameter, $q = \Delta Q_{\mathrm{SC}}/Q_s$.

Also, at $Q_y = 3.870$ and large emittance, one can imagine sitting just above a stopband (in one of the black passbands). Therefore, as the initial vertical emittance is reduced and q increases, the head-tail growth remains zero until the next stopband is reached. Further decreases in vertical emittance then result in entering the stopband which increases the head-tail growth rate, as observed below $30\,\pi$ mm mrad in simulations. However, it is noted that q changes considerably due to the change in vertical emittance: $q = 2.4$ at $50\,\pi$ mm mrad and $q = 12.0$ at $10\,\pi$ mm mrad. Considering figure 7.25, the simulations cover several pass and stopbands but this was not seen in the simulated growth rates. Therefore, further qualitative and quantitative comparisons with this model and that of Buffat *et al.* [57] are planned (see section 8.3).

7.3.4.4 Summary and Effect of Transverse Space Charge

PyHEADTAIL simulations of ISIS in BSRM, without transverse space charge, as a function of vertical beam size, produced head-tail intrabunch mode structures that matched reasonably well with those predicted from Sacherer's theory, as seen in the simulations as a function of vertical tune. As expected from theory with

an applied narrowband resonator impedance, varying the initial vertical beam size had no effect on the observed mode structure.

With the addition of transverse space charge, the simulations produced appreciably different mode structures, with $m = 0, 4, 5$ and possibly 6 and 7 observed. For $Q_y = 3.870$ and 3.880, an apparent threshold of mode structure with emittance was seen where the mode went from $m = 0$ to a much higher mode ($m = 5, 6$ or 7) when the initial vertical emittance was increased. As has been noted previously, Sacherer's theory does not include the effects of space charge, so full agreement should not be expected. However, from these simulations, it may be concluded that transverse space charge plays an important role in the head-tail instability on ISIS, even at the reduced beam intensities used in these simulations.

Importantly, all the head-tail instability modes simulated, with or without transverse space charge, occur over the entire bunch length. However, experimental observations as a function of vertical tune and vertical beam size consistently exhibited vertical dipole oscillations over a fraction of the full bunch length. Therefore, the simulations as a function of beam size provide further evidence that this discrepancy is likely neither due to direct transverse space charge nor the long bunches created on ISIS.

The simulated bunch spectra without transverse space charge matched well with predictions of the sideband envelope for the expected mode number. However, when transverse space charge was included, the spectra did not match predictions for the observed mode. As the initial vertical beam size was increased, and space charge reduced, the spectra began to align better with the predicted envelope.

The PyHEADTAIL simulations without transverse space charge produced head-tail growth rates as a function of tune (and vertical BB frequency) that matched very well with theory. This was expected as the impedance parameters were chosen to match the experimentally observed peak amplitude and width. Varying the initial beam size did not change the head-tail growth rate.

Including transverse space charge, PyHEADTAIL simulations still matched the frequency and width of the predicted growth rate peak but with an amplitude

dependent on the initial vertical emittance. Increasing the initial vertical beam size resulted in a lower peak head-tail growth rate and an approximately linear dependance of growth rate with vertical emittance. Head-tail models with transverse space charge, particularly Ho Chin *et al.* [54] and Buffat *et al.* [57], may begin to explain this phenomenon qualitatively. Further investigations are planned to study this effect (see section 8.3).

7.4 Summary

The results presented in this chapter indicate that predictions from theory, particularly Sacherer's and Rees' theories, did not accurately represent the head-tail instability dynamics (mode or spectra) for measurements on ISIS. In particular, in the case of Sacherer's theory, the observed mode was consistently lower than predicted, only part of the bunch length exhibited vertical dipole oscillations and the mode was observed to change rapidly with tune. Despite these differences, the predicted growth rate of the instability as a function of vertical tune (vertical BB frequency) matched well with predictions. However, this may be an artefact of utilising similar theoretical methods to obtain the measured effective impedance from growth rates in coasting beams, which was then used to predict the head-tail instability growth rates for bunched beams.

Another key difference from theoretical predictions was the variation of peak head-tail growth rate as a function of vertical beam size. Assuming a narrowband or resistive wall impedance, Sacherer's theory predicts no dependence of instability growth rate on vertical beam size, whereas experiment showed a strong correlation. However, theory does predict that the mode and associated spectra should be unaffected by changes in vertical beam size, which was largely corroborated in experimental measurements.

Although Sacherer's theory is the most benchmarked and well-established theoretical model available, it implicitly assumes $\beta = 1$, whereas the instability was observed (both in operations and in BSRM) at far lower β values. Also, Sacherer's theory does not include the effects of transverse space charge which

have been found to have a significant effect on head-tail instability dynamics, even at the reduced intensities used in these BSRM experiments. Therefore full agreement should not be expected.

PyHEADTAIL simulations have enabled a detailed look at the head-tail instability on ISIS and how it compares to theoretical predictions whilst also providing insight into the effect of transverse space charge. Simulations without transverse space charge largely matched with theoretical predictions in mode, spectra and growth rate, although simulations did show a small variation in mode with tune which was not predicted.

Adding a model of transverse space charge to the simulations had a significant effect on the head-tail mode excited and its frequency spectra. Some comparisons may be drawn between the simulations with space charge and recent head-tail models that include its effects, particularly the work of Ho Chin *et al.* [54] and Buffat *et al.* [57]; in particular, the qualitative comparisons of head-tail instability growth rates as a function of vertical beam size between these theories and corresponding measurements and simulations.

I have fought the good fight, I have finished the race,
I have kept the faith.

— 2 Timothy 4:7 (NIV)

8 Conclusion

8.1 Introduction

This chapter outlines the primary achievements of the thesis in relation to head-tail instability experiments on ISIS (section 8.2) in both RCS and BSRM, simulations aimed at replicating the experiments in BSRM (section 8.3) and comparisons between these experimental and simulation results with predictions from head-tail instability theory, particularly that of Sacherer (section 8.4). The application of this research on ISIS operations, and its contribution to the wider community of high-intensity hadron accelerators (both current and future), are briefly summarised in section 8.5. Each section also includes ideas for future research and development.

8.2 Head-Tail Instability Experiments on ISIS

8.2.1 Thesis Achievements

A new, original campaign of experiments was designed to explore the dynamics of the head-tail instability on ISIS. Beginning with analysis of the head-tail instability as manifested in ISIS RCS operations (chapter 4) and its impact on accelerator efficiency, complications were highlighted when comparing results with theoretical predictions, motivating further study.

To probe the core physics behaviour of the head-tail instability on ISIS, a series of new experiments was performed in a simplified mode of operation: Storage Ring Mode (SRM). The synchrotron was comprehensively reconfigured to minimise less relevant effects and isolate important observations for comparison with established theory and advance understanding of this key loss mechanism. As part of this study, a set of detailed measurements was taken in SRM to determine the dominant impedances on the machine (section 5.2) indicating a large, low-frequency narrowband impedance that could drive the observed vertical head-tail instability.

In order to investigate the head-tail instability the beam needs to be bunched. As such, a new operating mode for ISIS was developed: BSRM (section 5.3). This enabled study of the instability without the complexities of acceleration, sweeping revolution and betatron frequencies, making the experimental data easier to analyse, understand and interpret. Furthermore, the experiments were undertaken at a much lower beam intensity (in order to reduce the effects of space charge) and with only one RF harmonic, simplifying the particle dynamics and making measurements more readily comparable to theoretical predictions.

In the new operating mode, careful measurements were made of beam motion and associated frequency spectra, beam-loss and intensity to characterise the head-tail instability on ISIS systematically as a function of key, selected beam and lattice parameters (chapters 5 and 6). Observations of the head-tail instability on ISIS were presented as a function of vertical betatron tune (section 5.4) and of vertical beam size (section 6.2) as these provide important insights into the effects of the driving impedance and space charge. From these detailed new measurements, the head-tail instability was characterised by the intrabunch mode excited, the vertical betatron sideband spectra and the instability's growth rate as a function of the selected parameters. These new, original measurements provide important insight into the head-tail instability on ISIS and supply invaluable reference data for benchmarking of simulation codes and head-tail instability theory.

Key results were noted including a confirmation of a low-frequency narrowband impedance driving the observed vertical head-tail instability, intrabunch mode

variation with small changes in vertical tune, an increase in instability growth rate with a decrease in initial RMS vertical emittance and the novel phenomenon of an effective bunch length. These features provided important reference characteristics which were then explored in dedicated simulations (as a function of tune in section 5.5 and beam size in section 6.3) and compared to predicted behaviour from Sacherer theory (chapter 7).

8.2.2 Plans for Future Research

It is planned to continue investigations in BSRM, particularly focusing on behaviour as a function of beam intensity. This should enable a better understanding of the role transverse space charge is playing in the instability dynamics and help probe the possible observation of a TMCI (sections 5.4.4 and 6.2.3). The experimentally observed asymmetry in the head-tail intrabunch mode structure, particularly near to the peak in growth rate, could also be due to mode coupling or simply due to the size of the impedance. Recent research [68] on the head-tail mode structure before, during and after mode coupling is planned to be explored in more detail with experiments as a function of beam intensity.

Further experiments using BSRM are also planned, varying the bunch distribution both longitudinally and vertically. The vertical painting may be altered, using the dedicated "vertical sweeper", to create different painted distributions and the RF voltage can be changed during storage, altering the longitudinal distribution and synchrotron tune. Measurements will help characterise how the bunch distribution affects the head-tail instability characteristics.

Research is ongoing to build up the impedance model of the ISIS synchrotron [98]. Although a low-frequency narrowband impedance was found at around 82 kHz which drives the head-tail instability in BSRM, the source of the impedance is not confirmed. Studies currently point to the RF shields used in the fast ramping magnets with measurements planned to test this. Furthermore, the head-tail instability observed in RCS operation occurs at a higher vertical baseband frequency which did not excite appreciable head-tail motion in BSRM. Further calculations,

beam-based and bench measurements of impedance will improve the impedance model of ISIS and should help identify the driving impedance of the head-tail instability in operations as well as that in BSRM.

An extension of measurements made of the head-tail instability on ISIS in RCS mode is planned aimed at a more detailed exploration of the instability's behaviour as a function of intensity and beam distribution whilst beam frequencies are rapidly changing. Developments are also underway for a new Medium-Energy Beam Transport (MEBT) between the ISIS RFQ and DTL [100]. These include a beam chopper synchronised to the ring RF to enable chopped, multi-turn injection, lowering beam-losses associated with re-bunching the beam in the synchrotron. The chopper is also specified to be able to inject into only one of the two RF buckets, enabling the capture and acceleration of a single bunch. As such, the head-tail instability can be further explored in this different mode of operation.

Recent studies on the CERN PSB [101], have shown similar effective bunch length behaviour as well as mode structure asymmetries driven by a narrowband impedance (albeit in the horizontal plane at a higher frequency and quality factor). Of particular interest is the change in behaviour with chromaticity (currently not possible on ISIS). Similar experimental and simulation work has also recently taken place on the CERN SPS, exploring TMCI as a function of space charge by varying the transverse emittance [102]. Although there are some distinct differences in behaviour from those observed at ISIS (intrabunch motion is not centred on the bunch centre but shifted toward the tail). Further studies are planned to analyse ISIS measurements in the light of both these investigations.

8.3 Simulations of the Head-Tail Instability

8.3.1 Thesis Achievements

A new, detailed instability model of ISIS, including space charge, was established with the existing simulation framework PyHEADTAIL and verified with appropriate benchmarks and convergence tests to ensure reliable simulation results. The model was set up to replicate all the key aspects of the experimental campaign in BSRM

described in chapters 5 and 6. This included matching the longitudinal and vertical bunch distributions to idealised distributions and ensuring the beam and lattice parameters were as close to experimental settings as possible.

The experiments in BSRM were replicated in the PyHEADTAIL model and the results recorded and analysed in the same way. Simulated measurements were presented in the same manner as the experimental data as a function of vertical betatron tune (section 5.5) and initial vertical emittance (section 6.3) and the resulting instabilities characterised by intrabunch mode excited, betatron sideband spectra and instability growth rate. The simulations were also performed with and without transverse space charge in order to clarify its effects, thus providing the most advanced simulations of the instability yet achieved on ISIS and the most complete model of the experiments currently possible.

Comparisons were drawn between the simulated data (with and without transverse space charge) and the experimental measurements, providing critical information on the validity of the code and the influence of space charge. As with the experimental measurements, the simulated instability characteristics were also compared with predictions from Sacherer's theory (see section 8.4). The inclusion of transverse space charge in simulations had an appreciable affect on head-tail instability dynamics, even at the reduced beam intensities utilised in the experiments. Simulations with transverse space charge matched key features of the experimental data: the growth rate as a function of vertical tune and beam size. However, the experimentally observed head-tail mode number, the change in mode with tune, the associated BPM sideband spectra and the effective bunch length phenomenon were not replicated.

8.3.2 Plans for Future Research

It is planned to explore the nature of the instability further in simulations of BSRM as the intensity and bunch distribution are changed, matching the proposed experiments (section 8.2.2). As with the studies presented in this thesis, the simulations will illuminate the effect of direct space charge on the head-tail instability.

Simulations will be performed using PyHEADTAIL as well as a Vlasov solver recently developed at ISIS [98]. The resulting data should enable study of possible TMCIs and provide benchmarks for existing theories that include space charge (see section 8.4.2). This will include reference to intrabunch mode structures, and their assymetries [68] as well as the instability growth rate as a function of intensity.

PyHEADTAIL simulations are also planned to explore head-tail instability dynamics in the RCS mode of operation. It is proposed to utilise recent investigations into the impedances present on the ISIS synchrotron [92, 98] to explore their effects on vertical coherent motion in PyHEADTAIL simulations in RCS mode (and BSRM) and as a function of beam intensity. The aim being to pin down the driving impedances and head-tail instability mechanism in RCS operation, and explore what cures and mitigation techniques may be employed to improve accelerator efficiency.

Simulations will be particularly useful in finding the cause of the observed effective bunch lengths, with the ability to switch various physical processes on and off (*e.g.* space charge and applied impedances). Possible further avenues for research include the effects of low relativistic β, bunch distribution and those of image forces.

Collaborative work will continue in order to develop, enhance and maintain the various instability codes. These are essential in order to bridge the gap between experiment and theory, particularly with the addition of space charge and image effects. Further work is planned to improve the physics models available within the PyHEADTAIL framework, focusing on image effects and benchmarking against experiment and proposed theories.

8.4 Comparison with Head-Tail Instability Theory

8.4.1 Thesis Achievements

Relevant head-tail instability theory was reviewed (section 3.3.1) and various expanded theories, including the effect of transverse space charge, were briefly introduced (section 3.4). Using measurement of the effective transverse impedance (section 5.2) and simple beam and lattice parameters, Sacherer's theory was used to

make predictions of the dominant head-tail modes, frequency spectra and growth rates for comparison with the experimental and simulation results (chapter 7) as a function of vertical tune (section 7.2.2) and as a function of initial vertical beam size (section 7.3.2).

Experimental measurements agreed reasonably with theoretical predictions of the instability growth rate in both its amplitude and its variation with vertical tune. Also, as predicted, the observed intrabunch mode structures were largely unaffected by the vertical beam size. However, several discrepancies were found with experiments showing a consistently unexpected mode being driven, mode changes with vertical tune, the effective bunch length phenomenon, asymmetric betatron sideband spectra (around the chromatic frequency) and a growth rate dependent on the initial vertical beam size. Furthermore, measuring the head-tail behaviour as a function of vertical beam size on ISIS showed a possible threshold beam size for instability (below which the instability would occur).

Simulations without transverse space charge agreed well with predictions of head-tail characteristics from Sacherer's theory, as expected. The only difference noted being a mode change observed as a function of vertical tune which may be due to bunch distribution assumptions. However, with the addition of transverse space charge, simulations differed from the predicted behaviour with unexpected mode structures, mode changes with vertical beam size, asymmetric betatron sideband spectra (around the chromatic frequency) and instability growth rate changes as a function of beam size. These simulations still produced the expected intrabunch oscillations along the full bunch length (rather than the shorter, effective bunch length observed in experiments) with growth rates matching the predicted variation with vertical baseband frequency, although the simulated shunt impedance, R_s, had to be reduced to match the expected growth rate amplitude.

The discrepancies listed were discussed with reference to recently proposed head-tail theories including space charge for both experiment (sections 7.2.3.4 and 7.3.3.4) and simulation (sections 7.2.4.4 and 7.3.4.4). The addition of transverse space charge, both in simulation and in theory, appeared to explain the experimentally

observed variation of instability growth rate with vertical beam size. Particular note was made to the study of Ho Chin *et al.* [54] with the associated prediction of a series of pass and stopbands as space charge is increased. However, the proposed instability theories make little to no reference to changes in mode or betatron spectra with tune, or effective bunch lengths. Experimentally observed mode structure asymmetries, and the possibility of a TMCI, were discussed in reference to the work by Métral [68, 99].

8.4.2 Plans for Future Research

Further study and analysis of existing, and future experimental and simulated data is planned with reference to models of the head-tail instability with transverse space charge. Studies are expected to focus on calculated predictions using Blaskiewicz's "airbag" model [53], the intrabunch mode asymmetries of Métral [68, 99], the circulant matrix model of Buffat *et al.* [57] and the pass and stopbands of Ho Chin *et al.* [54]. Investigations will particularly focus on measurements and simulations of the head-tail instability on the ISIS synchrotron, as a function of beam intensity.

Simulations are planned to extend the initial study of Kornilov *et al.* [59], including the effects of indirect space charge on the beam in the hope of replicating the observed instability thresholds. The inclusion of image effects in simulation may also help identify if they are responsible for the effective bunch lengths observed.

Further research into the relative impact of low β operation (*i.e.* much below 1) and bunch distribution assumptions on predictions of Sacherer's theory will help ascertain their relative importance in the case of head-tail instabilities at ISIS and similar accelerators (*e.g.* those listed in section 1.1.1).

8.5 Application and Impact on ISIS Operations

8.5.1 Thesis Achievements

The challenges of operating a high-intensity hadron accelerator were briefly summarised in section 1.2 with beam instabilities often acting as the limiting factor in the intensity achievable (section 1.3). The ISIS synchrotron is amongst a small

number of accelerators worldwide (section 1.1) that push the intensity limits and are able to provide a testbed for new high-intensity hadron machines being proposed, including ISIS-II. The studies in this thesis provide evidence of the impact the head-tail instability has on these machines and provides much needed experimental and simulation data characterising the instability as a function of tune, beam size and the effect of transverse space charge.

Research into the head-tail instability is pivotal to understanding what drives the instability and whether it may be completely avoided, or what mitigation techniques are most effective in reducing beam-losses, associated machine activation and increasing accelerator efficiency. The experimental and simulation findings of this thesis are informing accelerator tuning techniques to mitigate the head-tail instability on ISIS more effectively (section 4.3). They also provide a key reference for theoretical models which, once benchmarked, allow for accurate prediction of instability characteristics and provide the best route for fully optimised accelerator operation.

A core part of this research is in the development of an impedance model of the ISIS synchrotron, with particular reference to those impedances that can drive instabilities. Beam-based measurements of effective impedance presented in section 5.2 show the low-frequency narrowband that drives the head-tail instability in BSRM. Research into the head-tail instability on the PSB at CERN, [101], concluded the source of the driving impedance to be the extract kickers. This was also a prime suspect in the case of ISIS, however measurements suggests this is not the case. Recent studies [98] suggest the driving impedance for the head-tail instability in BSRM, and the impedance that drives head-tail motion in high-intensity RCS operations, is produced by the RF shields utilised in the fast ramping magnets. Measurements are planned to check this.

The development of a new operating mode for ISIS, BSRM, was described in section 5.3. This has enabled a simplified experimental setup to analyse the head-tail instability on ISIS without the complexities of acceleration and providing

finer control of beam parameters. This new mode of operation has since been utilised for many other accelerator physics studies.

8.5.2 Plans for Future Research

Recent studies to build up the ISIS impedance model [98], together with planned experiments and simulations, will help to identify the driving force behind the head-tail instability observed in RCS operation. When found, research will focus on whether the source of the impedance can be completely removed or reduced. Regardless, identification of the impedances present in the machine is invaluable in being able to control them, providing essential data to benchmark simulations and theory and thereby give accurate predictions of beam behaviour.

Section 4.4 introduced the ongoing research and development into an active damping system on the ISIS synchrotron. It is planned to develop this system further, fully commissioning it to enable higher efficiency and maintainable operation of the ISIS synchrotron at the highest beam intensities [92]. Despite these developments, other instability mitigation strategies will continue to be researched in order both to understand the instability dynamics better and reduce the foreseeable operational dependence on the damping system. This is of particular importance with the recent drives toward increased energy efficiency and a smaller carbon footprint.

Work will continue towards a fully benchmarked instability model of ISIS enabling accurate predictions of beam behaviour in high-intensity RCS operations as well as new operating modes. Furthermore, if this model can also replicate behaviour observed at similar accelerators (section 1.1) then it will provide an invaluable tool both for current accelerator operations and for new and upgraded machines such as ISIS-II (section 2.2, [39]) or the HL-LHC [103].

If I have seen further it is by standing on the shoulders of Giants.

— Sir Isaac Newton, letter to Robert Hooke, 5th February 1675.

References

[1] I. Kapchinskij and V. Vladimirskij. "Limitations of Proton Beam Current in a Strong Focusing Linear Accelerator Associated with the Beam Space Charge". In: *Proc. of the International Conference on High Energy Accelerators and Instrumentation*. 1959, pp. 274–288.

[2] *ISIS Neutron and Muon Source, webpage*. `https://www.isis.stfc.ac.uk/`. Accessed: 19/01/2023.

[3] *SINQ, PSI, webpage*. `https://www.psi.ch/en/sinq`. Accessed: 19/01/2023.

[4] *European Spallation Source, webpage*. `https://europeanspallationsource.se/`. Accessed: 19/01/2023.

[5] *Spallation Neutron Source, ORNL, webpage*. `https://neutrons.ornl.gov/sns`. Accessed: 19/01/2023.

[6] *Japan Proton Accelerator Research Complex, webpage*. `http://j-parc.jp/c/en/`. Accessed: 19/01/2023.

[7] M. A. Plum *et al.* "SNS Proton Power Upgrade Status". In: *Proc. of IPAC19*. Melbourne, Australia, 2019, pp. 2124–2126.

[8] P. A. Zolnierczuk and R. Riedel. "Neutron Scattering Experiment Automation with Python". In: *Proc. of 17th Real-Time Conference*. Lisbon, Portugal, 2010.

[9] *ESS Activity Report 2021*. `https://europeanspallationsource.se/article/2022/07/04/ess-activity-report-2021`. Accessed: 19/01/2023.

[10] *Chinese Spallation Neutron Source, webpage*. `http://english.ihep.cas.cn/csns/`. Accessed: 19/01/2023.

[11] S. N. Fu *et al.* "Operation Status and Upgrade of CSNS". In: *Proc. of IPAC19*. Melbourne, Australia, 2019, pp. 23–27.

[12] H. Hotchi *et al.* "1 MW J-PARC RCS Beam Operation and Further Beyond". In: *Proc. of ICFA Advanced Beam Dynamics Workshop on High-Intensity and High-Brightness Hadron Beams (HB2021)*. Batavia, Illinois, USA, 2021, pp. 1–6.

[13] *European Organisation for Nuclear Research, CERN, webpage*. `https://home.cern/`. Accessed: 19/01/2023.

[14] *Neutron Time-Of-Flight Facility at CERN (n_TOF), webpage*. `https://ntof-exp.web.cern.ch/`. Accessed: 14/06/2023.

[15] *CERN High Luminosity Project, webpage*. `https://hilumilhc.web.cern.ch/`. Accessed: 19/01/2023.

[16] M. Meddahi *et al.* "LHC Injectors Upgrade Project: Towards New Territory Beam Parameters". In: *Proc. of IPAC19*. Melbourne, Australia, 2019, pp. 3385–3390.

[17] *International Workshop on Fixed Field Alternating Gradient Accelerators for 2022*. `https://indico.stfc.ac.uk/event/487/`. Accessed: 19/01/2023.

[18] S. Machida *et al.* "Conceptual Design Report: hFFA Task". Yet to be published.

[19] J. Alonso. "Beam Loss Working Group Report". In: *Proc. of 7th ICFA Mini-Workshop on High Intensity High Brightness Hadron Beams*. Lake Como, Wisconsin, USA, 1999, pp. 51–61.

[20] S. Henderson *et al.* "The Spallation Neutron Source Accelerator System Design". In: *Nuclear Instruments and Methods in Physics Research A* 763 (2014), pp. 610–673.

[21] L. Landau. "On the Vibration of the Electronic Plasma". In: *Journal of Physics (USSR)* 10 (1946), pp. 25–34.

[22] F. Sacherer. "Transverse Bunched Beam Instabilities". In: *Proc. First Course of the International School of Particle Accelerators of the 'Ettore Majorana' Centre for Scientific Culture*. 1977, pp. 198–218.

[23] A. Burov. "Head-Tail Modes for Strong Space Charge". In: *Phys. Rev. ST Accel. Beams* 12.044202 (2009).

[24] V. Balbekov. "Transverse Modes of a Bunched Beam with Space Charge Dominated Impedance". In: *Phys. Rev. ST Accel. Beams* 12.124402 (2009).

[25] V. Kornilov and O. Boine-Frankenheim. "Head-Tail Instability and Landau Damping in Bunches with Space Charge". In: *Phys. Rev. ST Accel. Beams* 13.114201 (2010).

[26] J. Gareyte and F. Sacherer. "Head-Tail Type Instabilities in the PS and Booster". In: *Proc. of 9th Int. Conf. High Energy Accel.* SLAC, Stanford, USA, 1974, pp. 341–346.

[27] P. J. Chou and G. Jackson. "Experimental Studies of Transverse Beam Instabilities at Injection in the Fermilab Main Ring". In: *Proc. of Part. Accel. Conf. and Int. Conf. High Energy Accel.* Dallas, Texas, USA, 1995, pp. 3091–3093.

[28] H. H. Gutbrod *et al. FAIR Baseline Technical Report*. Tech. rep. Facility for Antiproton and Ion Research, 2006.

[29] B. Boardman. *Spallation Neutron Source: Description of Accelerator and Target*. Tech. rep. RL-82-006. Rutherford Appleton Laboratory, 1982.

[30] *Science and Technology Facilities Council Digital Media Library, webpage*. `https://images.stfc.ac.uk/`. Accessed: 14/06/2023.

[31] D. C. Faircloth *et al.* "Understanding Extraction and Beam Transport in the ISIS H^- Penning Surface Plasma Ion Source". In: *Rev. Sci. Instrum.* 79 (2008), 02B717.

[32] A. P. Letchford *et al.* "Testing, Installation, Commissioning and First Operation of the ISIS RFQ Pre-Injector Upgrade". In: *Proc. of PAC05*. Knoxville, Tennessee, USA, 2005, pp. 695–697.

[33] N. D. West. "The Rutherford Laboratory 70 MeV Linear Accelerator". In: *Proc. of LINAC79*. Montauk, New York, USA, 1979, pp. 88–93.

[34] S. West *et al.* "Replacement of the ISIS White-Circuit Choke". In: *Proc. of EPAC08*. Genoa, Italy, 2008, pp. 3679–3681.

[35] M. A. Clarke-Gayther *et al.* "Global Beam Loss Monitoring Using Long Ionisation Chambers at ISIS". In: *Proc. of EPAC94*. London, UK, 1994, pp. 1634–1636.

[36] B. Jones *et al.* "Beam Loss Control with Scintillating Monitors at ISIS". In: *Proc. of IPAC2019*. Melbourne, Australia, 2019, pp. 2701–2704.

[37] B. G. Pine *et al.* "Modelling of Diagnostics for Space Charge Studies on the ISIS Synchrotron". In: *Proc. of EPAC 2006*. Edinburgh, Scotland, 2006.

[38] J. Thomason. *ISIS-II Roadmap*. `www.isis.stfc.ac.uk/Pages/ISIS-IIRoadmap.pdf`. Accessed: 19/01/2023.

[39] D. J. Adams *et al. Summary Design Report for the ISIS II RCS and AR Rings*. Tech. rep. TN-ISIS2-008. RAL, ISIS, STFC, 2022.

[40] G. H. Rees. "Interpretation of the Higher Mode, Head Tail Motion Observed on ISIS". In: *Particle Accelerators* 39 (1992), pp. 159–167.

[41] S. Heifets, A. Wagner, and B. Zotter. *Generalized Impedances and Wakes in Asymmetric Structures*. Tech. rep. SLAC/AP110. SLAC, CA, USA, 1998.

[42] W. K. H. Panofsky and W. A. Wenzel. "Some Considerations Concerning the Transverse Deflection of Charged Particles in Radio-Frequency Fields". In: *Review of Scientific Instruments* 27 (1956), p. 967.

[43] K. Y. Ng. *Physics of Intensity Dependent Beam Instabilities*. Singapore: World Scientific, 2006.

[44] A. W. Chao. *Physics of Collective Beam Instabilities in High Energy Accelerators*. John Wiley and Sons, 1993.

[45] A. Wolski. *Beam Dynamics in High Energy Particle Accelerators*. Singapore: World Scientific Publishing, 2014.

[46] S. Y. Zhang and W. T. Weng. *On Solutions of Sacherer Integral Equation*. Tech. rep. BNL-60557. BNL, Long Island, NY, 1994.

[47] R. E. Williamson. *Sacherer's Integral Equation*. Tech. rep. ISIS/IRUGS/TN/1/2018. Rutherford Appleton Laboratory, 2018.

[48] J. L. Laclare. "Bunch-Beam Instabilities - Memorial Talk for F. J. Sacherer". In: *Proc. of 11th International Conference on High-Energy Accelerators*. 1980, p. 526.

[49] R. D. Kohaupt. *Head-Tail Turbulence and the Transverse PETRA Instability*. Tech. rep. DESY 80/22. DESY, 1980.

[50] B. Zotter. *Transverse Mode-Coupling and Head-Tail Turbulence*. Tech. rep. ISR-TH-82-10. CERN, 1982.

[51] A. Hofmann. "Tune Shifts from Self-Fields and Images". In: *CERN Accelerator School: 5th General Accelerator Physics Course*. CERN-94-01. Finland, 1992, pp. 329–348.

[52] E. Métral *et al.* "Beam Instabilities in Hadron Synchrotrons". In: *IEEE Trans. Nucl. Sci.* 63.2 (2016), pp. 1001–1050.

[53] M. Blaskiewicz. "Fast Head-Tail Instability with Space Charge". In: *Phys. Rev. ST Accel. Beams* 1.044201 (1998).

[54] Y. Ho Chin, A. W. Chao, and M. M. Blaskiewicz. "Two Particle Model for Studying the Effects of Space-Charge Force on Strong Head-Tail Instabilities". In: *Phys. Rev. Accel. Beams* 19.014201 (2016).

[55] Y. Ho Chin *et al.* "Chromaticity Effects on Head-Tail Instabilities for Broadband Impedance Using Two Particle Model, Vlasov Analysis, and Simulations". In: *Phys. Rev. Accel. Beams* 20.071003 (2017).

[56] A. Burov. "Convective Instabilities of Bunched Beams with Space Charge". In: *Phys. Rev. Accel. Beams* 22.034202 (2019).

[57] X. Buffat *et al.* "Description of Beam Instabilities in Synchrotron with Wakefields and Space Charge Forces Using the Circulant Matrix Model". In: *Phys. Rev. Accel. Beams* 24.060101 (2021).

[58] O. Boine-Frankenheim and V. Kornilov. "Implementation and Validation of Space Charge and Impedance Kicks in the Code PATRIC for Studies of Transverse Coherent Instabilities in the FAIR Rings". In: *Proc. of ICAP 2006*. Chamonix, France, 2006.

[59] V. Kornilov. "Thresholds of the Head-Tail Instability in Bunches with Space Charge". In: *Proc. of ICFA Advanced Beam Dynamics Workshop on High-Intensity and High-Brightness Hadron Beams (HB'14)*. East Lansing, Michigan, USA, 2014, pp. 240–244.

[60] A. Macridin *et al.* "Simulation of Transverse Modes with their Intrinsic Landau Damping for Bunched Beams in the Presence of Space Charge". In: *Phys. Rev. Accel. Beams* 18.074401 (2015).

[61] *SYNERGIA Code, webpage*. `https://synergia.fnal.gov/`. Accessed: 19/01/2023.

[62] V. Balbekov. "Threshold of Transverse Mode Coupling Instability with Arbitrary Space Charge". In: *Phys. Rev. Accel. Beams* 20.114401 (2017).

[63] V. Balbekov. "Effect of Bunch Shape on its Transverse Mode Coupling Instability Spectrum and Threshold with High Space Charge". In: *Phys. Rev. Accel. Beams* 22.044401 (2019).

[64] T. Zolkin and A. Burov. "SCHARGEV: Vlasov Solver for Space Charge Bunched Beams". In: *Proc. of IPAC2015*. Richmond, Virginia, USA, 2015, pp. 640–642.

[65] T. Zolkin, A. Burov, and V. Lebedev. "Experimental Observation of Head-Tail Modes for Fermilab Booster". In: *Proc. of IPAC2015*. Richmond, Virginia, USA, 2015, pp. 636–639.

[66] T. Zolkin, A. Burov, and B. Pandey. "Transverse Mode-Coupling Instability and Space Charge". In: *Phys. Rev. Accel. Beams* 21.104201 (2018).

[67] E. Métral and M. Migliorati. "Longitudinal and Transverse Mode Coupling Instability: Vlasov Solvers and Tracking Codes". In: *Phys. Rev. Accel. Beams* 23.071001 (2020).

[68] E. Métral. "Intrabunch Motion". In: *Phys. Rev. Accel. Beams* 24.014401 (2021).

[69] E. Métral *et al.* "Destabilising Effect of the LHC Transverse Damper". In: *Proc. of IPAC18*. Vancouver, Canada, 2018, pp. 3076–3079.

[70] A. Oeftiger. *An Overview of PyHEADTAIL*. Tech. rep. CERN-ACC-NOTE-2019-0013. CERN, 2019.

[71] R. Singh *et al.* "Interpretation of Transverse Tune Spectra in a Heavy-Ion Synchrotron at High Intensities". In: *Phys. Rev. ST Accel. Beams* 16.034201 (2013).

[72] *GSI Helmholtzzentrum für Schwerionenforschung GmbH in Darmstadt, webpage.* `https://www.gsi.de/`. Accessed: 19/01/2023.

[73] Y. Shoduba *et al.* "Theoretical Elucidation of Space Charge Effects on the Coupled-Bunch Instability at the 3 GeV Rapid Cycling Synchrotron at the Japan Proton Accelerator Research Complex". In: *Prog. Theor. Exp. Phys.* 1.013G01 (2017).

[74] P. K. Saha *et al.* "Simulation, Measurement, and Mitigation of Beam Instability Caused by the Kicker Impedance in the 3-GeV Rapid Cycling Synchrotron at the Japan Proton Accelerator Research Complex". In: *Phys. Rev. Accel. Beams* 21.024203 (2018).

[75] A. Shishlo *et al.* "The Particle Accelerator Simulation Code PyORBIT". In: *Procedia Computer Science* 51 (2015), pp. 1272–1281.

[76] A. Vlasov. "On the Kinetic Theory of an Assembly of Particles with Collective Interaction". In: *Russ. Phys. J.* 9 (1945), pp. 25–40.

[77] N. Mounet. *DELPHI: an Analytic Vlasov Solver for Impedance-Driven Modes.* Tech. rep. CERN-ACC-SLIDES-2014-0066. CERN, 2014.

[78] Y. H. Chin. *User's Guide for New MOSES Version 2.0 (MOde-coupling Single bunch instability in an Electron Storage ring).* Tech. rep. CERN/LEP-TH/88-05. CERN, 1988.

[79] A. Burov. "Nested Head-Tail Vlasov Solver". In: *Phys. Rev. ST Accel. Beams* 17.021007 (2014).

[80] J. Qiang *et al.* "Recent Advances of Strong-Strong Beam-Beam Simulation". In: *Nuclear Instruments and Methods in Physics Research A* 558 (2006), pp. 351–355.

[81] R. Nagaoka *et al.* "Studies of Collective Effects in SOLEIL and Diamond Using the Multiparticle Tracking Codes SBTRACK and MBTRACK". In: *Proc. of PAC09.* Vancouver, Canada, 2009, pp. 4637–4639.

[82] M. Migliorati and L. Palumbo. "Multibunch and Multiparticle Simulation Code with an Alternative Approach to Wakefield Effects". In: *Phys. Rev. ST Accel. Beams* 18.031001 (2015).

[83] *PyHEADTAIL Code Repository.* `https://github.com/PyCOMPLETE/PyHEADTAIL`. Accessed: 19/01/2023.

[84] J. Nickolls *et al.* "Scalable Parallel Programming". In: *IEEE Hot Chips 20 Symposium (HCS).* Aug. 2008, pp. 40–53.

[85] G. Rumolo and F. Zimmermann. *Practical User Guide for HEADTAIL.* Tech. rep. SL-Note-2002-036-AP. CERN, 2002.

[86] J. Struckmeier *et al.* "On the Stability and Emittance Growth of Different Particle Phase-Space Distributions in a Long Magnetic Quadrupole Channel". In: *Particle Accelerators* 15 (1984), pp. 47–65.

[87] A. Oeftiger and S. Hegglin. *Space Charge Modules for PyHEADTAIL.* Tech. rep. CERN-ACC-NOTE-2016-342. CERN, 2016.

[88] M. Bassetti and G. Erskine. *Closed Expression for the Electrical Field of a Two-Dimensional Gaussian Charge.* Tech. rep. ISR-TH-80-06. CERN, 1980.

[89] R. W. Hockney and J. W. Eastwood. *Computer Simulation Using Particles*. Taylor and Francis Group, 1988.

[90] R. E. Williamson *et al.* "Simulation of the Head-tail Instability on the ISIS Synchrotron". In: *Proc. of ICFA Advanced Beam Dynamics Workshop on High-Intensity and High-Brightness Hadron Beams (HB'14)*. East Lansing, Michigan, USA, 2014, pp. 113–117.

[91] R. E. Williamson, B. Jones, and C. M. Warsop. "Development of Physics Models of the ISIS Head-Tail Instability". In: *Proc. of ICFA Advanced Beam Dynamics Workshop on High-Intensity and High-Brightness Hadron Beams (HB'16)*. Malmö, Sweden, 2016, pp. 155–159.

[92] R. E. Williamson *et al.* "Measurements and Damping of the ISIS Head-Tail Instability". In: *Proc. of ICFA mini-Workshop on Mitigation of Coherent Beam Instabilities in Particle Accelerators (MCBI 2019)*. Zermatt, Switzerland, 2019, pp. 357–361.

[93] C. M. Warsop. "Special Diagnostic Methods and Beam Loss Control on High Intensity Proton Synchrotrons and Storage Rings". PhD thesis. Phys. Dept., Sheffield University, UK, 2002.

[94] R. E. Williamson *et al.* "Beam Loss Mitigation for High Intensity Operation at ISIS". In: *Mitigation Approaches for Storage Rings and Synchrotrons*. Virtual Workshop, 2020.

[95] C. M. Warsop *et al.* "Understanding the High Intensity Behaviour of the ISIS RCS and the Lessons for ISIS II Designs". In: *5th ICFA Mini-Workshop on Space Charge*. Knoxville, Tennessee, USA, 2022.

[96] R. E. Williamson *et al.* "Analysis of Measurement Errors in Residual Gas Ionisation Profile Monitors in a High Intensity Proton Beam". In: *Proc. of EPAC08*. Genoa, Italy, 2008, pp. 1317–1319.

[97] E. Métral *et al.* "Simulation Study of the Horizontal Head-Tail Instability Observed at Injection of the CERN Proton Synchrotron". In: *Proc. of PAC07*. Albuquerque, New Mexico, USA, 2007, pp. 4210–4212.

[98] D. Posthuma de Boer. Personal communication.

[99] E. Métral. "Intrabunch Motion in the Presence of Mode Coupling". In: *5th Mini-Workshop on Space Charge, presentation*. Knoxville, Tennessee, USA, 2022.

[100] A. Letchford. "Upgrades and Developments at the ISIS Linac". In: *Proc. of LINAC2022*. Liverpool, UK, 2022, pp. 1–6.

[101] E. Koukovini-Platia *et al.* "Source of Horizontal Instability at the CERN Proton Synchrotron Booster". In: *Phys. Rev. Accel. Beams* 22.124201 (2019).

[102] X. Buffat and H. Bartosik. "Transverse Mode Coupling Instability with Space Charge at the CERN SPS". In: *5th Mini-Workshop on Space Charge, presentation*. Knoxville, TN, USA, 2022.

[103] I. Béjar Alonso *et al. High-Luminosity Large Hadron Collider (HL-LHC) Technical Design Report*. Tech. rep. CERN-2020-010. CERN, 2020.